The Design and Manufacture of Advanced Functional Composite Materials

A thesis submitted to The University of Manchester for the degree of

Doctorate of Philosophy

In the Faculty of Science and Engineering

2021

Olubukola Rufai

School of Natural Sciences

Department of Materials

Table of Contents

List of Figures

List of Tables

Abbreviations and Symbols

ASTM	American society for testing materials
BY	Braiding yarn
CF	Cover factor
CMC	Ceramic matrix composites
DOF	Distributed optical fibre
FBG	Fibre Bragg grating
FRP	Fibre reinforced polymer
FVF	Fibre volume fraction
FWHM	Full width at half maximum
GFRP	Glass fibre reinforced polymer
IFSS	Interfacial shear strength
OF	Conventional optical fibre
OFDR	Optical frequency domain reflectometry
OTDR	Optical time-domain reflectometry
MBOF	Micro-braided optical fibre
MMC	Metal matrix composite
PTFE	polytetrafluoroethylene
PMC	polymer matrix composites
SEM	Scanning Electron Microscope
SHM	Structural health monitoring
VARIM	Vacuum-assisted resin infusion moulding
2D	Two dimensional
3D	Three dimensional

Abstract

Optical fibre sensors are crucial in Structural Health Monitoring (SHM) applications for quasi-distributed and distributed sensing capability. This thesis reports on the progress made in improving the sensing performance of optical fibres (Fibre Bragg grating and distributed optical fibre) through the textile manufacturing process of micro-braiding. A novel micro-braiding technique is utilised to optimise the conventional optical fibre to improve their mechanical properties and handling during its installation for the manufacturing process. By comparing the tensile properties of the micro-braided and conventional optical fibres, experimental results show 85% improvement in the strain at failure for the micro-braided optical fibre. Also, the effect of embedding both micro-braided and conventional optical fibre in composite was investigated by a three-point bend test. Overall, the mechanical performance of the composite was not affected by the presence of micro-braided optical fibre.

A distributed optical fibre (DOF) sensor was embedded between glass fibre fabric plies during manufacture; part of the DOF length was micro-braided using glass fibres, while the remaining length was left 'bare' (as-received condition). *In situ* and real-time strain measurement during the laminate infusion and curing processes was completed. Cure monitoring of composite materials using different fibre orientations, sensor locations, raw materials, and manufacturing methods has been widely studied. However, no consensus was reached due to differences in raw materials, temperature profile, manufacturing method, fibre orientation, and sensor location. The manufactured composite plate was then subjected to repeated loading during a quasi-static four-point bending test, and the strain development along the length of the DOF was recorded. Comparable results were obtained from the micro-braided and bare sections of the DOF, showing the suitability of micro-braided optical fibres for real-time strain monitoring in composite structures. The micro-braided DOF facilitates handling for automated manufacturing methods and can be used to follow the full life cycle of a composite from fabrication till end-of-life.

The use of the micro-braided and conventional optical fibre for strain monitoring during braiding of preforms was also explored. The importance of micro-braiding was displayed on the grating part of the FBG sensor during the interlacement of the braiding yarn. The micro-braided and bare optical fibre's sensitivity to compression between layers, which causes tension in the layer underneath, was displayed.

Declaration

I declare that no portion of the work referred to in the thesis has been submitted in support of an application for another degree or qualification of this or any other university or other institute of learning.

Copyright Statement

i.   The author of this thesis (including any appendices and/or schedules to this thesis) owns certain copyright or related rights in it (the "Copyright") and she has given The University of Manchester certain rights to use such Copyright, including for administrative purposes.

ii. Copies of this thesis, either in full or in extracts and whether in hard or electronic copy, may be made only in accordance with the Copyright, Designs and Patents Act 1988 (as amended) and regulations issued under it or, where appropriate, in accordance with licensing agreements which the University has from time to time. This page must form part of any such copies made.

iii. The ownership of certain Copyright, patents, designs, trademarks and other intellectual property (the "Intellectual Property") and any reproductions of copyright works in the thesis, for example graphs and tables ("Reproductions"), which may be described in this thesis, may not be owned by the author and may be owned by third parties. Such Intellectual Property and Reproductions cannot and must not be made available for use without the prior written permission of the owner(s) of the relevant Intellectual Property and/or Reproductions.

iv. Further information on the conditions under which disclosure, publication and commercialisation of this thesis, the Copyright and any Intellectual Property and/or Reproductions described in it may take place is available in the University IP Policy (see http://documents.manchester.ac.uk/DocuInfo.aspx?DocID=2442 0), in any relevant Thesis restriction declarations deposited in the University Library, The University Library's regulations (see http://www.library.manchester.ac.uk/about/regulations/) and in The University's policy on Presentation of Theses

Dedication

This thesis is dedicated to **Almighty God** for his infinite mercies, provision, and guidance throughout this phase in my academic career.

Also, to the memory of my late grandmother, Alhaja Isimot Adamson, for her struggles in helping me pursue my academics even with her little education, maami your legacy lives on. I will forever Love and Cherish you, ma.

Acknowledgements

 I would like to profess my appreciation for the special people in my life. Firstly, my husband, Olufemi Rufai, has always been my most incredible support. You encouraged and motivated me to aim higher even when I thought the journey was difficult. During the Covid-19 pandemic, we experienced a lot of difficulties. I lost five of my family members back home during the last few months of my PhD, which affected me emotionally; you kept on encouraging me. When I had health, mental and physical challenges, you stood by me and cared for our four kids. Thank you for your love and support. My PhD journey brought about the creation of lives, which the timing was God's plan. My beautiful babies Anjolaoluwa, and the triplets Inioluwa, Tiwaloluwa, and Tiaraoluwa, you were the reason I kept pushing myself and striving harder. I am so happy and blessed to have you all and hope that my PhD achievement will motivate your academics.

My sincere appreciation goes to my PhD supervisor Dr Matthieu Gresil; thank you for the advice, encouragement, positive criticism, and guidance. I would also like to thank Prof. Prasad Potluri, who is also my PhD supervisor, for suggestions, advice, ideas, and help all through my research. I am honoured to be one of your protégé and hope to pass on the expertise to my students and colleagues back in Nigeria.

I would like to thank my sponsors, Schlumberger Foundation for women in STEM, for providing financial support. I am very much indebted to the Foundation for providing a platform for me in a male-dominated field.

I would also like to acknowledge Prof. Constantinos Soutis for his advice and encouragement.

I also thank my colleague Dr Mayank Gautam for moral support and training me to use the braiding machine. Dr Roy Shankhachur, Dr Aurelia Muller, Dr Neha Chandarana, and my other colleagues that helped me at different stages in my research.

I would also like to thank the staff of North West Composite Centre (NWCC) and National Composite Certification and Evaluation Centre (NCEFF), Dr Alan Nesbitt, Dr Chris Cowan, Mrs Carole Lever, Mr Stuart Morse, Mr Andy Zadoroshnyj and Ms Tracey Winspear for their help and support during my experiment and in the procurement of materials.

I would also like to appreciate my colleagues and mentors at the University of Lagos, Nigeria, especially Prof G.I. Lawal and Dr B.O. Bolasodun. I am very grateful to you for constantly

checking on my progress and encouraging me. I am happy to bring back a wealth of knowledge and ideas.

Finally, I would like to thank my family and friends for their patience and understanding during my PhD studies.

Chapter 1: Introduction

Composite materials are becoming increasingly valuable in a plethora of engineering applications because they offer advantages over traditional metallic materials like high specific strength and stiffness, good fatigue resistance, excellent corrosion resistance, and highly tailorable physical properties. The application of composite materials generally begun only in the aerospace industry in the 1970s. Nowadays, after over three decades, they are standard materials in rail, marine, wind energy, pressure vessels, automobile, aerospace, and sporting equipment and are currently making their way into many more applications [1].

During the manufacture of composites, flaws, such as voids, inclusions, dry spots, resin-rich regions, and several other imperfections, can be introduced [2,3]. These defects affect the operating performance of the composite. Also, structures are subjected to stresses and fatigue during service life, and they may unpredictably fail and cause loss of lives, properties, and money. Structures in areas of disasters (such as storms and earthquakes) may seem undamaged outside while the inside structure elements are failing. A system that can predict issues before damage occurs is desirable, so measures can be implemented to reinforce the structure and avoid catastrophic failure.

Non-destructive techniques (NDT) are employed to detect, locate and characterise defects and damage in composite structures through; electromagnetic methods [4,5], ultrasonic scanning [6,7], shearography [8,9], acoustic emission (AE) [10–12], simultaneous eddy current thermography [13,14] among others. NDT requires regularly scheduled maintenance of structures, which usually necessitate removing the test-piece from the structure, stopping working operations, consuming time, and leading to economic losses. Hall sensor, flux gate, and pick up coil are types of sensors used to determine magnetic flux density in eddy current test and magnetic flux leakage (MFL) [15]. Also, an acoustic emission test is achieved by coupling piezoelectric sensors on the surface of the structure for strain measurement [16]. These sensors cannot be embedded easily in structures and susceptible to electromagnetic interference. For these reasons, recent research deals with the fast-growing technique of Structural Health Monitoring (SHM); it assesses the state of structural health in real-time and, through appropriate data processing and interpretation, may predict the remaining life of the structure [17]. The sensory nerves in the human body act as a network that relays messages back and forth between the brain and some other parts of the body and makes it possible to

communicate with the outside world. The aircraft behaves similarly to the human body through the smart sensors in SHM structures that let us know what is happening in a structure by sending data to the processing unit through the communication bus, as depicted in Figure 1.1.
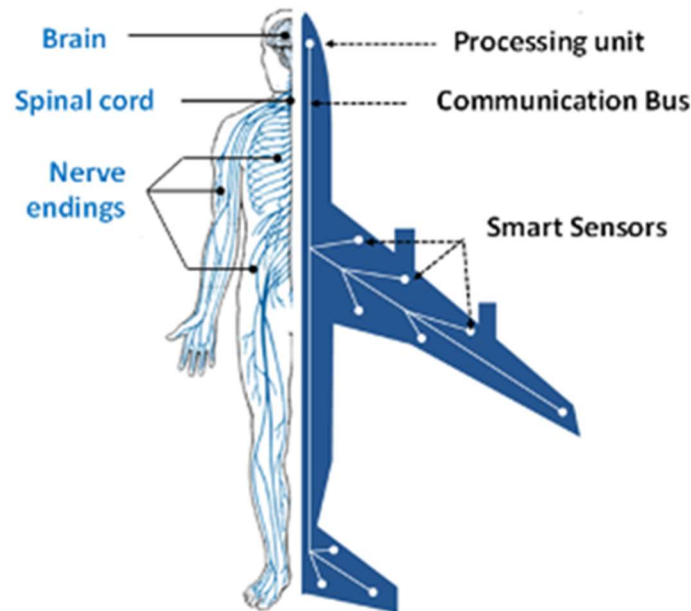
Figure 1.1 Analogy between the nervous system and a structure with SHM.

The vital step in achieving an SHM system is the potential of incorporating reliable and durable sensing techniques. These include the application of sensors such as; optical fibres, piezoelectrics, magnetostrictive (sensors restricted to ferromagnetic materials), and self-diagnosing fibre reinforced composites. Piezoelectric sensors have the disadvantage of only being surface mounted with sensitivity to the local area near the sensor and requires many sensors with lots of connecting wires. The self-diagnosing fibre reinforced composites are only capable of monitoring strain up to a point just before the fibre fracture, making them unsuitable for continuous monitoring.

The most common optical fibres that readily meet the need of SHM are Fibre Bragg Grating (FBG) sensor for localised and quasi-distributed (point-point) sensing and distributed optical fibre (DOF) for distributed sensing. Because of their size, ability to be multiplexed, immunity to electromagnetic interference, strain and temperature measurement, low attenuation, high-temperature resistance, and high sensitivity to external perturbation [18–21]. For these reasons, numerous researchers used optical fibres as embedded and surface sensors [22–30]. Optical fibre sensors have been used to successfully monitor the strain change during the life-cycle of

composite structures [31,32]. However, the optical fibres exhibit drawbacks such as brittleness and easy to break in bending, ease to break at low strain (~0.8%) [33,34], which makes their handling during installation difficult and generation of localised residual stress due to contact of the fibre with a hard surface.

Improvement of SHM can be achieved by enhancing the sensing technique, which makes up the integral part. It's been aforementioned earlier that the optical fibre sensor is the most commonly used of all sensors because of the properties they possess. However, because of the disadvantage of being brittle and ease of breakage, the focus of the thesis will be on the process of optimising them to improve their handling and mechanical properties.

The textile manufacturing process of braiding will be implemented to achieve a micro-braided layer which will act as a protective layer on the optical fibre. Micro-braiding involves braiding at the micro-level, making it hard to observe because of the small yarn tex (represents the mass of yarn in grams per 1000 linear meters). The process mentioned above is novel, and as such, an optimised process needs to be developed to achieve a micro-braided optical fibre. The braiding process involves the interlacement of 3 or more yarns such that they cross one another in a diagonally overlapping pattern. Achieving an effective micro-braid requires the implementation of the measures below;

- The selection of the braiding yarn, which could be either monofilament or multifilament.
- A 24 carrier maypole braiding machine was employed for micro-braiding. The optimum selection of the location of carriers and the number of bobbins to achieve full coverage of the optical fibre at a small diameter was intended.
- The effective positioning of the optical fibre such that it is well-aligned at the braiding centre without damage was achieved using a tension device.
- To achieve optimum braiding, the selection of the braiding yarn's optimum tension such that the interlacement is not too slack or overly strained, considering that 33 tex glass tow are susceptible to breakage at very high tension, is essential.
- The overall time taken to achieve micro-braiding includes the setup and micro-braiding time. The micro-braiding time was optimised by setting the machine speed and take-up speed to achieve braiding at the lowest time without damage to the optical fibre.

This process can be a bit challenging because the optimisation process needs to be implemented such that the sensitivity of the optical fibre remains intact without damage.

1.1 Research Aim

This project aims to develop a novel technique of optimising a conventional optical fibre (OF) through the textile manufacturing process of braiding; to improve the handling and mechanical property of the optical fibre. In the as-received state, an optical fibre typically has no flaw on the surface. However, handling and during processing/installation of optical fibres may lead to the introduction or growth of flaws on the surface. Through the novel concept of micro-scale braiding, a micro-braided optical fibre (MBOF) will be manufactured to achieve a protective surface that inhibits the introduction/growth of flaws.

1.2 Research objectives

This research has been carried out to develop a micro-braided optical fibre for SHM through the textile manufacturing process of braiding. An optimised process will be established to achieve safe micro-braiding at a limited time through trials and error. Multifilament S-glass fibre will be used to micro-braid the optical fibre because of its multiple fibres with small diameters and also the ability to maintain its strength in a vast range of conditions. Challenges and limitation encountered during the micro-braiding process will be examined to suggest a possible solution. The physical and mechanical characterisation of the MBOF is a crucial part of the development and process for predicting its behaviour in service.

Real-time health monitoring of composite structure plays an essential role in evaluating their performance and integrity. The MBOF and OF will be embedded in the composite during manufacturing to monitor the full process by measuring residual strain. Strain monitoring in composite subjected to mechanical four-point bending will be investigated with the embedded MBOF and OF to determine the ability of the MBOF to detect the initiation and progression of damage as loading increases.

1.3 Outline of the thesis

This thesis is divided into seven chapters that describe and discuss the investigations conducted in this study to optimise optical fibre to monitor a composite material's full life.

A detailed literature review is accomplished in chapter 2 by overviewing braiding technology and various braid architecture achievable, and the different optical fibres sensing technology used for Structural Health Monitoring (SHM). Understanding the operating principle of the optical fibres and their applications is also outlined. In chapter 3, the manufacturing process involved in the production of micro-braided optical fibres has been conducted. Braid parameters utilised for optimum micro-braiding of optical fibres were discussed. Details of materials selection, test equipment, composite manufacture and experimental procedures adopted for mechanical test and characterisation was presented. This is followed by chapter 4, where results from the processes involved in the characterisation and effect of embedding micro-braided and conventional optical fibres in composite laminate are analysed. Cure monitoring of composite laminate embedded with micro-braided and conventional optical fibre has been discussed in chapter 5. Details of strain monitoring during braiding of tubular preforms, which further exhibits the possibilities of utilising micro-braided optical fibres are discussed in chapter 6. Detailed conclusions and recommendations for possible future research of the studies in this thesis are presented in chapter 7.

1.4 List of research publications

1. Olubukola Rufai, Neha Chandarana, Mayank Gautam, Prasad Potluri, and Matthieu Gresil "Cure monitoring and structural health monitoring of composites using micro-braided distributed optical fibres" *Composite Structures* 2020, Vol. 254 1-9.

2. Olubukola Rufai, Mayank Gautam, Prasad Potluri, and Matthieu Gresil, "Optimisation of optical fibre using micro-braiding for structural health monitoring" *Journal of Intelligent Materials Systems and Structures* 2019, Vol. 30(2) 171-185.

Conference presentation

1. Olubukola Rufai, Matthieu Gresil, Prasad Potluri, and Mayank Gautam "Utilisation of optimised optical fibres for structural health monitoring" 9th European Workshop on Structural Health Monitoring. Hilton Manchester, 10th – 13th July 2018.

2. Olubukola Rufai, Mayank Gautam, Prasad Potluri, and Matthieu Gresil "Optimisation of optical fibres for structural health monitoring through micro-braiding" 11th

International Workshop on Structural Health Monitoring. Stanford University (California), 12th -14th September 2017.

Chapter 2: Literature Review

In this chapter, a comprehensive review of the literature and references relevant to this research has been conducted. The first section of the literature describes the general understanding, manufacture, and importance of composite materials. The second section explains the textile process of braiding, the machinery, and the importance of different braid architecture. The final section describes the importance of optical fibres in structural health monitoring (SHM), their application, and durability.

2.1 Composites

Composites are materials that contain two or more chemically and physically different phases separated by a distinct interface. The combination is such that the system achieved beneficial structural or functional properties unattainable by any constituent alone [35]. The constituent materials of a composite act together to give the necessary mechanical strength or stiffness. Composite materials comprise two or more distinct phases, such as the matrix and reinforcement phases, with its properties significantly different from those of any constituents. In composites, the reinforcing materials are embedded within a matrix material. The primary role of the reinforcing material is to reinforce the strength and stiffness. In contrast, the matrix contributes to several other composites' properties, such as transfer externally applied loads to the reinforcement and protects the reinforcement from mechanical, physical, chemical, and biological degradation. Strong fibres cannot be used alone in composite due to their low sustainability against compressive or transverse loads. That is why the matrix is weaker and less stiff than reinforcement and is used as a binder to hold the fibres together and provide protection to the fibres against environmental attack.

Before the innovation of composite materials, plastics, ceramics, and metals were the most popular and available engineering materials. Each of them has some distinct advantages and uniqueness to serve specific engineering purposes and some limitations. But composite materials come with a couple of superior properties over all other engineering materials. Some of the distinctive features of composites materials are [36–39]: superior specific strength, superior specific stiffness, corrosion resistance, high specific modulus, excellent corrosion resistance, and fatigue resistance. Because of these outstanding properties, the usage of

composite materials in various industries has increased, and understanding the constituent materials for further improvement in properties is paramount.

The matrix material of a composite is classified into; polymer, metal, or ceramic; hence composite materials are classified as polymer matrix composites (PMC), metal matrix composite (MMC), and ceramic matrix composites (CMC).

The majority of composites, Glass Fibre Reinforced Polymer (GFRP) and Carbon Fibre Reinforced Polymer (CFRP), are based on the polymer matrix. PMCs' development for structures started in the 1950s, and they are by far the most common fibre reinforced composite material in use today. The matrix is a crucial factor determining the characteristics of a composite material. This thesis is focused on polymer matrix composite precisely thermoset.

Fibres are the principal load-carrying component in fibre reinforced polymer (FRP). The effectiveness of fibres in composite materials depends on the size, type, volume fraction, and fibres orientation in the matrix. A large variety of fibre types are available for engineering fibre reinforced composite materials. The most common fibre types are glass fibre and carbon fibre. Glass fibre composites are popular for applications such as boats, body parts of vehicles, small aircraft, wind turbine blade, X-ray beds, computers, durable goods, and consumer goods applications because of their low cost [40,41]. They possess useful bulk properties like hardness, transparency, resistance to chemical attack, strength, and flexibility. The comparative strength with carbon fibre is less, but the cost and simple manufacturing technology make glass fibre popular in low-end applications.

Mishra et al. [42] investigated the level of improvement on the mechanical property by introducing glass fibre into bio fibre. Pineapple leaf fibre (PALF) and sisal fibre were incorporated with varying glass fibre percentages ranging from 0 - 12.9 wt %. It was reported that Ultimate tensile strength (UTS) of PALF/glass fibre hybrid composite increased at 8.6 wt % addition of glass fibre. An improvement in tensile strength was observed as the addition of glass fibre increased to 5.7 wt % in sisal/glass fibre hybrid composite. However, a 10% decrease in tensile strength was observed as the addition of glass fibre increase to 12.9 wt %. Flexural strength of PALF/glass hybrid increased from 85.61 to 101.25 MPa as glass fibre content increased from 4.3 to 12.9 wt%, a 25% increase was observed at 2.8 wt % addition of glass fibre for sisal/glass fibre hybrid composite.

Ramesh et al. [41] investigated the mechanical properties of sisal-jute-glass fibre reinforced polyester (GFRP) composite. The composite consisted of 5 layers fabricated by positioning

glass fibre at the top, middle, and bottom and then sisal and jute at the 2nd and 4th layers. Improved tensile strength was observed in the jute-GFRP specimen, followed by sisal-jute-GFRP and sisal-GFRP composite. It was reported that the UTS of sisal-GFRP, sisal-jute-GFRP, and jute-GFRP composites are 176.20, 200, and 229.54 MPa, respectively. Sisal-jute-GFRP showed better flexural properties compared to the other composite samples. The maximum impact strength was observed in sisal-GFRP followed by sisal-jute-GFRP.

Gojny et al. [43] investigated the influence of modifying nanoparticles on fibre reinforced composite mechanical properties. GFRP composite was fabricated using carbon nanotubes (CNTs) modified epoxy as a matrix. They discovered that the control sample (GFRP) showed better tensile strength than the nanotube-reinforced sample.

Davoodi et al. [44] investigated the mechanical properties of hybrid kenaf/glass-reinforced epoxy composite. The samples were prepared so that two layers of kenaf and three layers of glass fibre were individually attached to the mould frame. The reinforcement was infused with a mixture of epoxy and hardener before curing at 85ºC for 1 hr. Results show that tensile strength and Young's modulus of the hybrid composite were higher than glass mat thermoplastic (GMT) with an increase of 42 and 114%, respectively.

Aramide et al. [45] investigated composite laminate's mechanical properties using woven-mat glass fibre and polyester resin. Six samples were prepared such that glass fibre content varied at an interval of 5% from 5 to 30%. Results show that UTS and Young's modulus increases as the glass fibre content increase with maximum values of 2.03 MPa and 110.32 MPa. Improvement in the composite laminate's mechanical property was due to the glass fibre reinforcement's high strength.

From the literature cited, it is determined that glass fibres have been used for improving tensile strength, UTS and Young's modulus of hybrid natural fibre composite materials. However, this thesis will be attempting the novel process of improving the handling and mechanical properties of optical fibre using glass fibre, and it will be used for composite manufacture.

Carbon fibre provides tensile modulus of 291 GPa [46], which is more than ferrous alloys [47], and most importantly, the strength to weight ratio is superior. For this reason, carbon fibre composites have replaced the metallic parts used in most aircraft and military applications. Table 2.1, 2.2, and 2.3 shows the properties of some commercially available reinforcing fibres and thermoset resins and some structural materials' mechanical properties. It was observed that out of the glass fibres, S-glass possesses better properties in terms of tensile strength, Young's modulus, and elongation. However, carbon fibre has a higher Young's modulus when

compared to glass fibres. Regardless of this, glass fibres still find use in structural applications when considering low cost and properties [45].

It can be seen from the data in Table 2.2 that epoxy shows a significantly higher range of values for Young's modulus and tensile strength compared to other resin.

Table 2.1 Typical properties of some reinforcing fibres [40,48]

Fibre	Density (g/cm^3)	Young's modulus (GPa)	Tensile Strength (GPa)	Elongation (%)
E-glass	2.5	72.3	3.445	4.8
S-glass	2.5	86.9	4.890	5.7
Carbon (Std. Pan-based	1.4	230-240	4.0	1.4-1.8
C-glass	2.5	68.9	3.310	4.8
A-glass	2.4	68.9	3.310	4.8
D-glass	2.11-2.14	51.7	2.415	4.6
R-glass	2.5	85.5	4.135	4.8

A= Alkali glass, C= Chemical glass, D = Low dielectric constant glass, E = Electrical glass, R = Reinforcement glass and S = Strength glass

Table 2.2 Typical properties of thermoset polymers [48]

Thermoset	Density (g/cm^3)	Young's modulus (GPa)	Tensile strength (MPa)	Compressive strength (MPa)	Elongation (%)	Cure shrinkage (%)
Epoxy	1.1-1.4	3-6	35-100	100-200	1-6	1-2
Polyester	1.2-1.5	2-4.5	40-90	90-250	2	4-8
Vinyl ester	1.2-1.4	3.1-3.8	69-83	100	4-7	-

Table 2.3 Mechanical properties of structural materials [49]

Reinforcing Material	Yield Strength ksi (MPa)	Tensile Strength ksi (MPa)	Elastic Modulus ksi (GPa)	Strain at Break %
Steel	40-75 (276-517)	N/A	29,000 (200)	N/A
Glass FRP	N/A	70-230 (480-1,600)	5,100-7,400 (35-51)	1.2-3.1
Basalt FRP	N/A	150-240 (1,035-1,650)	6,500-8,500 (45-59)	1.6-3.0
Aramid FRP	N/A	250-368 (1,720-2,540)	6,000-18,000 (41-125)	1.9-4.4
Carbon FRP	N/A	250-585 (1,720-3,690)	15,900-84,000 (120-580)	0.5-1.9

In the present work, only glass fibre reinforced polymer specimens were used for experimental purposes. The reason for selecting S-glass fibre is because of the high strength and stiffness it possesses when compared to all other fibre reinforcement.

2.1.1 Glass fibres

Silica (SiO_2) sand is used to make glass fibres; SiO_2 is also the essential element of quartz, a naturally occurring rock. If SiO_2 is heated above 1200°C/2192°F then cooled to ambient temperature, it crystallises and becomes quartz. Glass is produced by changing the temperature and cool-down rates. If SiO_2 is heated to 1720°C/3128°F then cooled rapidly, crystallisation can be prevented. The process yields the amorphous or randomly ordered atomic structure known as glass. Glass fibres are manufactured by drawing molten glass into very fine threads and then immediately protecting them from contact with the atmosphere or hard surfaces to preserve the defect-free structure that is created by the drawing process. Synthetic fibres are as strong as any of the newer natural fibres, but they lack rigidity in their molecular structure. Table 2.4 shows the composition of various glass fibres [50]. It is observed from the table that the percentage of SiO_2 in S-glass is 12% lower than D-glass. However, S-glass has the highest

percentage of Al_2O_3, responsible for improved tensile strength and resistance from a chemical attack in a glass.

Table 2.4 Composition of selected Glass fibre types

	E-glass with Boron	E-glass without Boron	D-glass	ECR-glass	S-,R-and Te-glass	Silica/quartz
Oxide	%	%	%	%	%	%
SiO_2	52–56	59-60.1	74.5	58.2	60–65.5	99.9999
Al_2O_3	12–15	12.1-13.2	0.3	11.6	23–25	-
B_2O_3	4–6	3-5	22.0	-	-	-
CaO	21–23	22.1-22.6	0.5	21.7	0–9	-
MgO	0.4–4	3.1-3.4	-	2.0	6–11	-
ZnO	-	-	-	2.9	-	-
Li_2O	-	-	-	-	-	-
Na_2O	0–1	0.6-0.9	1.0	1.0	0–0.1	-
K_2O	Trace		<1.3	0.2	-	-
TiO_2	0.2–0.5	0.5-1.5	-	2.5	-	-
Zr_2O_3		-	-	-	0–1	-
Fe_2O_3	0.2–0.4	0.2	-	0.1	0–0.1	-
F_2	0.2–0.7	0.1	-	Trace	-	-

2.1.2 Epoxy resin

Epoxy is a thermoset polymer that contains an epoxide group in its chemical structure (one oxygen atom and two carbon atoms); see Figure 2.1. Diglycidyl ether of bisphenol A (DGEBA) contains two epoxide groups, is a low-molecular-weight organic liquid.
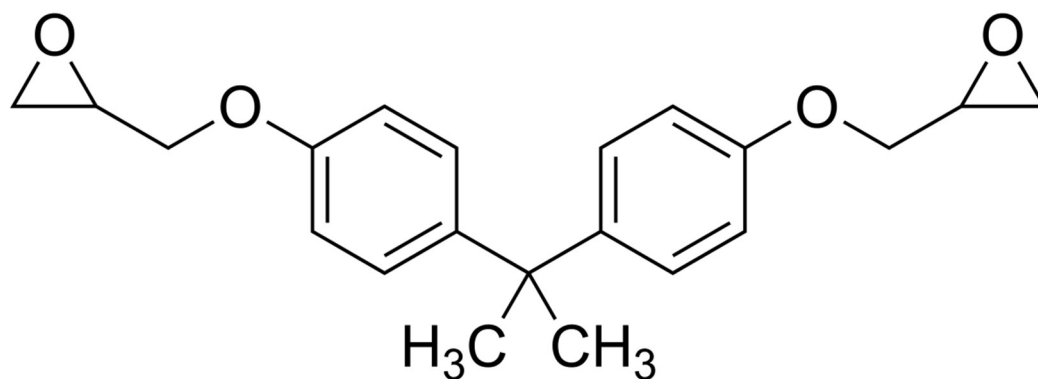
Figure 2.1 Chemical structure of Diglycidyl ether of bisphenol A (DGEBA).

Frequently, various additives can be employed to modify the characteristics of epoxies. For example, diluents are used to reduce the viscosity, while flexibilising agents make the epoxy flexible. Other agents help to protect against ultraviolet radiation. Hardener (usually amine) is used to cure epoxy resin by addition reaction [51]. Amines make bonding with two epoxy sites in two ends of resin and form a complex three-dimensional molecular structure. Curing agents are organic amino acid compounds, and cross-linking is obtained by introducing chemicals that react with the epoxy and hydroxyl groups between adjacent chains. A common curing agent for DGEBA epoxy is diethylenetriamine (DETA). The extent of cross-linking is a function of the amount of curing agent added. Generally, 10–15% by weight of amines or acid anhydrides is added. Then they constitute part of the epoxy structure. An accelerating additive can speed up the curing process. However, as cross-linking increases, characteristics such as stiffness, strength, and glass transition temperature increases, but toughness mainly decreases [52].

Epoxy resins are more costly than polyesters, but they feature better moisture resistance, excellent corrosion resistance, high strength to weight ratio, dimensional stability, lower shrinkage on curing (about 3%), higher working temperature and good adhesion with glass fibres. A substantial fraction of high-performance polymer matrix composites are fabricated with thermosetting epoxies.

Gonçalez et al. [53] investigate the modification of epoxy network with a block copolymer of polybutadiene and bisphenol A diglycidyl ether (DGEBA)-based on epoxy resin. Carboxyl end-capped (CTPB) was synthesised by reacting rubber (HTPB) with maleic anhydride in a stoichiometric epoxy/anhydride. Composite was manufactured by stacking five layers of already prepared carbon fibre/epoxy system pre-preg with a thickness of 5 mm. A tensile test

was carried out on the epoxy system and the corresponding composite. Results show that the composite prepared with the epoxy system modified with (CTPB) gave higher tensile yield stress and Young's modulus of 425 ± 50 MPa and 15.5 ± 2.0 GPa, respectively. The finding was due to rubber dispersion in the epoxy system, which gives additional adhesion between the polar groups of the fibre surface and the modified epoxy matrix.

Iijima et al. [54] investigated the Simultaneous epoxy grafting on SiO_2 nanoparticles during bead milling and their effects on epoxy-based composites' mechanical properties. The importance of making composite by grafting epoxy on Polyethyleneimine- oleic acid (PEI-OA) modified SiO_2 nanoparticles during bead milling and Polyethyleneimine and anionic surfant PEI-AS. Compared to plain resin, epoxy dispersed with SiO_2 nanoparticle modified with PEI-OA and PEI-AS shows an increase in strain at fracture from $10.6 \pm 1.6\%$ to $13.0 \pm 3.4\%$ and 14.0 ± 2.7 respectively. This behaviour is because the epoxy resin reacts partly with the un-complexed free amine in the PEI-complex in the SiO_2 nanoparticles, improving the adhesion between the SiO_2surface and the resin.

According to Bulut et al. [55], they made use of epoxy (HEXION-MGS L285) and hardener (HEXION-MGS H285) modified with borax (Bx), perlite (Pr), and sewage sludge ash (SSA) as the primary toughening material. In addition, the researchers investigated the interlaminar shear strength (ILSS) properties of S-glass/epoxy composites. Bx and SSA's weight content varied from 0 to 20% at 5% interval, and Pr filler was in the ratio of 0, 1, 3, 5, 10 wt %, respectively. ILSS was characterised using the short beam shear (SBS) test. Results show that epoxy modified with 10% Br filler had the highest ILSS of 44.6% compared to unmodified GFRP. The lowest value was observed in the Pr filler attributed to the poor adhesion characteristics of the Pr particles than other types of the particles.

Jafrey et al. [56] investigated the mechanical properties of hybrid natural fibre (bamboo/jute) using epoxy resin LY556 and hardener HY951. The stacking of the fibres was varied to achieve 4 different samples; A1 (JBJ), A2 (BJB), A3 (JJJ) and A4 (BBB). The experimental result shows that A2 had the highest UTS of 25.39 MPa followed by A4, A1 and A3 with values 24.22 MPa, 23.76 MPa and 21.22 MPa. Also, A2 recorded the highest UFS of 77.12 MPa followed by A4, A3 and A1 with values 64.57 MPa, 56.15 MPa and 44.15 MPa.

The importance of using epoxy as a matrix to bind and toughen the composite was displayed in the cited literature. Improvement in mechanical properties of the reinforcing fibre by the introduction of epoxy resin was also observed.

2.2 Manufacturing of Composites

Several different techniques for fibre reinforced polymer (FRP) composite manufacturing include direct and indirect processes. Composite fabrication can be of various types; when fibre and resin are brought together at the moulding point (direct process), examples are; pultrusion, contact moulding and resin transfer moulding. Indirect processes involve fibre impregnation in resin examples are vacuum-assisted resin infusion moulding (VARIM), compression moulding, hand layup and autoclave moulding.

This thesis is focused on vacuum-assisted resin infusion moulding (VARIM) manufacturing techniques, and braiding will be used as preforming method.

2.2.1 Vacuum-assisted resin infusion moulding (VARIM)

VARIM is a composite manufacturing process involving resin infusion in a mould containing vacuum-tight dry preform fabric. The resin binds the assembly to form a rigid composite. The process is cost-effective, and manufactured composite parts have high strength and quality [57].

The process of VARIM involves the following steps.

- Cleaning the mould with a mould cleaner and release agent to facilitate easy removal of the cured composite laminate.
- Lay-up of dry preform on the mould
- The preparation of vacuum bag by placing peel ply, infusion mesh and attaching the inlet and outlet spiral tube to the lay-up before sealing with sealant tape. A vacuum pump is utilised in removing the air under the bag, and a pressure of one atmosphere is applied to achieve the consolidation of the laminate. Figure 2.2 represents a typical vacuum bagging set up [58].
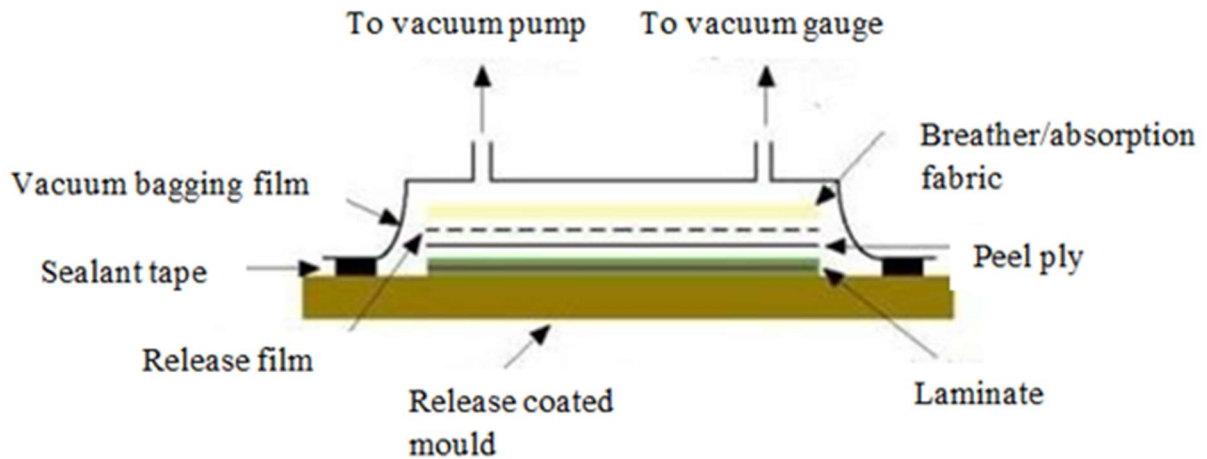
Figure 2.2 Vacuum bagging method of composite manufacture.

Tzetzis et al. [59] investigated the performance of vacuum-assisted resin infused scarf repair using an 800S4/TMS11 8HS glass woven fabric and a 411-200 vinyl ester resin. VARIM techniques were applied to the reinforcement, which was placed along the parent laminate scarf region. The repairs' configuration is denoted as D_1 representing typical aircraft composite repair and D_2, with the first ply placed along the scarf transition region. Three main specimen design was investigated; control specimen, repaired ones of designs (D_1 and D_2) with scarf angle of 2.8° and specimen manufactured according to D_2 at scarf angles of 3.8°and 5.8° respectively. Results show that the repaired specimen's failure load was close to the control sample with values of 1344, 1250 and 1290 N/mm for the control, repaired specimen of design D_1 and D_2, respectively. The result implies that the VARIM technique is a suitable repair procedure.

Zhang et al. [60] developed a silicon rubber sheet (SRS) heater-aided vacuum-assisted resin infusion moulding in shortening curing cycle. A unidirectional (T700SC) carbon fibre fabric was infused with epoxy resin (DGEBA E51). The VARIM process was modified by placing SRSs underneath the aluminium mould and between the vacuum bag and infusion mesh after which the fibre was preheated to 90°C. The laminate was heated from 90°C to 120°C after infusion. The effect of the cooling rate on the properties of the composite was investigated by varying the cooling process; cool in the air, water and air-water. The SRS-modified cure time and conventional VARIM showed that filling and curing time decreased from 300 to 118 s and

661 to 184 s for SVARIM while the cooling time of SVARIM was double the conventional methods. It was also reported that lower residual strain measured with strain gauges in the longitudinal direction was recorded by the traditional compared to SVARIM with the different cooling process. This behaviour was due to the non-uniform temperature distribution in the SVARIM process.

Gu et al. [61] investigated the improvement of mechanical properties of ramie fabric/epoxy composite using VARIM. The fibre preform was compacted by loading and unloading the vacuum cycle twice. Results show that the thickness of the cured laminate did not decrease with the vacuum loading cycle. However, at higher temperature and pressure, the preform's thickness decreased rapidly at 25°C from 2.32 to 2.1 mm and 0.5 MPa from 2.45 to 1.5 mm. Results show that hot compaction improves the composite's tensile and flexural properties but decreases at higher temperature and pressure. This behaviour is because the mechanical performance of the composite degrades at a specific temperature and pressure.

Zhang et al. [62] investigated the effect of rapid curing on the CF/EP composite properties using VARIM. Different curing condition was employed by infusing the resin at 25°C and curing in the oven at 120 °C, adding a 1hr post-cure cycle at 120 °C and preheating the preform before infusing the resin at 80 °C. Results show that the preheated process's flexural strength and ILSS were 29% and 7% higher than the non-preheated process. The result was due to the resin's lower viscosity during infusion, which caused improvement in the fibre's infiltration.

Xia et al. [63] studied the application of the vacuum-assisted resin infusion (VARI) process in calcium carbonate ($CaCO_3$) inorganic nanoparticles impregnation (INI) to improve the mechanical properties of kenaf fibre/polyester composite. Two types of composite were fabricated; (1) with INI-treated kenaf/polyester and (2) untreated kenaf/polyester composites. Results show that the treated fibre/polyester experienced an increase in modulus of elasticity, modulus of rupture, tensile modulus, tensile strength by 33.1%, 64.3%, 22.3% and 67.8%. The result was due to the enhancement in mechanical properties by the nanoparticles filling the fibre voids.

Rydarowski et al. [64] compared the mechanical properties of glass fibre reinforced polymer laminate by hand lay-up and Vacuum-assisted resin infusion method. Both plain weave and chopped strand mat were fabricated alternatively by hand lay-up and VARI method. Results indicated that plain weave fabric had similar fibre volume fraction results; however, for the chopped strand mat, the VARI method had higher value than the hand layup. The higher flexural and impact strength observed in the chopped strand mat was related to the fibre volume fraction in the resin inlet's directions, which resulted from the proper suction of the resin.

The importance of VARIM process is evident from the literature cited. However, it is vital to monitor the composite materials' manufacturing process to identify flaws such as dry regions, delamination, fibre waviness, foreign bodies, voids, and incomplete matrix cure [2,3]. These defects can result in residual stress or reduced dimensional stability of the manufactured composite. Residual stresses and strain are induced during heating and cooling of the fibres and matrix, potentially affecting the composite product's mechanical properties. Differences in the two constituents' thermal expansion coefficients lead to the matrix compressing the fibre, resulting in residual stresses and strains. The ability to monitor the resin flow during infusion and viscosity during curing serves as a potential method for conducting quality control of the final product.

Optical fibre sensors can be used for *in situ* cure monitoring of a composite since embedding them does not interfere significantly with the structure's mechanical properties [65–67]. Insensitivity to electromagnetic interference is another advantage of optical fibres compared with other dielectric analysis techniques [68–70]. Optical fibre sensors for cure monitoring during composite manufacture will be discussed in detail in sub-section 2.9.3.1.

2.3 Interface bond of fibre and matrix

The interface of fibre and matrix are essential factors in the performance of a composite. This condition is because the fibre's effective application strength and stiffness depend on the efficient transfer of load, which can only be achieved through good interfacial bonding. It is thus important to quantify the interfacial properties between the fibre and matrix. The interfacial shear strength of composites can be measured by a test on a single fibre system.

Various test methods have been employed by researchers [71–76] to evaluate interfacial properties such as micro-bond, pull out and push-out tests. Yang et al. [77] have carried out the micro-bond test, which involves a single fibre pull-out to evaluate glass fibre-polypropylene's interfacial shear strength. They observed an interfacial shear strength (IFSS) of 3.3 MPa through a straight-line fitting. However, Hoecker et al. [78] reported an IFSS of 5-6 MPa for glass fibre/polypropylene when under isothermal crystallisation condition and 9 MPa when produced non-isothermally by quenching. Favre et al. [79] also investigated the bonding between fibre and matrix for glass, kevlar and carbon fibre through a pull-out test. They reported good adhesion when the stored energy was enough to complete pull-out without experiencing friction. Poor adhesion was due to the stored energy being too high for complete

extraction of the fibre. Chean et al. [80] evaluated the interfacial adhesion of optical fibre embedded in epoxy vinyl ester resin. They studied the effect of varying the embedded length. They discovered when the length was above 4.9 mm, optical fibre extraction happens, but when above 15 mm, the optical fibre breakage occurred. They also reported that increasing curing time improved interfacial bonding stress. Wang et al. [81] developed an improved micro-bond test method to calculate the IFSS of carbon fibre/epoxy resin. They obtained an average IFSS of 7.08 MPa with a variance coefficient of 28%, which was reported to be lower than those of other researchers.

The most commonly used method for characterising the interfacial property is the pull-out technique. However, it is evident that different results were reported, which could be due to the different materials or method applied.

2.4 Braiding

The history of braiding is quite rich. Braiding began as an art practised by ancient people. Plaiting human hair first employed braiding for personal adornment purposes and has been argued to be as old as human civilisation [82]. Originally a hand process, braiding has evolved into an industrial construction with the modern braiding machine's advent. Although its fundamental operation has prevailed mostly unchanged, the modern braiding machine has undergone improvements in material construction as well as utilising sophisticated computerised controls and electric actuation. The first braiding machine emerged in the 18th century, patented by Thomas Walford, and later improved by Johann Bockmühl and others [83].

Braids have been used to harness the strength and utility of fibres in a simple construction. Chosen for its structural integrity, flexibility, and versatility in product use, braiding has been used to manufacture complex shapes [84,85]. Braided materials are inherently damage tolerant. Virtually any industry can benefit from braided products if it does not already.

Braiding is the method of producing a braided structure that was defined as "a narrow tubular textile structure produced by the intertwining of three or more parallel strands together". The conventional use of these structures was limited to ornamental textile articles; however, industrial braiding equipment's development expanded its use to manufacture cord followed

by rope [86]. Ko et al. [87] presented a chronological history of braided structures evolution in the field of composite materials. The potential of the braided perform as engineered materials specifically for use in composite structures was first explored by researchers in the aircraft company McDonnel Douglas [88]. Meanwhile, attention to braiding for composite manufacturing has increased due to the requirement of a high production rate in manufacturing and flexibility in fibre layup in a different orientation. Braided textile composite has been evaluated for primary aircraft structures due to their formability, damage tolerance, and low-cost manufacturing; with high stiffness to weight ratio, the ability to resist delamination and reinforce shaped parts makes it desirable.

2.4.1 Application of Braids

Braids are used in many industrial applications such as; textile industry, aerospace, civil infrastructures, medical, electrical fields and transportation. Some of the most common applications of braids in the textile industry are the manufacture of cords/laces, domestic ropes, water ski rope, parachute lines, fishing lines, mountaineering ropes and candlewicks.

Braiding has also found use in sporting goods such as baseball bat, golf club, hockey sticks, etc. The use of braided structure in the transportation industry includes; energy-absorbing crash structures in racing cars, truck winch rope, and front end aprons for automobiles. The use of braided structure in the aerospace industry has improved over the years due to high strength, lightweight, non-corroding, high stiffness and low manufacturing cost. It is used to manufacture aircraft engine parts, fan blade containment, aircraft propellers and stator vanes in jet engines. Braiding has also been used in the medical field for various applications such as the manufacture of a stent, dental implant and artificial limbs.

2.4.2 Braiding machinery for composite manufacturing

Braiding has many useful applications in engineered materials and particularly composite materials. Composites can be produced by over-braiding or braiding around a mandrel, and the result is a structure with dramatically varying cross-sections. The construction of composites preforms of complicated shapes is facilitated by utilising a low-cost manufacturing solution of braiding [89]. This inherent conformability of braids offers a simple and efficient alternative for the manufacture of complex shapes. Mechanised braiding is often achieved by the horn

gears' movement carrying bobbins in a serpentine-like path around a track plate. The motion of yarns on one track is clockwise, and the other is anti-clockwise, causing the yarns to interlace, which is only achievable when the yarn is in tension (by the spring tensioner). At the convergence point, the yarns interact as one yarn travels over and the other yarn under. The interlacing of the two yarns is the primary mechanism responsible for the formation of the braided structure. Yarn is wound on bobbins to store the necessary material for a desired length of the braid. The carriers are responsible for transporting the bobbins along with the track plate. The carrier also controls the tension magnitudes and provides constant tension during the braiding mechanism [90,91]. Different types of braiding machine can be used; however, the maypole braiding machine is commonly used to produce braid preforms. Figure 2.3 shows the schematics of the yarn delivery system of a maypole braiding machine.
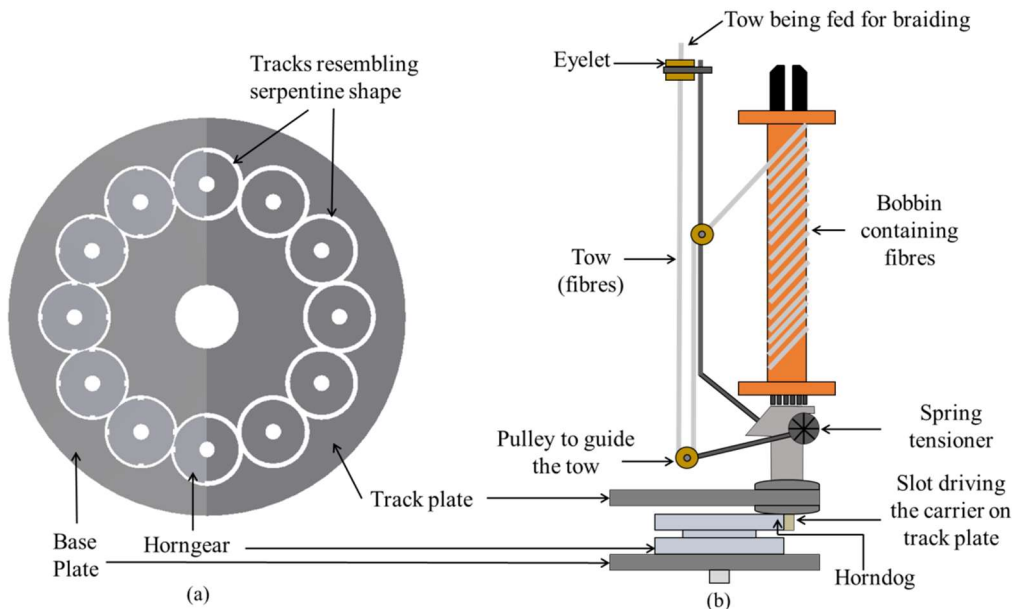
Figure 2.3 Illustration of a braiding machine showing the (a) track plate and (b) Carrier mounted with a bobbin.

A take-up machine's importance is to enable continuous and usable braid by ensuring the braid is drawn smoothly and at a precise uniform rate. Parameters of the braid can be obtained by controlling the take-up of the braid. The take-up machine helps produce consistent braid by maintaining a constant speed relationship to the braiding machine. The take-up machine controls the braid speed and the tension of the braid.

2.5 Classification of braids

The braid structures can be classified into two main groups:

- two-dimensional (2D) braids;

- three-dimensional (3D) braids.

The principal difference between a 2D braid and a 3D braid is the through-thickness interlacement which is not present in a 2D braid. 3D braiding technology is an extension of 2D braiding technology. The fabric is constructed by intertwining or orthogonal interlacing of three or more yarns to form an integral structure through position displacement [52,92–94].

Only 2D braiding technique will be used in this thesis because of the braid architecture that can be developed with the process. Details of the 2D process are provided in the sub-section below.

2.5.1 Two-dimensional braids

Two-dimensional braids (2D) are either biaxial or triaxial in configuration, as seen in Figure 2.4a and b. The most commonly used is the biaxial construction, which has two bias yarn, with yarns in one direction passing under and over the other. Biaxial architecture is a popular structure because the construction is predictable, it has consistency in lay-up, and the braid can match any shape.

(a)   (b)
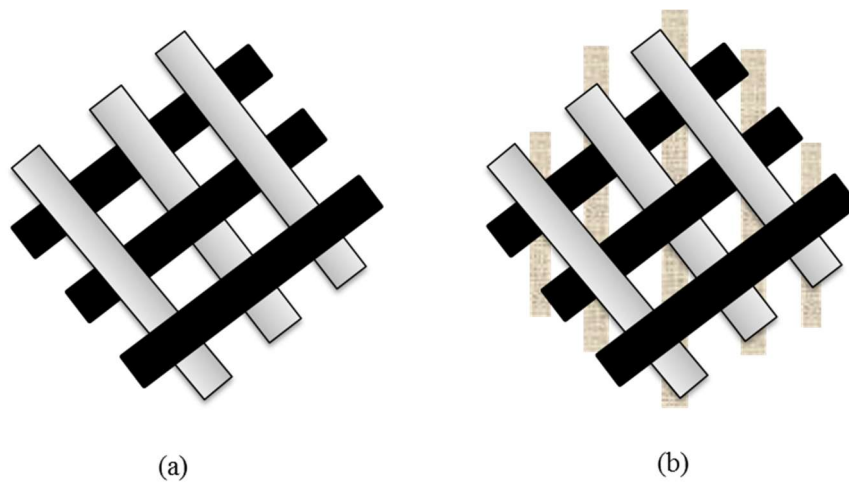
Figure 2.4 (a) Biaxial and (b) Triaxial braid architecture

The third set of longitudinal yarn (zero degrees yarn) positioned parallel to the mandrel is contained in the triaxial braid. The biaxial interlacing yarns contribute to the overall braid performance [95]. They are supplied from a stationary creel or take-up device and fed through the centre of horn gears. The longitudinal yarns are often referred to as axial yarns. The axial yarn provides the braid with its essential characteristics such as tensile and compressive strength and improvement to its modulus in fibre reinforced composite applications [96]. However, the use of these axial yarns can lock the braid's diameter and prevent its natural tendency to expand and contract. During braid interlacement, different repeat pattern can be formed such as;

- Diamond (1/1) yarn crosses over and under the yarn in the opposite direction during braiding, resulting in a diamond braided structure, as represented in Figure 2.5a, similar to the plain-woven fabric structure.

- Regular (2/2) interlacement is represented in Figure 2.5b, and the braid structure is similar to 2/2 twill in woven fabric structure.

- Hercules (3/3) interlacement of yarn results in Hercules braided structure as represented in Figure 2.5c, which as similarity to the 3/3 twill woven fabric structure.

(a) (b) (c)
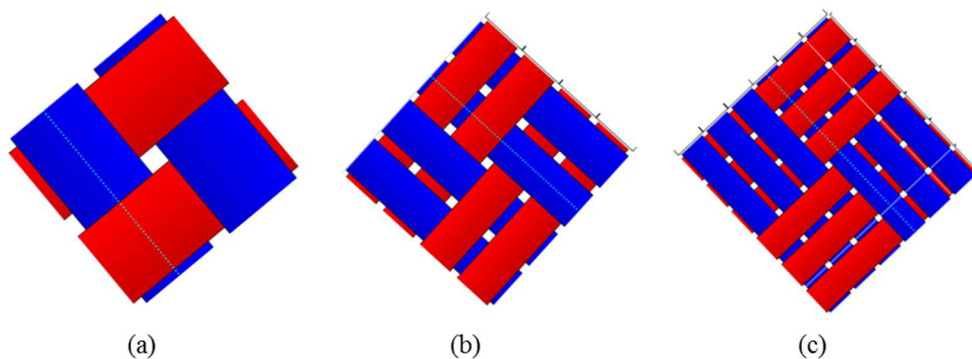
Figure 2.5 Different repeat patterns during braid interlacement: (a) Diamond (1/1), Regular (2/2) and, Hercules (3/3) [97]

2.6 Geometric parameters of braids

The determination of constituent critical parameters during the manufacture of braids is essential for determining the braided preform's mechanical properties [98]. In this thesis,

optical fibres represent the core of a smart braid that can be used as a modified actuator/sensor. The key specifications of a braided preform are braiding angle, cover factor and layer thickness. These specifications are primarily dependent on the take-up speed, the carriers' rotational speed, and the core diameter. Change in any of these parameters influences the braid angle, ultimately affecting the preform's fibre density.

2.6.1 Braid angle

The braid angle can be described as the angle between the braided preform's longitudinal direction (braid axis) and the interlacing yarn (a strand of multiple untwisted filaments), as shown in Figure 2.6. The braid angle can range between 10º and 85º along the braid axis, unlike woven fabric limited to fibre orientations only at 0º and 90º [99].
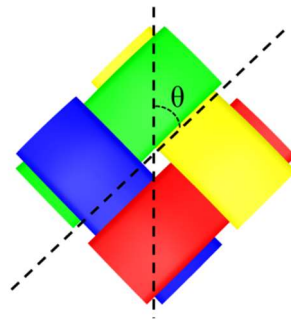
Figure 2.6 Computer-aided drawing of a braid depicting braid angle using TexGen Software [97]

The braid angle can be calculated mathematically from the radius of the mandrel/core, the rotational speed of the braiding machine (ω) and, the take-up speed (ν) as shown in Equation 2.1 [100,101].

$$\theta = tan^{-1}\left(\frac{D\omega}{2v}\right) \tag{2.1}$$

Where θ is the braid angle, $R = D$ is the core/mandrel diameter, ω is the angular velocity, and v is the take-up speed.

Braid angle is an essential parameter in determining the mechanical property of braided preform, according to Tate et al. [102]. They investigated the effect of braid angle on in-plane mechanical properties of carbon/epoxy braided composite. They reported that a decrease of

75%, 70% and 96% in UTS, tensile modulus and Poisson's ratio was observed as the braid angle increased from 25º to 45º. Similar behaviour was also reported by Falzon et al. [103], with an increase in strain to failure, ultimate strength and Poisson's ratio observed at a braid angle of 30º compared to the lower values observed at braid angle of 45º and 60º. However, Del Rosso et al. [105] had a different discovery in terms of the effect of braid angle on the mechanical properties of dry micro-braided Dyneema®SK75 and dry micro-braided Kevlar, respectively. They observed that as the braid angle increased, the strain to failure and the dry microbraids tenacity decreased. However, they observed that the tensile strength of laminates manufactured by filament winding of the dry micro-braid decreased with increasing braid angle[104].

Rajiv et al. [105] studied the effect of fibre architecture parameters on deformation fields and elastic moduli of 2-D braided composites. They manufactured a 2D triaxial braided composite using an AS4 graphite preform impregnated in 1895 epoxy resin. Braid angle, yarn size and axial yarn were varied 45º/75º, 6k/15k (k is thousands of filament) and 12%/16%. The researchers discovered that by increasing the yarn size and keeping braid angle and axial yarn constant, it was found that Young's modulus, shear modulus and Poisson's ratio were the same. When the braid angle increased from 45º to 70º, the longitudinal modulus decreased by 4%, the shear modulus by 65% and Poisson's ratio by 30%. Simultaneously, an increase of 144 % was observed for transverse modulus as the braid angle increases.

The researchers also investigated the effect of axial yarn content. They discovered that increase in axial yarn content caused 100% increase in longitudinal modulus and a 9.7, 40 and 17% decrease in transverse modulus, shear modulus and Poisson's ratio, respectively. It was concluded by the researchers that mechanical properties of triaxially braided preforms are sensitive to braid angle and axial yarn content but not to yarn size.

Birkefeld et al. [106] investigated the characterisation of biaxial and triaxial braids fibre architecture and mechanical properties. They manufactured a biaxial and triaxial regular braid with Tenax HTS 40 12 k F13 multifilament rovings. Three different braided preforms with angles 30º, 45º and 55º were produced. The preforms were infused using vacuum-assisted resin infusion (VARI). A tension test was performed on the six specimens for each configuration. The researcher compared experimental results with analytical results. It was concluded by the researchers that for biaxial braids, according to experimental and analytical findings, non-linear behaviour in the longitudinal and transverse moduli as the braid angle increased from 30º to

55° was observed. For triaxial braids, the longitudinal and transverse moduli show linear dependency with an increase in braid angle.

Omeroglu [107] showed the importance of take-up speed and braid pattern on the tenacity and yield strain. It was concluded that the 2/2 braid pattern at high take-up experienced the highest maximum tenacity and yield tenacity. In comparison, the 1/1 braid pattern at low take-up experienced the highest value of maximum strain and yield strain.

Charlebois et al. [108] investigated the mechanical properties of braided fabrics manufactured using a resin infusion process. The Young's modulus, tensile strength, and Poisson's ratio for the ±35°, ±45° and, ±50° braided glass/epoxy composite compared to UD laminate showed higher Young's moduli which was due to orientation during loading. They reported that the braiding yarn's undulation did not influence the tensile strength of the braided composite. Because the reorientation of fibre was likely to occur during loading, they suggested that they did not experience that during compressive loading. They also reported an increase in braid angle caused a slight increase in Poisson's ratio due to the fibre's orientation and decreased fibre undulation.

Chun et al. [109] have predicted analytically that fibre undulation reduces the tensile moduli of the composite. However, the researcher cited that fibre undulation and intertwining were not severe enough to affect the braided composite's tensile properties. Compression test for all braid angles showed that fibre undulation in the braided reinforcement led to a decrease in the compressive strength at a low braid angle. Stress concentration due to fibre undulation was probably the cause of the drop in the strength of 56% for ±35° and 25.8% for ±50° braid angles. The increase in the undulation severity was observed due to the low angle between the fibre and loading direction. This is because sample with fibre waviness tends to stretch the waved fibre under tensile loading and undulates more under compressive loading. Hence, stress concentration increased during the test of samples with low braid angle.

2.6.2 Braid cover factor

The braid cover factor (C_f) refers to the braided area covering the surface of the mandrel/core [110]. The cover factor can be expressed in terms of the braid angle, the mandrel/core diameter, and the yarn's width described in Equation 2.2 [111].

$$C_f = 1 - \left(1 - \frac{W_y N_c}{4\pi R cos\theta}\right)^2 \qquad\qquad (2.2)$$

Where W_y is the yarn's width after micro-braiding, N_c is the number of carriers, R is the mandrel/core radius, and θ is the braid angle. The cover factor is a crucial geometrical parameter, especially a cover factor of 1, which indicates full coverage of the braid's mandrel. According to Equation 2.2, variation in braid parameters such as; width of yarn and number of carrier leads to variation in the braid coverage. Research conducted by Zhang et al. [110] concluded that keeping all factors such as the width of yarn, the number of carriers, the radius of core/mandrel constant as braid angle increases, cover factor decreases till 45° beyond which it starts to increase. Heieck et al. [112] studied the influence of the cover factor of 2D biaxial and triaxial braided carbon composite on their in-plane mechanical properties. They showed that low coverage decreases the mechanical property, especially with triaxial braids tested in the axial direction. The reason for this is because of the fibre undulation of the axial yarn at low coverage. The researchers concluded that the cover factor strongly influences braided composites' mechanical properties depending on the direction of testing and type of braid. Rebelo et al. [113] investigated the braid angle and mandrel diameter on the cover factor of braids. They also discovered that the cover factor decreased with an increase in mandrel diameter. However, the braid cover factor increased with an increase in braid angle.

From the literature cited by the researchers, the relationship between the braid angle and cover factor is exhibited.

2.6.3 Braid crimp

During braid manufacture, yarn/tow develops crimp due to interlacement at many points. Crimp forms when a tow/yarn departs from a straight line and follows a complex irregular wavy path, as shown in Figure 2.7.
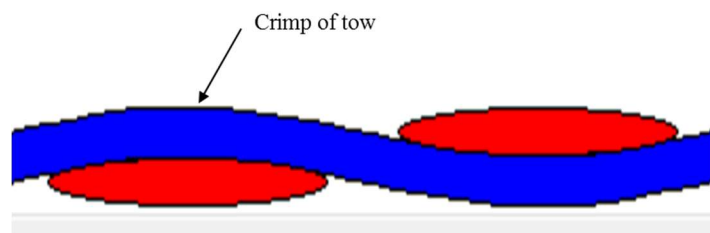
Figure 2.7 Computer-aided drawing of a depicting braid crimp using TexGen Software [97]

Crimping also results from the braid architecture, where the axial fibre tow is forced to undulate through the thickness to accommodate the neighbouring braider tows, allowing for higher fibre packing. Naik et al. [105] found a significant axial yarn crimp angle as high as 7.5° was present in manufactured triaxial braids. They also discovered that crimp in the axial yarn resulted in a reduction in compressive strength compared to non-crimp triaxial braid strength. A crimp index of zero (C = 0) indicates that the fibre is straight with no crimp. A crimp index of one (C = 1) at stable jammed state cause decrease in helical length [110,114]. Crimp percentage or crimp index is the ratio of the difference of extended length L_{nc} and crimped length L_c of fibre, in percent of the extended length of the fibre L_{nc} Equation 2.3. In braided/woven preforms, the crimp is inevitable due to the basic principle of braid formation, which involves interlacement of tow/yarn. Crimp value increases with an increase in braid angle (θ), i.e. crimp is minimum when the braid angle is closer to 0° and maximum when closer to 90°. The yarn or tow jamming which also contributes towards crimp introduction during the braid manufacturing occurs due to a high tow deposition per unit area, at a higher braid angle. The jamming position is a point after which the braided fabric can no longer be expanded or constricted. As the braid cover increases, the possibility of tow jamming also increases, resulting in increasing the possibility of tow distortion. Zhang et al. [110] reported the importance of jamming position on the cover factor.

$$C = \frac{L_{nc} - L_c}{L_{nc}} 100 \tag{2.3}$$

2.7 Structural Health Monitoring (SHM)

Almost all private industries and government organisations want to detect damage in their products and their manufacturing infrastructure at the earliest possible time. Such detection requires these industries to perform some form of SHM and are motivated by this technology's potential life safety and economic impact. SHM is applied for damage identification in aerospace, civil and mechanical infrastructure [115]. The health state of a structure is assessed through SHM by appropriate data processing and interpretation to predict the remaining life of the structure [116]. In 1981, Louis F. Pau defined failure as the inability of a system to fulfil

its intended purpose before discussing the role of performance monitoring and failure diagnosis, as shown in Figure 2.8. He also defined degradation as an event that impairs structure's ability to perform its task, malfunction (inability to operate at expected level), and failure modes (particular ways in which failure occurs [117].
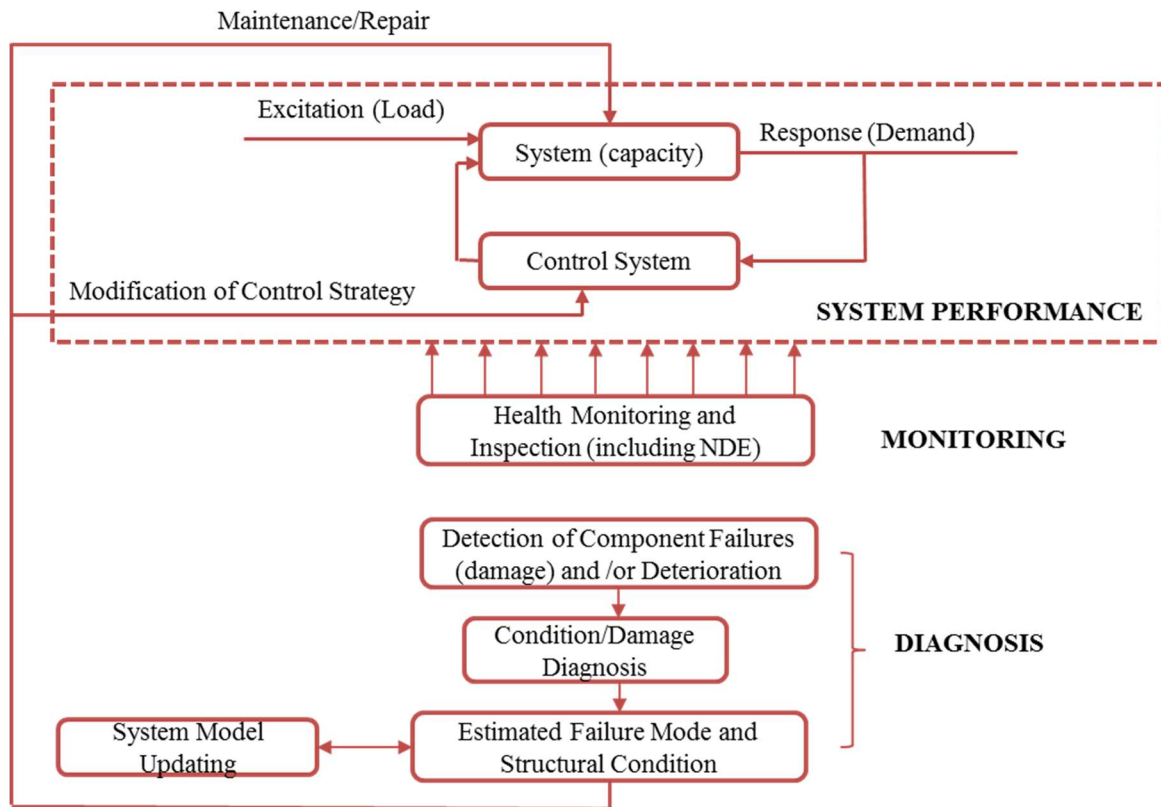
Figure 2.8 Relationship between system performance, monitoring and diagnosis (acquired from Pau's definitions) [117]

From the information obtained and the interpretations made after measuring and comparing results, either maintenance labours may occur or a part change/replacement.

For a few decades, different sensors have been used and installed to detect structural disturbances and changes during steady-state operating conditions. SHM uses sensors to obtain information about a structure's performance online and in situ [118]. This process is achieved principally through vibrations and temperature change analysis. Sensors then respond utilising physical deformation within the same sensors, variations in induced electrical currents and magnetic fields or changes in sensing waves (light, ultrasound), depending on the type of sensor utilised.

2.7.1 Active and passive structural health monitoring for damage detection

Some of the most commonly used SHM techniques can be grouped into two categories - active and passive. An active approach is when an actuator sends a diagnostic signal picked up by neighbouring sensors for analysis. The impairments or flaws are measured by assessing the eventual alterations found in the response signal compared to the previous signal. One of the most widely used active SHM for damage detection in composite materials is ultrasonic sensing with Lamb waves. This method is useful in detecting internal and external cracks in materials. In a passive approach, sensors are used in the listening mode and pick up signals generated due to environmental changes and damage growth, such as in Acoustic Emission. This method effectively monitors changes in the structure due to external loads, impacts, changes in temperature, etc. [119,120]. Figure 2.9 shows an illustration of active and passive techniques for SHM.

Measurements of strain, acceleration, velocity, displacement, rotation and other parameters have always been essential in engineering. However, recent developments in sensing, measurement, communications and computational technology had facilitated the application of health monitoring of large structures, transport vehicles and operating machines by detecting structural disturbances, changes and irregularities during operating conditions [121]. This phenomenon has helped in maintenance tasks and in validating and improving designs and guaranteeing a safe operation.

Active SHM
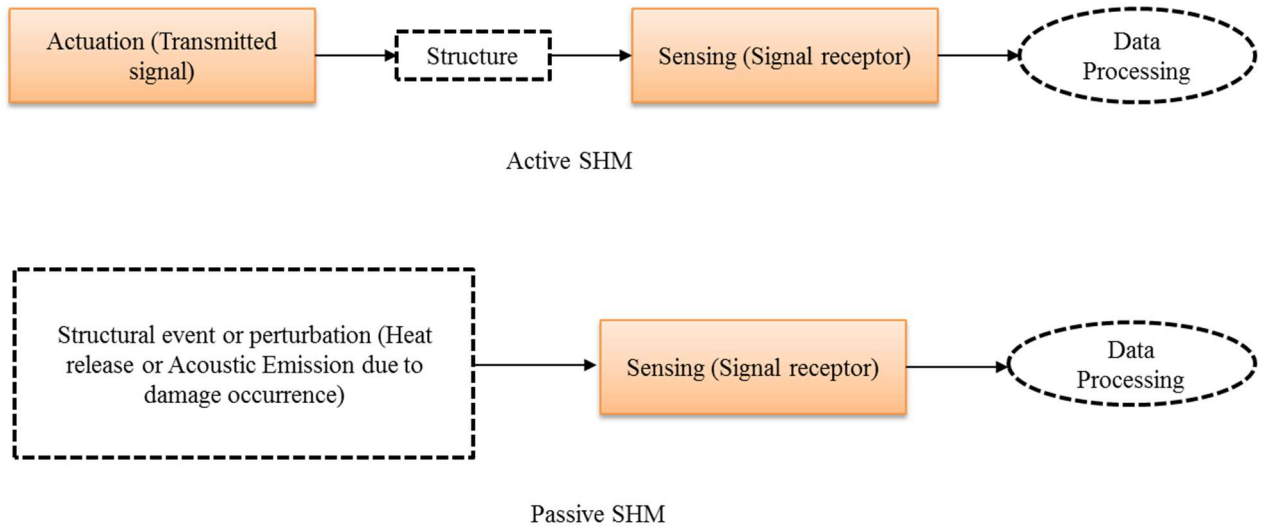
Passive SHM

Figure 2.9 Schematics of active and passive Structural Health Monitoring technique.

Ultrasonic waves are acoustic waves transmitted above the human-detectable frequency range, usually greater than 20 kHz. The ultrasonic wave's propagation is affected by damage in the structure, which is identified when the detected ultrasonic signal defers from the reference signal. The time of flight (TOF) of the response signal of an ultrasonic wave is used to determine the presence of damage. Cantero-Chinchilla et al. [122] developed a robust Bayesian technique to estimate the time of flight of individual sensors, respectively. They created a model to give a probabilistic description of the TOF while accounting for uncertainties in the material property and the model itself. Wang et al. [123] studied the Lamb wave time reversal method by substituting the backward time-reversal pitch-catch procedure with a virtual operation. Breakage of time reversibility was experienced, related to the damage types, damage characteristics and the interrogating wave mode. Zhao et al. [124] studied the detection of delamination in composite double cantilever beam using ultrasonic guided wave with signals recorded by the piezoelectric sensor (PZT). A_o and S_o are types of wave propagation for lamb wave mode, with So called symmetric mode having the motion of particles parallel to wave propagation and A_o (Antisymmetric) being perpendicular to wave propagation. The presence of damage was identified by the appearance of wave-packet in front of A_o mode when S_o mode passes through a damaged area. The amplitude of A_o decreased with an expansion of delamination.

The use of piezoelectric sensors for detecting ultrasonic wave requires cables and wires for linking sensors which aggravates the degradation of adhesive layers between the host structure and the sensor network under cyclic loading, signal processing and inability to integrate the sensors in composite structures during manufacture. This thesis is focused solely on optical fibre strain sensors.

2.8 Optical fibres

Sensors play an essential role in any SHM systems. They are used to acquire data regarding the structure's response to the presence of damage. Some of the most commonly used sensors for damage detection in composites as a part of an SHM system are described in this section.

The invention of Optical fibre sensors (OFS) appeared just after the practical optical fibre invention by Corning Glass Works in 1970 (now Corning Incorporated). In the beginning, optical fibres were costly. Still, with the great diffusion of optical fibre technology during the 1980s and on, optoelectronic devices became less expensive, which favoured the use of OFSs [125]. Optical fibre is made of glass or polymers and is used to transmit light along its length. Optical fibres are widely used in communication, which permits transmission over longer distances and at higher data rates "bandwidth" ~10-100 Gbps than other forms of communications. Fibre optic is used instead of metal wires because signals travel along with them with less loss. Optical Fibre has many advantages: lightweight, multiplex capability, high sensitivity, high broadband, immunity to electromagnetic interference, chemical inertness, and electrical isolation with minimum impact on host structure, quasi-distributed or distributed sensing capability and immunity to radio frequency interference (RFI). Numerous physical properties can be sensed with optical fibres like light intensity, temperature, pressure, rotation, strain, sound, magnetic field, electric field, radiation, liquid level, chemical analysis, and vibration [126].

An optical fibre is composed of three parts: the core, the cladding, and the coating or buffer, as shown in Figure 2.10. One of these materials is placed in the centre is called core (ranges from 9 to 50 μm) which has a high refractive index [127]. The cladding (around 125 μm) has a low refractive index. It decreases the loss of light from the core into the surrounding material. It reduces the scattering loss at the surface, shielding the fibre from absorbing surface

contaminants, and adds mechanical strength. The coating or buffer (around 250 μm) protects the optical fibre from external conditions and physical damage. The range of wavelength for optical fibres is 1310-1550 nm being typical for single-mode fibres with minimal losses and 850-1300 nm for multimode fibres.

Coating, typ. OD = 250 μm
(0.057-0.0098 inch)

Cladding, typ. OD = 125 μm
(0.0049 inch)

Core, typ. OD = 5-50 μm
(0.0002-0.0020 inch)
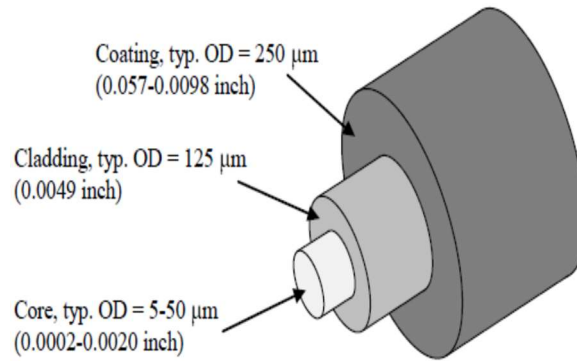
Figure 2.10 Optical fibre structure [128]

Single-mode optical fibre

These are optical fibres with a small diameter core that allows only single light to propagate. Due to this, the number of light reflections created as the light passes through the core decreases, lowering the attenuation and developing the ability for the signal to travel further. This application is mainly used in long-distance, higher bandwidth applications and SHM applications.

Multimode optical fibre

These have a large-diameter core that allows multiple modes of light to propagate. Because of this, the number of light reflection created as the light passes through the core increases, making the capability for more data to pass through at a given time. High dispersion and attenuation of the fibre cause the quality of the signal to reduce over long distances. It is used for short-distance application and SHM applications at a short distance. Figure 2.11 shows single and multiple mode optical fibres with core 9, 50 and 62.5 μm and cladding of 125 μm, respectively.
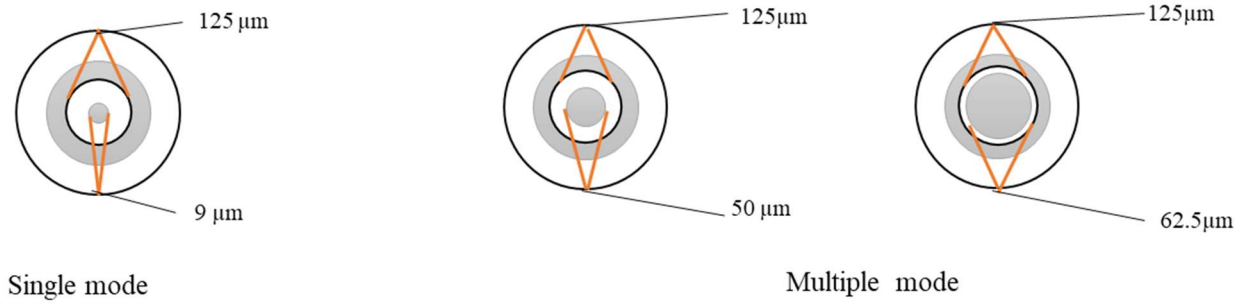
Figure 2.11 Single-mode and multiple mode optical fibres with cores to claddings diameter ratio of 9 to 125 µm, 50 to 125 µm and 62.5 to 125 µm, respectively.

2.9 Classification of optical fibre sensors for structural health monitoring

Methods of classifying sensing mechanism of optical fibre sensor (OFS) is based on the light characteristics; phase-modulated sensor, polarimetric sensors, signal attenuation, intensity-modulated sensor and wavelength modulated sensor.

Extrinsic optical sensors use the fibre only as a mechanism to transmit light to and from a sensing element. In contrast, intrinsic optical sensors use the optical fibre itself as the sensing element. Distributed sensors retrieve information directly as a function of linear position, while quasi-distributed sensors comprise the incorporation of several sensors in fibre at designated points. Table 2.5 shows a list of optical fibre sensors for structural health monitoring.

Table 2.5 Optical fibre sensors for Structural Health Monitoring [18]

	Sensor	Measurands	Linear response	Resolution	Range	Modulation method	Intrinsic/extrinsic
Local	Fabry-perot Long range sensor	Strain Displacement	Yes Yes	0.01% gage length 0.2% gage length	10,000 μɛ 50 m	Phase Phase	Both Intrinsic
Quasi-distributed	Fibre Bragg Grating	Strain	Yes	1 μ strain	5000 μɛ	Wavelength	Intrinsic
Distributed	Raman/Rayleigh (OTDR) Brillouin (BOTDR)	Temperature/strain Temperature/strain	No No	0.5 m/ 1°C 0.5 m/ 1°C	2000 m 2000 m	Intensity Intensity	Intrinsic Intrinsic

Fibre-based measurement systems involve an active monitoring unit, which is connected to the optical fibre sensor. The monitoring unit then transmits light into the fibre from either a tunable frequency laser or a broadband source. Characteristics of the light travelling within the fibre are modified as a consequence of temperature and strain changes. These changes alter the back-scattered light, which is later collected by the monitoring unit, analysed, and converted into strain and temperature data [129].

Optical fibres have been used in telecommunication for a long time, OFS have very high strength (with actual fibre strength of about 5 to 10 pounds of maximum theoretical tensile strength of 2 million pounds per square inch) [130], but one significant drawback is the brittleness of the sensors. This drawback affects the handling and can lead to the breakage of the OFS, interrupting the signal transmission and becoming almost impossible to repair once installed. In such a situation, the replacement of the sensor will then be required by surface mounting.

2.9.1 Interferometric sensors

Interferometric optical fibre sensors rely on the principle of optical interference for the measurement of physical or chemical properties. An intrinsic or extrinsic interferometric cavity

creates an interferometric sensor along an optical path [131]. Changes in the optical phase difference between two interference light waves reflect physical changes in structures. Popular and practical interferometric sensors include Fabry-Perot interferometric sensors, Mach-Zehnder, Michelson and low coherent interferometric sensors (SOFO interferometric sensors).

Fabry-Perot Interferometric sensor (FPIS)

In a Fabry-Perot interferometric configuration, the incident light is divided into multiple beams. One or more beams will experience a change in the optical path due to physical or chemical changes in the surrounding environment. The change will translate to a phase difference between these beams and a reference beam. Figure 2.12 shows extrinsic and intrinsic FPIS.
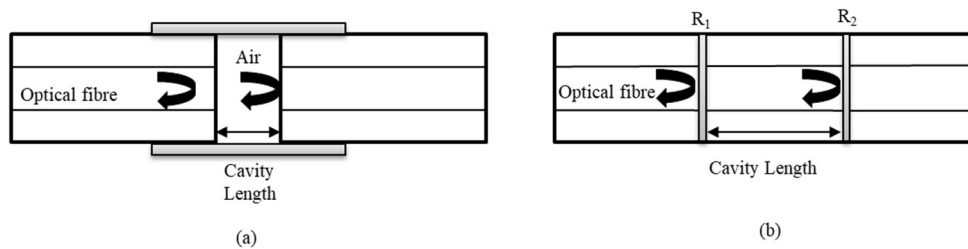
Figure 2.12 Schematic of a Fabry-Perot interferometric sensor (a) Extrinsic and (b) Intrinsic[132]

2.9.2 Distributed optical fibre (DOF) sensor

Distributed optical fibre (DOF) sensing is a technique that utilises the optical fibre's special properties to make concurrent measurements of both the spatial and temporal behaviour of a measurand field [133]. DOF can be installed along the whole length of a structure, and this makes each cross-section of the structure practically instrumented. DOF is sensitive at each point of its length, and this provides discrete sensing elements for continuous monitoring and thus is promising for strain/temperature measurement in large structures [29,134].

Principle of DOF sensor

DOF generally operate under the principle of optical time-domain reflectometry (OTDR) or optical frequency domain reflectometry (OFDR). The effect of external disturbance on the optical fibre causes attenuation, as shown in Figure 2.13.
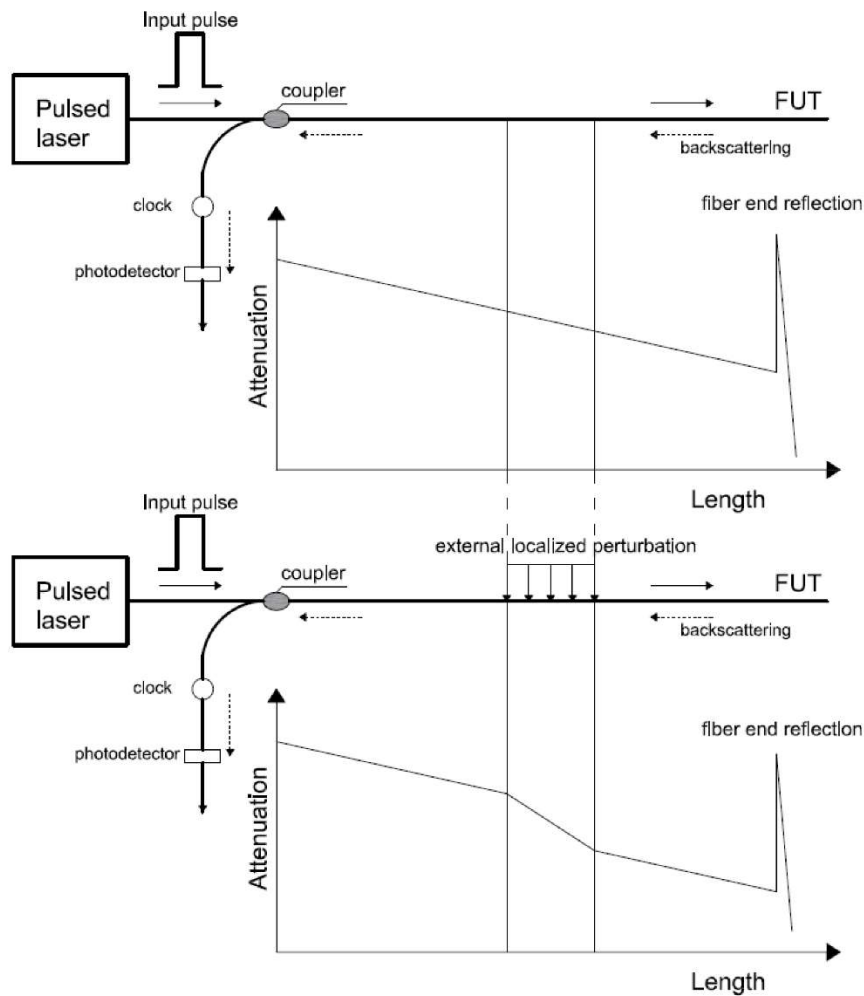
Figure 2.13 Schematics of operating an Optical Time Domain Reflectometry (OTDR) system [68]

In the OTDR, Rayleigh and Fresnel scatterings are used for sensing structural perturbation. On the other hand, Brillouin scattering detects the Doppler shift in light frequency which is related to the measurements. The main scattering techniques exploited for DOF are Rayleigh, Raman and Brillouin scattering [128,135–137]. Each technique is based on the relation between the measured parameters, i.e., strain and/or temperature, and encoding parameter, i.e., the change

in the scattered light's optical properties, as shown in Figure 2.14. Minakuchi et al. [31] have used a Brillouin based system to monitor the life cycle of CFRP manufactured through vacuum-assisted resin transfer moulding (VARTM), as shown in Figure 2.15. They observed the frequency distribution during the manufacturing and impact test. The Raman backscattered light has two frequency-shifted components: the Stokes and Anti-Stokes Components. Anti-Stokes Components gain energy in the scattering process and therefore have a higher frequency, and Stokes components lose energy and have a lower frequency. The amplitude of the anti-stokes component is dependent on temperature, while the amplitude of the stokes component is not. The Rayleigh backscattering component is the strongest one due to composition fluctuations and density and possesses an identical wavelength as the primary laser pulse. Brillouin Scattering effect can also be used for monitoring both strain and temperature. Brillouin scattering occurs due to an interaction between the propagating optical pulse and the acoustic waves present in the silica fibre, generating frequency-shifted components.
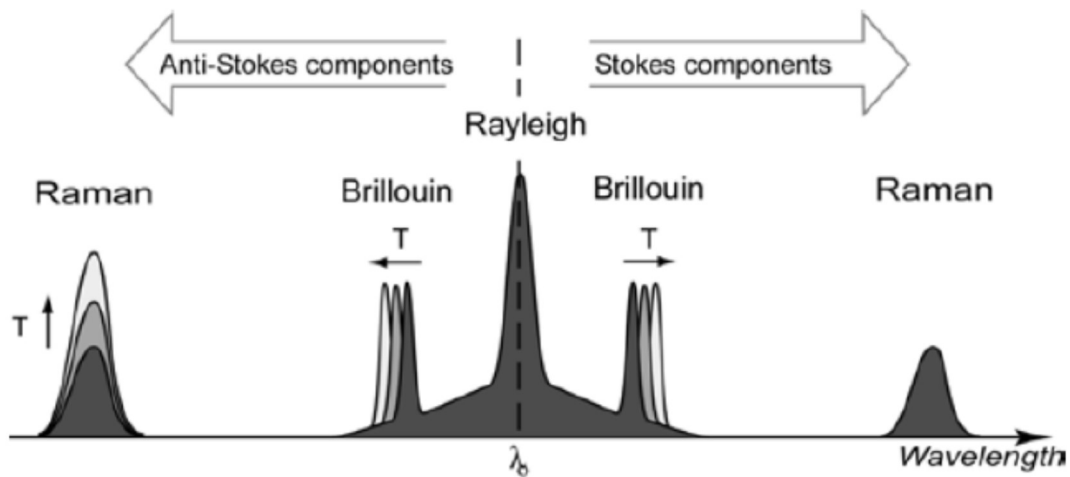
Figure 2.14 Typical scattering spectrum [138]
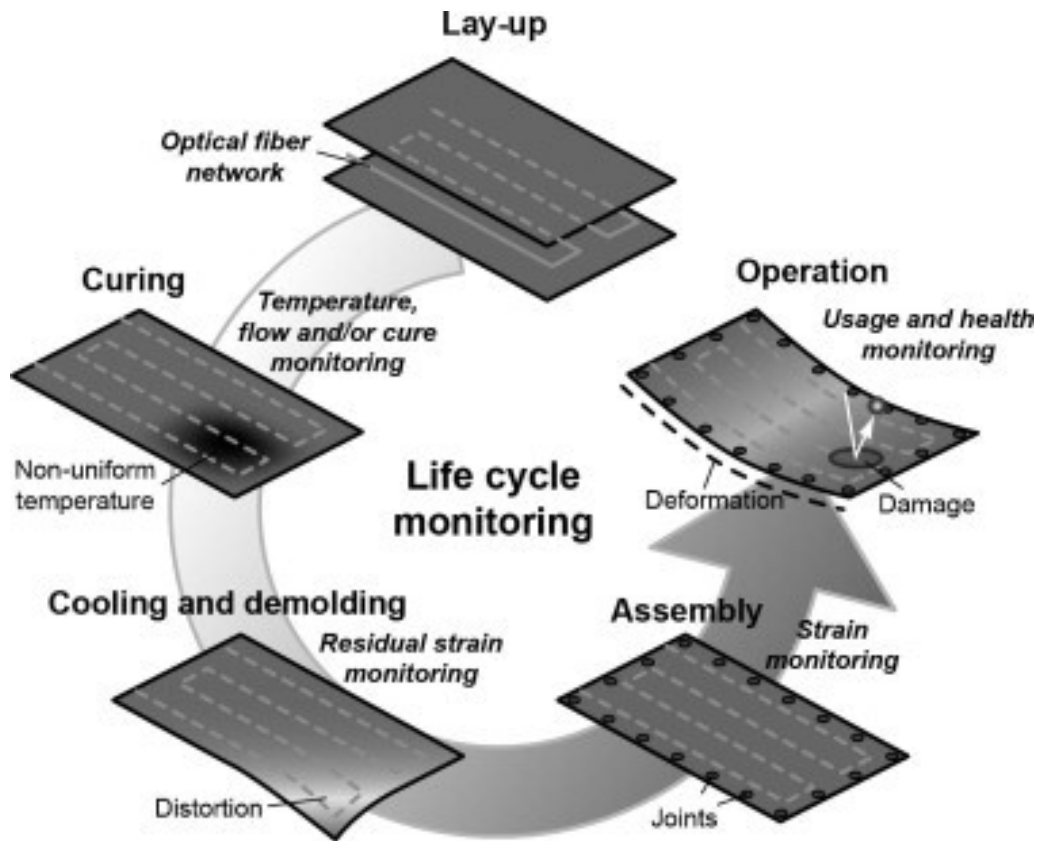
Figure 2.15 Diagrammatic illustration of life cycle monitoring [31]

OFDR is commonly used because of its high spatial resolution of 1 μm compared to OTDR with a lower spatial resolution of 0.1 m. OFDR is known to have a large dynamic range because of the possibility of coherent detection [139,140]. A swept frequency pulse is used to interact with the optical fibre. The sensing fibre measures Rayleigh backscatter, which results from interactions between the light and imperfections in the silica glass core. The frequency of backscattered light is dependent on its location, enabling localised strain sensing. OFDR allows monitoring structures with a spatial resolution of 10 μm to a few mm and with strain and temperature resolutions as fine as 1 μstrain or 0.1°C [129,139].

2.9.3 Fibre Bragg Grating (FBG) sensor

An FBG sensor is a short length of FBG contained in polyimide coated optical fibre meant for fibre optic strain sensing purposes. FBG sensors are extremely sensitive to strain/temperature. They can provide accurate axial strain measurements of a structure by monitoring the returned

signal's peak wavelength shift due to the linearly-proportional relationship between the peak wavelength shift and applied strain. They can be easily and quickly embedded in between plies of composite panels during composite manufacture and require minimal training to operate and obtain data without any calibration necessary. The multiplexing capability of FBG sensors allows for up to 100 sensors to be embedded in a single optical fibre, thus providing many damage monitoring points (for quasi-distributed sensing) in a structure without complicating the manufacturing process. Embedding the FBG sensor in a composite structure has an insignificant effect on the structure's material properties. The sensor gauge length varies in size (~mm) to accommodate multiple damage types and sizes. FBG sensors remain reliable for great lengths of time due to their passive sensing ability. They are suitable for applications in which the expected service time of a structure is multiple decades.

Evolution of FBG sensors

Fibre Bragg Grating is formed by a periodic modulation of the index of refraction of the fibre core along the longitudinal direction and can be produced by various techniques. The term FBG was borrowed from the Bragg law and applied to the periodical structures inscribed inside the core of conventional telecom fibre. Sir Lawrence Bragg discovered the Bragg law of X-ray diffraction in 1912 [141]. Hill et al. [141] made the Hill's gratings with fibre core by a standing wave of 488nm argon laser light. In this case, the exposure of the grating was shown to be a two-photon process. They observed a 4% backward reflection due to the difference in refractive index. However, a renewed interest appeared years later with the demonstration of the side writing technique by Gerry Meltz and Bill Morey of United Technology Research Center. They proposed that fibre gratings could be formed by exposure through the cladding glass of two interfering beams of coherent UV light, consequent exciting the 240 nm band directly by one-photon absorption [142]. Reliable Bragg gratings fabrication depends on detailed knowledge of the fundamental mechanisms of photo-induced index changes. The basis of all proposed mechanisms is the ionization of GeO_2 deficiency centres that exhibit an absorption band centred at 240 nm. The fabrication of FBG sensors has been developed to a commercial level and the main techniques used are Split Beam Interferometer, Phase Mask Technique and Point-by-Point method.

Principle of an FBG sensor

A fibre Bragg grating is a wavelength-dependent filter/reflector formed by introducing a periodic variation in the refractive index within the core of optical fibre [143]. Whenever a broad spectrum of light beam impinges the grating of an FBG, a portion of the incoming light is transmitted through without altering its property. The remaining part is reflected at a particular wavelength called the Bragg wavelength shown in Figure 2.16. Any local changes along the FBG can be manifested as that of shifts in λB (Bragg wavelength). *T*herefore, it is possible to monitor any strain-resulting parameters, from temperatures to stress waves [18]. This sensor's major advantage is that an array of wavelength-multiplexed FBGs can be deployed in a single fibre for quasi-distributed measurements, which is very attractive for SHM of large structures [144,145]. With the possibility of all segments of an optical fibre acting as sensors, quasi-distributed sensing can be achieved using an FBG sensor.
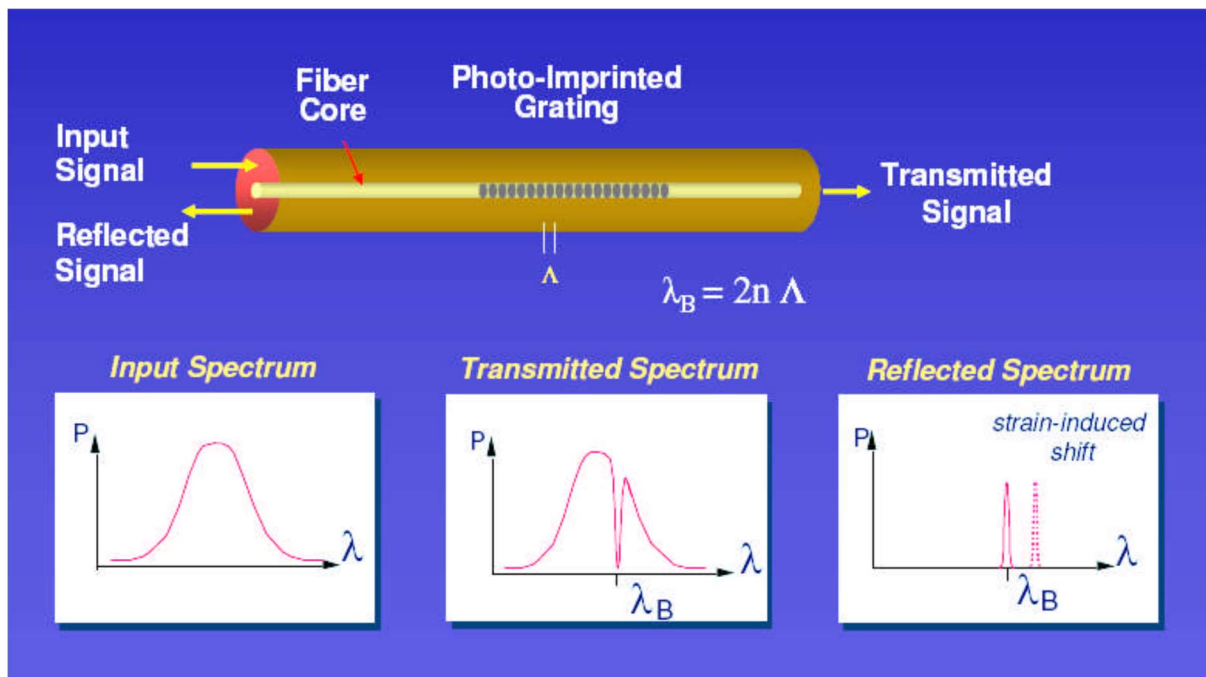
Figure 2.16 Fibre Bragg Grating sensor structure with transmission and spectral response [146].

Strain and temperature sensing of FBG sensor

The Bragg wavelength is given by the expression [27]:

$$\lambda_B = 2n_{eff}\Lambda \tag{2.4}$$

Where λ_B is the Bragg wavelength, n_{eff} is the effective refractive index of the fibre core, and Λ is the FBG's grating period. Effect of strain $\Delta\varepsilon$ and temperature change ΔT on the FBG causes a shift in wavelength peak accordingly. Strain can be calculated using Equations 2.4-2.7 [147].

$$\Delta\lambda_B = \lambda_B(1 - P).\Delta\varepsilon + \lambda_B(\zeta + \alpha).\Delta T \tag{2.5}$$

$$\text{and } \Delta\lambda_B = \lambda_{Bi} - \lambda_B \tag{2.6}$$

$$\Delta\varepsilon = \frac{\left(\frac{\Delta\lambda_B}{\lambda_B}\right)_S - \left(\frac{\Delta\lambda_B}{\lambda_B}\right)_T}{k_\varepsilon} \tag{2.7}$$

Where λ_B is the Bragg wavelength, λ_{Bi} is the wavelength at the point of concern, P is about 0.22 for optical fibre made from silicon dioxide (SiO_2) and strain sensitivity coefficient is 1.2pm/$\mu\varepsilon$ for FBG sensors whose wavelength is around 1550nm, $k_\varepsilon = 1 - P$ is the gage fact or (strain sensitivity), and thermal sensitivity $k_T = \zeta + \alpha = 6.67x10^{-6o}C^{-1}$ for optical fibre made of silicon dioxide (SiO_2). The temperature sensitivity coefficient is about 10 pm/°C for FBG sensor with a wavelength of about 1550nm.

2.9.3.1 Application of FBG sensors for SHM

The FBG sensor is one of the standard sensors for the SHM of structures. Embedding FBG sensors in composite part during manufacture is achievable because of its diminutive size. The significance of the sensor is because of the properties they possess, which are small size, immunity to electromagnetic fields, absolute measurement compared to electric sensors, measurement over long distance with little or no noise in signal integrity, non-conductive and multiplexing ability are some of the advantages of FBG sensors. The use of an FBG sensor for the structural health monitoring of composite structures has become increasingly prevalent due to the low cost of introducing embedded FBG sensors relative to the benefits of creating self-diagnostic composite structures. The use of embedded FBG sensors could prevent the costly and time-intensive teardown inspection of structural components by providing structural

integrity information. The real-time structural health monitoring ability increases the safety of composite structures by delivering information to operators as soon as the structure becomes compromised. This phenomenon allows the opportunity to immediately determine if the structure can continue service or if it must be repaired. When an FBG sensor is subjected to a non-uniform strain distribution along the gauge length, the spectral response will change as a function of the non-uniform strain distribution. The linear relationship in Figure 2.17 will no longer hold through. The reflection spectrum will become wider and may contain multiple peaks as the non-uniform strain increases, as shown in Figure 2.18. The spectrum broadening and various peaks due to the non-uniform strain fields can be used as indicators of strain concentration caused by the defects and damage in composite structures. The strain has been monitored by measuring the shift in wavelength of the light reflected from the FBG sensor, often implemented in conventional health monitoring [148–150] have successfully used embedded FBG sensors to measure internal strain and examined the change in spectral shapes and change in strain in the region of the damage.
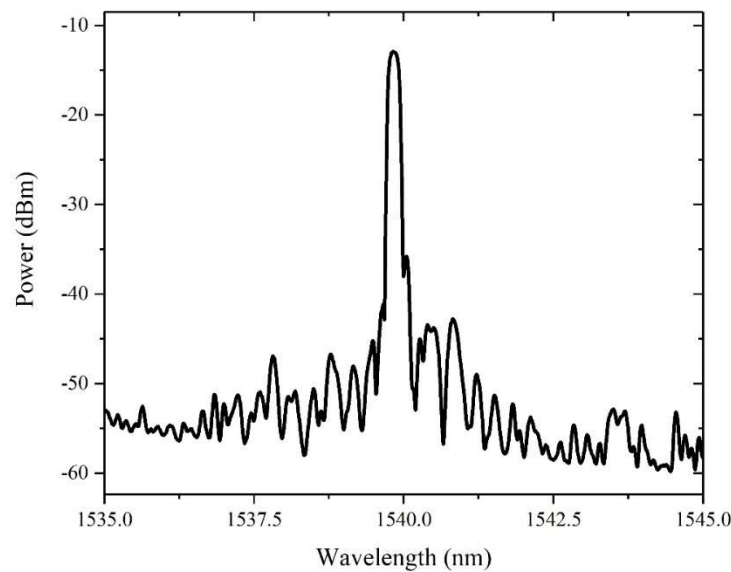
Figure 2.17 Response spectra of a Fibre Bragg Grating sensor (undamaged)
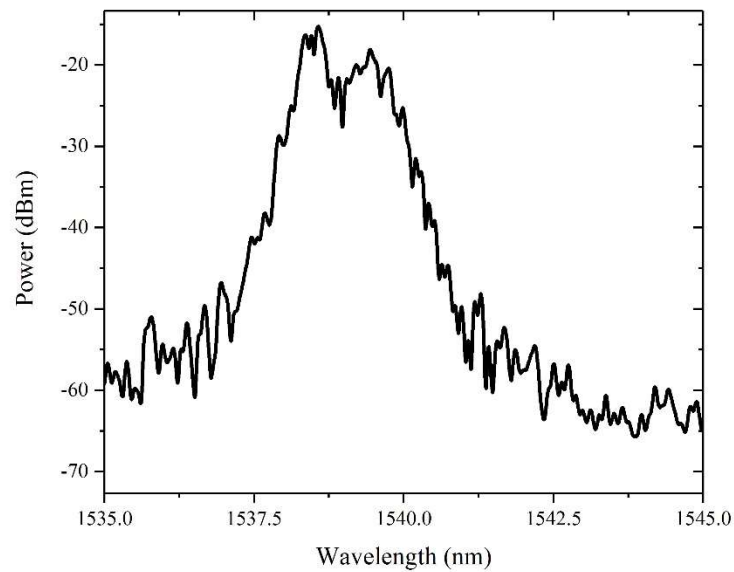
Figure 2.18 Response spectra of almost damaged Fibre Bragg Grating sensor with wider spectra

Integration in composites

Embedded optical fibre sensors are a promising way to monitor composite structures' health state in real-time reliably. However, issues of fibre placement and how properties of the composite are affected by the presence of the optical fibre sensor under a given set of parameters could cause potential defects. This defect could be delamination due to interlaminate stresses, increases of interlaminate stress near the sensors and stresses at the interface between the sensors and composite. Sensors can lose sensitivity due to the delamination failure between the embedded sensors and the composite. For these reasons, several researchers studied the mechanical properties of composite materials with embedded optical fibre sensor.

Lee et al. [151] studied the effect of embedding an optical fibre sensor on the mechanical properties of glass fibre/epoxy composite. Specimens with embedded optical fibre experienced an increase in stiffness, strength and Poisson's ratio compared to specimens without optical fibre. They suggested that embedding the optical fibre at low volume fraction has insignificant effect on the mechanical properties of the composite. Hufenbach et al. [152] studied the effect of integrating a flexible printed circuit board (FCB) and an application-specific integrated

circuit (ASIC) in a GF/PP. Microscopic examination of the cross-sectional image of the integrated FCB shows a homogeneous distribution of GF and PP while the ASIC shows inhomogeneous distribution. The embedded FCB also recorded a 5.2% increase in flexural strength compared to ASIC. Javdanitehran et al. [153] embedded a printed circuit board (PCB) in a GFRP. They reported that distortion in the area of the structure caused by embedding the PCB led to a reduction in the composite's load-bearing capability. Hamouda et al. [67] embedded a POF with a cladding diameter of 750 µm between layers of an E-glass formed into a 3D orthogonal weave. The microscopic image showed a resin-rich pocket due to local distortion caused by the POF. They, however, reported that the distortion did not affect the mechanical properties of the composite. Wei et al. [154] however, reported that the orientation of the sensor aligned parallel and perpendicular to reinforcing fibre influences the composite's mechanical properties. They reported that perpendicular embedment could influence the formation of transverse crack and affect the composite's mechanical properties. S.S.J Roberts et al. [155] also reported that embedding optical fibre sensor has some effect on composite strength. Silva et al. [156] reported that the presence of optical fibre in CF/Ep composite did not affect the mechanical properties in the static flexural test. Still, in impact, test samples showed fibre/matrix splitting appearance and a 12% decrease in stiffness for fatigue test.

The literature cited has shown that embedding optical fibres in composite does not significantly affect the mechanical properties of the composite.

Manufacturing monitoring

Several researchers [157–161] have studied the residual strain induced in composites during cure using various types of optical fibre sensors. Strain gauges have also been employed for this purpose [162]; however, the data they give is local, and many gauges are needed to meet a large sensing region. To achieve global sensing of the whole structure, it is preferable to integrate either distributed or quasi-distributed (fibre Bragg grating) optical fibres [128,163].

A summary of residual strain measurement embedded with different optical fibres in relation to cure monitoring and the residual strain recorded in the longitudinal and transverse direction is presented in Table 2.6.

Table 2.6 Residual strain values reported in the literature due to the curing process of composites.

Reference	Material	Sensor	Fibre layup	Manufacturing method	Residual strain in LD (µε)	Residual strain in TD (µε)
[29]	CF/Ep	DOF	Fabric$\{90\}$/fabric$_2\{90\}$/fabric$_2\{90\}$fabric	VARIM	-405/-347/-291	-
[158]	CF/Ep	DOF	$[0_7/\{0\}/0_8]$	Autoclave	-1500	
[164]	GR/Ep	(FBG/EFPI) Hybrid	$[0_{12}/\{0,90\}/0_{12}]_T$ $[0_3/\{0\}/0_3/90_6/\{90\}/90_6/0_6]_T$ Fabric$_8/\{0,90\}$/fabric$_8]_T$	Autoclave	-140 -410/-470 -210/-240	-4000
[165]	CFRP	EFPI	$[0/\{0\}/0_2/90_4/90_3/\{90\}/0_4]^{ND}$ $[0/\{0\}/0_2/90_4/90_3/\{90\}/0_4]^{(WD)}$	Heat press	$-230^{(ND)}$ $-260^{(WD)}$	$4400^{(ND)}$ $4360^{(WD)}$
[1]	GF/EP	FBG	-	Autoclave	-2200	
[166]	GR/EP	(FBG/EFPI) Hybrid	$[0_6/\{0\}/0_6/90_6/\{90\}/90_6]_T$	Autoclave	-440 -440	-520
[167]	GR/Ep	FBG	$[90/0/90/0/\{90\}/0/90/0-0/90/0/90/0/90/0/90]$	Hot mould	-	1290
[168]	GR/EP	MIDG	Unidirectional laminate $[0_{16}]$	Autoclave	0	-5000
[169]	CF/EP	FBG	Unidirectional laminate	Autoclave	-4500	-4500
[170]	GF/EP	FBG	Unidirectional laminate	-	-120/	-280
[171]	GR/EP	FBG	Unidirectional laminate (FBG embedded mid-ply)	Hot press	-385/-453, -20/-87	-

			Unidirectional laminate (FBG embedded surface-ply)			
[172]	CF/EP	FBG	$[0_5/90_5/FBG/90_5/0_5]$	Hydraulic press	-360	-
[173]	GFRP	FBG	$[(+45/-45/0)\{0\}(0/-45/+45)]_s$ $[(0/-45/+45)(+45/-45/0)\{0\}(0/-45/+45)]_s$ $[(+45/-45/0)(0/-45/+45)(+45/-45/0)\{0\}$ $(0/-45/+45)]_s$	VARIM	-330 -470 -540	-

CF = Carbon fibre, GF = Glass fibre Ep= Epoxy, GR= Graphite, CFRP = Carbon fibre reinforced polymer, FBG =Fibre bragg grating, DOF = Distributed optical fibre, EFPI =Extrinsic fabry-perot interferometer, MIDG = Moire interometry diffraction grating, TD = Transverse direction, LD = Longitudinal direction, ND = No damage, WD = With damage, {} = Location of the optical fibre sensor.

Lots of researchers have investigated strain monitoring during the manufacture of a composite. The different location of the optical fibre during layup has been adopted. Sanchez et al. [29] embedded a distributed optical fibre between the top (5th and 6th ply), middle (3rd and 4th ply) and bottom (1st and 2nd ply) of a CF/Ep laminate. From top to bottom, residual strains of -405, -347 and -291 µε respectively were recorded, with the highest at the top reducing at the middle. Huang et al. [158] have also embedded a pre-tensioned optical fibre longitudinally between the 8th and 9th plies (centre of plies) of an AS4/3501 unidirectional carbon fibre/epoxy pre-preg tape. A residual strain of -1500 µε was recorded due to the thermal contraction of the composite panel. Kang et al. [164] have also reported various residual strain values depending on the FBG/EFPI hybrid sensors' position in the GR/EP pre-preg. The residual strain of the longitudinal and transverse direction sensors to the reinforcing fibre axis was -140 and -4000 µε, respectively. Results show higher residual strain in the transverse direction due to higher thermal and chemical shrinkage of unidirectional laminate because of its anisotropic behaviour. Ifju et al. [168] also reported a residual strain value of -5000 µε in the transverse direction and zero in the longitudinal direction of a GR/EP (AS4/3501-6) pre-preg using a thin film of moire interferometry diffraction grating placed between fibres. Leng et al. [165] also experienced different strain reading in transverse and longitudinal direction using an Extrinsic Fabry–Perot interferometer (EFPI) and Fibre Bragg grating (FBG) to monitor curing of a CFRP. The residual strain of the CFRP composite in the transverse and longitudinal direction without damage was 4400 and -230 µε and with damage was 4360 and -260 µε respectively. Results show that residual strain in the longitudinal direction is compressive with higher strain magnitude present with the introduction of damage. Hsieh et al. [167] also reported a positive residual strain of 1290 µε with a FBG sensor embedded between a GR/EP pre-preg. This was related to inducing of shrinkage and non-uniform strain by the epoxy matrix during cooling. Ferdinand et al. [1] reported a residual strain of -2200 µε when an FBG sensor was embedded between a glass/epoxy pre-preg during manufacturing. Kang et al. [166] reported a different residual strain of 440 and -520 µε with an EFPI/FBG hybrid sensor position at 0° and 90°to fibre axis of a CU-125 NS GR/EP pre-preg. Results show that the cured un-symmetric laminate curvature is directly related to the intensity of the induced residual stress. Minakuchi [169] measured a strain of -4500 µε using a short-tailed FBG sensor embedded through-thickness and in-plane direction of a carbon/epoxy pre-preg was cured in an autoclave. Chehura et al. [170] used a highly linearly birefringent (HiBi) FBG sensor in glass fibre/epoxy composite. The HiBi FBG sensor's residual strain was -280,-120 and -100 for the sensors embedded normal and parallel to the reinforcing fibre and in neat resin, respectively. They reported the reason

could be due to loading situation around the HiBi FBG sensor during shrinkage. Menendez et al.[171] used photoelastic method and lamination theory to predict the residual strain value of a unidirectional graphite/epoxy laminate using a FBG sensor. Residual strain or -385, -453, -20 and -87 $\mu\epsilon$ were calculated for the 4 FBG in the middle and outer laminae using photoelastic model. Also using lamination theory, the calculated residual strain were -530 and -190 $\mu\epsilon$ in the middle and outer laminae respectively. Lawrence et al. [172] used an EFPI and FBG to monitor the curing of a HyE 6049U CF/EP laminate. The measured strain by the EFPIs were -200 and -240 $\mu\epsilon$ respectively while the FBG recorded a strain of -360 $\mu\epsilon$. The reason for the difference in strain reading of the FBG and EFPI 1 was reported to be due to the sensitivity of the FBG sensor to transverse strain. Montanini et al. [173] investigated the effect of the number of layers on residual strain for a GFRP composites. Results shows that longitudinal residual strain increased with the number of layers with values of -330, -470 and -540 $\mu\epsilon$ respectively. This was reported to be due to thermally induced deformation and matrix volumetric shrinkage which accumulates in the cured resin.

In summary, various researchers have studied cure monitoring in GF/EP, CF/EP and GR/EP composites using different fibre orientations, sensor locations, raw materials, and manufacturing methods. Some agreement was found with the negative and positive residual strain values recorded by the sensors oriented longitudinal and transverse to the fibre direction, respectively. However, no consensus was found in the residual strain values, which could be due to the difference in raw materials, temperature profile, manufacturing method, fibre orientation, or sensor location.

Testing Manufactured composite

Kuang et al. [69] have utilised a 1000 μm plastic optical fibre (POF) to measure axial strain during 3 point bending of a beam. Bend sensitivity of the POF was improved by abrading segment of the cross-section surface with a razor blade. During cyclic loading of the specimen, the difference in sensor response was experienced by the POF due to the sensitivity of the sensor to bending influenced by the circumferential position of the segment. Yashiro et al. [150] also demonstrated that an embedded FBG sensor's reflection spectrum was useful for identifying damage patterns within the gauge section for notched Fibre-reinforced polymer laminates. Takeda et al. [22] developed a small diameter FBG to detect delamination in CF/EP composite. They investigated the relationship between change in spectrum shift and

delamination size. The reflection spectrum was found to be sensitive to delamination length by the appearance of multiple peaks. Ussorio et al. [174] investigated the use of FBG sensor for matrix crack detection in GF/EP composite. Broadening of the reflected spectra's width was reported as the crack grew; this was due to the contribution of both unchanged FBG sections far from the crack and the sections local to the crack. Okabe et al. [175] utilised an FBG sensor to detect transverse cracks in carbon fibre reinforced plastics (CFRP). Broadening of the spectrum and multiple peaks were detected when the transverse crack density increased in the 90° ply. The also observed the importance of full width half maximum (FWHM) in evaluating transverse crack.

2.9.3.2 FBG sensor durability and survivability

The method of embedding FBG sensors in FRP composites are complex. The difficulty level is primarily dependent on the part's geometry, lay-up configuration, and embedding location of the sensors. The possibility that FBG sensors could be too fragile and fail before the composite structures they are embedded in, resulting in a loss of structural health monitoring capabilities, is a concern that must be addressed. The manufacturing difficulty is the main problem of placing FBG sensors in a complicated location. For example, in advanced manufacturing technologies used in the aerospace industry, the autoclave process creates hazardous environments for the brittle sensor. Every precaution needs to be taken not to apply loads on the sensor in the non-cured resin matrix during the process. With applied pressure as high as 700kPa, there is a need to support the egress ends of the sensors to avoid breakage. Developing methods to protect the FBG sensors is essential during the manufacturing process of FRP composite. Because there are no ways of replacing damaged FBG sensors after manufacturing the component, a strict set of procedures must be developed to optimise the FBG before incorporating it in the manufacturing process. Anastasi et al. [176] reported discrepancies in the mechanical and optical strain reading using a distributed strain sensor system in a woven E-glass composite. They attributed the disparity to the slippage of optical fibre from its position in the weave. Also, it was reported that inaccuracies in measurement were due to the optical fibre sensor's durability. Due to the brittleness of the optical fibre, the breakage of many optical fibres was experienced during fabrication. To save cost, the durability of the optical fibre needs to be ensured by improving its robustness.

During the fabrication processes, breaking of sensors means wasting resources and time, which is not suitable for a system intended to last long and concern the safety of human lives.

2.10 Summary

This chapter gives a detailed literature review on composite manufacture, braiding technology, structural health monitoring (SHM) and optical fibre sensors (OFS). The importance of braiding technology for engineering applications was described. Details of various SHM techniques for various applications were described. Research work with the use of OFS for SHM applications was reported in this chapter. Some research has been conducted using OFS such as DOF and FBG sensors for damage detection in composite materials. However, due to the brittleness of this OFS, their handling becomes difficult, leading to breakage of fibre during installation and handling. This limitation indicates the need for improvement/modification of the OFS. Overview of the textile manufacturing process of braiding was discussed, and this process is intended for micro-braiding of optical fibres. The importance of braid architecture on the mechanical properties of the braided preform was also highlighted. Different work on the consequence of various braid architecture on mechanical properties of braided ropes/preforms has been described.

Details of the novel process of micro-braiding of optical fibre will be studied extensively in the thesis.

2.11 Gap in literature

Of all the SHM techniques mentioned in the literature, the use of optical fibre sensors has improved over other techniques. The PCB is regarded as intrusive to host materials. The PWAS can only be surface bonded and requires lots of connecting wires and strain gauges that can only monitor local strain.

Improvement in SHM has been experienced over the years; however, further growth is dependent on the progress of sensing techniques. It is essential to have a durable sensor for real-time health monitoring of structures during the life cycle (fabrication and in-service). Little

attention has been paid to optical fibres' brittleness, making their handling difficult and reducing their robustness.

The thesis strives to bridge this gap by developing a novel technique of micro-braiding the optical fibre sensor to improve its handling and mechanical properties. Details of the geometrical parameter of the MBOF will be investigated. Characterisation of the conventional and micro-braided optical fibre will be studied to understand the effect of micro-braiding on the optical fibre. Finally, the conventional and micro-braided optical fibre will be implemented for SHM of composite structures.

Chapter 3: Materials, manufacture, methodology and characterisation

This chapter presents details of all equipment, characterisation and general experimental procedures used during this research.

A novel manufacturing procedure of micro-braided optical fibre (MBOF) is presented. The manufacturing process and parameters have been described and the challenges encountered during the process. The production of composite samples and the procedure used for mechanical testing will also be described.

3.1 List of experiments performed

Table 3.1 List of specimens and types of test performed

Specimen	Types of test	Parameter monitored
Micro-braided optical fibre (MBOF)	• Tensile test • Micro-bond test	• Effect of micro-braiding on handling and mechanical properties • To determine interfacial shear strength (IFSS)
Glass fibre reinforced epoxy composite laminate with embedded FBG (OF/MBOF)	• Three-point bending test	• Effect of embedding OF/MBOF on the mechanical proper
Glass fibre reinforced epoxy composite laminate with embedded DOF with sections bare and micro-braided	• Cure monitoring of laminate • Four-point bending test	• To determine the suitability of bare and micro-braided section of DOF for full lifecycle monitoring.
Braiding of tubular preform with embedded FBG and DOF (bare and micro-braided)	• Strain monitoring during braiding • Cure monitoring of tube	• To determine the suitability of bare and micro-braided section in monitoring strain during braiding of preform.

3.2 Materials

3.2.1 Optical fibres

Fibre Bragg Grating (FBG)

FBG sensors manufactured by AtGratings technology with the following properties were used:

Wavelength: 1540+/- 1 nm, Bandwidth: of 0.22 nm, SLSR: >15 dB, Reflectivity: >90%, Fibre type: polyimide coated SMF-28 and grating length: 10 mm.

Distributed Optical Fibre (DOF)

A single-mode polyimide coated silica glass DOF sensor with length 2 m, 155 µm diameter and 304 stainless steel termination of diameter 286 µm manufactured by LUNA was used.

3.2.2 Epoxy and Glass

Epoxy resin

Commercial epoxy resin and hardener were used for this study. Araldite LY 564 [177] supplied by Huntsman UK and Aradur 2954 hardener [177] supplied by Mouldlife. The mixing ratio of the resin and the hardener was 35 g of hardener for every 100 g of resin which is in accordance with the manufacturer's requirement [177].

Fibres

The fibre used for micro-braiding was an S glass tow [178] supplied by AGY with 33 Tex linear density, 207 filaments with each filament diameter of 9 µm as shown in Figure 3.1. A Tex can be defined as the weight of yarn/tow in grams with a length of 1km and is commonly used to express yarn/tow's linear mass density.

Figure 3.1 Multifilament S-glass tow for micro-braiding

E-glass fibre Twill 2 x 2 woven preform (876 gsm) supplied by Sigmatex (UK) Ltd was used to manufacture the composite laminate in this thesis. Figure 3.2 shows an image of the woven fabric.
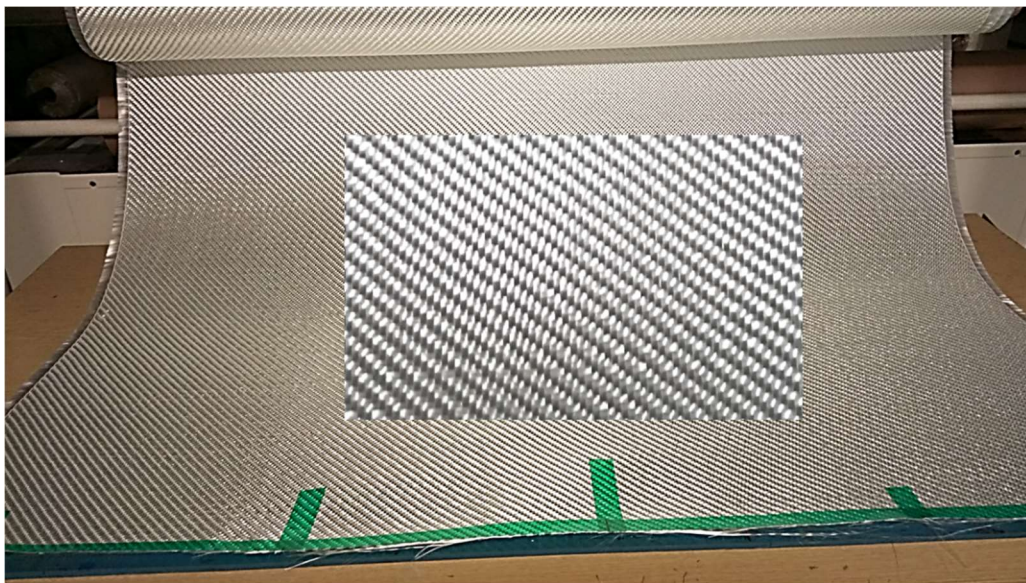
Figure 3.2 E-glass twill 2 x 2 woven preform with the magnified image of the repeated unit cell shown inset

3.3 Methodology

3.3.1 Manufacture and optimisation of braiding machine for micro-braiding

The manufacture of micro-braided optical fibre was carried out with a Cobra 450 maypole braiding machine with 12 horn gears, equipped with 24 carriers, as shown in Figure 3.3. A horn gear is a notched disk driven by a spur gear below on the same shaft; bobbins are transferred between notches of adjacent gears. However, only four carriers were used to braid the optical fibres, as shown in Figure 3.3a, since more than four carriers produced a braid with a looser grip on the conventional optical fibre (OF). A higher number of carriers resulted in braid diameter (braid with no core) becoming higher than the optical fibre. Moreover, the topology of a braid depends on the number of bobbins and the choice of the carriers' location on the braiding machine. The schematic of the micro-braiding setup is shown in Figure 3.3b. The use of 4 carriers (specifically chosen) on the 24 carrier braiding machine resulted in a diamond braid (1/1 topology) as shown in the schematic image in Figure 3.3c. If a tow continuously passes over one tow and then under one of the opposing groups, it is called a 1/1 braid or a diamond braid [99]. The use of four bobbins also resulted in a complete braid coverage of the OF. The bobbins that feed the yarn/tows were mounted on the selected carriers and were wound with 33 Tex, S-glass tow. A uniform yarn/tow feed tension of 150 g was kept constant for all carriers to keep the yarn/tows under tension to avoid non-uniform braid formation, as the tows will be slack at very low carrier tension. For the production of the micro-braid with the given set-up, ultra-high molecular weight polyethylene (DSM® Dyneema) [179] was bonded to one end of the optical fibre before passing it through the tension device and the centre of the braiding machine. The other end of the optical fibre was then taped to the device to hold it in place. The process was followed by micro-braiding a few millimetres over the optical fibre till the braid reached its convergence point (this is the distance from the braid ring to the point of interlacement). At a convergence point, a stable and uniform formation of braid occurs. The convergence point was kept constant at 90 cm because of the small braid angle achieved during micro-braiding. Micro-braiding was initially done using monofilament yarn details in Appendix 1A.
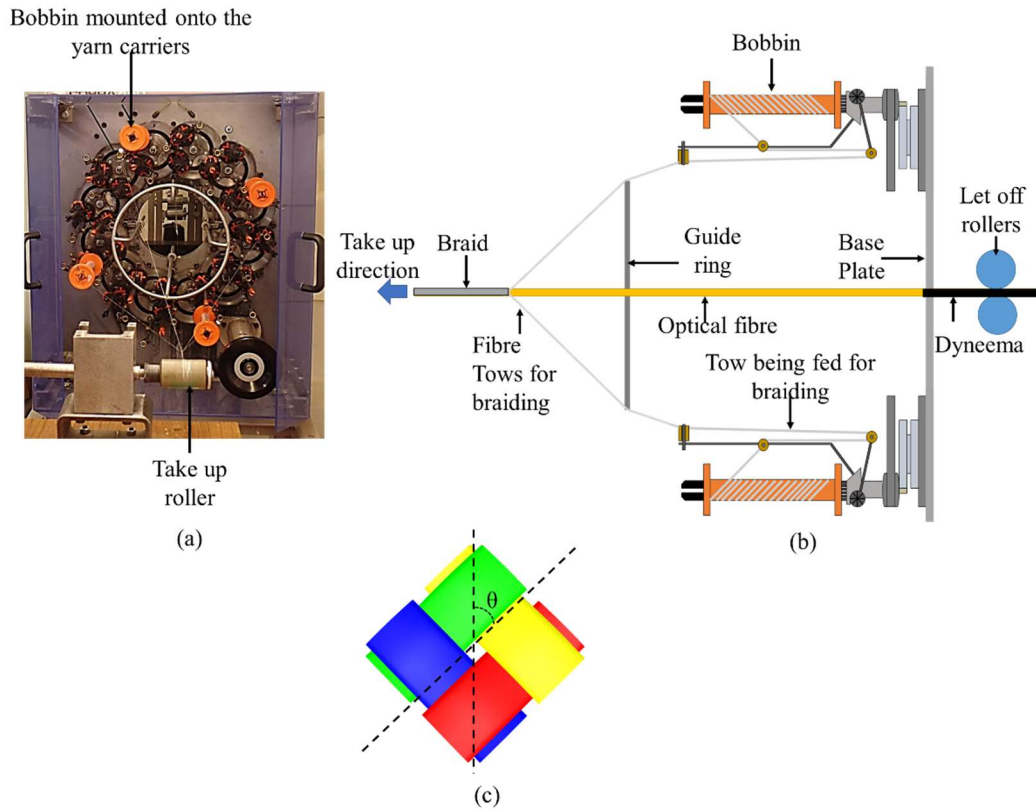
Figure 3.3 (a) 24 carrier braiding machine set up for micro-braiding the optical fibre, and (b) schematic image of braiding process (c) Schematics of diamond braid geometry TexGen [97], θ is the braid angle.

The machine speed

Machine speed is the speed at which the carrier (the machine frame housing the prime mover, bobbins, silver ring etc.) runs. It provides the average angular velocity of the bobbins around the machining centre. It is ideal for running the machine at maximum speed, for obtaining a maximum amount of production. However, because of the brittleness of glass fibre (braid yarn), when the machine speed is too high, then the friction between the fibres may cause them to cut each other, leading to braid yarn failure. After much trial and error, the optimum machine speed for micro-braiding was set at 5 rpm.

Take-up speed

Take-up speed is the mandrel linear speed, at which the device takes up the fibre delivered by the bobbins. Two different take-up mechanisms, such as the roller and horizontal take-up, were used during micro-braiding, as shown in Figure 3.4 a and b. The Take-up speed of a braiding

process determines two things; the braid angle and the production amount. The faster the take-up speed, the higher the amount of micro-braid produced. The principle of operation of both the roller and the horizontal take up mechanisms are similar. The horizontal take-up mechanism is CNC controlled and developed as an improvement to the roller mechanism because MBOF output winds around the roller, and this can affect the sensitivity of the optical fibre. Comparison of the sensitivity of the MBOF with a roller and horizontal take-up will be investigated in Chapter 4.

After much trial and error, the optimum take up speed was derived. The roller take-up speed at 1 rpm was converted to 0.0015 m/s, knowing the roller's radius as 1.5 cm and using Equation 3.1. For the horizontal take up, when the device was set at a speed of one, the achievable length of MBOF was 7.8 cm in 1 min to obtain 0.0013 m/s. At optimum speed for both roller and horizontal take up, 1 m optical fibre was micro-braided in 13 mins. The time taken to set up the braiding machine should also be considered to determine the total time needed. Because of the braiding machine's size and a limited number of bobbins required, set up time was reduced to the barest minimum.

$$V(m|s) = \frac{2\pi}{60} * R \qquad\qquad (3.1)$$

Where v is the velocity in m/s and R is the radius in m.
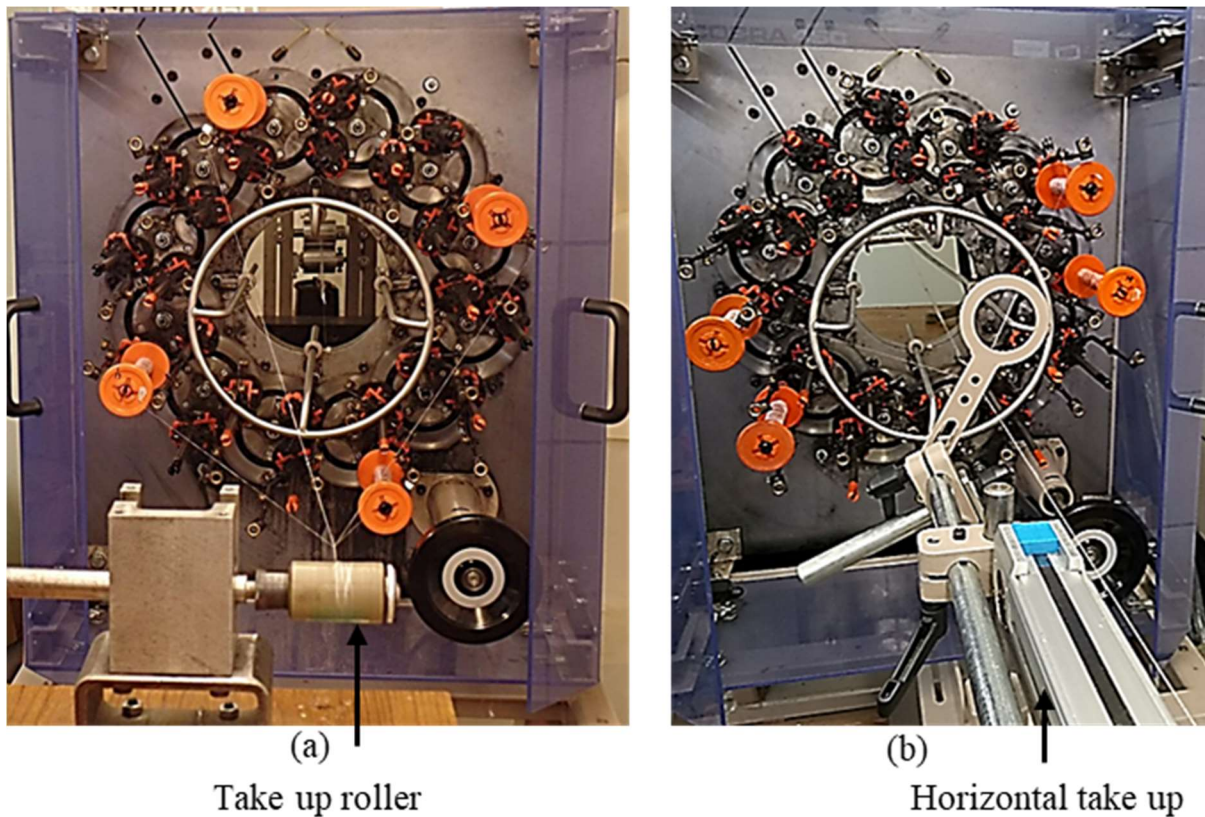
Figure 3.4 Braiding machine with two different take-up mechanism

3.3.1.1 Challenges during micro-braiding

During micro-braiding of optical fibre, several challenges were encountered. These include selecting bobbins configuration, winding bobbins with braiding yarn, initial machine set up, and determination of optimum parameters such as machine speed and take-up speed.

Other challenges encountered during manufacturing are:

Breakage of yarn filament

The winding of yarn on the bobbin influences the final quality of micro-braids formed. Fibre breakage during winding or the passing of the tow through multiple contact points on the machine's carrier can cause filamentation (the appearance of fibrous web generated by entangled broken filaments) when drawn from the spool; this causes increased tension of the affected yarn. This situation eventually leads to a gap and broken fibre in the micro-braiding.

Broken yarn can cause interruption of process and lead to machine downtime to fix the problem. Figure 3.5 shows the influence of filamentation on MBOF.
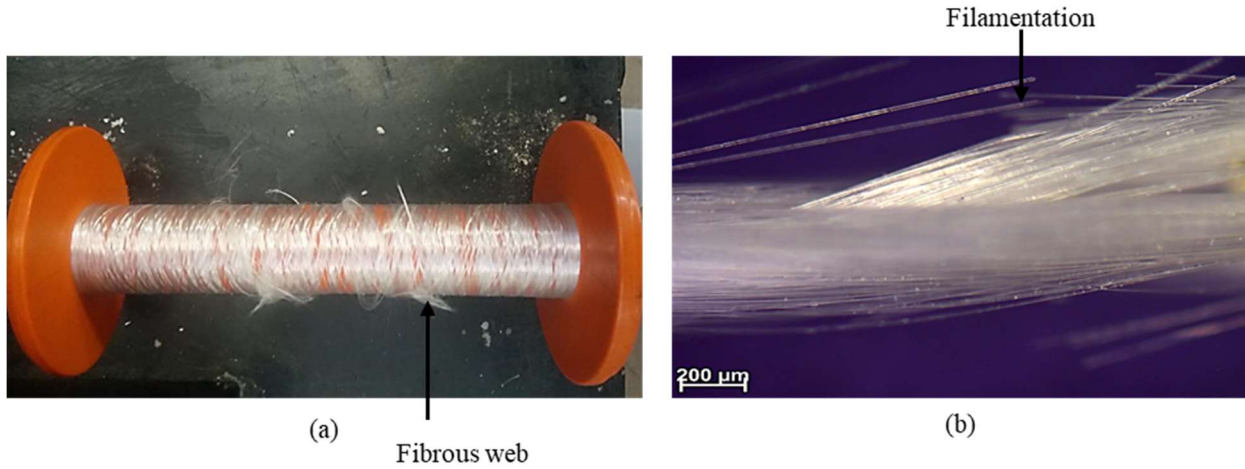
Figure 3.5 (a) Fibrous web on wound yarn (b) Fibre breakage/Filamentation in the micro-braided optical fibre

Debonding of optical fibre from Dyneema

During the manufacturing process, optical fibre was bonded to Dyneema for two reasons; 1) to act as extra length when micro-braiding the optical fibre, 2) allow easy release of length and avoid compression of optical fibre from the let-off roller as braiding progresses. Debonding of the optical fibre from Dyneema occurred when the bonding area is not given enough time to cure and also when the pull from the take-up device is too much (i.e. when take-up speed is high).

3.3.2 Manufacture of tubular braid preform

A 48-carrier Radial braiding machine at the University of Manchester, manufactured by Herzog Maschinenfabrik GMBH & Co. KG was used to produce braid preforms, as shown in Figure 3.6. Before the braiding process, initial preparations and selection were carried out for easier removal of the composite tube from the mandrel (mould). Only the mandrel with a uniform diameter around the cross-section was selected. The mandrel was cleaned with Easy-Lease™ mould cleaner, seven layers of release agent (Easy-Lease™ release agent) applied at every hour. The reason for this is to ensure the separation of the mandrel from the cured resin. The braided preform was then produced using a 675 tex 449 S-2 Glass roving by Agy [180]. Sixteen out of the 48-carrier radial braiding machine were used to achieve a (2 x 2) regular braid pattern**.**

The mandrel (mould) used to form the over-braid preform was Aluminium-based with a mandrel diameter of 20 mm. The mandrel was clamped using a chuck, part of the braiding machine set up, capable of moving forward and backward, with its movement controlled using a CNC controller. Yarn/tow feed tension of 500 g was maintained for all the carriers.

The braiding machine speed used was 20 rpm, and with take-up, speed yielding a lay length of 10 mm. After the first layer of each braiding, two different sensors (FBG and DOF) were carefully aligned axially on the braid and held in place with tape before the second layer was braided on it. The braided preforms were manufactured embedded with FBG (OF and MBOF separately) and DOF (bare and micro-braided), maintaining the same braiding parameter. The braiding process and data collection setup are shown in Figure 3.7a, Figure 3.7b and 3.7c show the OF and MBOF on the first layer. For the FBG sensor, data was recorded from the optical fibre via a static optical sensing interrogator sm125 manufactured by Micron optics. Spectral analysis, peak detection and data logger was recorded using an ENLIGHT sensing analysis software. For the DOF, data acquisition was achieved using a LUNA Inc. (ODiSI-B model) interrogator.
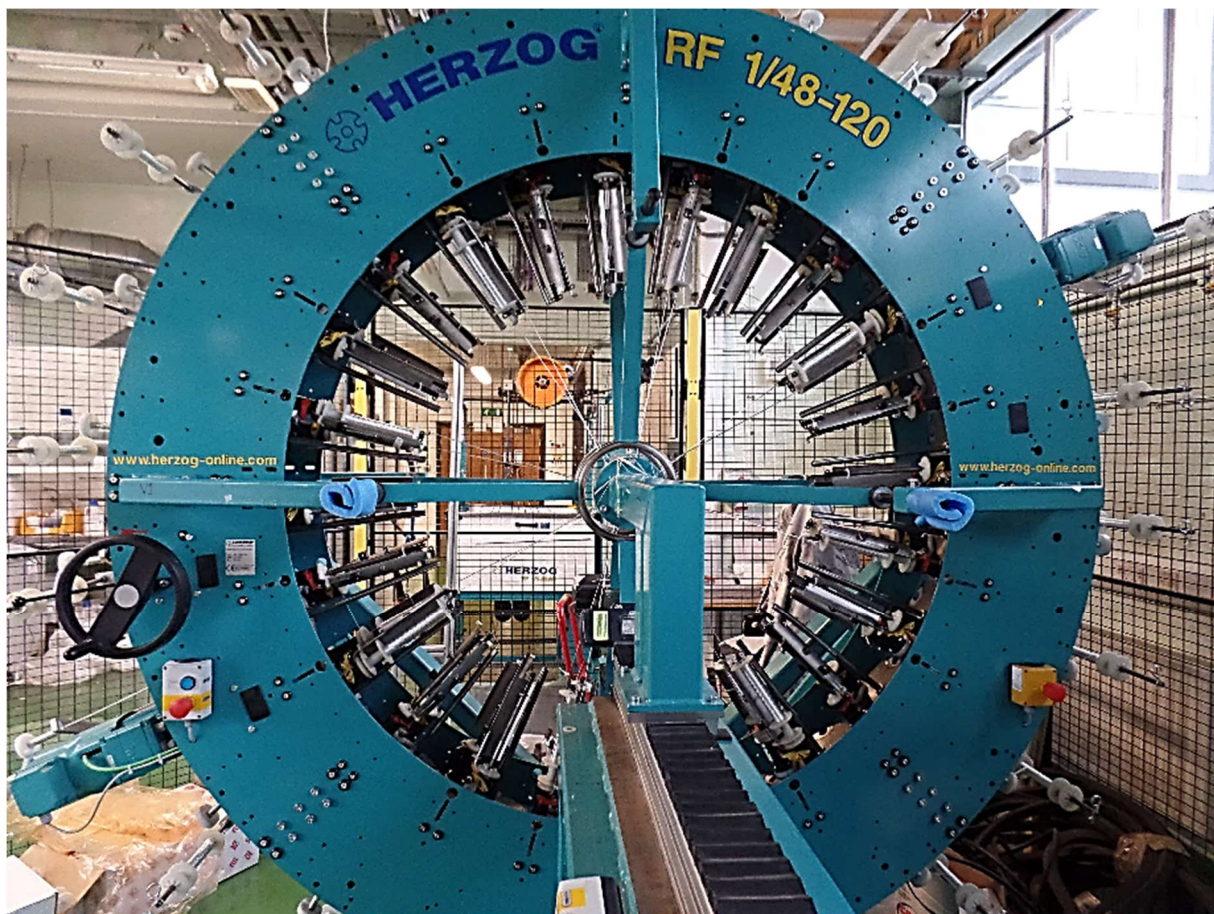
Figure 3.6 48-carrier radial braiding machine
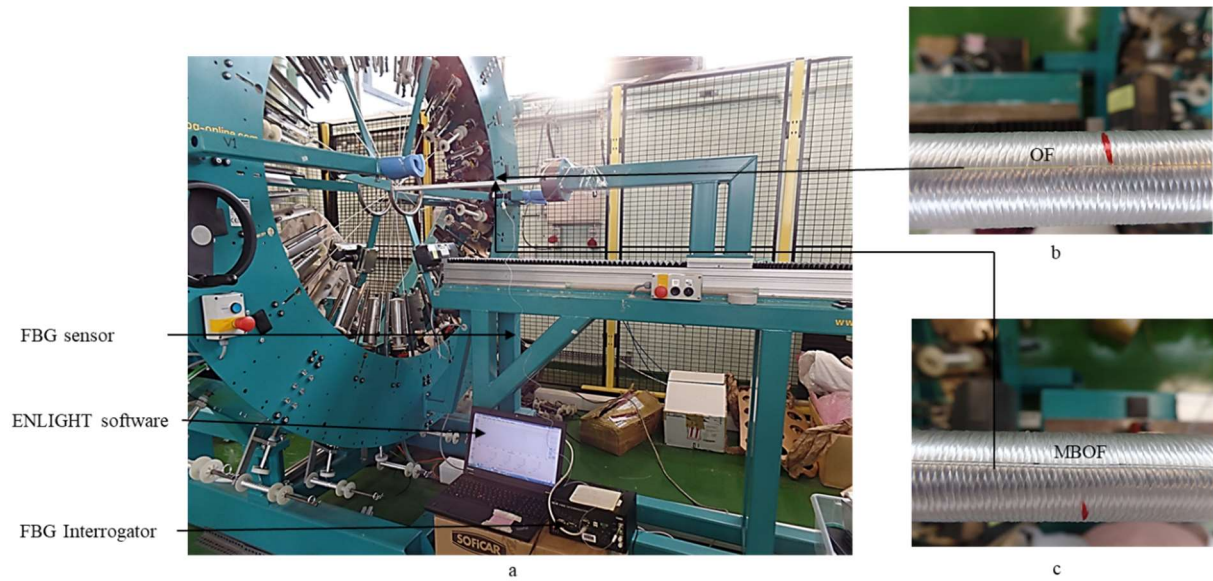
Figure 3.7 (a) The setup of the braiding process with FBG interrogator for measuring induced strain for (b) conventional optical fibre (OF) and (c) micro-braided optical fibre (MBOF).

3.3.3 Manufacture of composites

An Aluminium plate of dimension 50 cm x 50 cm was used as a mould for making the composite panel. The mould was first cleaned with a mould cleaner, then coated with a mould release agent and allowed to dry for 1 hr before applying two more layers of the release agent. This allows for easy removal of the composite panel from the mould.

3.3.3.1 Layup of fabrics

The 2x2 E-glass woven fabric was cut at 90° along the axis and laid upon the mould. Edges of the fabric cut-out were held with tape to prevent fibre fraying.

Composite panels were manufactured for different experiment with details below;
Four-point bending test was utilise for strain monitoring with embedded OF and MBOF, while three-point bending was used for studying the effect of embedded OF and MBOF on the mechanical properties of the manufactured composite.

Lay-up of the composite panel for cure monitoring and four-point bend test

Six layers of 400 mm x 200mm woven fabric cut at 90º along the axis, and the path for the optical fibre were marked for easy embedding. Part of the DOF length was micro-braided to facilitate the handling and improve its strength before the embedding process, while the remaining length was left bare. The DOFS was carefully inserted and secured beneath fibre floats in the fabric to avoid the need for a bonding agent. In this way, the composite's overall mechanical properties remain intact even with the sensor's presence. The DOF was embedded between the fourth and fifth layer of fabric. The bare DOF segments were positioned close to the long edge and at the mid-point of the laminate, while the micro-braided optical fibre (MBOF) part was positioned close to the other long edge, as shown in Figure 3.8. Three strain gauges were also bonded to the surface of the plate. The three OF sensing regions were positioned 50 mm apart. The ingress point, which is the termination end of the DOF, was protected between fibre float while the egress point was protected using a 0.6 mm diameter polytetrafluoroethylene (PTFE) capillary tube to prevent breakage of the DOF. The PTFE capillary tube was sealed to avoid resin flow into the tube.
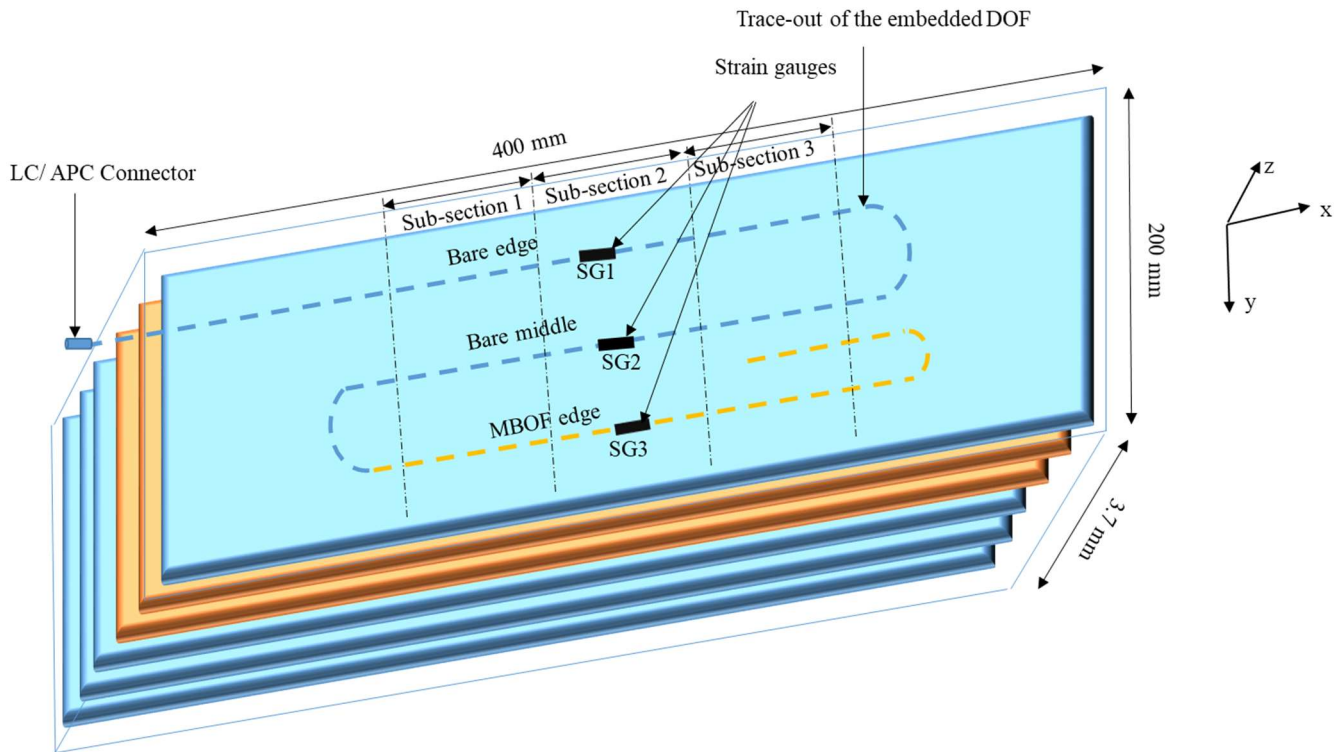
Figure 3.8 Schematic representation of the composite panel (with DOFS between the orange fabric layers).

Lay-up of three-point bending test sample embedded with OF and MBOFs

Four layers of 30 cm x 30 cm woven fabric were stacked together with the OFs and MBOFs embedded 5 cm apart between the 1st and 2nd layer, as shown in Figure 3.9. The three-point bending test was selected for investigating the effect of embedding OF/MBOF on the integrity of composites to explore different mechanical tests.
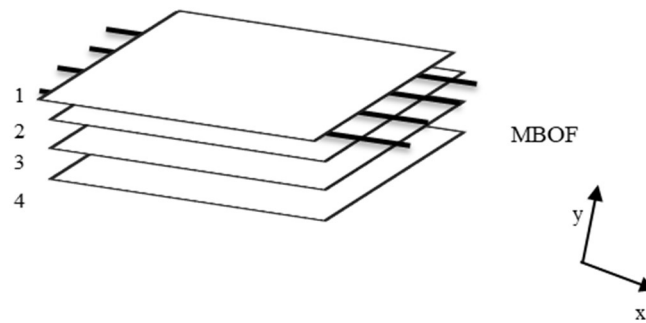
Figure 3.9 The layup of fabric with micro-braided optical fibre (MBOF) or conventional optical fibre (OF) embedded between the first and the second layers (y-axis is through the fibre thickness and x-axis is along the warp direction).

3.3.3.2 Vacuum bagging

Following the layup of fabric, a vacuum bag was prepared to infuse the reinforcement with the resin. The vacuum bagging was achieved as described below:

- Cover the laid up fabric with peel ply for easy removal of the composite after curing;
- An infusion mesh for proper flow of resin during infusion;
- Inlet and outlet spiral tube at two ends of the mould for uniform resin flow into the reinforcement;
- Vacuum bag nylon and sealant tape was used to cover the whole arrangement, as shown in Figure 3.10.
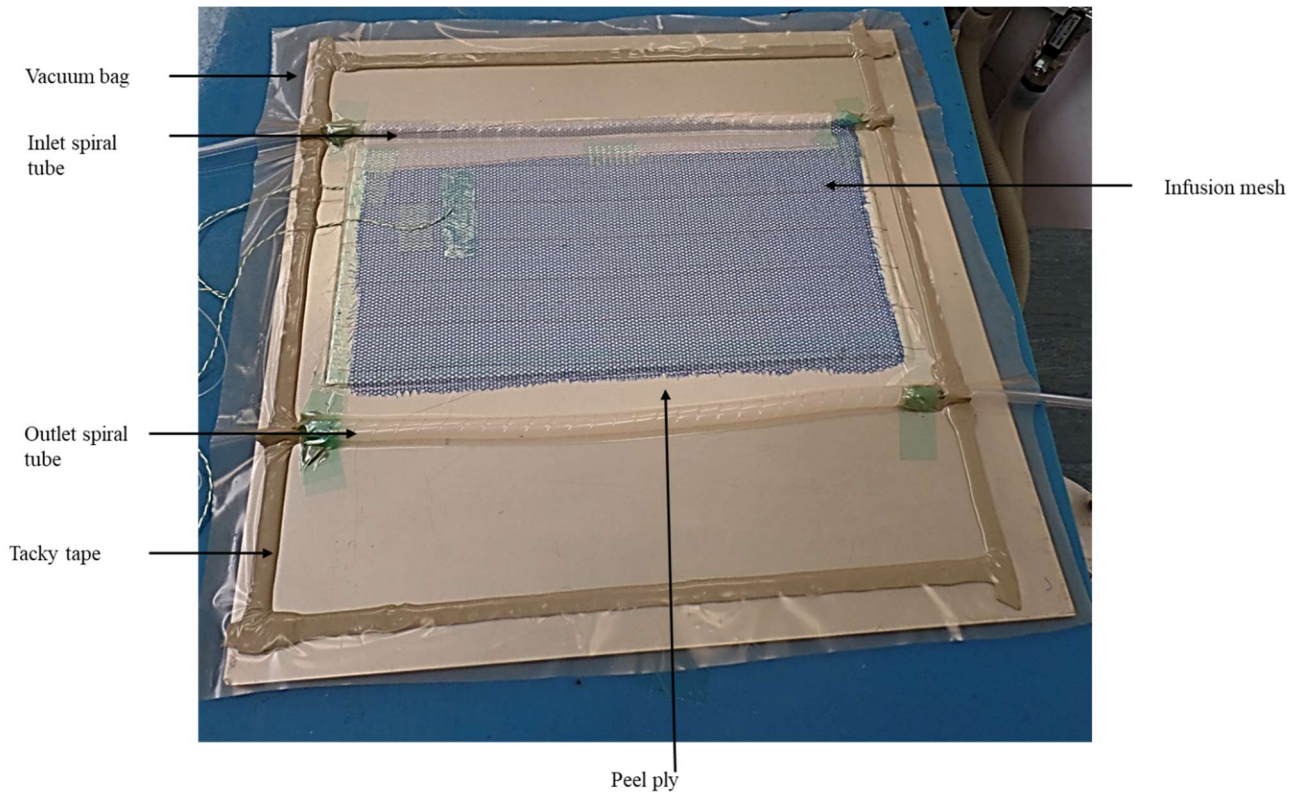
Figure 3.10 Completely vacuum bagged panel

Vacuum bagging of tube preform

The vacuum bagging of the braided preform tube is almost similar to the flat panel. In this case, the preform on the mandrel was first wrapped with a woven release fabric generally known as peel ply, allowing for easy flow and absorption of excess resin. The peel ply creates a textured appearance on the outside of the composite, suitable for bonding during further processing. An infusion mesh was placed on the peel ply, which acts as a medium for transporting the resin from the inlet to the whole preform. A spiral tube was wound around the preform's circumference and other infusion materials on both edges to allow resin flow in and out of the tube and around the preform. An extended bit of peel ply was present at the outlet spiral tube to enable the resin to flow into the spiral tube once it reached the preform's end. Vacuum bag nylon was placed around the materials, and the PTFE protected section of the OF was gently passed out through the bag before sealing the whole setup using sealant tape to create an airtight seal. Figure 3.11 shows a vacuum-bagged tube perform.

Figure 3.11 Vacuum bagged tube preform

3.3.3.3 Resin infusion

Before infusing the resin into the preform, a mixture of epoxy and hardener was degassed in the degassing chamber to remove air bubbles and also prevent void in the final composite panel. Vacuum-assisted resin infusion moulding (VARIM) was employed. In this process, the inlet tube was inserted into the resin mixture and the outlet tube into a vacuum trap in the vacuum pump to dispense excess resin. A vacuum pressure of about 1 bar was used to pull the resin into the preform, increase compaction, and produce a composite with sufficient resin content. Once the system's infusion is complete, both inlet and outlet tube was clamped to maintain vacuum before removing the inlet tube from the resin mixture and cutting off the outlet tube from the vacuum pump. Figure 3.12 shows the process of resin infusion.

It is challenging to infuse a resin in cold weather, as the infusion process becomes very slow with time. This drawback is because the pot life of the mixture becomes lower when cold. To achieve a longer pot life, the resin was pre-heated during degassing to 20°C to increase the pot life and increase the resin's flow rate.
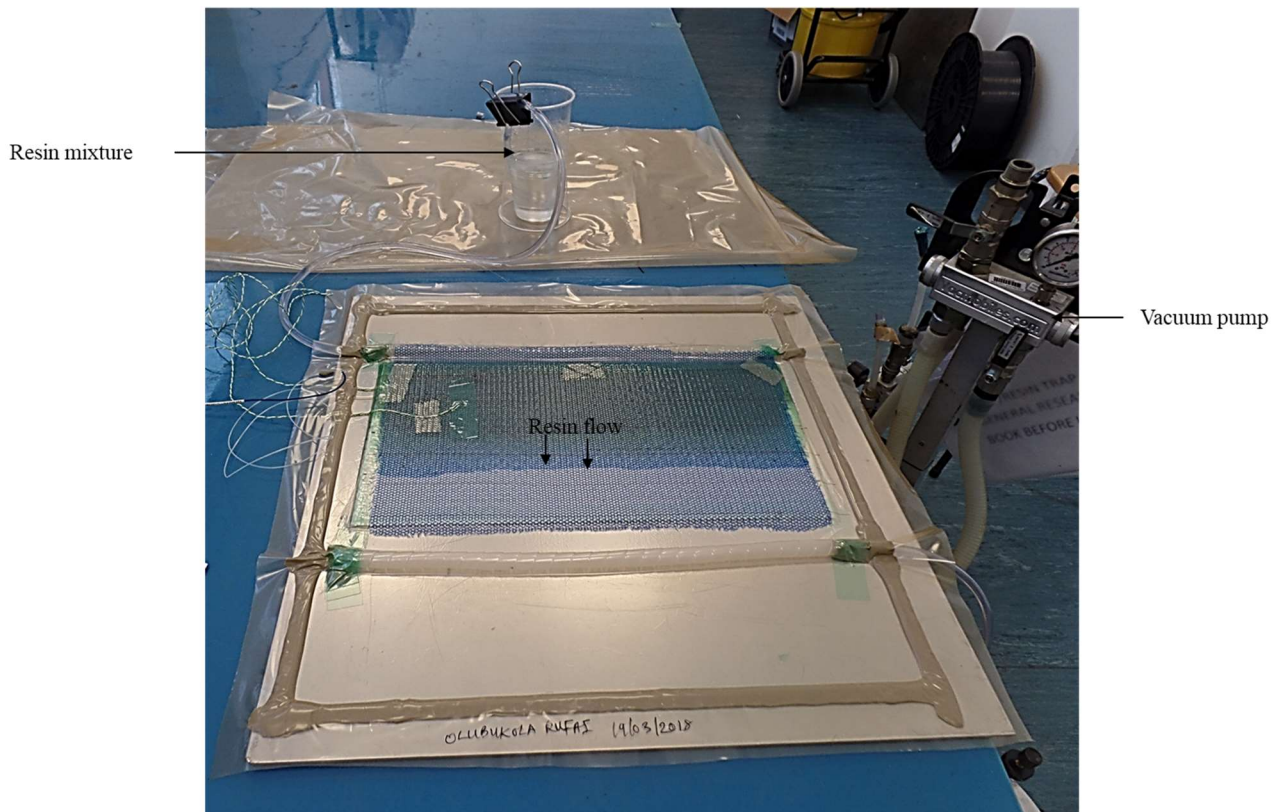
Figure 3.12 Infusion process showing the flow of resin in the preform

3.3.3.4 Curing

The infused preform was held at 80°C for 2 hrs after 1 hr ramp time, followed by 8 hrs at 140°C after a ramp-up time of 1 hr. The initial increase in temperature causes softening and a decrease in the viscosity of the resin. At the second stage of cure, the resin system becomes polymerised, causing an increase in viscosity till it reaches a state when it is no longer liquid and has lost its ability to flow, known as the gelation point. As the temperature increases further at the third stage, viscosity increases and the gel point transitions to a glass state due to increase in the amount of crosslinking of molecules; this stage of cure is crucial because it has a good reflection of the mechanical properties. The final stage of cure involves the solid-state reaction within the glass state.

After curing, the composite is carefully de-moulded to avoid damaging the composite panel. A diamond cutter is later used to cut the composite to specification with sufficient allowance for finishing. The specimens were then dried in the oven to remove water from the composite specimen.

Details of cure monitoring during the manufacture of a composite panel with embedded optical fibre will be discussed in Chapter 5.

Challenges encountered during the manufacture of composite tube

The manufacture of a composite tube is a very tedious procedure because debagging and demoulding can be very demanding, and extra care is required when an optical fibre has been integrated into it.

Debagging

Because the length of the intended composite tube is long, it took several hours to debag. It was discovered that the infusion mesh and the peel ply was fused, making debagging difficult, as shown in Figure (3.13). It was observed that the surface of the composite tube is rough due to scratches made on it by the knife used for debagging. After much trial and error, this was rectified by applying a perforated release film layer to create an interface between the peel ply and infusion mesh, as shown in Figure 3.14. A smoother surface of composite was achieved as there was no excessive use of a knife during debagging.

Demoulding

To demould a composite tube, the tube's edge was held with a vise for pulling the composite off the mandrel. The diameter of both sides of the mandrel exposed was measured to determine the side with a smaller average diameter and from which the composite will be pulled out. On most occasions, there is a need to keep the mandrel in the freezer for extraction; this aids thermal contraction of the mandrel. This process will make mandrel extraction easier.
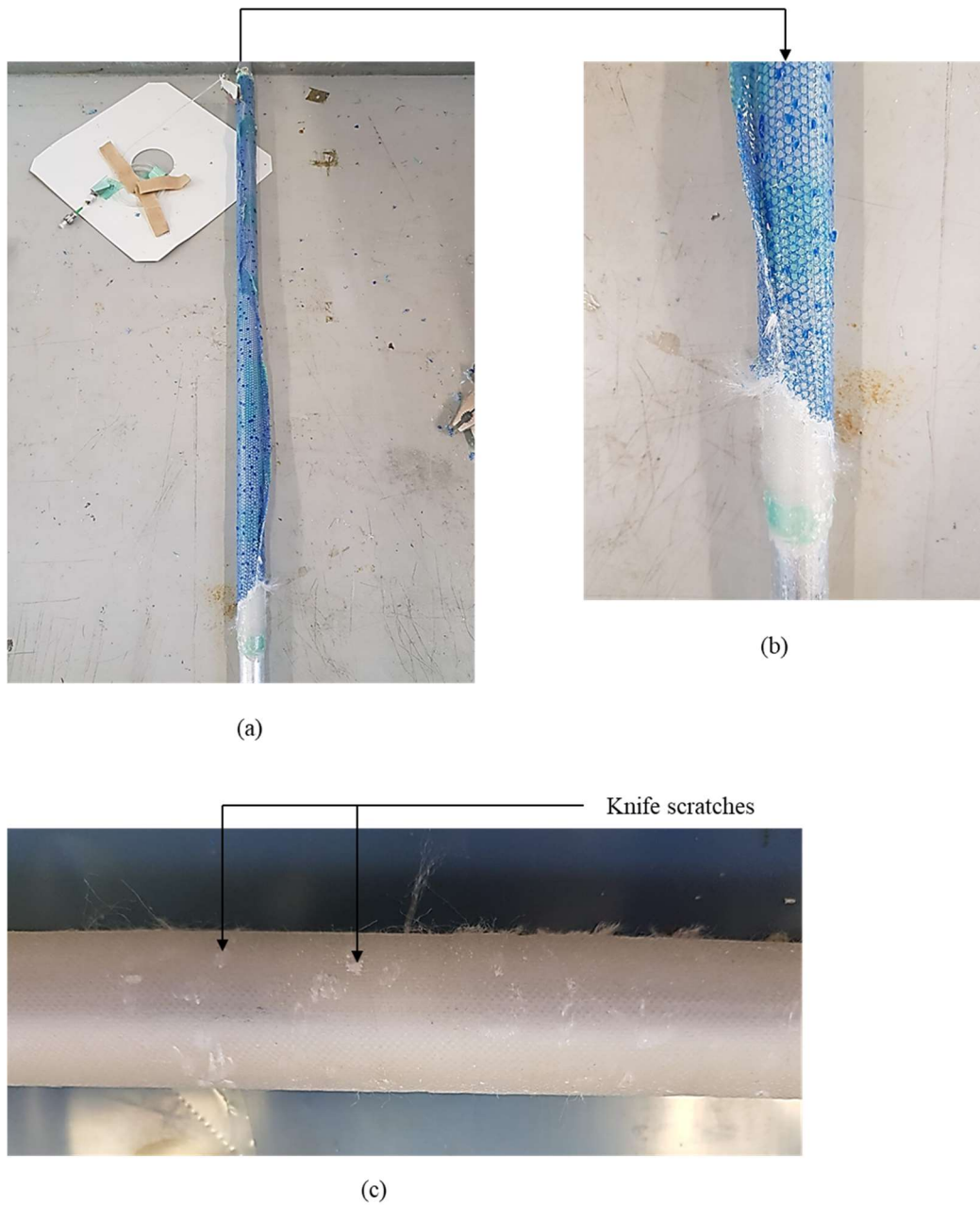
Figure 3.13 (a) Composite tube during debagging (b) shows infusion mesh tighly infused on the peel ply and (c) scratches on the composite tube during debagging

(a)

(b)

(c)

(e)

(d)
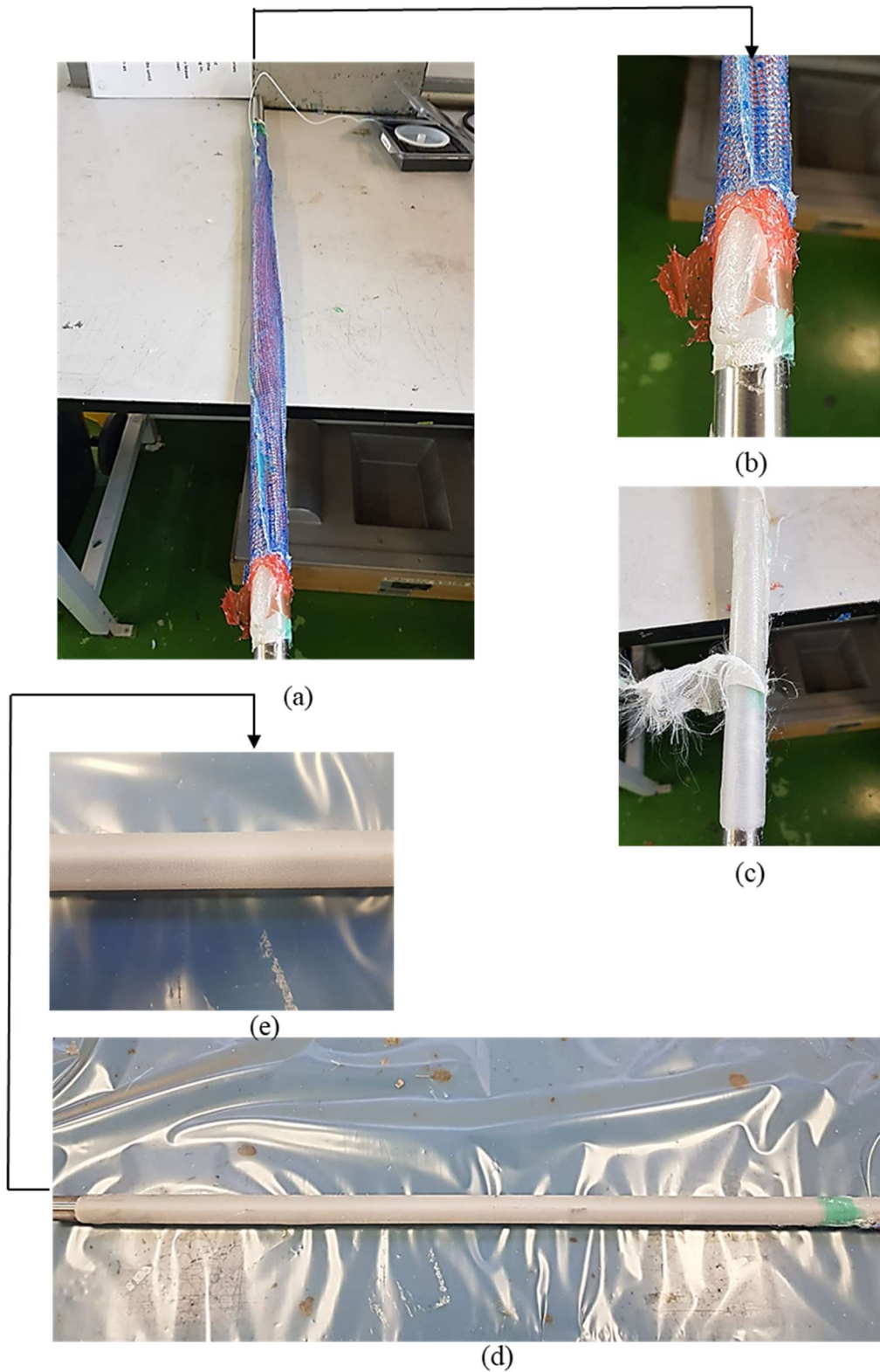
Figure 3.14 (a and b) shows the interface created by the perforated release film, (c) easy removal of peel ply, (d) composite tube after debagging and (e) zoomed image showing no scratch on the composite tube.

3.4 Mechanical tests

3.4.1 Tensile test of OF and MBOF: Specimen preparation and experimental process

Tensile test at room temperature was conducted by closely following ASTMD2256/D2256M [181]. It is crucial to tab the specimens because the Instron machine with pneumatic grip caused damaged on the samples (OF and MBOF) at the grip point. Tabbing of the test samples was achieved by bonding the OF/MBOF specimens in-between the glass tab (already sandblasted for firm grip) using a two-component epoxy paste adhesive Araldite 2011 (ADF0224600). The specimens' length is 25 cm, and the tab dimension is 3 cm x 3 cm, as shown in Figure 3.15a. 4 specimen each was tested for the OF and MBOF. The instrument used for the tensile test is an Instron 3344 tensile testing machine with a load capacity of 2 kN and a crosshead speed of 2 mm/min was used. The effective strain on the FBG and its integrity was also monitored during the tensile test using an optical sensing interrogator (Micron-Optics sm-125). Figure 3.15b shows the setup of the tensile test with the FBG interrogator.
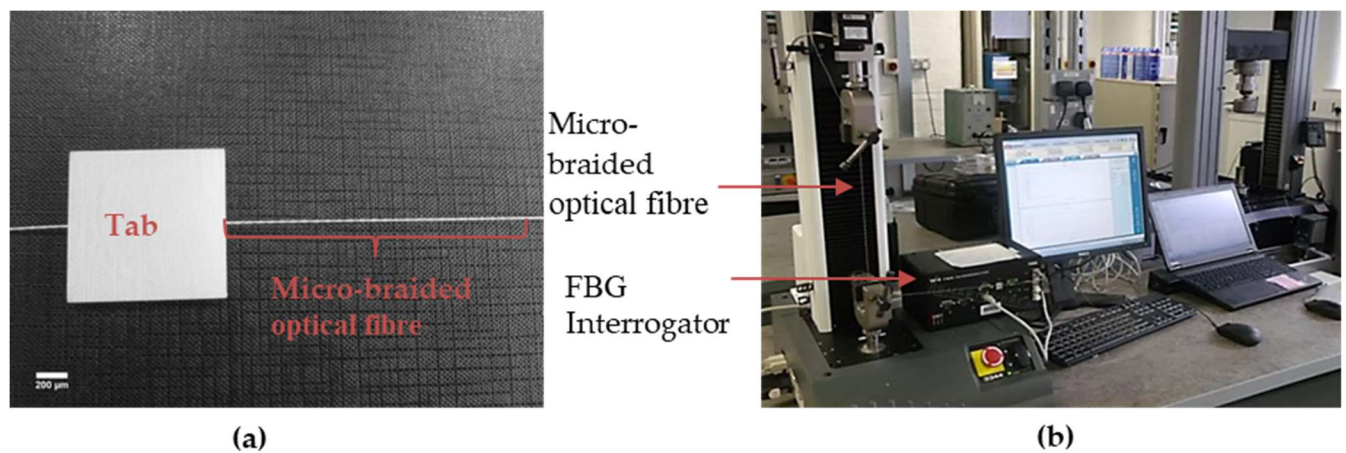
Figure 3.15 (a) Zoomed image of the glass tabbing of the micro-braided optical fibre (MBOF) and (b) setup for strain measurement with FBG interrogator during the tensile test.

3.4.2 Three-point bending test: specimen preparation and experimental approach

A three-point bend test was conducted on the Instron 5969B11590 machine with a load cell of 50 kN. The cross-head displacement used was 2 mm/min. The specimen and test setup are shown in Figure 3.16. Specimen dimensions were as follows: span length 96 mm, width 15

mm and thickness 3 mm. The dimension and procedures for the three-point bending test were in accordance with ASTMD7264/D7264M [182]. Three different samples were prepared: (1) with no embedded optical fibre, (2) with embedded optical fibre and (3) with embedded micro-braided optical fibre. Six specimens each were tested for the different category of sample. The flexural strength σ was calculated using the Equation below.

$$\sigma = \frac{3FL}{2bh^2}$$ (3.2)

Where

σ is the flexural strength (MPa)

F is the maximum load applied to the specimen (N)

L is the span length (mm)

h is the thickness of specimen (mm)

b is the width of the specimen (mm)
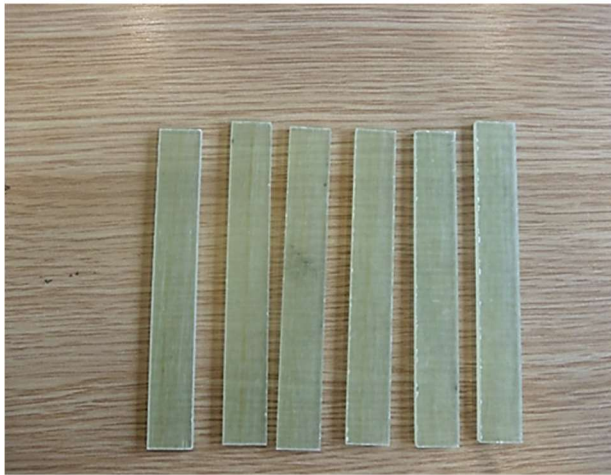
(a)

(b)

Figure 3.16 (a) Three-point bending test specimens (b) machine setup for the three-point bend test.

3.4.3 Micro-bond: Sample preparation and test

Microdroplets of resin were deposited on single fibres held horizontally on a cardboard tab using individual fibres from S-glass tow (BY), conventional OF and MBOF. No standard way of preparing samples for the micro-bond test have been reported in the literature. However,

different techniques have been developed by researchers. A mixture of epoxy resin Araldite LY564 and hardener Aradur 2954 were deposited on the fibre using strands of each fibre and cured. The samples were heated to 80°C (glass-transition temperature) in 1 hour and held for 4 hours because the cardboard tab could not be heated to a higher temperature [177]. Sixty samples of each fibre (BY, OF and MBOF) were prepared. Micrographic image of the specimens was taken using an Axio-Zeiss optical microscope. After carefully scrutinising the micrographic images, only fibres with symmetrical resin droplet were selected for the test. This process is essential to avoid huge variation in the calculated interfacial shear strength (IFSS). Embedded length, droplet area, and fibre diameter were measured using microscopic images shown in Figure 3.17.
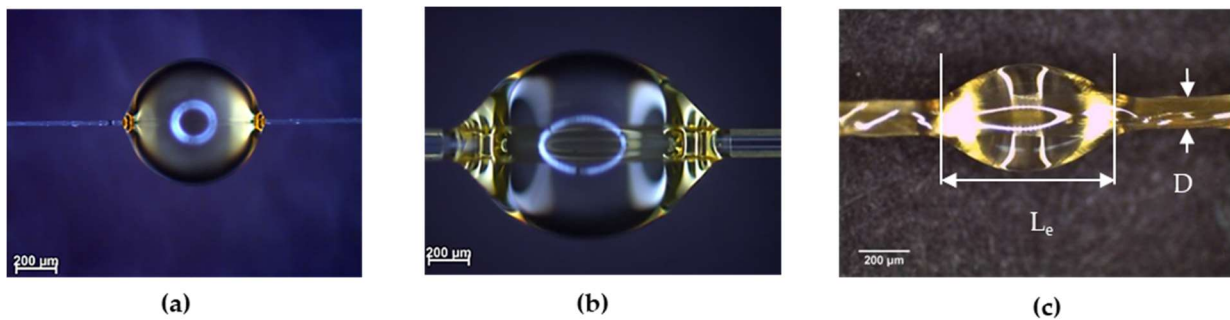
Figure 3.17 Optical image of typical resin droplet onto (a) S-glass yarn, (b) conventional optical fibre and (c) micro-braided optical fibre.

To perform the micro-bond test, an Instron 1122 mechanical testing machine with two movable knife edges controlled by a micro-meter head was utilised. This is shown in the machine setup and schematic image in Figure 3.18. The load cell varied from 5 to 100 N was used according to the specimen diameter. The test was conducted at room temperature with a displacement speed of 1 mm/min. The micro-bond specimen is gripped at one end by a jaw in the testing machine, which is pulled upward. Constant distance between the knife edge and resin droplet was maintained, and a movable knife edge obstructs the movement of the droplet. Due to the obstruction of the resin droplet movement, the shearing force is transferred to the fibre through the fibre/matrix interface. When the shearing force reaches a critical value, pull-out occurs, and the droplet is displaced downward along the fibre axis. Some samples experienced sliding of resin from the fibre and breakage of fibre instead of de-bonding the resin from the matrix. Data from these samples were discarded. Only de-bonding samples were used in this analysis.

During the test, force and displacement were recorded. From each curve, the de-bonding peak force (F_D) was recorded.
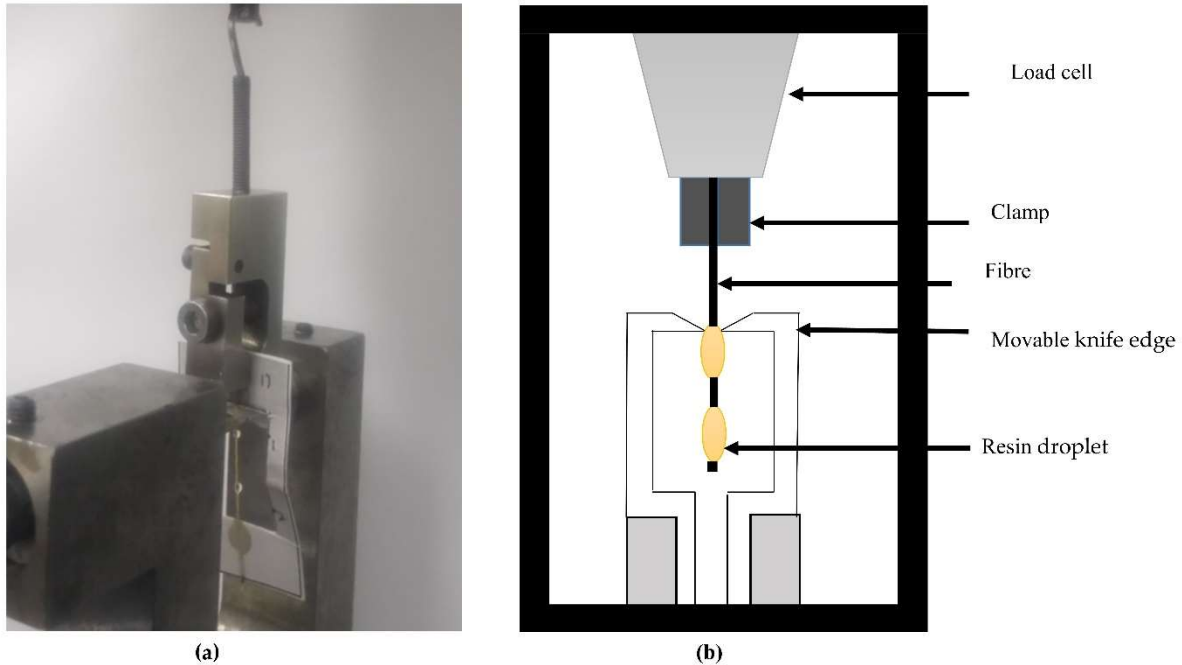
Figure 3.18(a) Machine setup for micro-bond test and (b) schematic image of the micro-bond test setup.

Taking the braiding yarn (BY), for example, resin droplet was made using a strand of the BY fibre to make droplet on the BY sample; this method was also used for the OF and MBOF using fibres of the OF and MBOF. The higher diameter of fibre absorbs more resin droplets to completely cover the fibre diameter [78,80,184–186]. As seen in Table 3.1, the embedded length increased as the sample diameter increased. The embedded length distribution of the three different samples is shown in Figure 3.19; the highest relative frequency of embedded length for BY is between 0.5-0.6 mm;+ OF is between 1.2-1.3 mm and for MBOF 1.8 and 2.0 mm. It has been reported by [183,184] that variation in IFSS data for fibres is influenced by factors such as fibre diameter, embedded length, surface morphology and quality of the prepared samples for the test. Wang et al. [183] reported a variation of 4–10 MPa in IFSS data for bamboo fibre with nearly the same embedded length of 200 mm due to surface morphology.

Table 3.2 The average value of embedded length, droplet area and fibre diameter for different samples.

Sample	Embedded length (mm)	Droplet area (mm^2)	Fibre diameter (mm)
BY	0.65 ± 0.23	0.02 ± 0.008	0.01 ± 0.0035
OF	1.14 ± 0.17	0.54 ± 0.08	0.15 ± 0.004
MBOF	1.90 ± 0.22	2.7 ± 0.31	0.45 ± 0.065
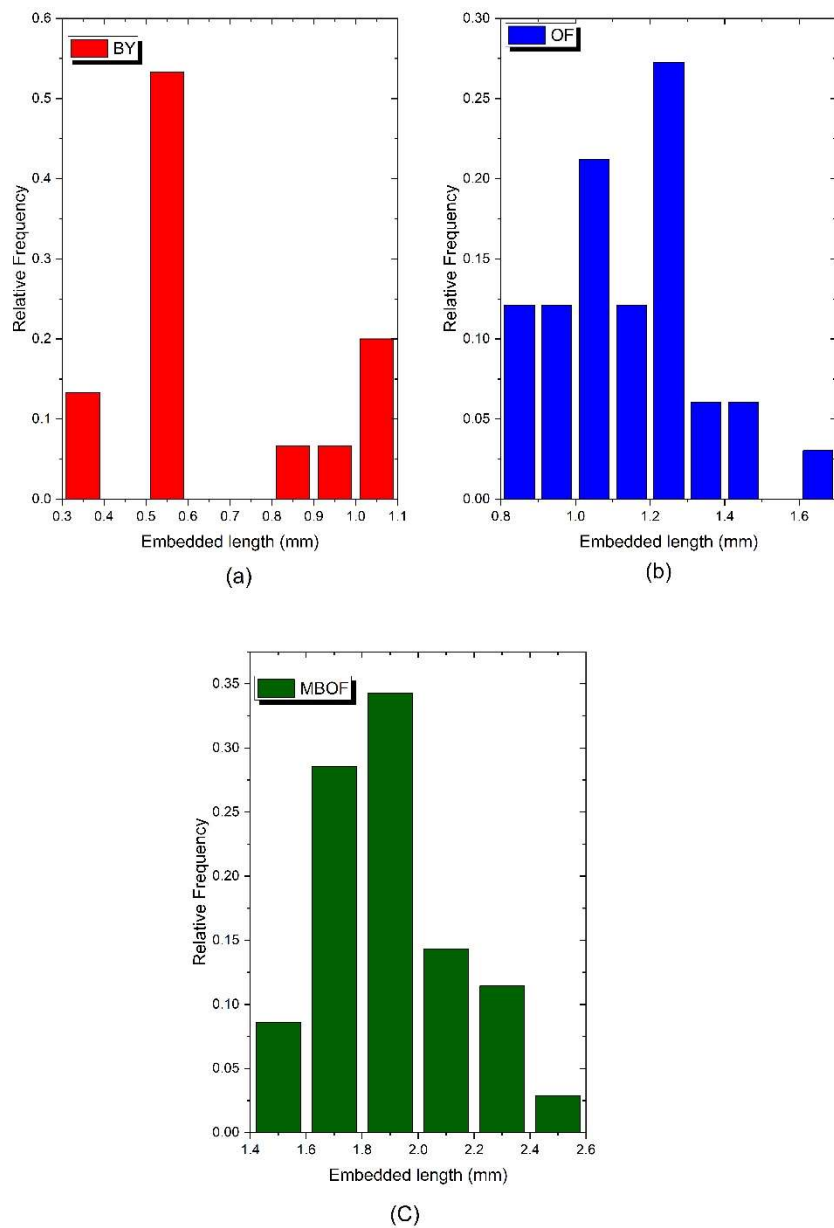
Figure 3.19 Embedded fibre length distribution of (a) Braiding yarn (red), (b) Conventional optical fibre (blue) and (c) Micro-braided optical fibre (green)

Interfacial shear stress (IFSS) between the fibres and epoxy resin was calculated using Equation 3.3, assuming that shear stress is uniformly distributed along the embedded length.

$$IFSS = \frac{F_D}{D\pi L_e}$$

(3.3)

Where D is the fibre diameter, and Le is the embedded length.

3.4.4 Four-point bend test composite panel

After manufacture, the composite panel was trimmed to 385 mm x 150 mm without touching the egress side because of the distance of the DOF to the edges. Quasi-static four-point bending was then conducted on an Instron 5969 testing machine equipped with a 50 kN load cell Figure 3.20. The distance between the loading noses is one half of the support span in accordance with ASTM standard D6272 [185]. Aluminium spreader bars were placed between the test machine and specimen to ensure uniform load distribution across the panel width. During the test, a crosshead speed of 1 mm/min was maintained. Loading was completed in a series of loading/unloading cycles to determine the repeatability associated with strain measurement in the bare and micro-braided OF segments. During each loading cycle, the surface strain was measured using uniaxial electrical strain gauges positioned on the surface of the laminate, in the centre of each OF sensing region. Table 3.2 shows the average strain measured by the strain gauges. The acquisition rate of the DOF is 23.8 Hz with a gauge length of 1.25 mm; data from the embedded DOF was recorded at 5 Hz using an OFDR-bases interrogator (ODiSI-B system, supplied by LUNA Inc.).

(a) (b)
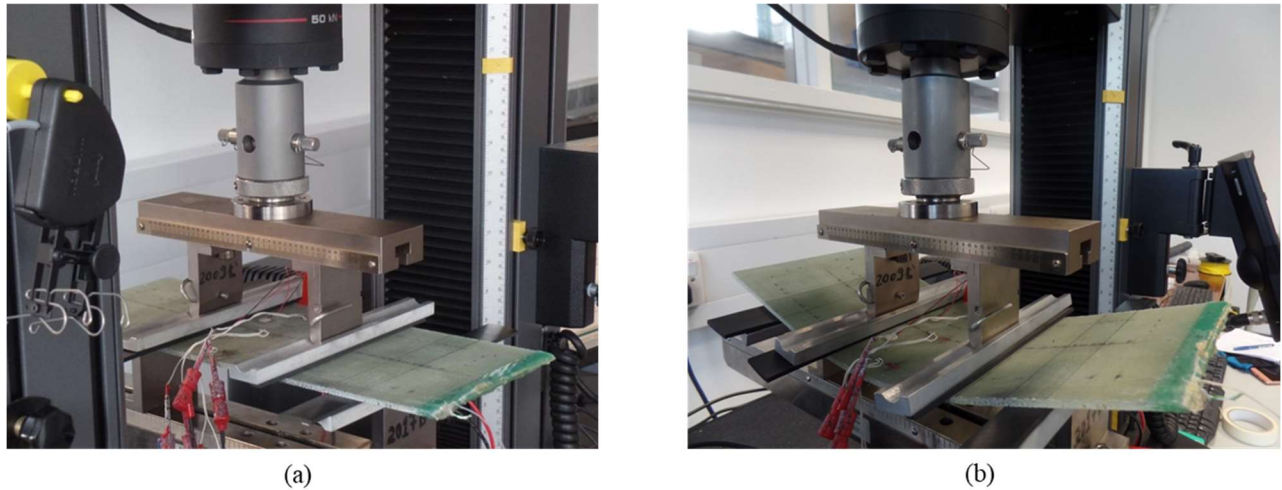
Figure 3.20 Four-point bending experimental set up: (a) before loading, (b) during loading.

Table 3.3 Loading cycles of four-point bending test

Loading cycle	Mean compressive strain (SG1 to SG3) (με)	Standard deviation
1	972	42
2	1908	80
3	2846	122
4	3790	166
5	4729	212
6	5638	281
7-11	7511	381
12-21	9385	481
22-26	10404	469

3.5 Characterisation

3.5.1 Scanning Electron Microscope (SEM)

SEM is a kind of electron microscope that utilises focused electron beams to create images of a specimen by scanning its surface. Sample preparation is essential in SEM; inadequate sample preparations can undermine the quality of the image produced. The size of the sample, shape

and conductive properties were put into consideration during sample preparation. The double-Sided copper tape was stuck to a sample stub to create a conductive environment around the sample. A bamboo stick was then wound with copper tape and stock to the stub. The samples were gently handled with a tweezer to avoid contamination and exposure to moisture by the bare hand. Epoxy glue was applied to the wound stick before placing the FBG/MBOF sample on it, and another layer of glue is applied and allowed to cure for 15 minutes. Highly conductive silver paint (PELCO Conductive Silver paint) was applied around the FBG/MBOF sample, wound bamboo stick and some areas of the stub and allowed to dry for 1 hr. The silver paint creates a conductive path or conductive bonding for the SEM sample. Carbon tape was pasted in the middle of the stub using a tweezer. Figure 3.21 below shows steps for SEM sample preparation.

(a)

(b)

(c)

(d)
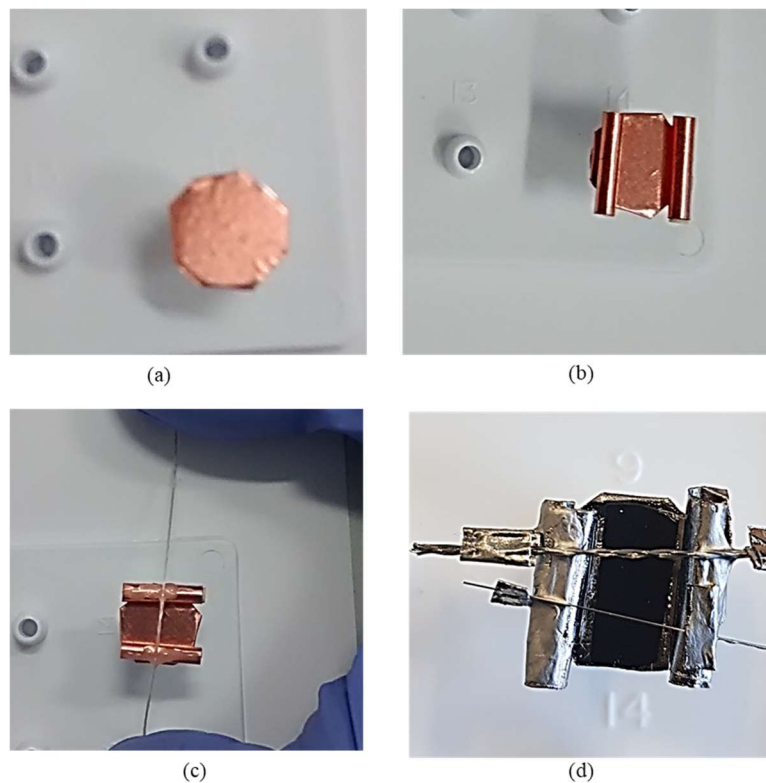
Figure 3.21 Scanning Electron Microscope (SEM) sample preparation

The sample was further coated using a Quorum Q150T ES (a combined system capable of both sputtering and carbon coating) to deposit a thin layer of conductive Gold-Palladium of 20 nm on the sample. This process prevents charging (i.e. accumulation of static electric charges on the sample's surface), heat build-up, reduces beam damage, and allows imaging at a higher voltage.

The diameter of the FBG was measured from the SEM image, as shown in Figure 3.22. The average measured FBG diameter at different points along the optical fibre was 150±4 μm.
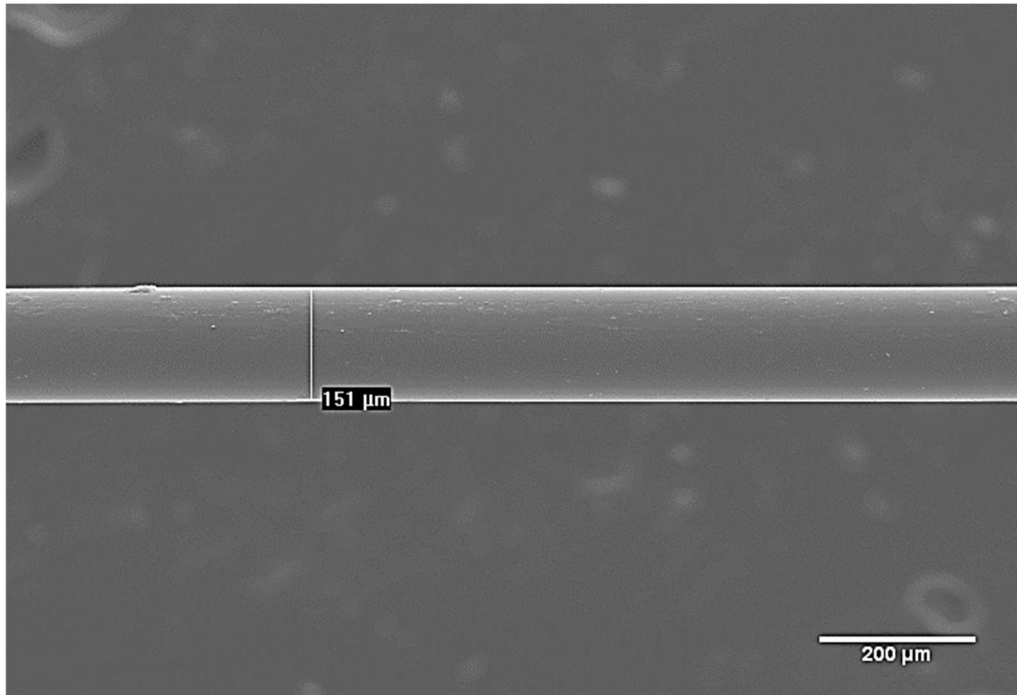
Figure 3.22 Scanning electron micrograph (SEM) of a conventional optical fibre (OF) sensors.

3.5.2 Density measurement

The density of the S glass tow for micro-braiding was determined using the Archimedes principle (weight loss by a solid immersed in a liquid is equal to the amount of fluid it displaces), by measuring the weight of the sample in air and then in water. Mettler Toledo, density measurement device, was used as shown in Figure 3.23 a and b. Density was calculated by dividing the weight to the sample by the difference in the weight of the sample in air and water, as shown in Equation 3.4.
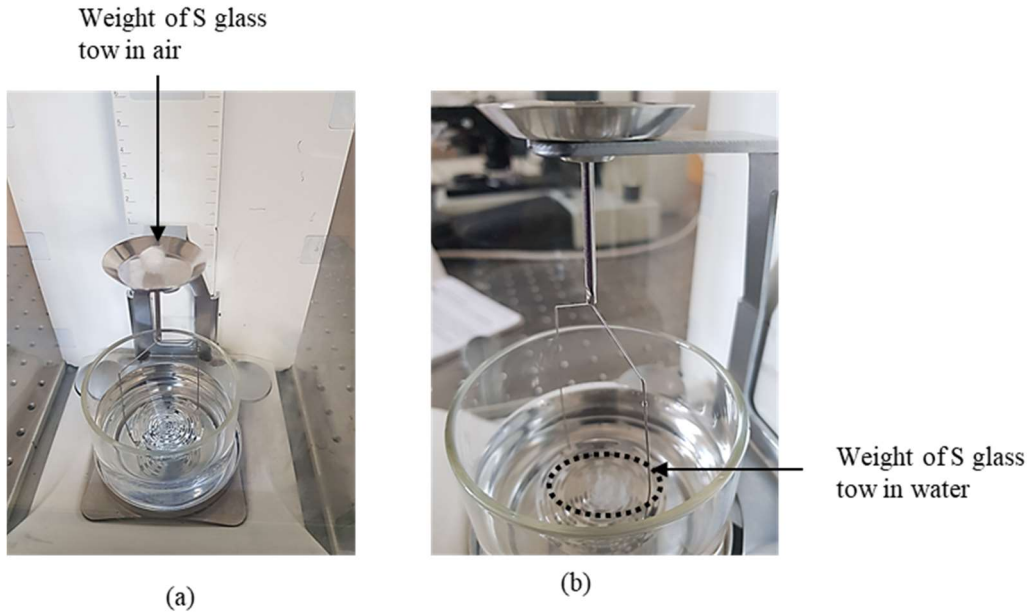
Figure 3.23 Measurement of density of S glass tow in (a) air and (b) water

$$\rho = \frac{A}{A-L}(\rho_L - \rho_A) + \rho_A \qquad (3.4)$$

Where ρ is the density of the sample, A is the weight of sample in air, L weight of sample in liquid, ρ_L is the density of the liquid and ρ_A is the air density. The density of S glass tow was found to be 2.54 ± 0.03 g/cm^3

3.5.3 Tensile property

The tensile properties of the S glass tow were measured experimentally following the standard BS EN ISO 2062:1995. Instron 3345 series tensile machine with a 5 kN load cell and pneumatic grips clamping at a pressure of 90kPa were utilised. The tows were clamped using the special gripping system present at both ends. This gripping system consisted of two pneumatic action grips, two parts, as shown in Figure 3.24. The fibre tows were wrapped (3 turns) in the first part, and then the two parts were closed using pneumatics, locking the wrapped tow in its position. A total of 9 specimens were tested at a strain rate of 250 mm/min. The Young's modulus was found to be: 61 ± 2 GPa and the tensile strength was found to be: 1663 ± 230 MPa.
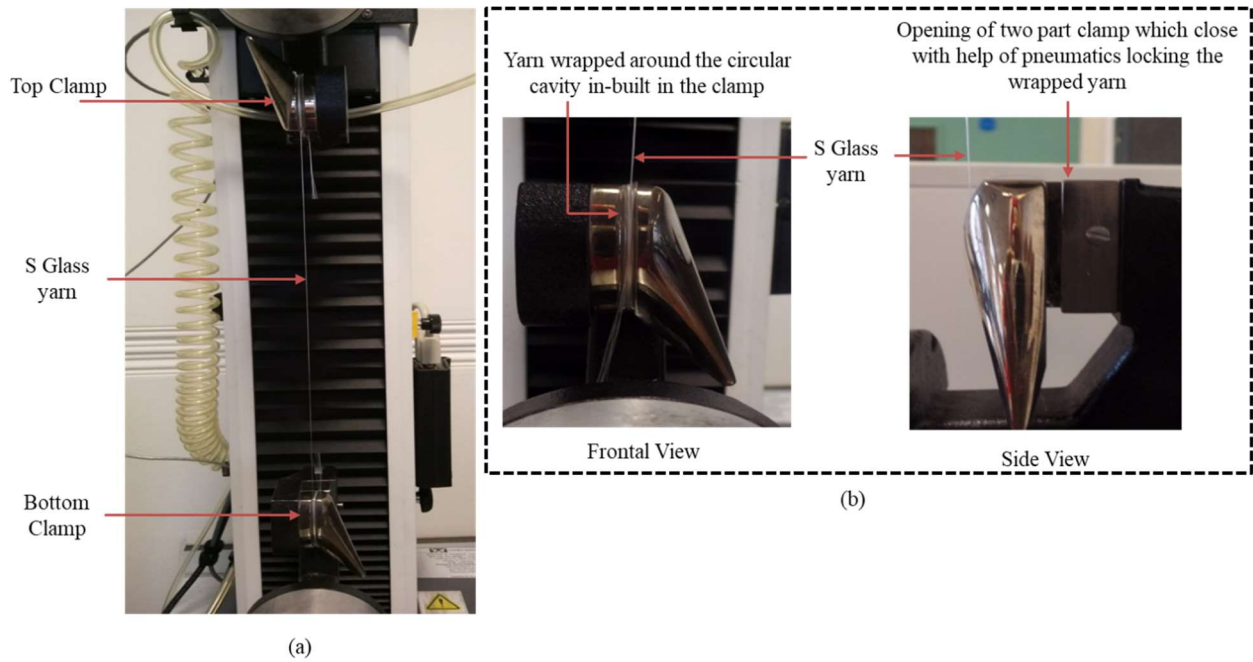
Figure 3.24 (a) Setup for the tensile test of S-glass and (b) zoomed clamping procedure.

3.5.4 C-Scan probe of manufactured composites

C-scan is widely used for NDT examination of composite structures after manufacture to ensure high quality [186]. The composite laminate was examined for voids or porosity, which could have been caused by trapped air during the curing process using a 2 m x 2 m MIDAS water jet c-scan. The c-scan machine is highly automated, allowing scanning, data collection, and advanced image processing to present the c-scan image. The laminates were carefully clamped unto the specimen holder and fired with water on both sides with a water jet shown in Figure 3.25. The water jet transmits an ultrasonic beam to the specimen, and this transverses the specimen and travels through another water stream on the other side to the receiving transducer. From the c-scan image in Figure 3.26 of composite laminate embedded with MBOF and OF, it was evident that no void or porosity is present in the specimen. The red dots shown in the image signifies foreign materials like the tape at the edge of the panel and clamp used to hold the samples together.

Figure 3.25 Configuration of specimen in a c-scan machine

$$(a) \qquad\qquad (b)$$
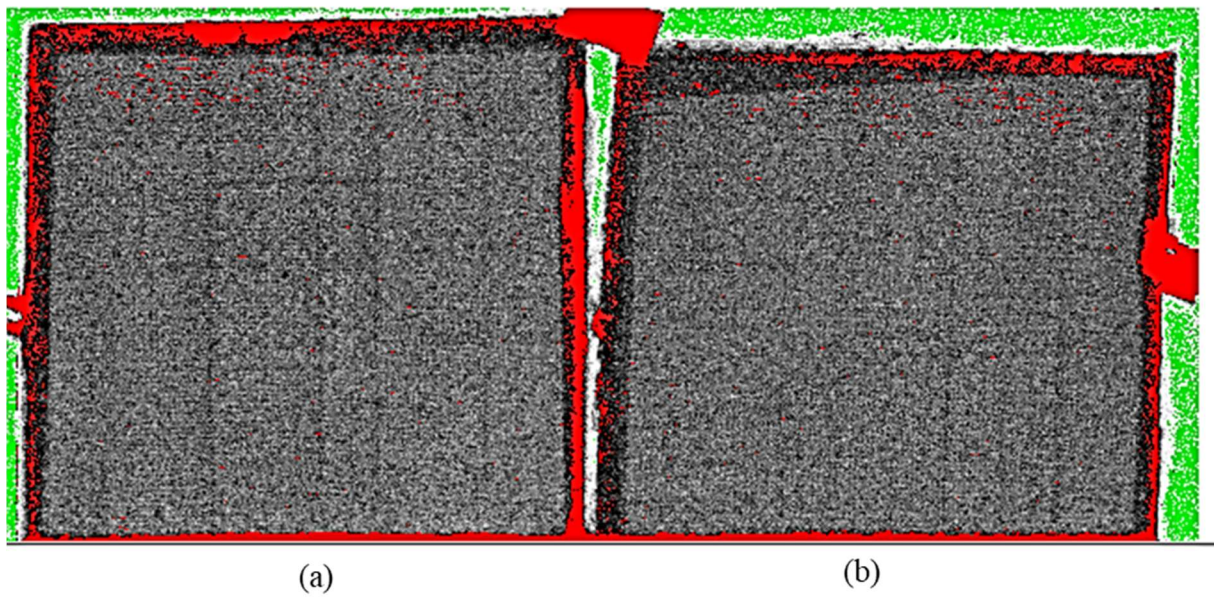
Figure 3.26 C-scan of composite laminate embedded with (a) MBOF and (b) OF

3.5.5 Determination of fibre volume fraction (V_r) by Burn-off test

Fibre volume fraction (V_f) was determined by putting the composite specimen in a crucible and placing it in the furnace to allow the matrix to degrade, leaving only the reinforcement.

The analysis was performed on the burn-out remains in accordance with ASTM 3171-15 [187]. A digital weighing scale was used to determine the mass of the composite specimen, the mass of crucible before and after rein burn-off, and the mass of the reinforcement after burn-off. The specimens were then inserted into a Carbolite muffle furnace, and resin burn off was conducted at temperatures between 500-600ºC for 6 hours, as shown in Figure 3.27.

Figure 3.27 Muffle furnace for burn off test.

The initial mass of the specimen was measured (S), followed by the mass of the crucible (M₁) and the final mass of the crucible with the specimen residue/fibre (M₂).

Fibre volume fraction was calculated using the Equations below;

$$M_f = M_2 - M_1 \tag{3.5}$$

$$W_r = \frac{M_f}{S} \tag{3.6}$$

$$V_f = \left(W_r \left(\frac{\rho_s}{\rho_f} \right) \right) \qquad (3.7)$$

Where M_f is the mass of the residue/fibre in (g), W_r is the fibre weight fraction, ρ_s is the density of specimen and ρ_f is the density of fibre in (g/cc).

V_f is one of the significant factors which vary the composite strength. The fibre volume fraction of between 50-65% shows improved mechanical strength; many works have been reported to support this statement [188,189]. The measured V_f for laminate embedded with OF was determined as 52% ± 1%, while the V_f for laminate with MBOF was found to be 50% ± 1%. This is an important sign that indicates the mechanical properties of the manufactured composite are intact even with the embedded optical fibres. Table 3.3 shows the result of the Fibre volume fraction table.

Table 3.4 Volume Fraction of glass fibre/epoxy composite

Specimen		Specimen wt (g)	Density g/cc	Crucible wt (g)	Crucible + fibre (g)	Fibre wt (g)	Fibre weight fraction	Fibre volume fraction	Matrix weight fraction	Matrix volume fraction
OF	1	1.07	1.91	27.34	28.11	0.77	71.68	52.37	28.32	47.97
	2	1.04	1.93	46.74	47.49	0.75	72.01	52.96	27.99	47.74
	3	1.07	1.90	47.92	48.68	0.77	71.39	51.85	28.61	48.18
Mean			1.92	40.67	41.42	0.76	71.69	52.39	28.31	47.96
MBOF	1	1.06	1.85	27.34	28.07	0.73	69.38	49.07	30.62	50.212
	2	1.02	1.86	47.20	47.93	0.73	70.89	50.33	29.10	47.90
	3	1.074	1.87	46.74	47.50	0.77	71.51	51.01	28.49	47.13
Mean			1.86	40.43	41.17	0.74	70.59	50.14	29.41	48.42

3.6 Summary

The process of manufacturing a micro-braided optical fibre for structural health monitoring was described in this chapter. Challenges encountered during the micro-braiding of optical fibre in machine set-up, materials selection and process configuration were discussed and elucidated. Details of continuous fibre layup technique using a CNC controlled mandrel to braid the tubular preform was described. Stages and processes involved in the manufacture of composite laminate and tube with embedded optical fibre for structural health monitoring were described. Debagging and demoulding a composite tube was more tricky than the laminate because of the complexity of the shape.

Necessary discussions on sample preparation for image analysis (SEM) and mechanical tests equipment with the operating procedure has been described in this chapter.

Chapter 4: Results and Discussion: Optimisation of optical fibre using micro-braiding for structural health monitoring

Optical fibres (OFs) are used for detecting damage in composite structures due to their lightweight, size and immunity to electromagnetic interference [22,135]. SHM requires the use of online sensing techniques to provide continuous assessment of engineering structures such as aircraft, automobiles, building, train and bridges. Available practical experience has proven that continuous improvement of the sensing techniques will further accelerate SHM technology's growth. The main advantages of FBG sensors over other OF sensors are its low cost, good linearity, availability of wavelength multiplexing and elimination of transduction mechanism, which is available in interferometric sensors. However, these OFs have the disadvantage of being brittle and easy to break at a low strain of <0.8%; this makes their handling very difficult.

In this chapter, braiding will be used to improve the handling and mechanical properties of conventional OF. The potential of optimising OF through the textile manufacturing process of braiding will be investigated. The modification of the OF will be achieved through a novel process of micro-braiding. Mechanical and handling properties of the micro-braided optical fibre (MBOF) will be studied to determine the effect of micro-braiding on the OF.

4.1 Characterisation of micro-braided optical fibre (MBOF)

Figure 4.1 shows the SEM of the MBOF. The image was analysed using Image J an open-access software, to determine the braid parameters such as the braid angles, the diameter and yarn width, which is reported in the physical property of the MBOF shown in Table 4.1.
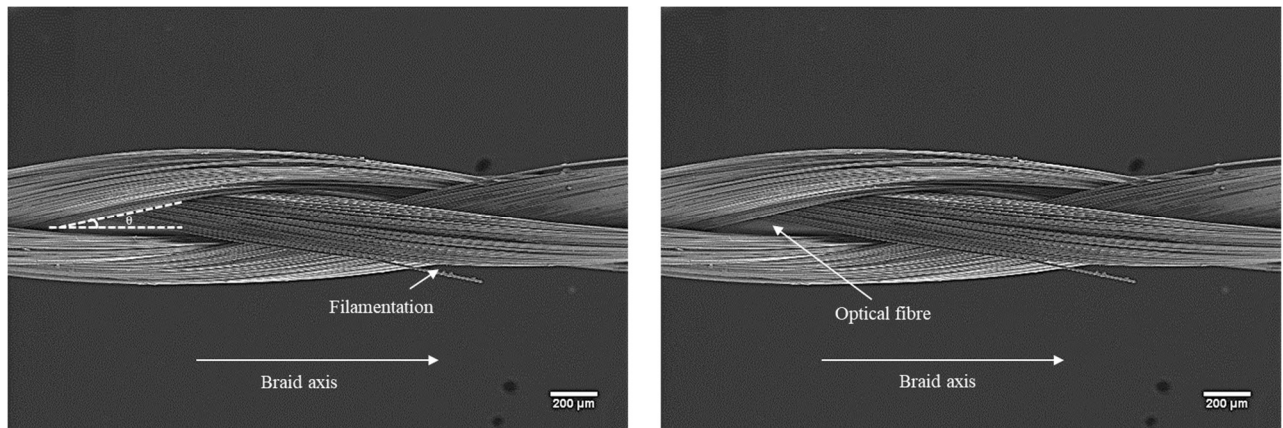
Figure 4.1 Scanning electron micrograph (SEM) of micro-braided optical fibre (MBOF), where θ is the braid angle

Table 4.1 Physical properties of manufactured micro-braided optical fibre (MBOF)

Take-up mechanism	Braid angle (°)	Braid Diameter (μm)	Coverage (%)	Yarn width (μm)	Crimp angle (°)	Linear Density (tex)	Crimp ratio	Density (kg/m³)
Roller	16.9 ± 1.2	423 ± 61.4	98.4 ± 0.19	208 ± 11	4.4 ± 0.03	168 ± 5	0.0034 ± 0.00005	2.214±0.07
Roller	17.3 ± 1.7	382 ± 53.7	98.3 ± 0.27	210 ± 10	4.8 ± 0.07	170 ± 8	0.0029 ± 0.00004	1.956 ± 0.06
Roller	16.0 ± 1.5	407 ± 54.3	98.5 ± 0.21	200 ± 9	3.94 ± 0.06	160 ± 3	0.0027 ± 0.00005	2.286 ± 0.08
Roller	16.9 ± 0.9	372 ± 52	98.3 ± 0.14	209 ± 8	4.11 ± 0.02	173 ±4	0.0033 ± 0.00003	2.304 ± 0.03
Horizontal	13 ±2.0	390 ± 57	98.6 ± 0.09	205 ± 12	3.77 ± 0.03	154 ± 6	0.0035 ± 0.00006	2.219±0.02
Horizontal	15 ± 2.3	400 ± 20	99.0 ± 0.11	206 ± 10	3.92 ± 0.02	156 ± 7	0.0031 ± 0.00003	1.974 ± 0.03
Horizontal	15.5 ± 1.3	367 ± 22	99.2 ± 0.20	208 ± 6	3.96 ± 0.01	159 ± 2	0.0032 ± 0.00004	1.927 ± 0.01
Horizontal	12.9 ± 1.4	393 ±12	99.0 ± 0.15	203 ± 9	3.87 ± 0.05	150 ± 4	0.0034 ± 0.00006	2.315 ± 0.02

4.1.1 Measurement process of braid parameters

Braid angle

The braid angle was measured along the braid axis, as shown in Figure 4.2. The value of the braid angle (θ) was taken at ten different points along the length of the MBOF. The braid angle was also calculated theoretically using Equation 4.1, and the value obtained was 16.8º. It is observed in Table 4.1 that there is a deviation in the values of braid angle even with the same operating condition of the braiding machine. This deviation is because it is impossible to achieve a perfect braid angle irrespective of measuring it theoretically or through image analysis. All braid angles in this thesis were measured through image analysis.

$$\theta = tan^{-1}\left(\frac{R\ x\ \omega}{v}\right) \tag{4.1}$$

Where;

θ = Braid angle

R = Radius of mandrel cross-section (mm)

ω = Rotational speed of horn gear (rad/s)

v = take up speed (cm/s)
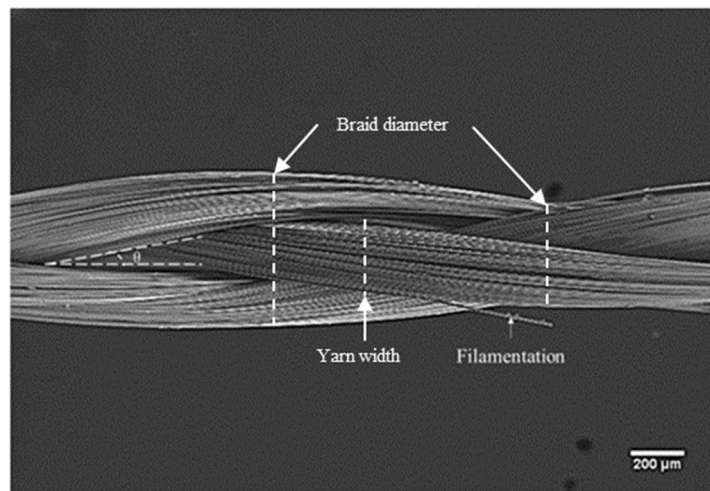
Figure 4.2 Micro-braided optical fibre (MBOF) showing braid parameters.

Braid diameter

The diameter of the MBOF was measured using Image J software. Due to the nature of interlacement of the fibres, crests and troughs were created, resulting in high and low braid diameter values, as shown in Figure 4.2. Both values were used to determine the diameter of the braid.

4.1.2 Yarn width

The yarn width of the MBOF was measured through image analysis using Image J software, as shown in Figure 4.2. Similar to the other braid parameters, the tow width was measured at ten different points along the length of the MBOF, and the average value was then utilised.

As seen in Table 4.1, the yarn width increased as the braid angle increases for both the take-up mechanism (roller and horizontal). This could be due to an increase in waviness of the braided yarn as the braid angle increases. During interlacing, the braiding yarn's width at the point of interlacement reduces, causing waviness in the preceding yarn. Because the yarn width was measured by determining the mean value of both the width of the yarn at the point of interlacement and the wavy point, this is assumed to be the reason for the increase in yarn width with braid angle.

4.1.3 Braid crimp

Crimp in a braid is referred to as undulation or waviness of tow as a result of interlacement. Crimp is also considered as the degree of deviation from linearity of a tow. Crimp for a braid can be quantified as the ratio of the difference between the length of un-crimped tow (L_{nc}) and crimped length (L_c) to the un-crimped length (L_{nc}). Braid crimp ratio (C) is determined using Equation 4.2. The crimp angle (the angle the tow makes on crossing over and under another tow during micro-braiding) as shown in Figure 4.3 was derived from the yarn width (W_y) and length of the braiding yarn undulation in a unit cell (L_c) in Equation 4.3.

$$C = \frac{L_{nc} - L_c}{L_{nc}} \tag{4.2}$$
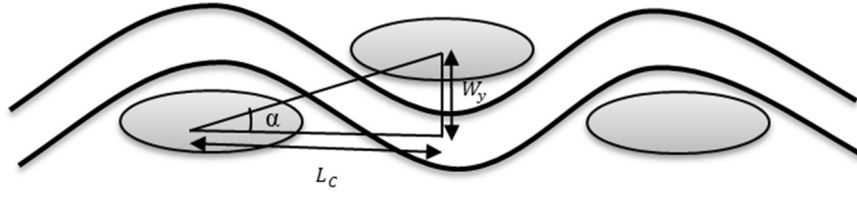
Figure 4.3 Schematic of a crimp tow

$$\alpha = tan^{-1}\left(\frac{W_y}{L_c}\right) \hspace{6cm} (4.3)$$

As observed in Table 4.1, the crimp angle on the micro-braided optical fibre (MBOF) increased as the braid angle increases. This finding could be due to the increase in wavy length as the yarn width increases. A 5% difference was observed between the highest and lowest crimp for both take-up mechanism. The deviation between the highest and lowest crimp was not significant as the degree of crimp is still within the same range.

4.1.4 Braid linear density

Linear density is an expression of the fineness of a yarn. The linear density of the MBOF was determined by cutting the sample into measurable lengths and drying it in the oven for 4hrs to remove moisture. The weight of the samples' known length was measured, and the value was used to calculate the linear density using Equation 4.4 below. Care was taken when weighing to avoid touching with the bare hand, and a tweezer was used instead.

$$L_d = \frac{1000 \; x \; W}{L} \hspace{6cm} (4.4)$$

Where;

L_d = average linear density in tex (1 tex = 10 dtex),

L = length of specimen in metres (m)

W = mass of the specimen in gram (g)

Equation 4.4 was taken from ASTM D1577-07 [190].

4.1.5 Braid cover factor

The Cover factor (C_f) is used to define the extent of fibre deposition on the braid surface (mandrel or core). The coverage value by the braided yarns or tows on the surface they are braided on has been determined in terms of cover factor (C_f), which was quantified using Equation 4.5 [111].

$$C_f = 1 - \left(1 - \frac{W_y N_c}{4\pi R \cos\theta}\right)$$ (4.5)

The terms in calculating C_f are given below:

W_y = width of the yarn or tow

N_c = number of carriers employed (i.e. the number of selected bobbins = 4)

R = radius of the core (optical fibre)

θ = braid angle

The cover factor was calculated as the percentage of the optical fibre where yarn/tow was deposited. As observed in Table 4.1, good coverage was recorded for both the take-up mechanism. Coverage of a braid was determined by both the number of carriers and the yarn width; because the number of carriers is constant through the micro-braiding process, no significant difference in braid coverage was recorded. Only an insignificant variation of 0.92% was observed between the lower and the higher coverage.

For all the braid parameters recorded, the take-up mechanism's difference did not significantly affect the braid parameter as both take-up mechanisms gave similar results.

4.1.6 Fibre volume fraction of MBOF

In the MBOF, the optical fibre representing the core lays axially while the braiding yarn interlaces it at an angle. The fibre volume fraction of constituent fibres will determine the tensile properties of the MBOF. Researchers have used FVF of axial and braiding yarn as a parameter for determining tensile properties of tri-axial braided preform [191–194].

To determine the FVF of MBOF, Equation 4.6 was used to determine the sleeve percentage in the micro-braiding [111].

$$FVF_s = \frac{N_c(1+C)T}{2\pi R \rho t_c \cos\theta} 10^{-6}$$ (4.6)

The terms in calculating FVF_s are;

T = Linear density of the yarn (g/km),

ρ = Density of the MBOF (kg/m^3),

N_c = the number of yarn carriers,

C = the crimp ratio due to interlacement,

t_c = the thickness of MBOF (m),

R = the effective mandrel radius (m) and

θ = the braid angle.

The calculated average FVF_s was 0.41±0.04.

Figure 4.4 shows the total area of the MBOF and the OF were measured using Image J. The OF was then subtracted from the total area to get the area occupied by the braid sleeve. Because the braided sleeve did not cover the OF completely, it is important to determine the braid's actual area. This was calculated by multiplying the FVF_s by the area occupied by the braided sleeve. The FVF of the micro-braiding and the OF was calculated using Equations 4.7 to 4.9;

$$A_{AB} = FVF_s \; x \; A_B \tag{4.7}$$

$$FVF_{MB} = \frac{A_{AB}}{T_a} \tag{4.8}$$

$$FVF_{OF} = \frac{A_{OF}}{T_a} \tag{4.9}$$

Where A_B is the area of braid, T_a is the total area, A_{OF} is the area of OF and A_{AB} is the actual area occupied by braid.
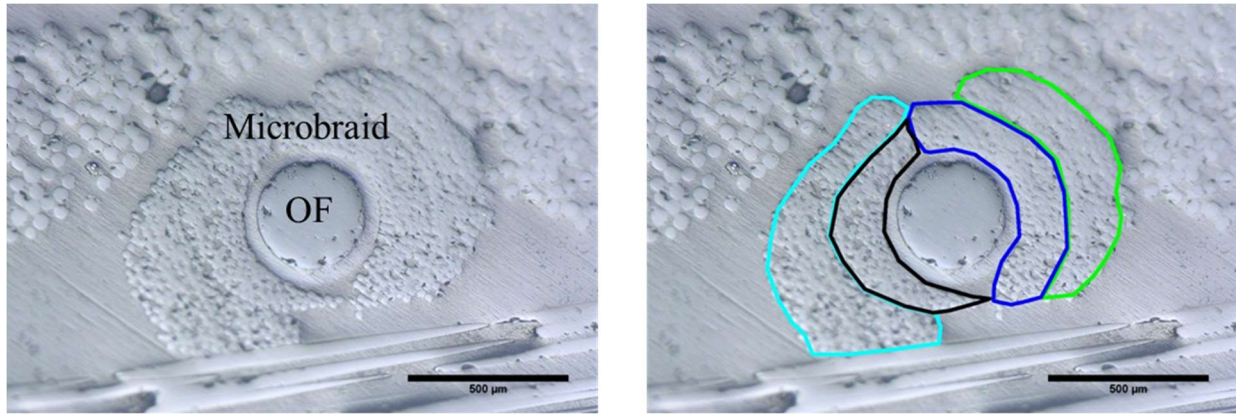
Figure 4.4 Micrograph of a cross-section of embedded micro-braided optical fibre (MBOF). The OF and the microbraid layer is visible and different colours highlighted represents the four braiding tows

4.2 Effect of micro-braiding of FBG sensor

The FBG sensor's sensitivity is the relationship between the sensor output and the corresponding variation in measurand. A good sensor is expected to have high sensitivity, i.e. the small variation of the measured magnitude should correspond to large variations in the output [195]. After micro-braiding, it is essential to determine if optical power loss will be experienced in the MBOF and if the attenuation will still allow strain measurement. The effect of micro-braiding on the FBG sensor was monitored by measuring the change in wavelength before and after micro-braiding. The interrogation techniques allow one to extract information from the spectrum produced by the FBG sensors. The extent of perturbation can be determined from the Bragg wavelength shift or the full width at half maximum (FWHM).

Bandwidth change

It is crucial to study the signal performance of the MBOF in comparison to the OF by investigating the broadening of the bandwidth. An increase in bandwidth reduces wavelength division multiplexing (WDM) and reduces the signal-to-noise ratio for peak detection [196]. FWHM denotes the bandwidth at 50% of the sensor peak. Figure 4.5 shows the wavelength spectra of 5 different FBG sensors before and after micro-braiding. Figure 4.5 a and b represents MBOF manufactured with horizontal take-up mechanism while Figure 4.5 c, d and e represent roller take-up mechanism.
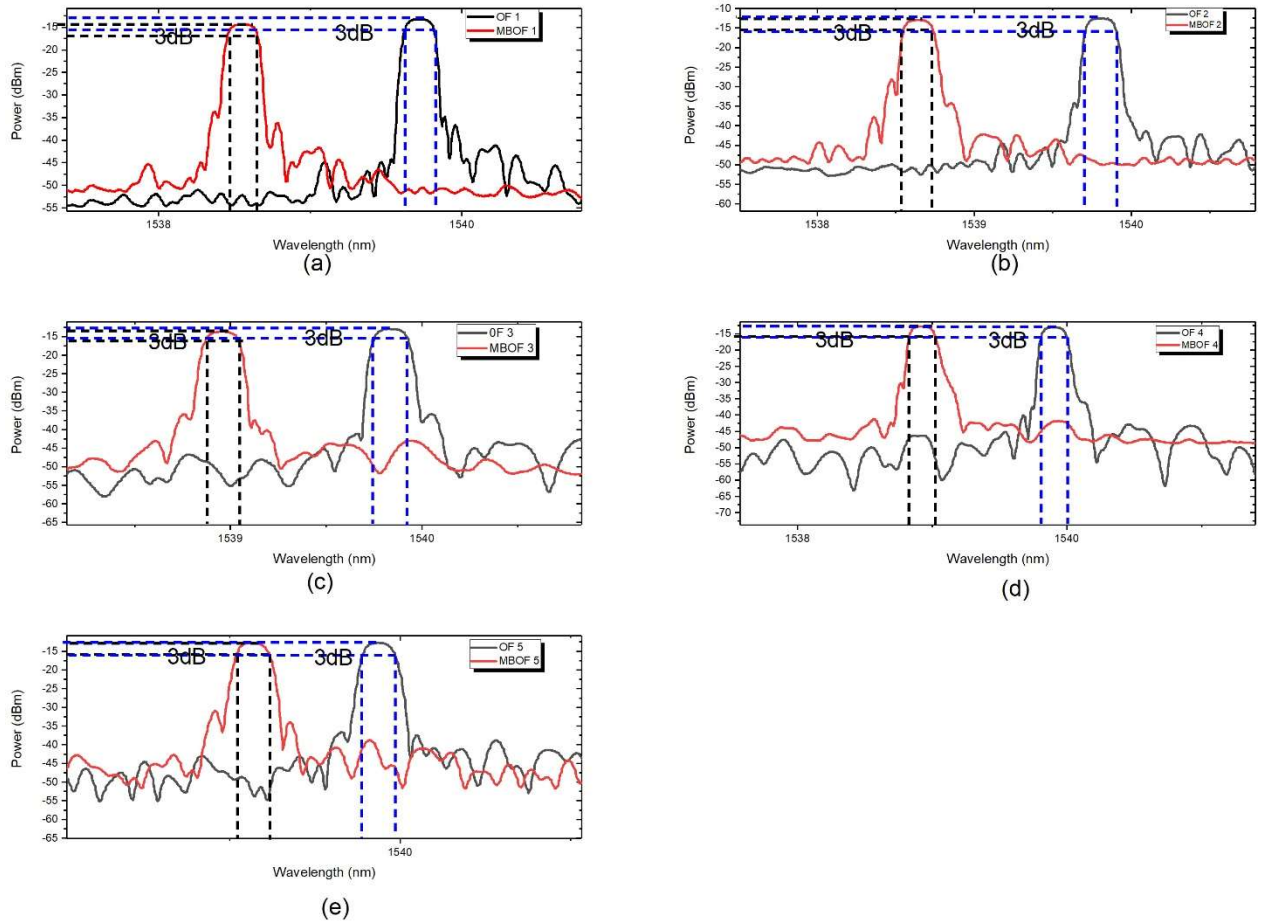
Figure 4.5 Wavelength spectra of five FBG sensors: Conventional optical fibre (black) and micro-braided optical fibre (red).

With the presence of damage, the response spectrum of an FBG sensor broadens (FWHM increases), while the spectrum's peak power decreases. This phenomenon can be used to determine if the optical fibre's sensitivity has been affected by micro-braiding. The reflection spectrum in Figure 4.5 shows a slight difference in the MBOF and OF's peak power. This change in peak power is assumed to be negligible, which implies no damage to the optical fibre due to micro-braiding. The change in peak wavelength was used to calculate the induced strain resulting from micro-braiding in Table 4.2. It was observed that all the MBOF experience compressive strain shown by the negative strain value. The negative strain was due to the compressive effect the braiding yarn impacts on the optical fibre. However, the average FWHM of the OFs and MBOFs was 0.19 ± 0.0063 and 0.19± 0.0097, respectively. Both OF and MBOF show similar FWHM value; however, this also indicates that handling of OF can affect its bandwidth. The typical FWHM of most sensors has been reported by Werneck et al. [125] to be between 0.05-0.3 nm. Because the FWHM of the MBOF falls below 0.3 nm, this indicates

that MBOF has not been damaged and is still a functional sensor. The MBOF manufactured with roller takes up showed lower induced residual strain compared to the horizontal take up. This slight difference could be because the MBOF had to experience long-distance pull in the horizontal take-up mechanism, which could have caused additional strain on the optical fibre before finally winding it in a secure package. It was also observed that there was noise in the response spectra of the OF and MBOF. The noise could be due to the effect of the light source or the photodiode (coupler) [197]. But because we are interested in the peak, the noise will not disturb the sensitivity of the OF.

Table 4.2 FWHM for conventional optical fibre and micro-braided optical fibre

Conventional optical fibre (OF)			Micro-braided optical fibre (MBOF)			
Sample	Bragg wavelength (nm)	FWHM (nm)	Sample	Peak wavelength (nm)	FWHM (nm)	Strain (%)
OF 1	1539.71	0.20	MBOF 1	1538.51	0.21	-0.09
OF 2	1539.76	0.19	MBOF 2	1538.62	0.19	-0.09
OF 3	1539.81	0.18	MBOF 3	1538.98	0.18	-0.07
OF 4	1539.95	0.19	MBOF 4	1538.93	0.19	-0.08
OF 5	1539.85	0.19	MBOF 5	1539.12	0.19	-0.06

4.3 Tensile test

Tensile test results of conventional OF and MBOF are presented to demonstrate the effect of micro-braiding on enhancing the mechanical properties of the optical fibre. The stress-strain curve for MBOF manufactured with both roller and horizontal take-up mechanism is presented in Figure 4.6. As seen in Figure 4.6, strain at failure occurred between 2.2-2.5% strain for both take-up roller and horizontal take-up mechanism. The stress value for the MBOF was between 720-1010 MPa for the roller mechanism and 800-1080 MPa for the horizontal take-up mechanism. Regardless of the micro-braiding process's take-up mechanism, the deviation in the stress-strain value of the MBOF remains with the same range of values.
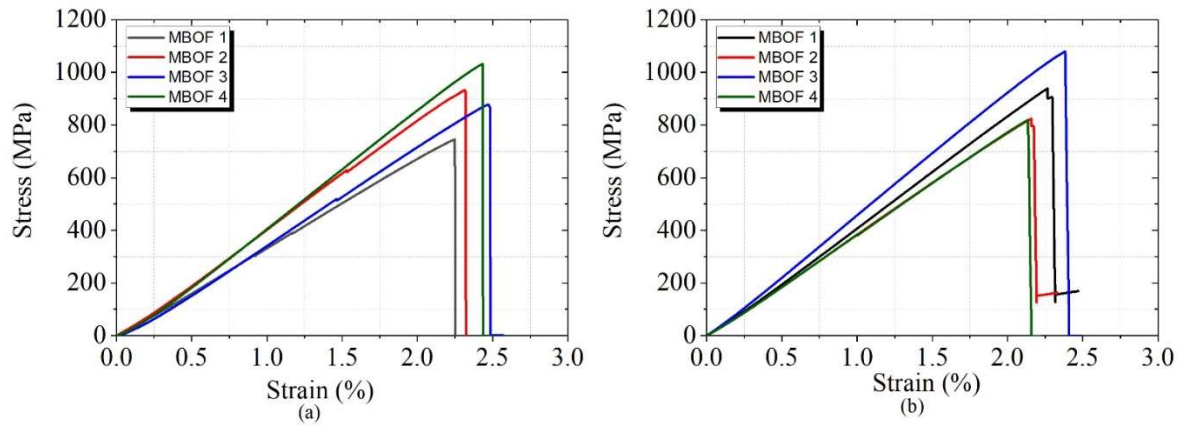
Figure 4.6 Shows stress-strain curve of MBOF with (a) Roller and (b) Horizontal take up mechanism

Figure 4.7a shows the stress versus strain curve for conventional OF; 20% –25% deviation was observed between each stress value, while 11%–32% deviation was observed between each strain value. This deviation could be due to handling (holding, gripping, or touching) on the OF's intrinsic property. Deviation in stress and strain of conventional OFs has also been reported by Antunes et al.[198]. The difference in the stress values observed in Figure 4.7b for MBOF might be due to variation in the braid diameter and the braid angle. The increase in stress value observed in the MBOF is due to glass fibre tows that have high strength (1663 ± 230 MPa). However, due to braid angle [199–202] and due to the presence of crimp (due to interlacement), the overall contribution of glass tows towards the tensile strength gets reduced. Figure 4.7c shows the zoomed image of the stress versus strain curve for the MBOF; it can be seen that the sample failed at the gauge length in between the grating as shown in Figure 4.7d, and this can be due to the stress concentration around the grating. Some of the samples showed an apparent failure of the OF in the micro-braiding. This result shows why OFs often get damaged when incorporated between or along with the interlaced tows in a woven or braided fabric. When used as axial tows in a triaxial braid or when knitted into fabric. With the help of a micro-braid layer, this problem can be eliminated, as the braid layer provides a protective layer to the OF, preventing it from getting damaged. The strain at failure for MBOF is between 1.45% and 1.525%, which is contrast to ~0.8% experienced in OF. However, the S-glass yarn carried the load until the final failure of about 2.5% because strain at failure of S-glass is

between 1.2%-3.1% [203]. There was about an 85% increase in the strain limit of the MBOF compared to the OF.
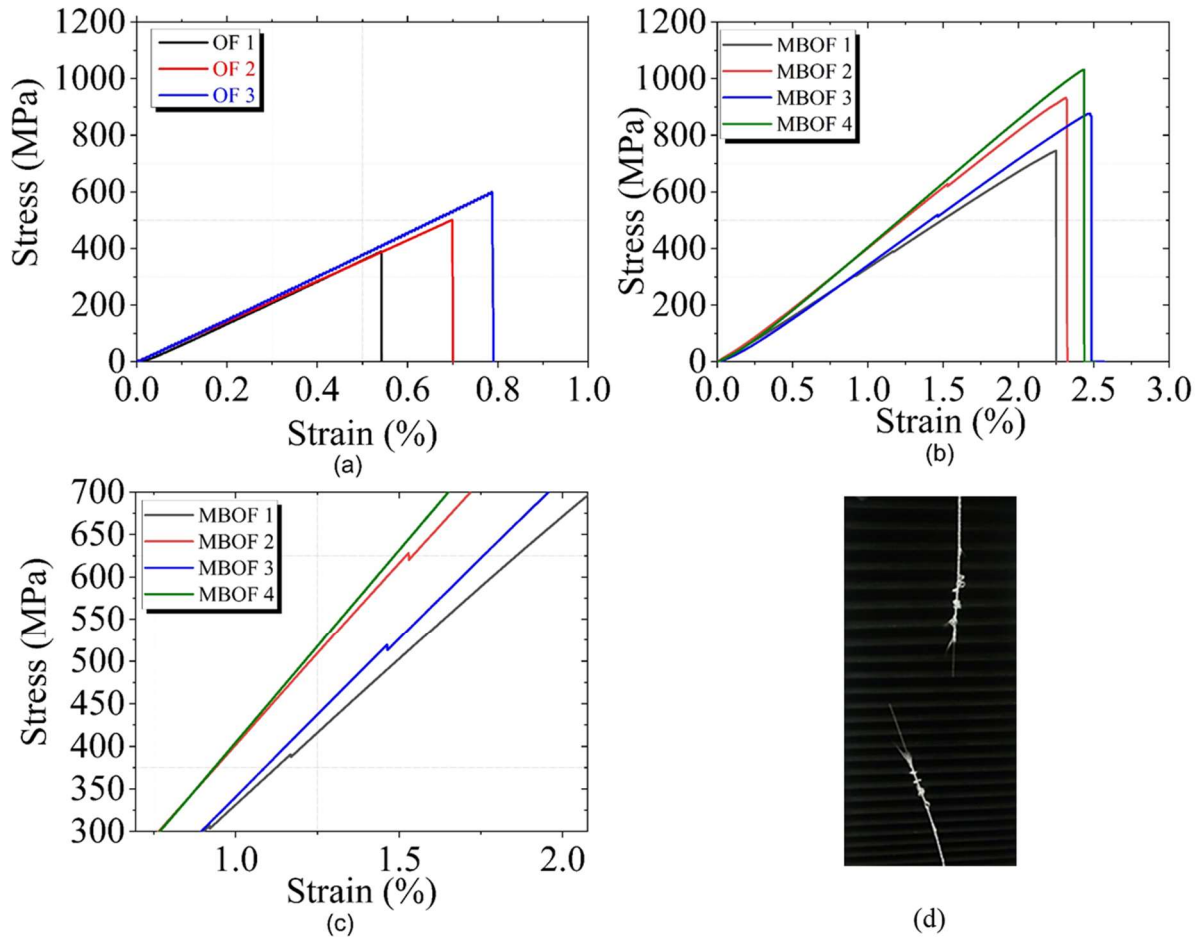
Figure 4.7 Stress versus strain curve for (a) conventional optical fibre (OF), (b) micro-braided optical fibre (MBOF), and (c) zoomed image of MBOF graph to describe the failure of the conventional optical fibre (OF) in the micro-braiding and (d) sample after test.

The strain at failure reading of the FBG interrogator was calculated using wavelength shift and then plotted against time, as shown in Figure 4.8a and b.

The strain measured by the FBG interrogator and the tensile machine for both OF and MBOF is plotted together to show accuracy in the measurement, as shown in Figure 4.9. The graph shows a similar strain value recorded by the FBG interrogator and the tensile machine for the OF and MBOF.
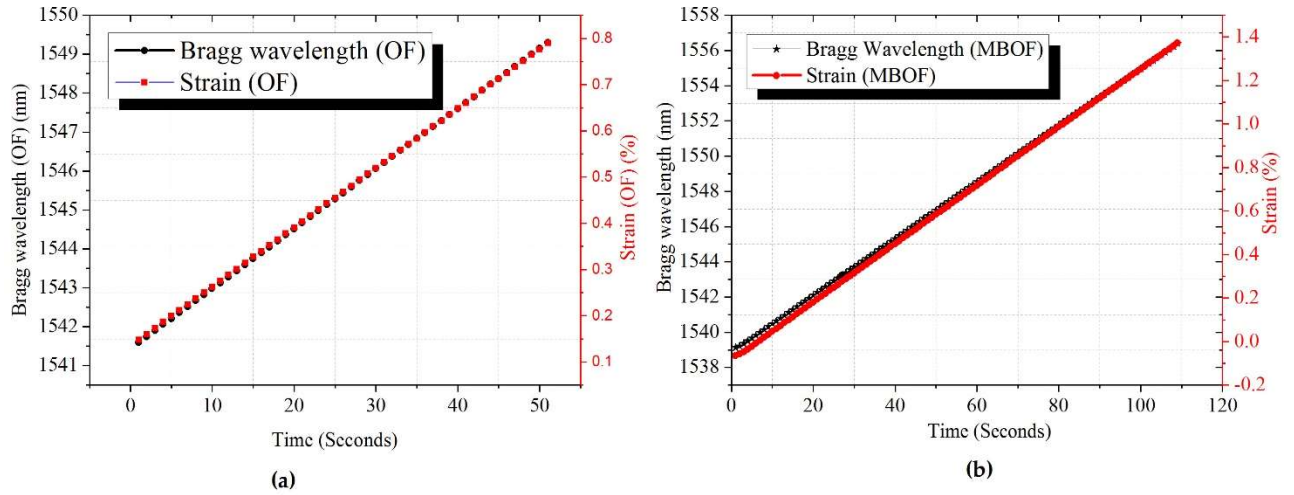
Figure 4.8 Plot of Bragg wavelength shift and strain as a function of time for (a) micro-braided optical fibre (MBOF) and (b) conventional optical fibre (OF).
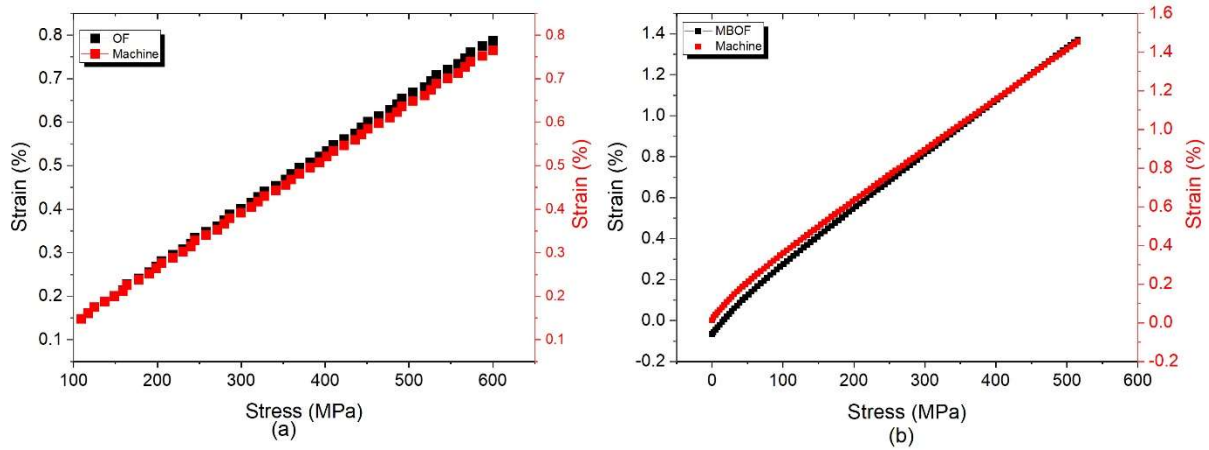
Figure 4.9 Graph of strain measured by the FBG interrogator and tensile machine for (a) conventional optical fibre (OF) and (b) micro-braided optical fibre (MBOF).

The micro-braiding of conventional OF has shown so many advantages, such as improved handling and increased strain at failure. Figure 4.10 shows the average value of Young's modulus, UTS, and strain at UTS for OF and MBOF. Young's modulus value for the conventional OF correlates well with the value in the literature. However, Young's modulus of the MBOF decreased due to the micro-braiding. This could be due to the increase in diameter due to micro-braiding, the undulation of the tows in the braid, and the fact that the braid's tows are not aligned along the load axis.
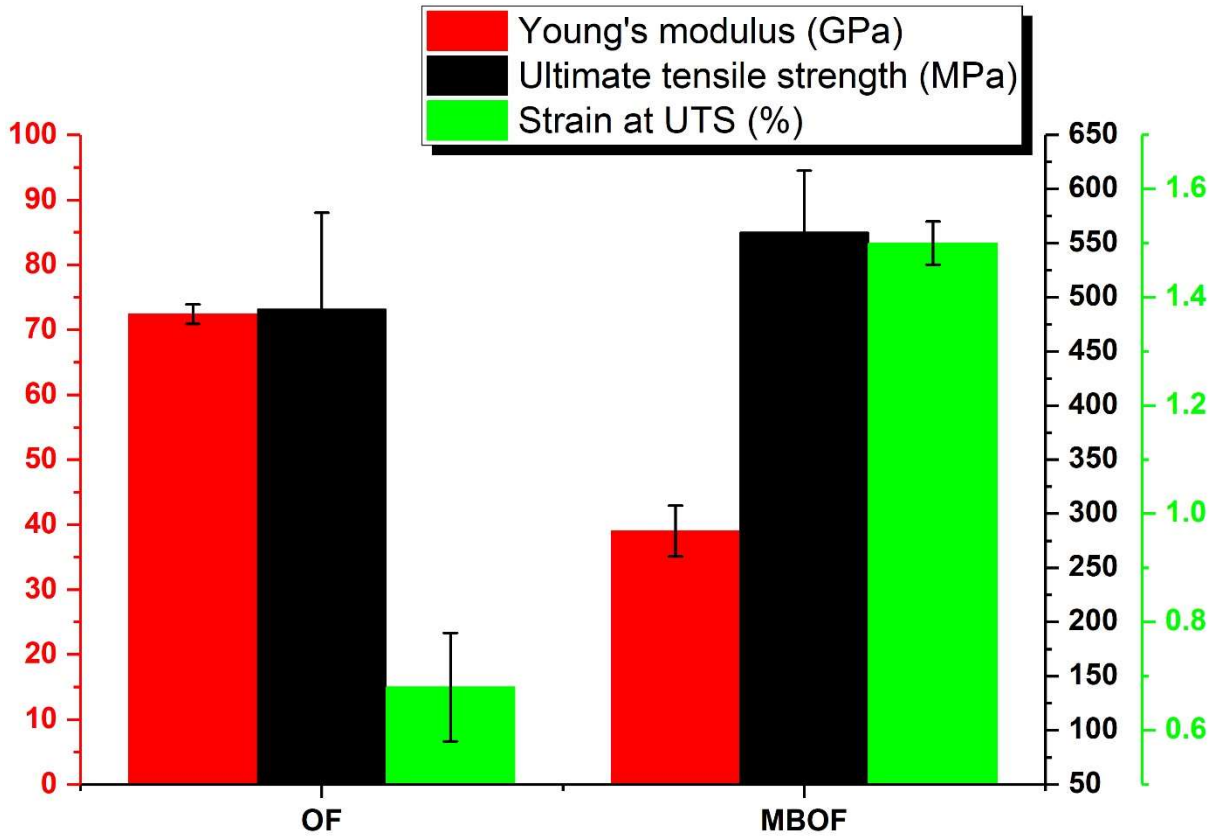
Figure 4.10 Average values of Young's modulus, ultimate tensile strength (UTS) and strain at UTS for micro-braided optical fibre (MBOF) and conventional optical fibre (OF).

Young's modulus of the MBOF was estimated using the rule of mixture [191]. This is given by Equation 4.10.

$$E_{MBOF} = V_{MB}E_{BY} + V_{OF}E_{OF} \tag{4.10}$$

Where E_{MBOF}, E_{BY}, and E_{OF} are Young's modulus of the MBOF, BY, and the OF, and V_{MB} and V_{OF} are the volume fraction of the micro-braiding and the OF, respectively. Derived experimental Young's modulus was 39 ± 3.99 GPa, while theoretical Young's modulus was 34 ± 3.10 GPa.

4.4 Micro-bond test

The micro-bond test for different fibres (S-glass yarn, conventional OF and MBOF) is discussed. The typical stress-strain curve for the samples is shown in Figure 4.11. From the stress-strain curve of BY in Figure 4.11a, no noticeable friction was observed during the pull.

However, breakage of fibre occurred between the droplet and the fibre due to high embedded length, that is, Le = Lc (critical length). This is also the reason for the high value of stress observed. Favre et al. [79] also reported good adhesion for similar load-displacement curves that showed a sharp breakage when $\Delta L > L_e$. It is assumed that the stored elastic energy is enough to pull the fibre without any noticeable friction.

The stress-strain curve of a typical OF is shown in Figure 4.11b. De-bonding of droplet starts as the pull force increases up to the peak, after which a sudden decrease of about 55% was observed. After the peak force, it showed fluctuation until the resin droplet was pulled out of the OF completely. This phenomenon indicates that friction force exists between the droplet and the fibre during the pull, as observed by other researchers [204,205].
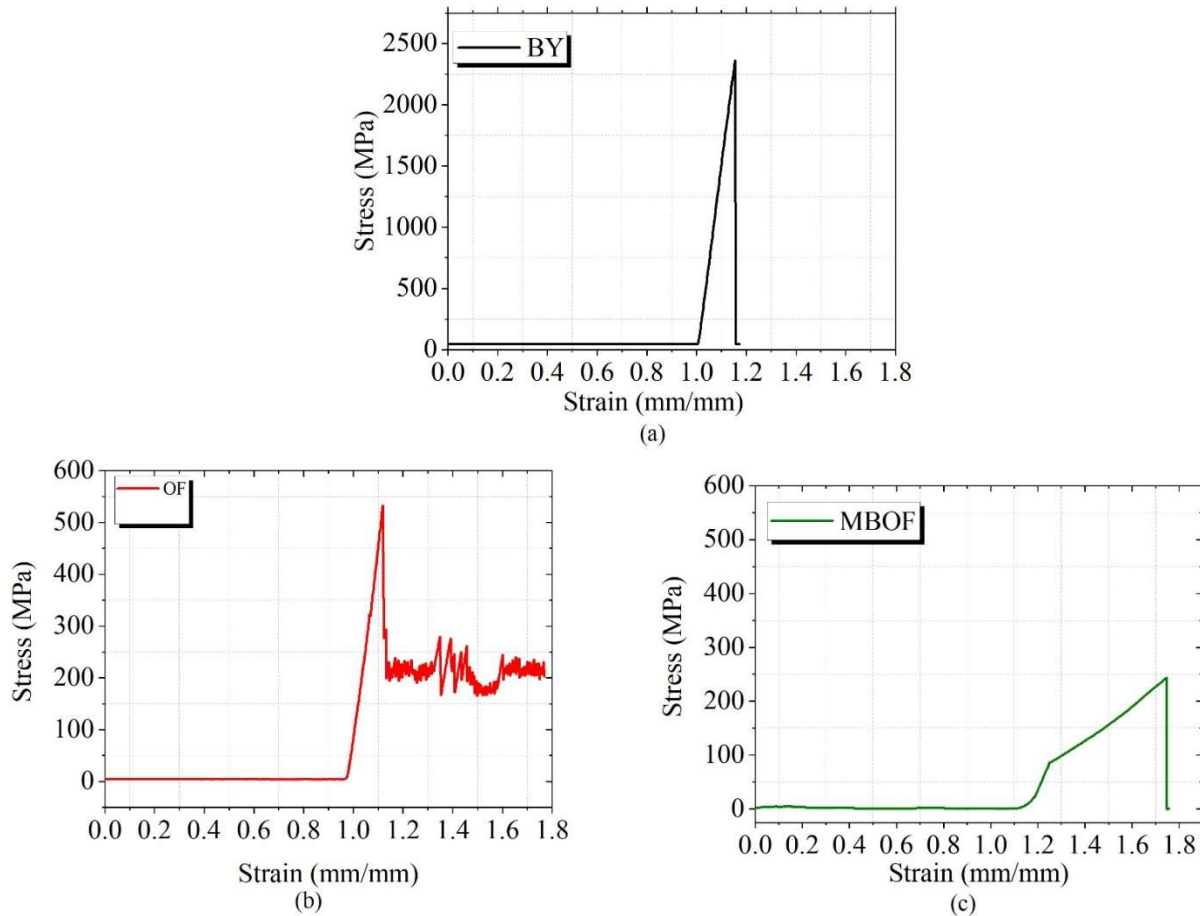
Figure 4.11 Typical stress versus strain curve of (a) braiding yarn (BY), (b) conventional optical fibre (OF) and (c) micro-braided optical fibre (MBOF).

A typical stress-strain curve for MBOF is given in Figure 4.11c, and an initial deviation in stress was observed due to the breakage of resin that wet the MBOF before it increased up to the peak value. It was observed that the stress value for the MBOF is low due to the removal

116

of part of the resin droplet leaving behind some resin residue on the fibre as shown in Figure 4.12a. It has also been reported that fibre wetting causes a meniscus region to form around the fibre [206]. Because the resin coating is thinner in the meniscus, it causes rupture prior to debonding. The presence of residual resin indicates cohesive matrix failure, which affects the IFSS of the sample [77].
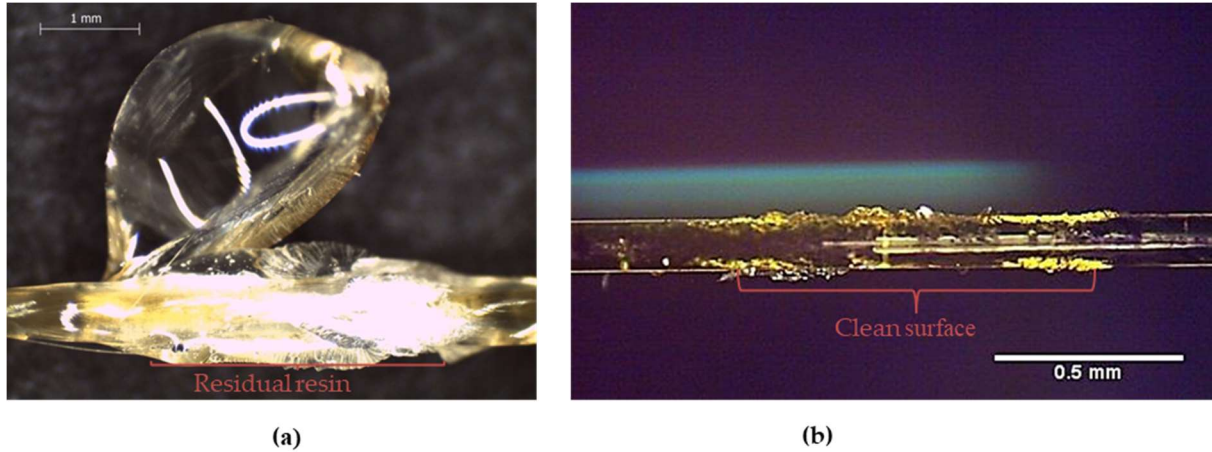
Figure 4.12 Optical image of (a) micro-braided optical fibre (MBOF) showing residual resin after micro-bond test and (b) conventional optical fibre (OF) showing cleaner fibre surface.

Straight-line has been fitted to a plot of debonding force against embedded area as shown in Figure 4.13 for the data obtained from BY, OF and MBOF by micro-bond test. The straight-line fits for BY yield an average IFSS of 5.57 ± 0.5 MPa, which agrees well with the IFSS value of glass fibre published in the literature (~ 5 MPa) [78,206,207]. The Average IFSS according to the straight-line fit for conventional OF and MBOF are 20.5 ± 1.8 and 15.3 ± 1.8 MPa, respectively. The low IFSS in MBOF could be due to the cohesive matrix failure caused by the surface morphology of MBOF as a result of the undulation of fibre due to crimp. At the same time, the increase in IFSS of OF could be attributed to the presence of adhesive interfacial failure (fibre with cleaner surface), as shown in the debonded fibre surface in Figure 4.12b.

(a)

(b)

(c)
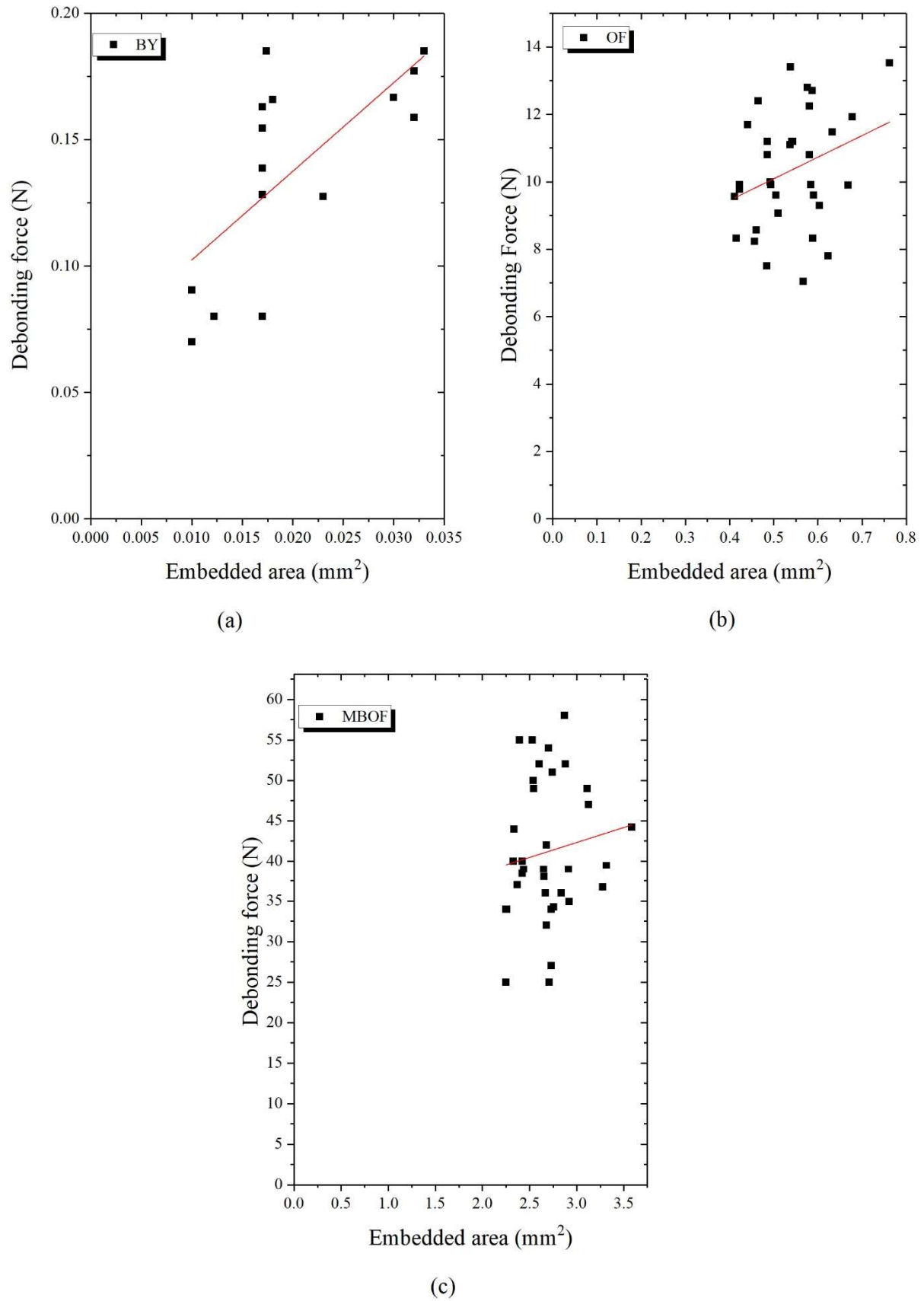
Figure 4.13 Graph of de-bonding force versus embedded area of braiding yarn (BY), conventional optical fibre (OF) and micro-braided optical fibre (MBOF).

4.5 Three-point bending test

This test's primary objective is to determine the effect of embedded OF (both conventional and micro-braided) on the integrity of the composite panel. The manufactured composite was subjected to a three-point bend test with the embedded layer in the compressive direction; this will make it possible to study the effect of the embedded OF and MBOF on the structural integrity of the composite panel. A cross-sectional image of the composite panel embedded with OF and MBOF is shown in Appendix 2A. The main reason to use MBOF is to protect the brittle OF during handling and automated manufacture of composite materials (i.e., braiding and winding).

The stress-strain curve for all the composite samples (No OF, OF, and MBOF) are given in Appendix 3A. The typical stress-strain curve is shown in Figure 4.14. Linear behaviour was observed up to the initial breakage of the first plies. This behaviour was possibly due to the elastic deformation of the composite panel. After the flexural stress reached a peak in the first region, a drop in peak stress was observed in the composite panel in the second region, and this drop was due to fibre cracking and delamination. A 21% drop in peak stress value was observed in the composite panel with no OF, and 20%–22% was observed in the composite panel with OF and MBOF, respectively. All the specimens could still withstand load application but never reached the peak till final failure. Figure 4.14b shows slight slippage for laminate embedded with MBOF at about 265 MPa, indicating early delamination but still carried the load up to 280 MPa. The premature delamination could be due to the increased diameter of the MBOF; however, this did not pose any major challenge on the composite panel. The early delamination observed was about 5% less than the peak value of the composite panel with no OF and 3.8% less than the composite panel with OF. This difference is not significant enough to affect the integrity of the composite panel. This also confirms that the localised distortion observed in the optical image due to embedding MBOF and OF did not cause deterioration in the mechanical property. This type of behaviour was also observed by Hamouda et al. [67]. The diameter of the conventional OF was 150 ± 4 μm, while that of the MBOF is 450 ± 64 μm. This difference in the diameter of the OF and MBOF did not cause any significant change in the mechanical performance of the composite panel from the experimental test results. The optical micrograph of the damaged composite under three-point load for both types of OFs

(conventional OF and MBOF) shows inter-layer delamination due to compressive loads, as observed in Figure 4.15.
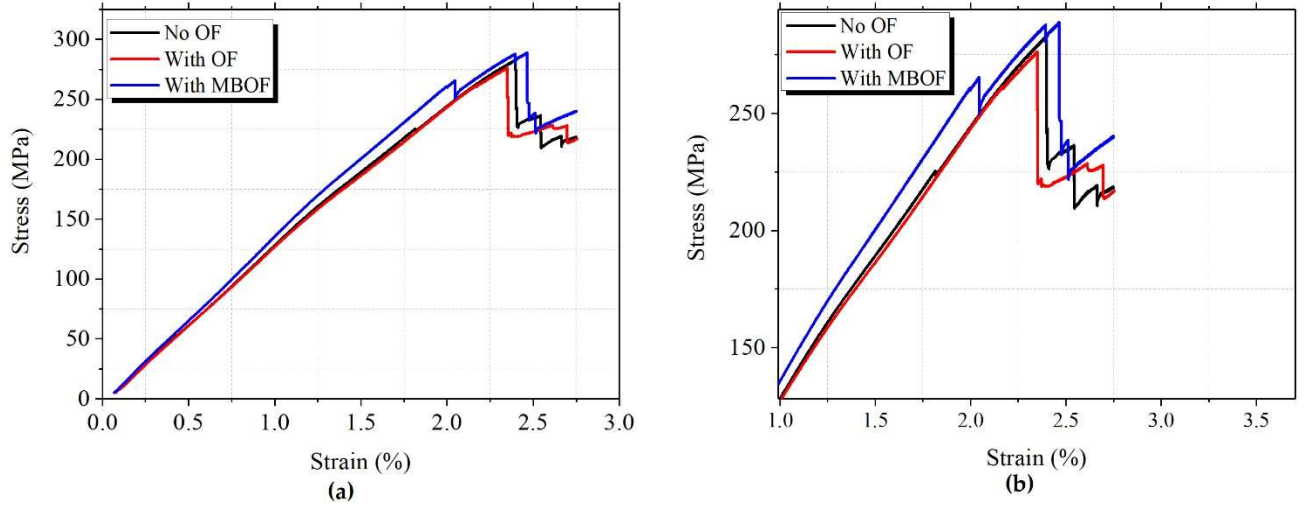
Figure 4.14 (a) Typical stress-strain curve of the composite panel with no optical fibre, with optical fibre and with micro-braided optical fibre (MBOF) and (b) zoomed image showing slippage.
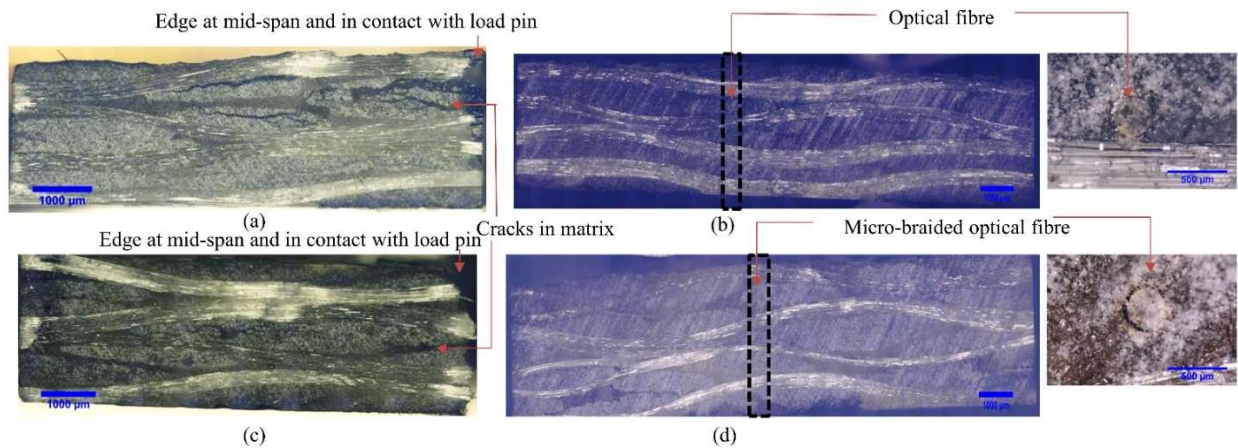
Figure 4.15 Micrograph of the damaged composite sample after three-point bending embedded with conventional optical fibre (OF) and micro-braided optical fibre (MBOF) (a) along the length for OF, (b) along the cross-section for OF, (c) along the length for MBOF and (d) along the cross-section for MBOF.

The average value of the flexural test result is presented in Figure 4.16. It was observed that there is a 3.2% difference in ultimate flexural strength (UFS) of MBOF compared to the composite panel with no OF. The percentage difference is not high enough to cause any significant effect in composite structures. The strain at UFS of the composite panel with MBOF showed a 5% increase compared to the panel with conventional OF; this could be due to the BY acting as another layer to protect the OF, thereby allowing the OF to experience more elongation before failure. However, the flexural modulus of the samples is between the range of 14 and 14.4 GPa, which indicates that embedding of MBOF has no significant effect on the modulus of elasticity of the composite panel. It can be inferred from this result that MBOF would have little or no influence on the integrity of the composite structure.
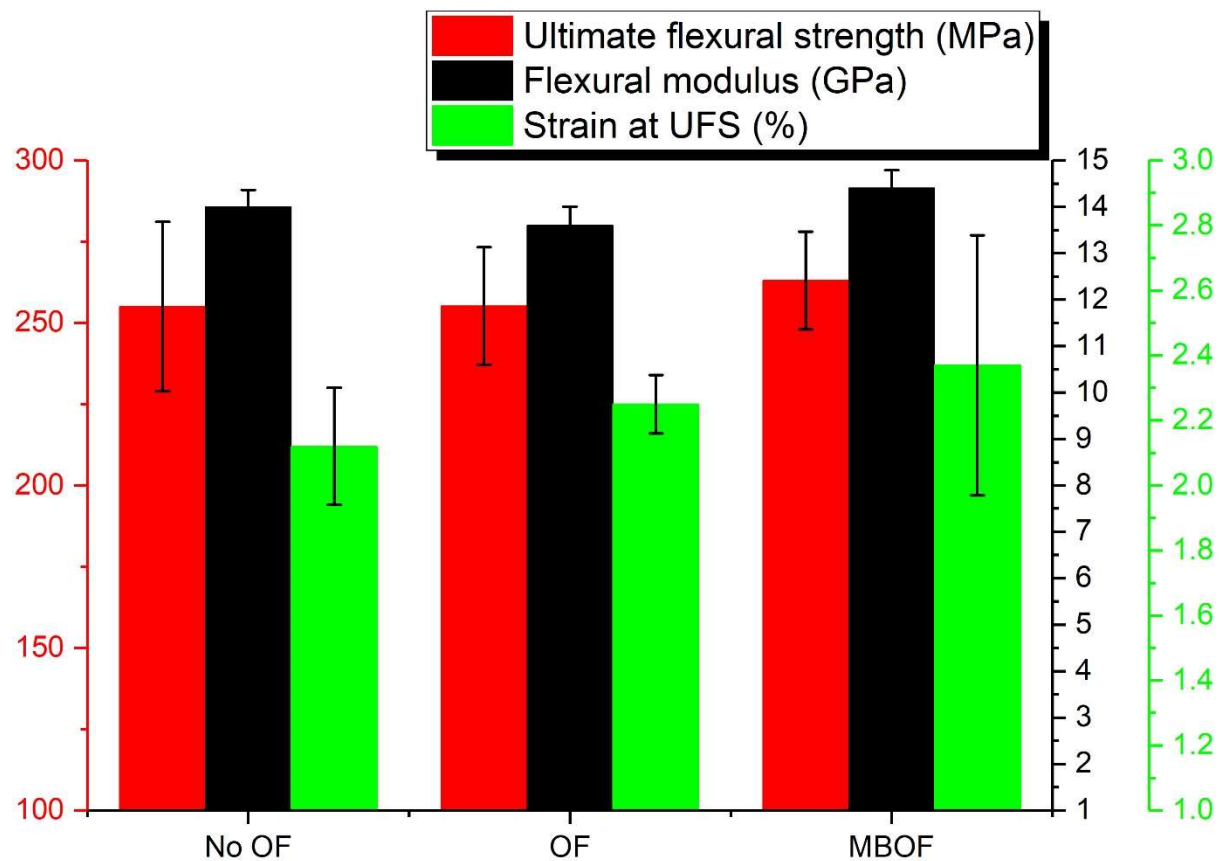
Figure 4.16 Average values of ultimate flexural strength (UFS), flexural modulus and strain ultimate flexural strength for micro-braided optical fibre (MBOF) and conventional optical fibre (OF).

4.6 Summary

In line with the experiments performed in this chapter, the following conclusions were made:

- The technique of optimising (improved handing and mechanical properties) the OFs through micro-braiding was presented. This study showed that the developed technique does not affect the sensitivity or causing any damage to the OF (that are micro-braided).

- The tensile response of both conventional OF and MBOF was investigated. MBOF showed an 85% increase in strain at failure compared to conventional OF. This was due to the cushion effect the micro-braiding has on the OF, which increased the elongation of the OF. However, the decrease in Young's modulus observed could be attributed to the effect of crimp, causing undulation of braid yarn.

- IFSS of conventional OF was higher than MBOF. The difference in IFSS was possibly due to cohesive matrix failure observed in the MBOF due to its surface morphology.

- Three-point bend test of composite laminate with no OF, with MBOF and conventional OF shows that the integrity of the composite laminate was not affected by the presence of the MBOF.

Chapter 5: Result and Discussion: Cure monitoring of composites using optimised distributed optical fibre

Structural health monitoring (SHM) involves the permanent integration of sensors into the host structure for continuous and periodic inspection [116,208–211]. SHM methods facilitate several levels of damage assessment [118], including the detection and location of damage, classification of damage type, quantification of severity, and prognosis on the remaining life of the structure [28,29,157,212,213]. Since SHM can provide *in situ* on-demand assessment without the need for significant downtime of components, the relative cost can be much lower than conventional NDT.

Monitoring flaws such as dry regions, delamination, fibre waviness, incomplete matrix cure, and voids [2,3,217] can result in residual stresses or reduce dimensional stability during heating and cooling of the matrix and fibre, which affects the mechanical properties of the composite product. The difference in the thermal expansion coefficient of the constituent leads to the matrix compressing the fibres, resulting in residual stresses and strains. Monitoring the resin flow during infusion and viscosity during curing serves as a potential for conducting quality control of the final product.

In this chapter, a single distributed optical fibre was embedded during the manufacture of a glass fibre reinforced polymer (GFRP) composite plate. Prior to embedment, a length of the optical fibre was micro-braided using glass fibres to compare *in situ* strains monitored by the micro-braided and 'bare' fibre segments. A novel process of implementing a micro-braided and bare section of a DOF in a composite laminate for measuring residual strain during curing is investigated. Strain development from both sections of the DOF during cyclic loading under four-point bend was also evaluated. The reason for four-point bending as opposed to three-point bending discussed in previous chapter was to understand how samples with embedded OF and MBOF behaves in different mechanical test. Readings from the micro-braided and bare sections were also compared to determine the effect of micro-braiding on the optical fibre.

5.1 Strain monitoring during curing

The cure cycle can be divided into five temporal stages, as shown in Figure 5.1.

I: increase from room temperature to 80°C in 1 hour;

II: temperature dwell at 80°C for 1 hour;

III: temperature increase from 80°C to 160°C in 1 hour;

IV: dwell at 160°C for 2 hours;

V: the composite is allowed to cool to room temperature in the oven.

The composite panel experiences several temperature changes, which lead to strain and stress developments. The shift in the light spectrum scattered in the fibre in response to strain and temperature can be defined by Equation 5.1.

$$\frac{\Delta\lambda}{\lambda} = \frac{\Delta v}{v} = k_T \Delta T + k_\varepsilon \varepsilon \qquad (5.1)$$

Knowing that

$$k_T = \alpha + \xi$$

and

$$k_\varepsilon = 1 - \frac{n^2}{2}\left(p_{12} - \mu(p_{11} + p_{12})\right)$$

Where v is the mean optical frequency, λ is the wavelength, α is the coefficient of thermal expansion (CTE), ξ is the thermo-optic coefficient, n is the refractive index, μ is Poisson's ratio and p_{11}, p_{12} are a component of strain-optic tensor. The values of temperature and strain calibration constants for germanium-doped silica core are k_T (6.45 x 10^{-6} °C^{-1}) and k_ε (0.78) [214].

The thermal strain was measured by the un-bonded part of the DOF protected with the PTFE capillary tube but still inside the oven. The change in temperature in the absence of mechanical strain is calculated from the frequency shift of the un-bonded part and scaled to temperature (°C) using Equation 5.2.

$$\Delta T = -\frac{\bar{\lambda}}{ck_T}\Delta v \qquad (5.2)$$

Where c represents the speed of light and $\bar{\lambda}$ the central wavelength, by substituting the constants into the equation, Equation 5.2 become:

$$\Delta T = -0.801 \frac{°C}{GH_z} \Delta v \qquad (5.3)$$

Δv represents the spectral shift in GHz. The value of -0.801 is specific to the system utilised in the present work: LUNA's ODiSI-B interrogator with a central wavelength of 1550 nm [215].

The change in mechanical strain $\Delta \varepsilon$ in the absence of temperature is given by Equation 5.3:

$$\Delta \varepsilon = -\frac{\bar{\lambda}}{c k_\varepsilon} \Delta v \qquad (5.4)$$

By substituting constants, Equation 5.4 becomes:

$$\Delta \varepsilon = -6.67 \frac{\mu \varepsilon}{GHz} \Delta v \qquad (5.5)$$

5.1.1 Monitoring of total strain during cure

The total strain recorded by each DOF section during curing is shown in Figure 5.1. The strain recorded by bare and micro-braided OF sections is comparable, indicating that the MBOF is suitable for strain measurements in the composite structure. To fully understand what was happening during curing, the mechanical strain needs to be analysed in isolation from the thermal strain.
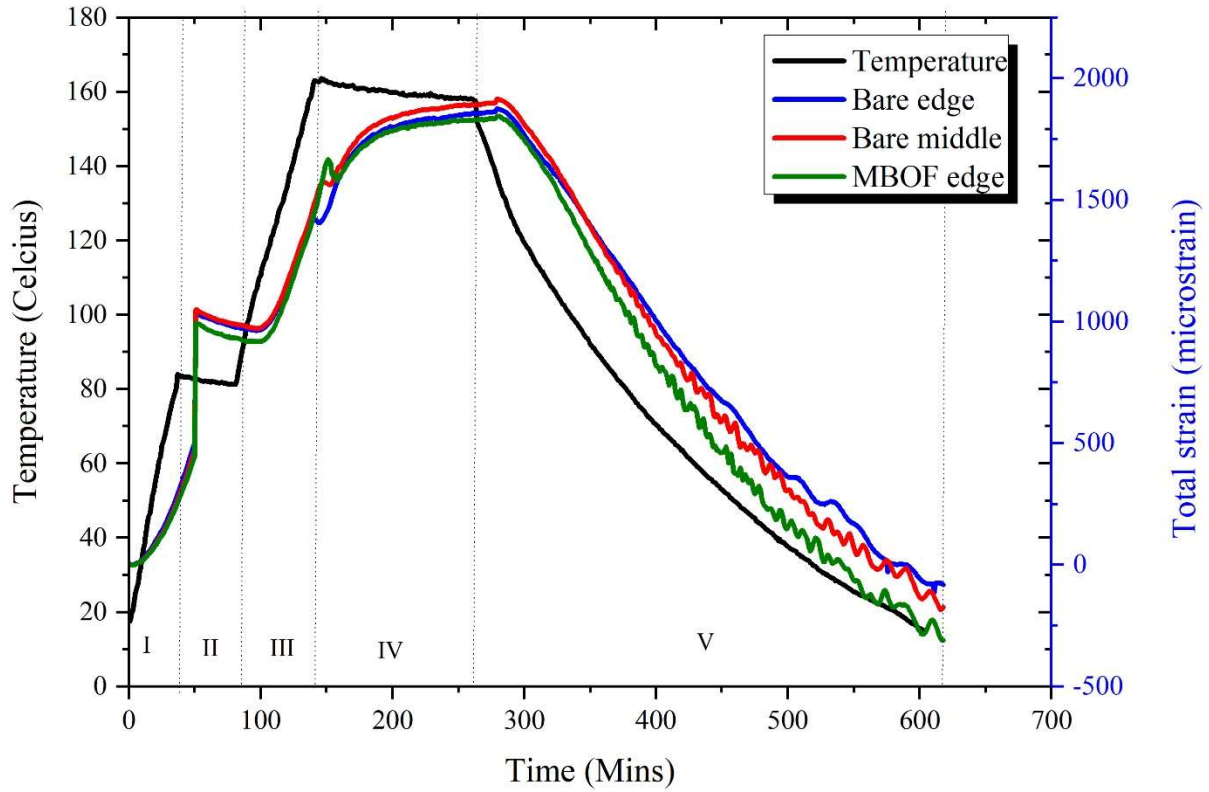
Figure 5.1 Temperature measured by distributed optical fibre sensor (black) and total strain measured by DOF in different sections of the optical fibre: bare optical fibre at the edge, (blue): bare optical fibre at the middle and (red): micro-braided optical fibre (MBOF) at the edge (green).

5.1.2 Determination of mechanical strain

The mechanical strain induced on the composite as a result of curing is derived from the total strain and thermal strain, which is given in Equation 5.6:

$$\varepsilon_T = \varepsilon_m + \varepsilon_t \tag{5.6}$$

Where ε_m is the mechanical strain, ε_T is the total strain, and ε_t is the thermal strain.

The mechanical strain and temperature curve during the curing of the composite panel are presented in Figure 5.2. Interpretation of the measurements enables ease of identifying and controlling every step of the cure cycle. The following steps below explain what is happening at each stage of the cure cycle:

I.   As the viscosity of the resin decreases due to an increase in temperature, the distribution of resin was experienced, which caused the compression of the resin on the DOF leading to the compressive strain (negative strain) recorded.

II.   Change in strain was observed (positive strain) during the dwell period. This change could be due to thermal expansion of the matrix caused by changes in the adhesive condition between the resin and the optical fibre. At this stage, the viscosity of the resin is increased, causing a reduction in the flow of resin known as the gel point [1,157].

III.   A positive strain was observed, possibly due to an increase in temperature on the material's thermal expansion. A reduction follows this in the positive strain, which could be due to resin shrinkage associated with polymerisation[1,157].

IV.   At the post-cure cycle, a near-constant strain level was observed because most of the polymerisation reaction has occurred during the curing cycle.

V.   During the cooling stage, the DOF detects an increase in compressive strain (negative strain) due to thermal shrinkage of the epoxy resin [165].
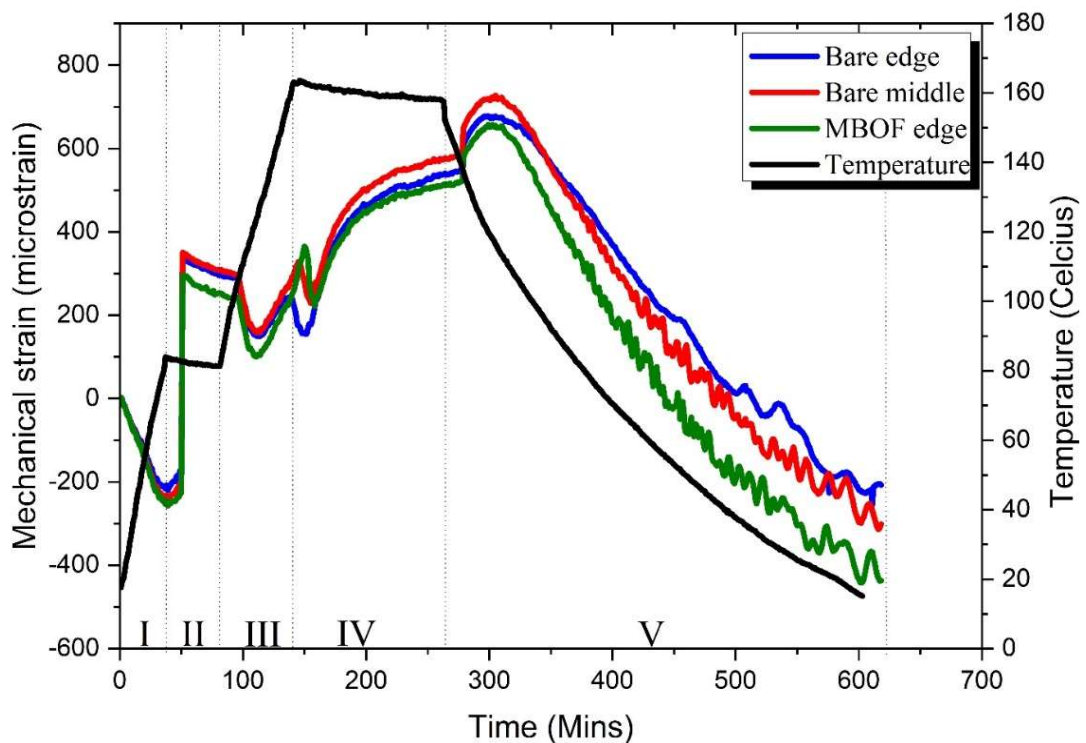
Figure 5.2 Mechanical strain profile for bare optical fibre at the edge of the panel (blue), bare optical fibre at the middle of the panel (red), and micro-braided optical fibre (MBOF) at the edge of the panel (green).

In all DOF regions, a compressive strain developed in a short period during cooling, as shown in Figure 5.2. The average residual strain observed in the bare DOF close to the panel edge was -254 µɛ, while the change in compressive strain from the beginning to the end of the cooling stage was -932 µɛ. The average strains observed in the mid-line of the panel were higher: -310 µɛ and -1028 µɛ, respectively. Compressive strain was observed in both sections of the bare DOF, because, during cooling, the panel is already cured, and strain is induced due to thermal contraction of the matrix [164].

The green curve in Figure 5.2 shows the strain profile of the MBOF located at the other edge of the panel. The average residual stain observed was -411 µɛ, while the change in strain due to cooling was -1063 µɛ. The MBOF recorded the highest residual strain as temperature decreases compared to the bare OF's. The reason for the 47% difference in the residual strain of the bare OF edge and the MBOF edge could be due to the increase in diameter of the MBOF (~470 µm). The larger diameter introduces resin pockets around the MBOF, as shown in Appendix 2A. Consequently, this results in larger compressive strains being recorded when the resin undergoes thermal shrinkage during cooling.

The residual strain and the percentage difference between the bare and MBOF sections, which were both 24 cm long, are shown in Figure 5.3. Axial strain reading in the straight section of the DOF was only considered. The bare edge and the MBOF edge recorded different strain values, likely due to the differences in diameter, 155 and ~470 µm, respectively, and the formation of resin pocket around the MBOF.
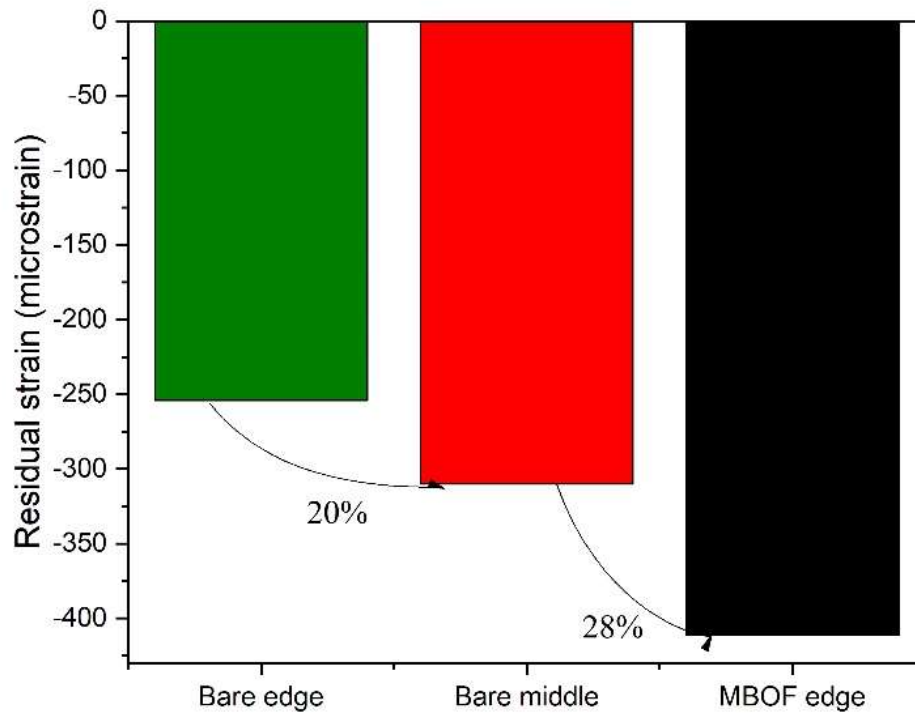
Figure 5.3 Percentage difference in measured residual strain at different sections of distributed optical fibre (DOF): bare edge (green), bare middle (red), MBOF edge (black).

5.1.3 Evaluation of strain in DOF sub-sections

To further understand the differences in strain value recorded by each DOF section, the three sections were subdivided into sub-sections 9 cm apart. Figure 5.4 shows the mechanical strain evolution during curing in each of the DOF sub-sections. Table 5.1 shows the average negative strain recorded during cooling for all sections and sub-section of the DOF. Sub-section 3 recorded the highest strain value in all cases. However, all the sections and sub-section of the DOF strain value fall within the range of uncertainty.
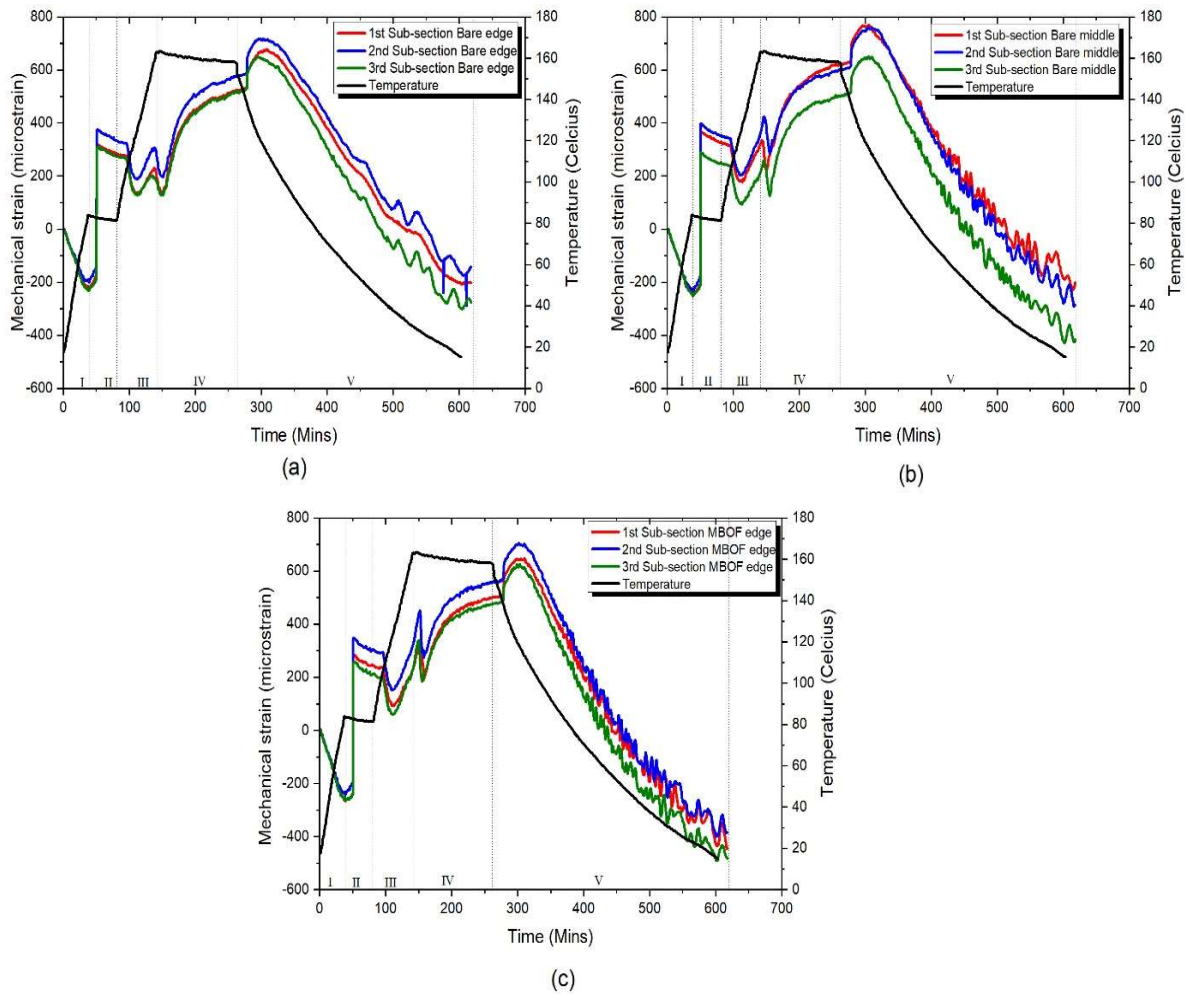
Figure 5.4 Mechanical strain for sub-sections: 1 (red), 2 (blue), and 3 (green) of each DOF section: (a) bare edge, (b) bare middle, and (c) micro-braided optical fibre (MBOF) edge.

Table 5.1 Average residual strain in each of the OF sub-sections.

Section of DOF	Residual strain (µε)			
	Full section	Sub-section 1	Sub-section 2	Sub-section 3
Bare edge	-126 ± 77	-119 ± 77	-116 ± 53	-164 ± 91
Bare middle	-154 ± 90	-109 ± 60	-144 ± 77	-239 ± 110
MBOF edge	-239 ± 124	-237 ± 115	-218 ± 108	-291 ± 129

5.1.4 Comparison of infusion and residual strain

The residual strain profile along the length of each DOF section is shown in Figure 5.5. When the residual strain profile is compared to the strain profile of the infused panel, there was a similar trend. The compressive strain was experienced as a result of the compacted mould for easy resin flow and distribution. This profile indicates that strain starts to build up during wetting of the glass fibres within the laminate during resin infusion. This type of behaviour was also reported in [28,29,165]; this trend can be useful in predicting the final residual strain and avoiding curing time if residual strain after the infusion is abnormal (i.e., issue with the final product).
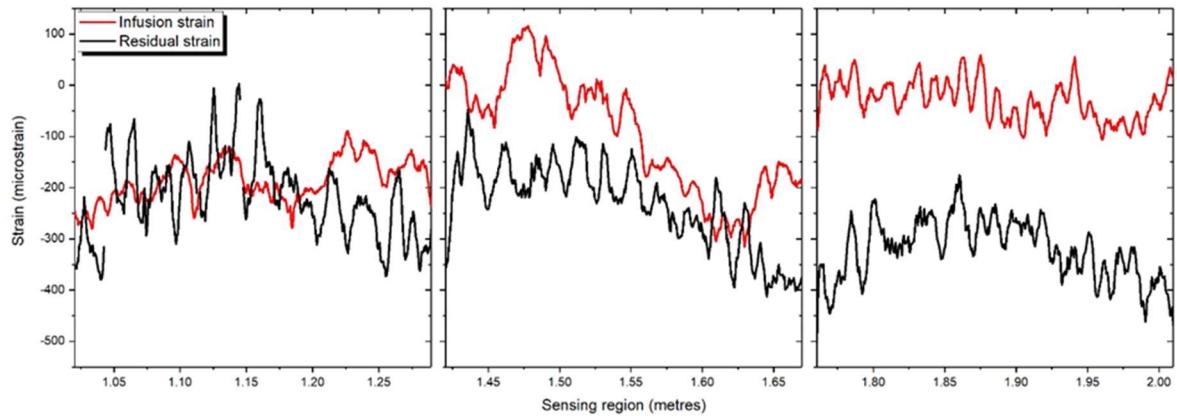
Figure 5.5 Strain profiles resulting from infusion (red) and residual strain after manufacture (black) along the length of the optical fibre.

5.2 Strain monitoring during four-point bending

The durability of the MBOF was estimated by comparing strain measurement with bare DOF when the composite panel was subjected to four-point bending. Figure 5.6 shows the strain development recorded by the sections of DOF during the 11th and 14th cycle of loading. All sections of the DOF recorded compressive strain because of their position in the composite, which lies between the fourth and fifth layer and loaded in compression. However, the DOF recorded lower strain compared to the strain gauge located at the top of the panel. Figure 5.7 shows the development of strain during the final loading cycle 26. Similar strain histories were observed between the different sections, except for the dropout in the strain values. It was

observed that as the bending force increased in cycle 26, a spike in strain value of the sections of the DOF appeared, which could be due to strain gradient on the composite caused when the strain exceeds 517 με for a 1.25 mm gage [216]. The strain profile along the sections of the DOF for cycle 11, 14, and 26 are presented in Figure 5.8. Due to the loading and unloading associated with each cycle, the strain data recorded by the DOF sections returned to the initial starting point. The location of the peak remained the same in successive loading cycles. The peak in cycle 11 could be an indication of micro-crack initiation in the composite panel. Barrias et al. [217] reported a peak in a strain in the vicinity of a crack, which progressed as loading increased in reinforced concrete. The increase in strain peak evolved in all sections of the DOF which could be due to local interaction with fibres or delamination. Delamination was suspected due to the emergence of whitening in the panel as loading progressed (this is possible because the panel is a GFRP).

The increase in peak strain was consistent for the three sections of the DOF. Researchers [172,218] have reported a sudden spike in strain values due to improper bonding of the sensor to the host surface or local interaction with adjacent fibres. Improper bonding could not have happened in this case because the DOF was gently inserted in-between the fibre interlacement for proper hold. The photographic and c-scan image of the laminate is shown in Figure 5.9. The location of the peak for the sections of the DOF is marked out on the specimen. The whitening observed in the laminate due to delamination corresponds with the points where the peak strain was recorded by the sections of the DOF in Figure 5.8. This observation shows a good indication that all the sections of the DOF, both bare and MBOF, were sensitive to the initiation and growth of damage in the laminate.
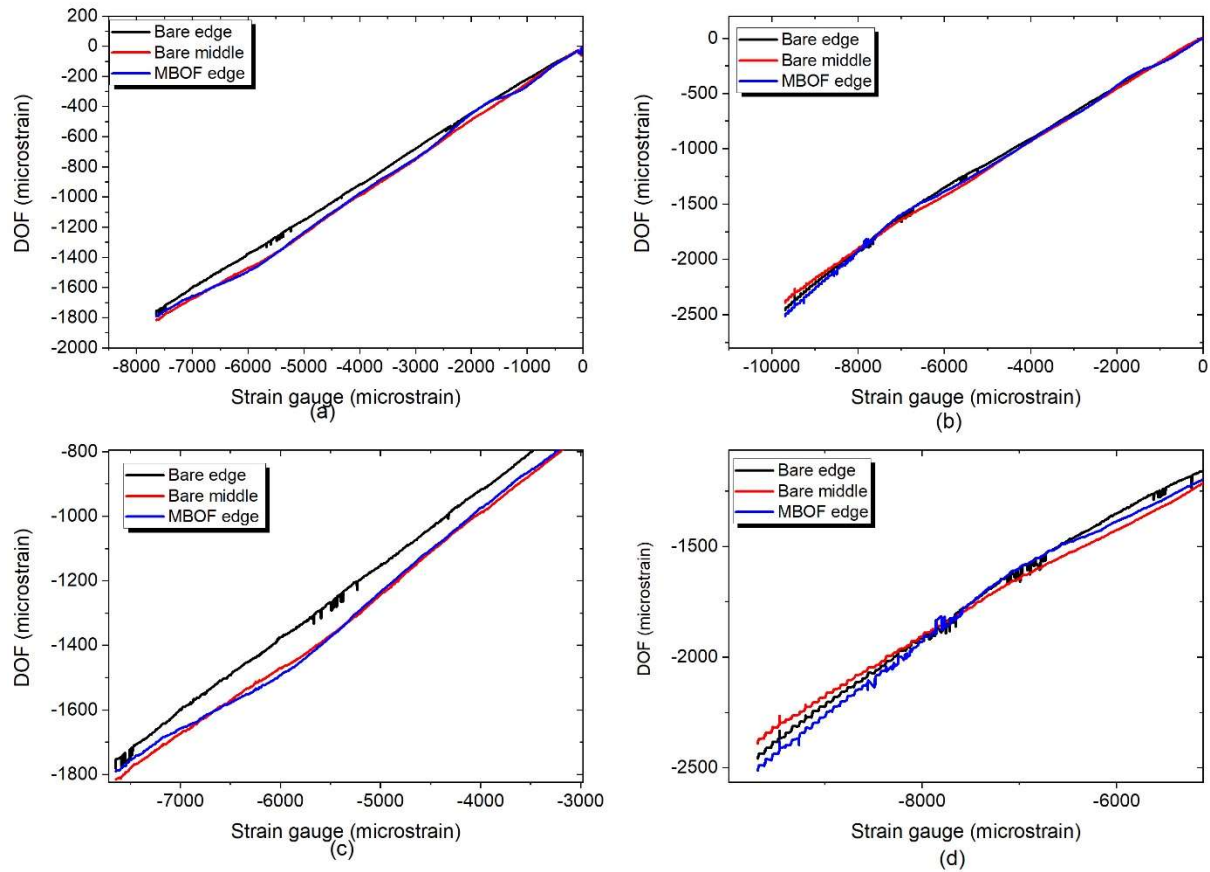
Figure 5.6 Strain development from four-point bend test by sections of the distributed optical fibre during (a) 11th cycle and (b) 14th cycle (c) enlarged image of cycle 11 and (d) enlarged the image of cycle 14 showing little spikes.
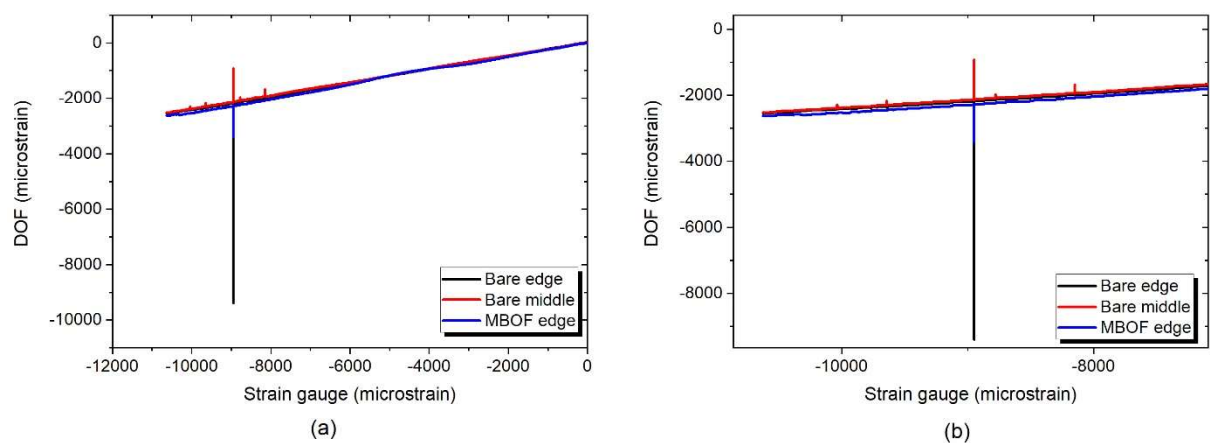
Figure 5.7 (a) Strain development from four-point bend test by distributed optical fibre during the 26th cycle (b) enlarged image
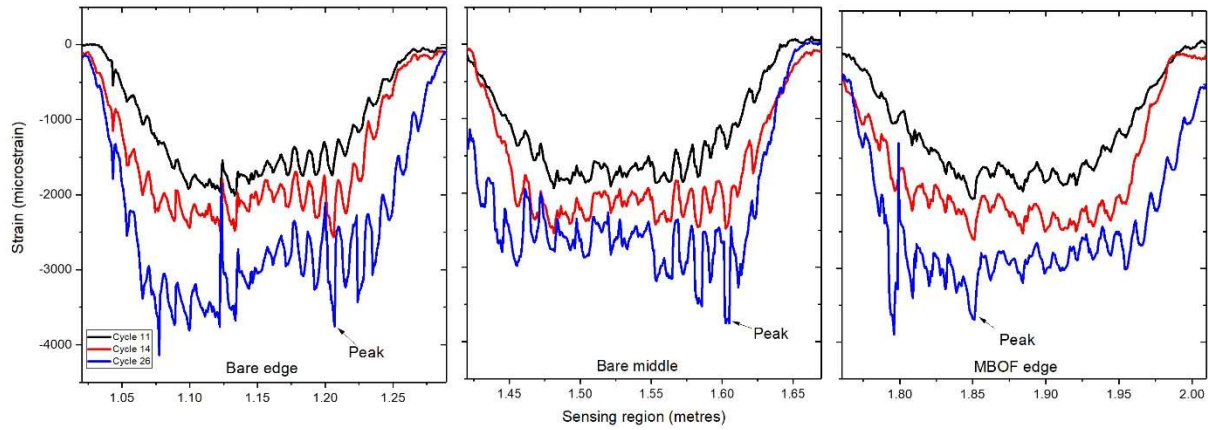
Figure 5.8 Strain profile of cycle 11 (black) at maximum load of 2766 N, cycle 14 (red) at maximum load of 4375 N, and cycle 26 (blue) at maximum load of 3293 N
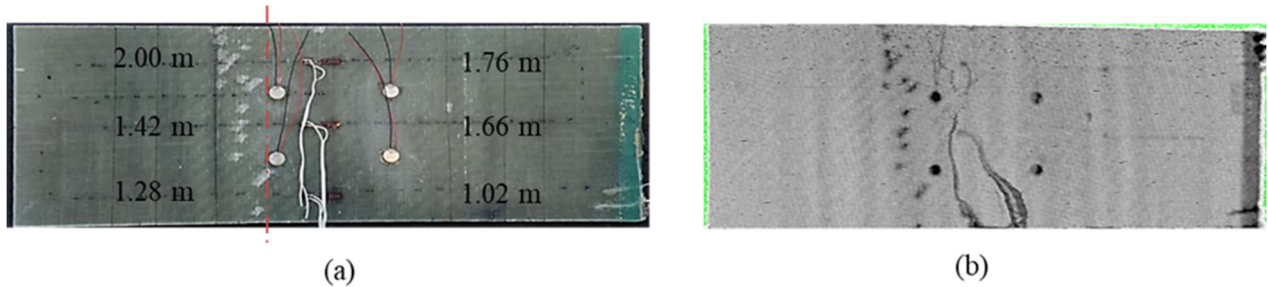
Figure 5.9 Whitening in the laminate might be due to defect growth (a) photograph (b) ultrasonic c-scan.

5.2.1 Theoretical vs experimental strain

To evaluate the functionality of the optical fibre (bare and MBOF) for four-point bending measurement, the strain reading was compared to the theoretical strain measure from Instron deflection data. Figure 5.10 shows a schematic of the 4 point bend test setup.
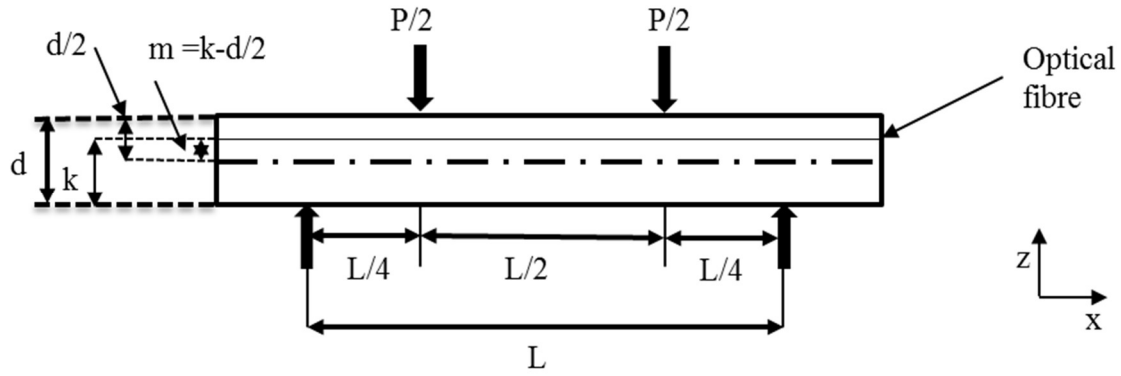
Figure 5.10 Schematic illustration of 4 point bend test

The theoretical strain in optical fibre was calculated using Equation 5.7 [70,219].

$$\varepsilon_{OF} = \varepsilon \ x \ \frac{m}{\left(\frac{d}{2}\right)} = \frac{4.36 \ x \ \delta \ x \ d}{L^2} \ x \ \frac{2m}{d} \tag{5.7}$$

Where ε_{OF} is the strain measured by the different sections of the distributed optical fibre, δ is the deflection, d is the thickness of the composite panel (3.7 mm), m is the depth of the optical fibre, L is the support span. The theoretical and experimental compressive strain (E_ε) and their percentage differences (%D) is shown in Table 5.2. It was observed that all the sections of the DOF experience decrease in strain compared to the theoretical strain. The lower value could be due to the uneven strain field caused by the induced strain on the sections of the DOF. Theoretical strain and values of strain recorded by the optical fibre sections are plotted against time in Figure 5.11. It can be seen that both the theoretical and experimental strain behaves similarly.

Table 5.2 Percentage difference of theoretical and experimental strain

Theoretical compressive strain (με)	Bare edge		Bare middle		MBOF edge	
	E_ε (με)	%$_D$	E_ε	%$_D$	E_ε	%$_D$
259	204	21	245	5	222	14
469	438	7	425	9	429	8
682	621	9	626	8	642	6
899	832	7	799	11	871	3
1128	926	18	999	11	1097	3
1354	1159	14	1169	14	1160	14
1862	1602	14	1712	8	1748	6
2769	2320	16	2237	19	2394	14
3011	2539	16	2536	16	2607	13
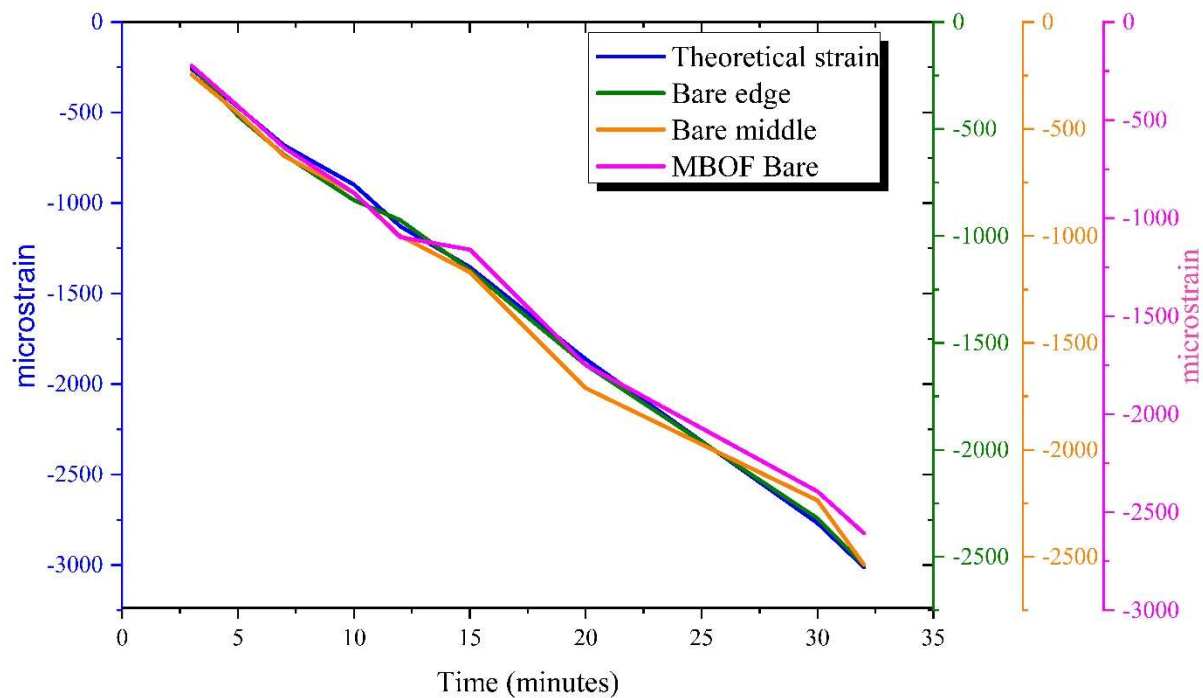
Figure 5.11 Theoretical strain (blue) and measured strain by distributed optical fibre: (a) bare edge (green), (b) bare middle (orange) and (c) micro-braided optical fibre (MBOF) edge (pink)

5.3 Summary

This chapter investigated the real-time cure monitoring of a composite laminate using an embedded distributed optical fibre sensor. When a part of the optical fibre is micro-braided, the integrity of the strain measurement was studied and compared against strain measurements obtained with the bare (as received) optical fibre. It was possible to follow the full curing process of the laminate. Isolation of mechanical strain allowed us to interpret the strain reading as temperature changes at every stage of curing, which was impossible with total strain. During the cooling stage, compressive strain was recorded by the DOFS due to stress relief of the low viscosity resin. This phenomenon has been reported by many researchers but rarely quantified. The variation in the residual strain measure by the bare edge and MBOF edge could be due to the difference in the diameter of the bare and MBOF. This consequently caused an increase in resin pocket around the MBOF, resulting in higher compressive strain. It was also observed that when the DOF sections were divided into sub-sections, sub-section two closer to the middle recorded the lowest residual strain; this was suggested to be due to the DOF sections experiencing complete axial strain. The repeated loading cycle of the four-point bending test showed that both the bare and micro-braided section of the DOF embedded during manufacture monitoring could perform structural health monitoring of the composite panel. Through the experiments performed, we can provide a basis for efficient smart processing of composite with MBOF, which shows good sensitivity of strain measurement.

Chapter 6: Result and Discussion: Integration of optical fibre sensor in the braiding process for online strain monitoring of composite tube

This chapter describes the process of embedding bare and micro-braided optical fibre during over-braiding and composite tube manufacture. Continuous measurement of strain is desirable using highly sensitive optical fibre sensors, with low influence of the sensor on the geometry of the monitored structure. The bare and micro-braided optical fibre (FBG and DOF) sensitivity to different braid configurations (braid angle) is described. Strain monitoring at various manufacturing stages with the bare and micro-braided optical fibre has been described with a summary of induced residual strain at each stage.

6.1 Characterisation of tubular preform

Tubular braid preforms were manufactured with embedded FBG and DOF, as mentioned in sub-section 3.2.2. Braid angle and tow width for the various preforms were determined using ImageJ software to measure images of the braid along 10 data points on the length of the specimen. As shown in Figure 6.1, the braid angle was measured with full braid coverage observed at 80º braid angle. An increase in braid coverage with braid angle has been reported by Rebelo et al. [113]. As seen in Figure 6.2a and b, the response of the FBGs (bare and micro-braided) and DOF (with bare and micro-braided sections) at three different stages of braiding (beginning, middle, and end) will be analysed. A total of 28 mm of each section was integrated. The thickness of the braid (t) was calculated using Equation 6.1 by measuring the thickness of the 1st (T_1) and 2nd (T_2) layers of the braid using a Vernier calliper.

(a)

(b)
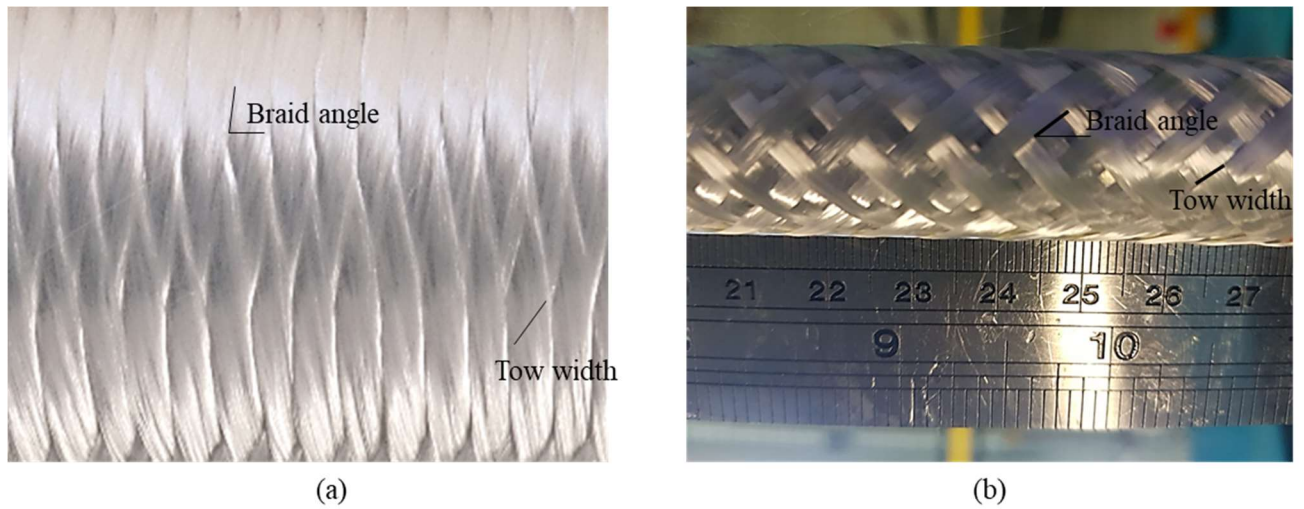
Figure 6.1 Braided preform showing tow width and the braid angle at (a) 80° and (b) 45°.

(a)

(b)
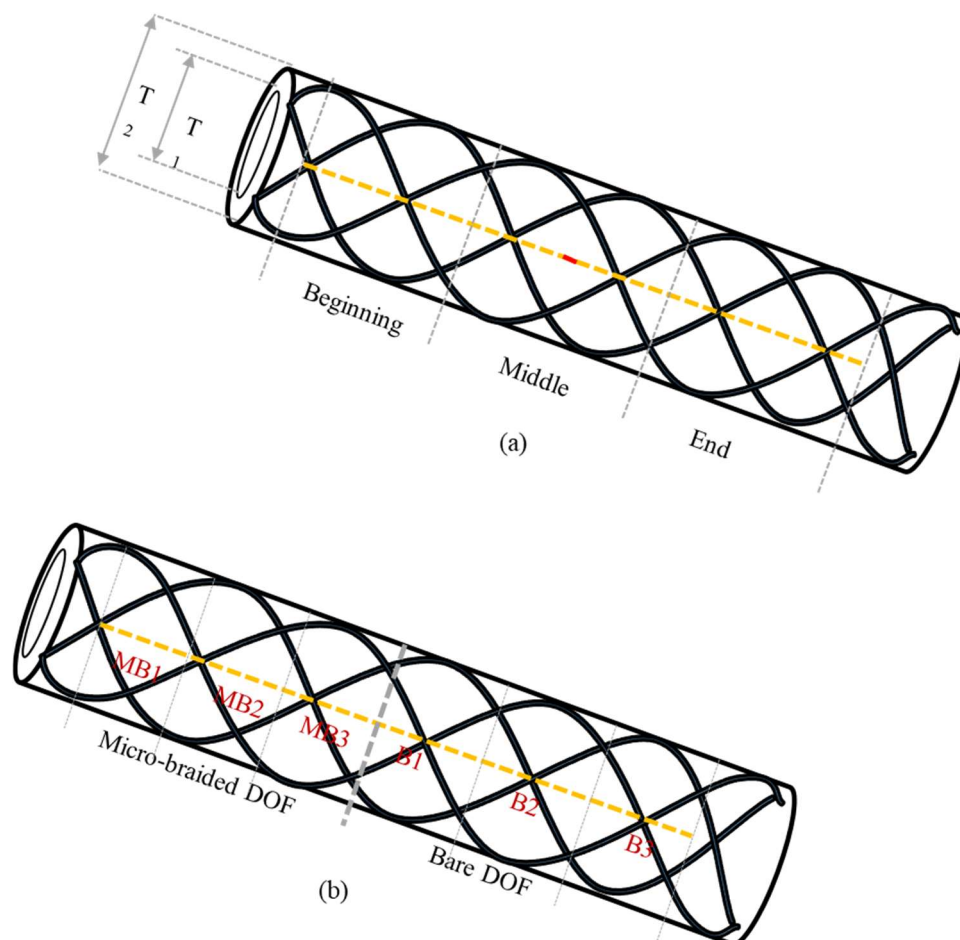
Figure 6.2 Schematics of the braided preform embedded with (a) Fibre Bragg grating (FBG) sensor and (b) Distributed optical fibre (DOF) with bare (B) and micro-braided section (MB)

$$t = \frac{T_2 - T_1}{2}$$ (6.1)

6.2 Behaviour of preform during braiding

Over-braiding involves the covering of the mandrel using the braiding process. During braiding, interlacing fibre tow wraps the mandrel following a helical path causing force underneath due to the wrapping angle and tension. Hoop pressure is the measure of the applied pressure by the fibre tow on the preceding layer. The grip/tightness of the braided sleeve on the optical fibre can be determined by measuring the hoop pressure. The tightness of the braid is dependent on the tow tension, which is set during braiding by adjusting the bobbin spring tension. However, for this braiding process, the tow tension remained constant 0.5N per braid carrier. Hoop pressure was calculated using Equation 6.2 [220,221].

$$H_p = \frac{2T Sin^2 \theta}{r W_y}$$ (6.2)

The hoop pressure parameters are; mandrel radius (r), tow tension (T), braid angle (θ), and tow width (W). As illustrated in Table 6.1, the hoop pressure increased with an increase in the braid angle. The 45° braid is loosely griped on the mandrel due to the hoop pressure and its lower coverage.

Table 6.1 Physical properties of the braided preforms

Braid angle (°)	Tow width (mm)	Thickness of braid (mm)	Hoop pressure (MPa)
45 ± 1.4	2.82 ± 0.06	0.40 ± 0.03	0.087 ± 0.003
80 ± 1.2	2.86 ± 0.43	0.78 ± 0.06	0.313 ± 0.04

6.3 FBG spectrum during braiding of preform

During braiding of the preform with embedded OF and MBOF, data acquisition was achieved using an sm125 Micro-optics interrogator. The Bragg wavelength of the OF and MBOF are 1539.877 and 1539.749 nm, respectively. The wavelength spectrum for both the OF and MBOF before braiding is shown in Figure 6.3. Shift to the left-hand side was observed in the peak wavelength for the MBOF due to the uniform longitudinal strain of about -1000 με experienced

by the MBOF resulting from the compressive strain imposed on the optical fibre during micro-braiding. Because the shape of the reflection spectrum remains the same as the OF, this indicates the uniformity of the applied strain along the grating. Values of residual strain imposed on different MBOF was mentioned previously in chapter 4. Regardless of the induced strain, both the OF and MBOF displayed a single peak, with no significant difference in power [222]. The presence of a single peak indicates both the OF and MBOF were functioning well before integrating them during braiding of the preform.
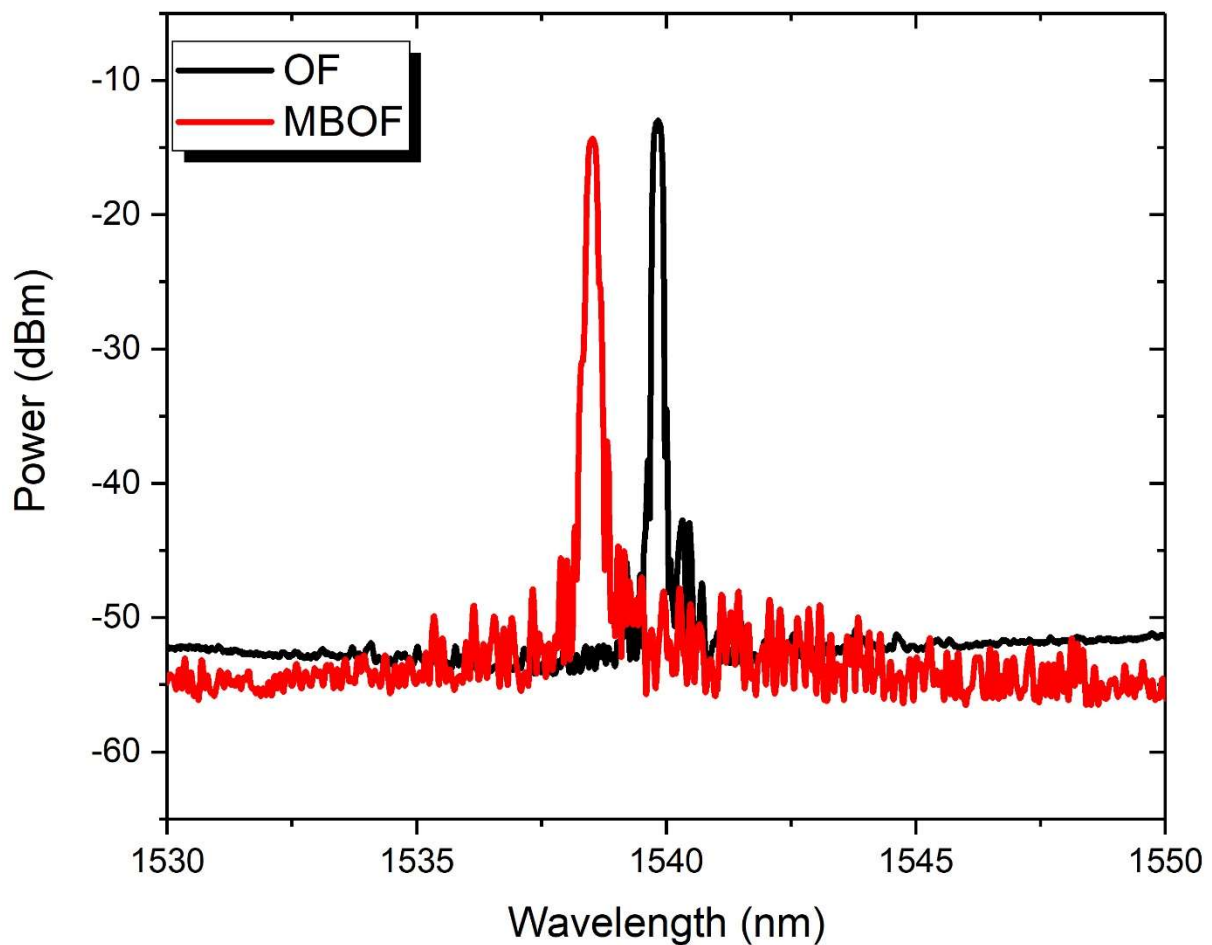
Figure 6.3 Reflection spectrum of the OF and micro-braided FBG (MBOF) before the braiding of preform

After over-braiding the 1st layer on the mandrel, the FBG sensors (OF and MBOF) were carefully integrated axially on it before braiding the 2nd layer. Reflection spectra at different stages during the braiding of the 2nd layer recorded with OF is shown in Figure 6.4. It can be seen that at the beginning of the braiding, no significant change was observed in the reflection

spectrum. This behaviour was because the farther away from the grating, little or no distortion was experienced [174]. At the end of braiding, distortion of spectral shape was observed due to broadening and multiple peaks with weaker intensity. The extent of distortion is detailed in Appendix 4A.

According to Endruweit et al. [223], when a braid is formed over another braid layer, the fibre tow forming on the braid compresses the layer underneath, often termed nesting, which can have impact on the optical fibre between the layers. The compressed layer underneath the forming layer then undergoes extension. Birkefeld et al. [106] also reported nesting as braided layers' compaction. The axial tension recorded by the OF could be due to the effect of the compression of the braid layers.
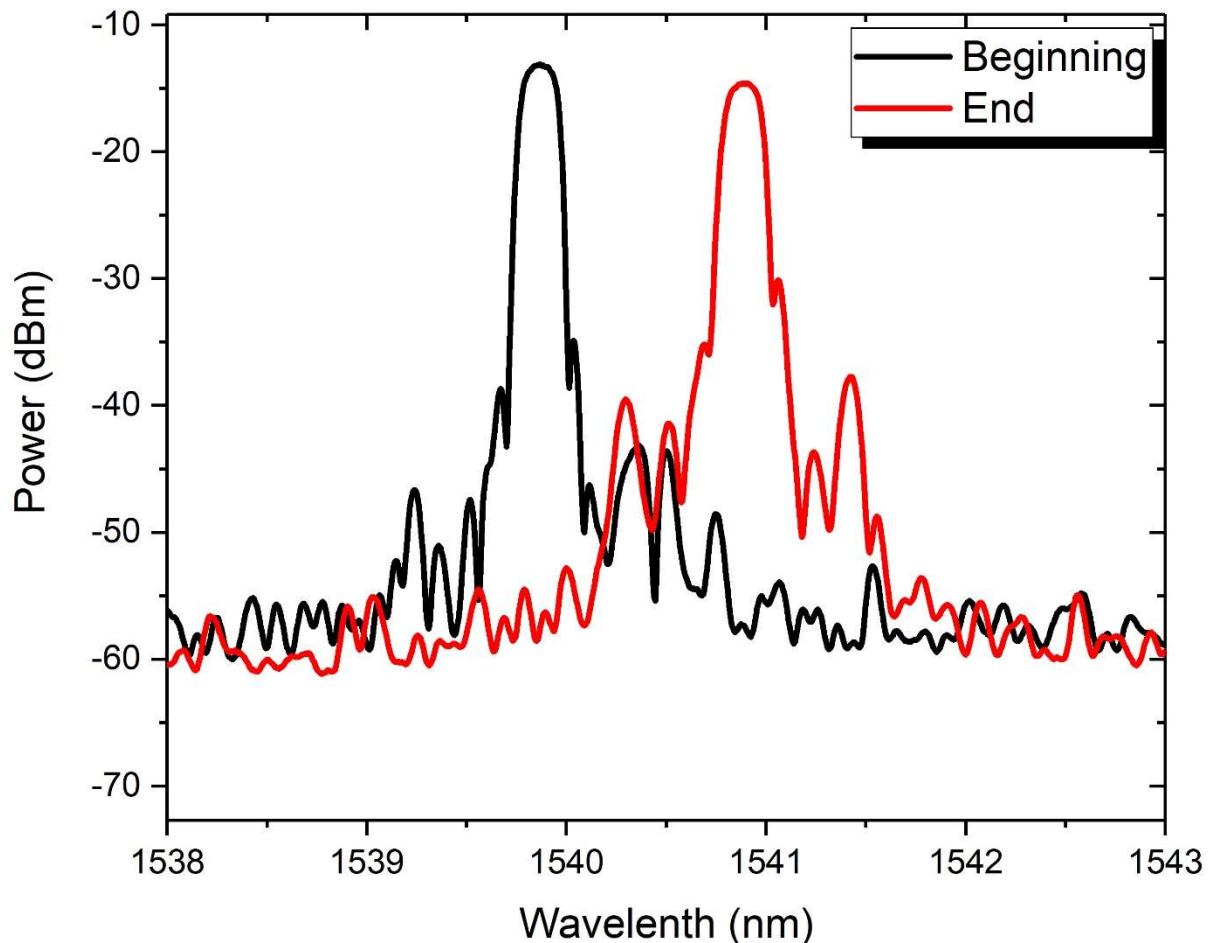
Figure 6.4 (a) Reflection spectra of the conventional optical fibre (OF) at the beginning and end of the braiding

Figure 6.5 shows the reflection spectra from the MBOF integrated between the 1st and 2nd layer during braiding of the preform. The reflection spectra recorded by the MBOF shows similar behaviour with the OF. Broadening and multiple peaks were present at the end of braiding due to induced strain on the optical fibre. However, the attenuation in power observed in the MBOF was not an issue because the measurement was still being recorded by it [222]. The difference in the wavelength shift of the OF and MBOF observed in Figure 6.4 and 6.5; OF shifting to the right (tension) and the MBOF to the left (compression). The shift in the OF was consistent with the result reported by Selezneva et al. [224]. The fibre tow forming on the braid compresses the layer underneath because of the multiple layers. This causes the layer beneath to undergo extension, which the OF recorded. Although the MBOF was sensitive to the extension of the layer underneath, like the OF, it remained in compression. This was due to the residual strain induced on the MBOF due to micro-braiding.
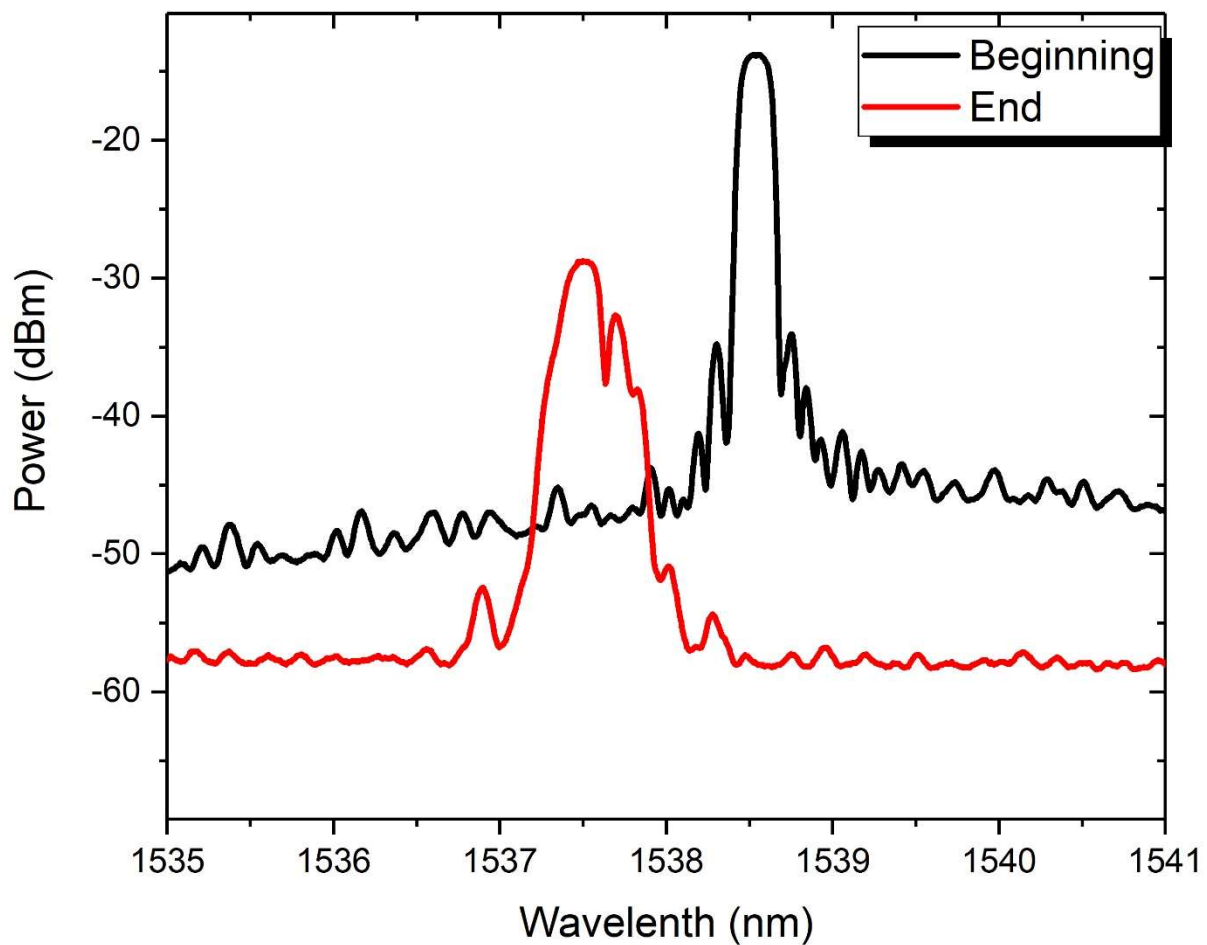
Figure 6.5 (a) Reflection spectra of the micro-braided optical fibre (MBOF) at the beginning and end of the braiding

Orientation of peak wavelength

The shift in peak wavelength and the corresponding strain resulting with the time taken to braid across the length of the FBG sensor is shown in Figure 6.6. For both the OF and MBOF, no significant change in wavelength was observed at the beginning of braiding; this type of behaviour was also reported by Ussorio et al. [174]. The researchers reported no change in strain when a crack is further away from the grating. A sudden increase in peak wavelength for the OF was observed in the middle of braiding. The sudden peak in strain was not experienced by the MBOF, as seen in Figure 6.6b. A steady increase in wavelength was observed due to the axial tension in the optical fibre caused by the braiding tow compressing it. However, the MBOF remained in compression due to the residual strain induced during micro-braiding. The lower change in strain around the grating for the MBOF shows the importance of the micro-braiding layer as a protection for the optical fibre. Both the OF and MBOF did not return to the initial strain due to the induced residual strain.
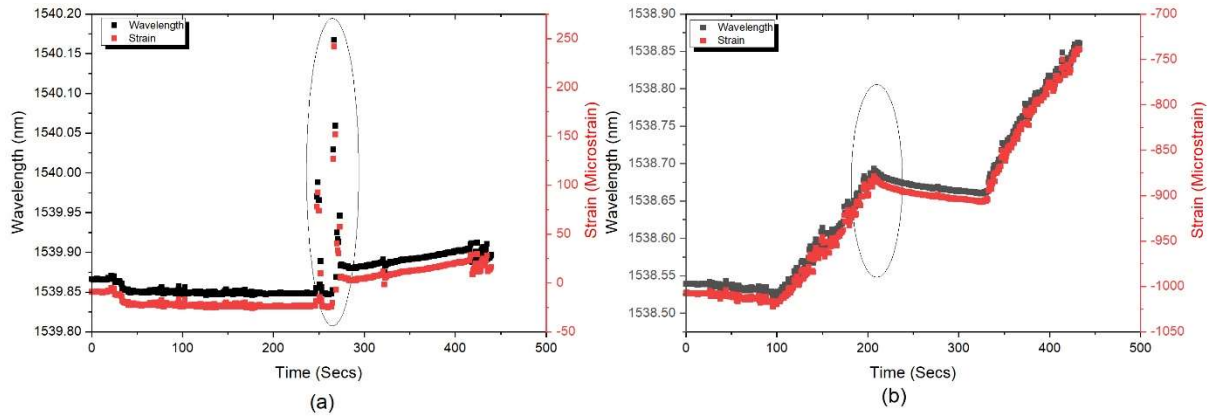
Figure 6.6 Change in peak wavelength and strain with time at 45° braid angle, highlighted region indicating grating part (a) conventional optical fibre (OF) and (b) micro-braided optical fibre (MBOF)

6.4 Strain measurement with DOF during braiding of preform

During braiding of the preform, lateral compression due to nesting was experienced in the braiding layers. This was measured at both the bare and micro-braided sections of the DOF. Strain behaviour at each sub-section of the 45º braided preform embedded with bare DOF is shown in Figure 6.7.

The bare DOF recorded axial tension due to the compression experience between braid layers. The increase in tension became uniform after rising to about 500 µε. The behaviour trend was similar to the bare FBG; however, no spike in strain was experienced in the bare DOF.
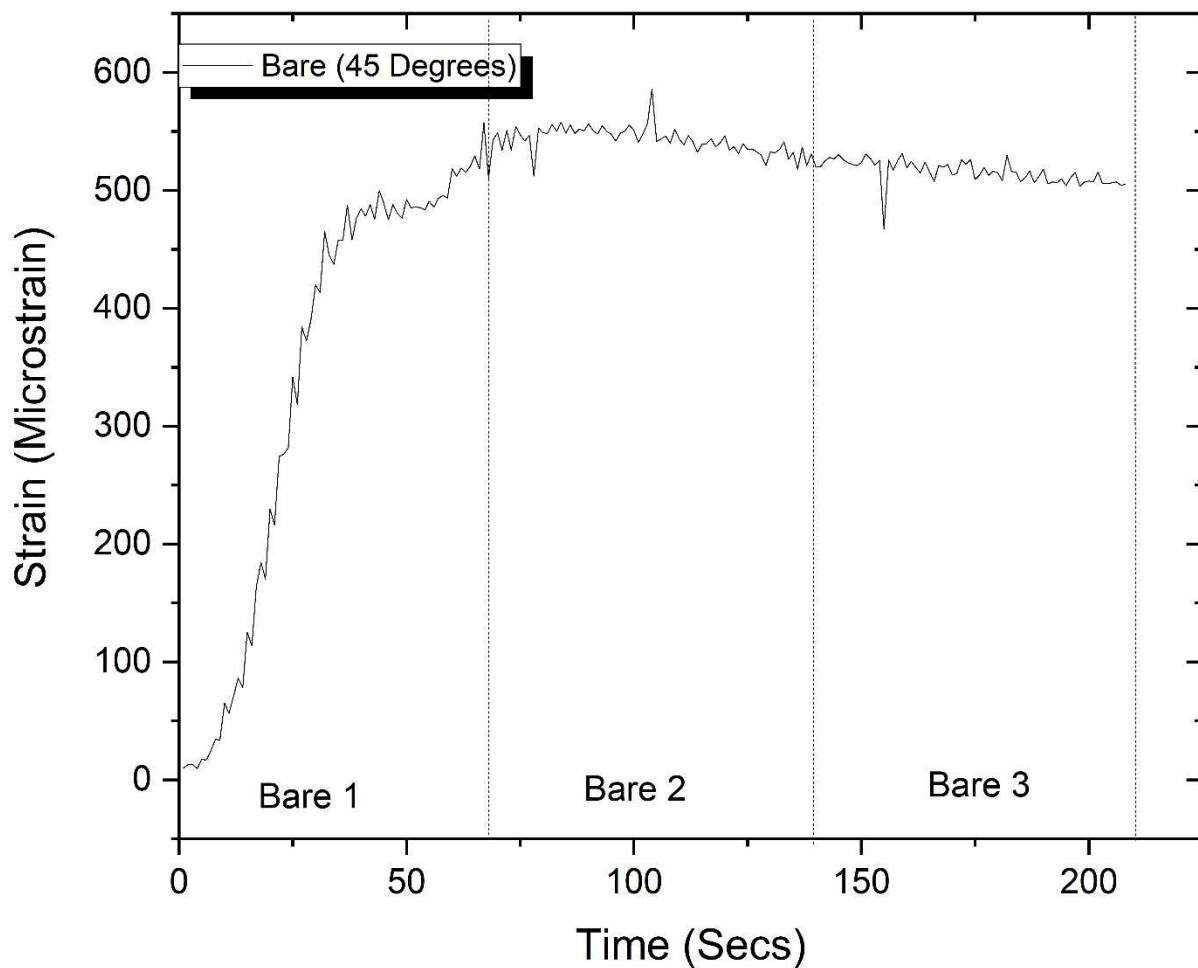
Figure 6.7 Strain measurement with time for bare DOF at 45º braid angle

The strain change recorded by the 45º braided preform embedded with micro-braided DOF is shown in Figure 6.8. The result obtained by the micro-braided DOF was similar to the MBOF. As seen in Figure 6.8, there was change in strain from about -580 µε in MB_1 to -300 µε in MB_3

due to the axial tension experienced resulting from compaction of the braid layers. The strain remained in compression due to residual strain induced during micro-braiding.

The micrograph in Figure 6.9 and 6.10 shows the compaction of the bare and micro-braided DOF between braiding layers. The measured resin-rich areas for the bare and micro-braided DOF are 0.11 ± 0.0015 and $0.243 \pm 0.0065mm^{2,}$ respectively. The higher resin-rich area observed in the micro-braided DOF was due to increased optical fibre diameter resulting from micro-braiding. The entire sample preparation, grinding and polishing are presented in Appendix 2A.
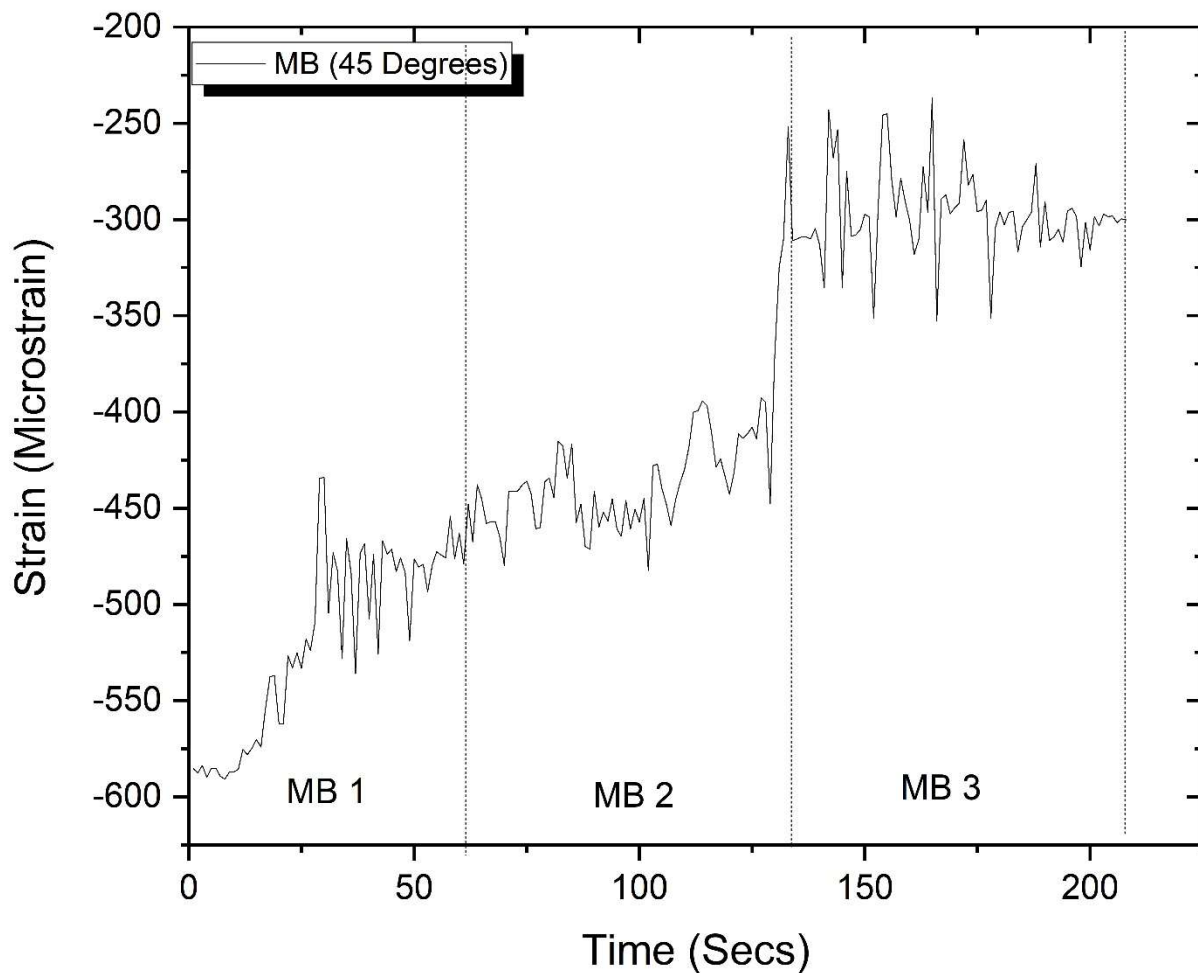
Figure 6.8 Strain measurement with time for micro-braided DOF at 45º braid angle
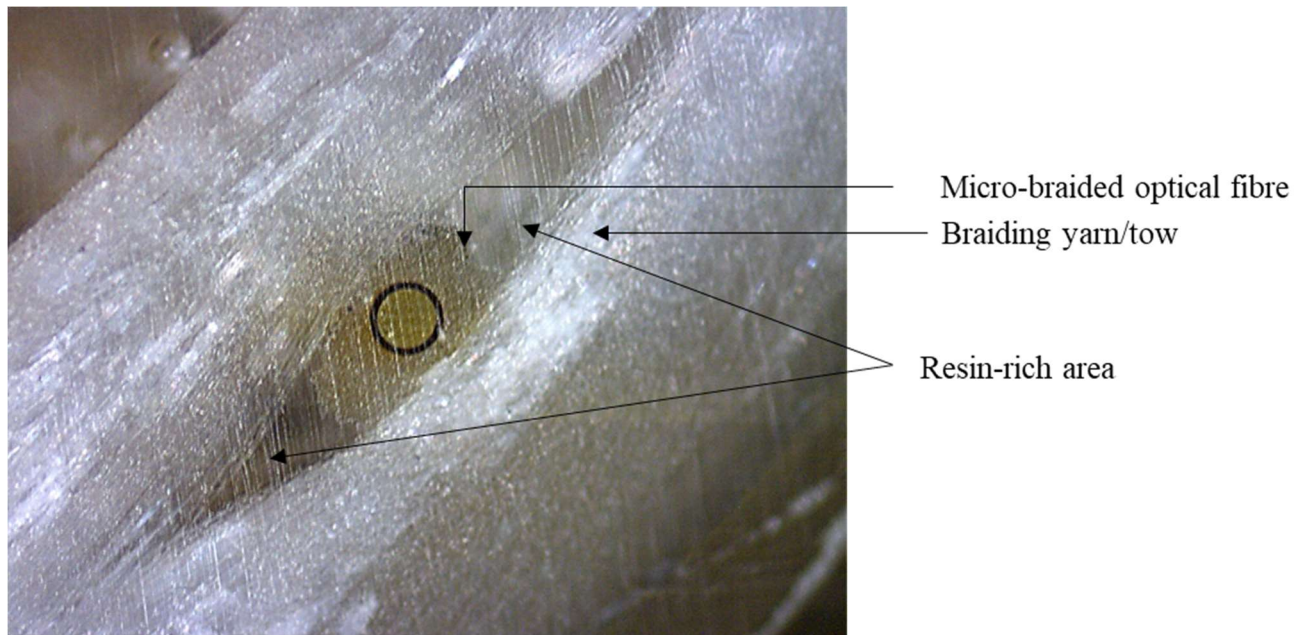
Figure 6.9 Micrograph of the micro-braided DOF embedded in-between the 1st and 2nd layer.
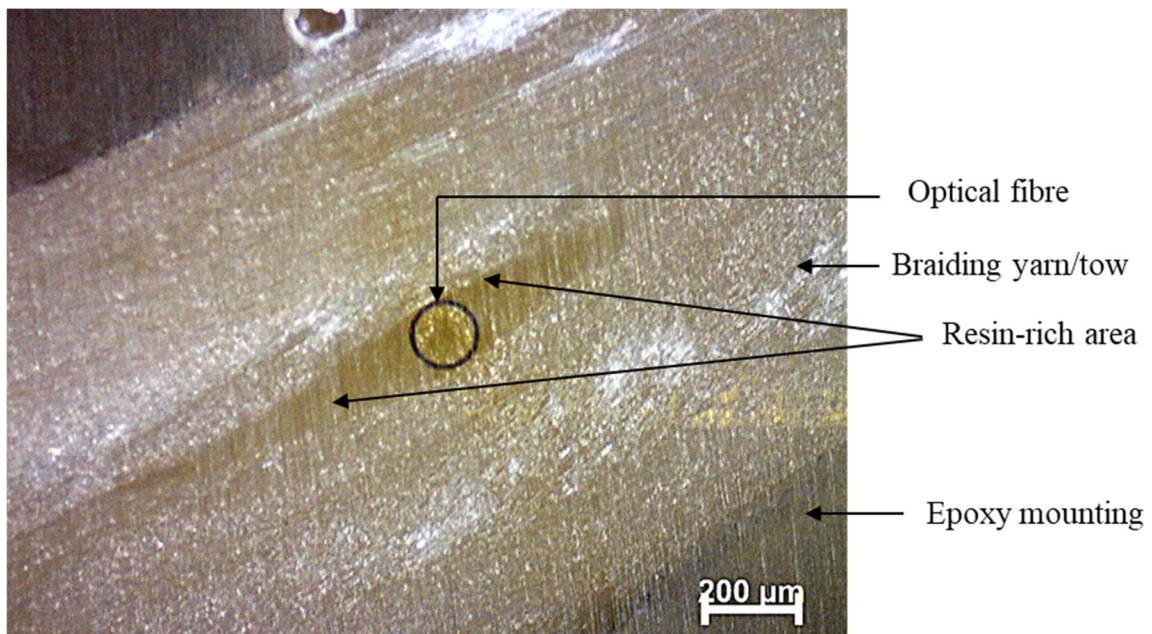
Figure 6.10 Micrograph of the embedded bare distributed optical fibre (DOF) in-between the 1st and 2nd layer.

6.5 Cure monitoring during composite manufacture

The temperature profile of the cure cycle and the total strain recorded by both FBG and DOF sensor is shown in Figure 6.11. Different curing stages such as heating, isothermal cure and cooling are displayed in the graph. The first temperature ramp allows the resin to flow, while the second ramp and dwell is the polymerisation part of the cure cycle. During this stage, cross-linking of resin commences, which is completed during the isothermal dwell. The ratio of the wavelength shift of the strain-free FBG and thermal sensitivity (k_T) was used to calculate the temperature. Since the sensors are located in the same thermal environment, by subtracting the temperature component from the total strain, the mechanical strain was obtained using Equations (2.9-2.12) in sub-section 2.10.3. Readings from the OF was not included because it was damaged somewhere during the composite manufacture. The bare and micro-braided DOF could sustain the cure cycle without any damage to either of them.
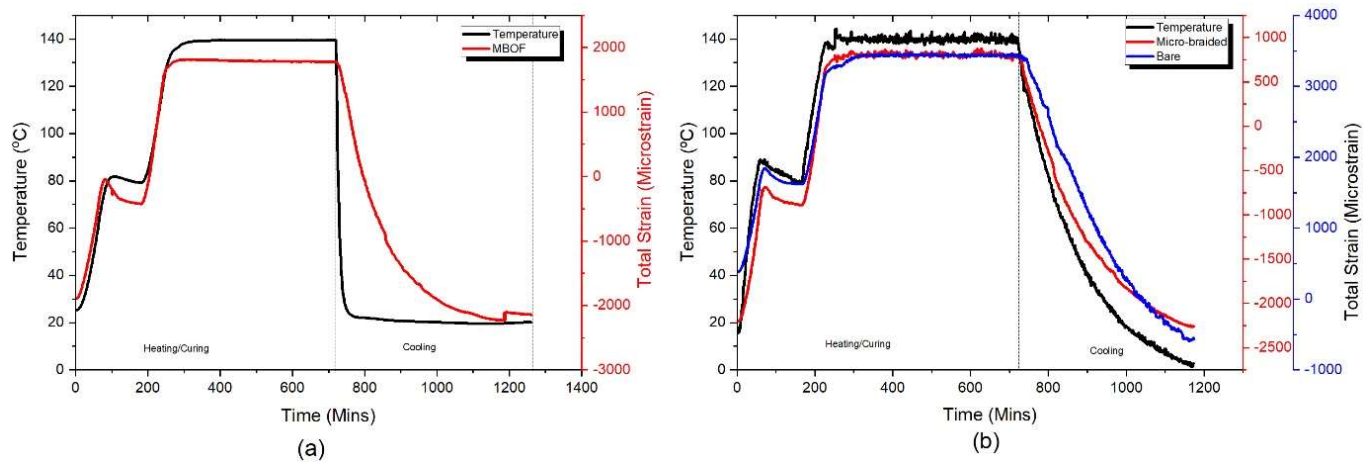
Figure 6.11 (a) Temperature profile of the strain-free FBG sensor (black) and total strain of micro-braided optical fibre (MBOF) (red) and (b) Temperature measured by DOF (black) and total strain of bare DOF (blue) and micro-braided DOF (red).

The mechanical strain curve for the FBG and DOF is shown in Figure 6.12. It can be seen in Figure 6.12a that as temperature increased from room to polymerisation temperature, both negative and positive strain was recorded by the MBOF due to the thermal expansion and chemical shrinkage as a result of the transition of resin from liquid to rubber (gelation). This same behaviour was also experienced by the bare and micro-braided section of the DOF, as shown in Figure 6.12b. During the second ramp and hold, an increase in positive strain was experienced; this could be due to the subjection of the specimen to external tension due to the

148

expansion of the mould. Zhang et al. [225] reported similar positive strain behaviour due to the nearness of the sensor to the mould. A steady strain was observed during the second dwell. Unlike the mechanical strain profile of composite laminated discussed in Chapter 5, the optical fibre was not inserted beneath the fabric's fibre floats. During cooling, a sudden increase in positive strain was experienced; this could be due to the detachment of the sample from the mould. The compressive strain was recorded by the MBOF with a residual strain value of -2320 με. A similar result of sample detachment from the mould during cooling has been reported by [147,226,227]. Ferdinand et al. [1] have also reported a residual strain of -2400 με using an FBG sensor to monitor the curing of a glass/epoxy pre-preg. The residual strain recorded by the bare and micro-braided section of the DOF were -600 and -2250 με, respectively. The difference between the residual strain for the bare and micro-braided section of the DOF could be due to the cumulative residual strain induced during micro-braiding and braiding of preform on the optical fibre, as shown in Table 6.2.

Because of the unexpected reading obtained from the OF due to breakage, the reflection spectra of both the OF and MBOF was plotted to identify when damage happened with the OF as seen in Figure 6.13. It was observed at the beginning of cure (1 min), both OF and MBOF have a single peak reflection spectra with little or no power loss. Has the cure time increased, the OF began to experience power loss and eventually experienced a complete loss of power. The MBOF shows no power loss; however, splitting of the peak was observed after cooling. This type of behaviour was also observed by Parlevliet et al. [228], they reported splitting of the peak due to strain variations perpendicular and parallel to the length of the grating axis. This result shows improvement in the robustness of the MBOF compared to the OF.

(a)

(b)
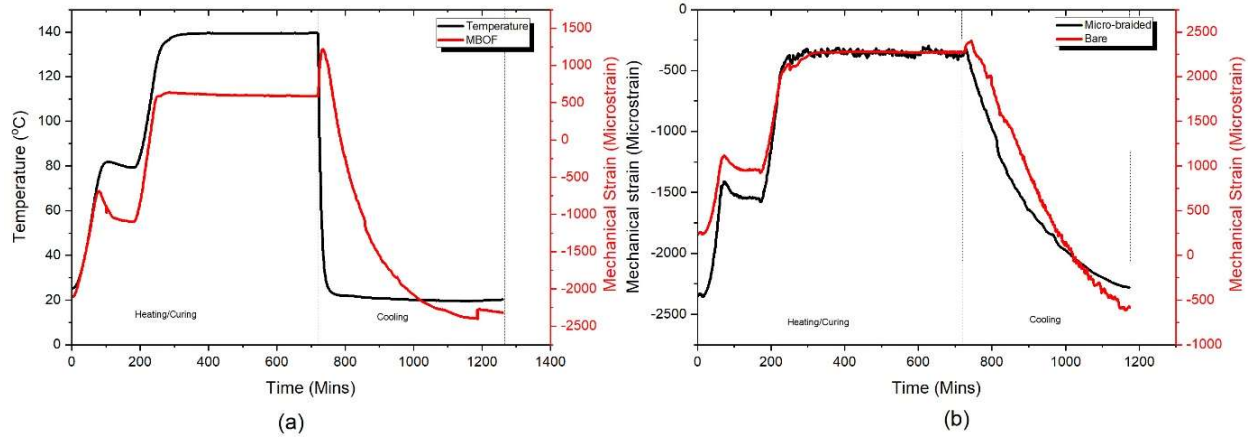
Figure 6.12 Temperature profile of the (a) strain-free FBG sensor (black) and mechanical strain for micro-braided optical fibre (red) (b) bare DOF (red) and micro-braided DOF (black)

Table 6.2 Induced residual strain at different stages of manufacture

	Residual strain after Micro-braiding (µε)	Residual strain after Braiding of preform (µε)	Residual strain after Curing (µε)
DOF	-580	-300	-2250
FBG	-1000	-700	-2320
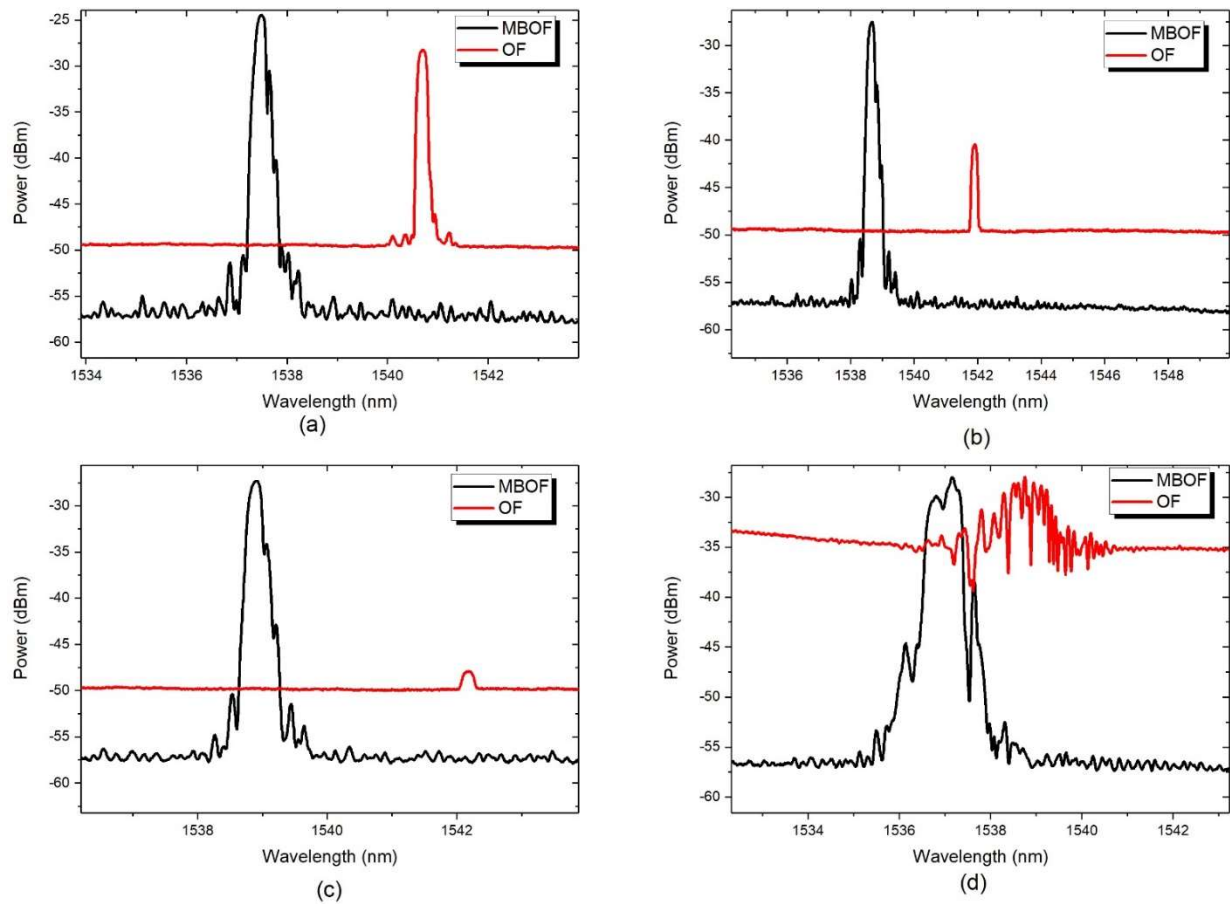
Figure 6.13 Reflection spectra of micro-braided optical fibre (MBOF) (black) and conventional optical fibre (OF) (red) at different times during curing; (a) 1 min, (b) 49 mins, (c) 55 mins and (d) 1261 mins.

6.6 Summary

In this chapter, the process of embedding both bare and micro-braided optical fibre during the braiding of the preform was described. Two different optical fibres (FBG and DOF) were used to study the effect of micro-braiding on their performance when monitoring strain during braiding and composite manufacture.

The effect of varying braid angle from 80º to 45º during braiding of preform was studied, and it was discovered that exerted hoop pressure increased as braid angle increased. The result in this chapter indicates the same trend for the bare and micro-braided FBG and DOF. They all experienced axial tension during braiding of preform due to compaction between the braid layers. The significance of micro-braiding was displayed when the MBOF recorded a steady

increase in strain, unlike the spike in strain recorded by the OF. When in service, this could act as a region of stress concentration which could affect the durability of the FBG. This situation can be mitigated by micro-braiding the optical fibre.

During the cure cycle monitoring, it was discovered from the reflection spectra that the OF experienced signal loss and this was not experienced by the MBOF. This was due to the breaking of the OF sometime during the curing. However, no damage was experienced in the bare and micro-braided section of the DOF. These findings provide insight into micro-braided optical fibre's suitability for overall structural monitoring.

Chapter 7: Conclusions and Future works

This thesis was centred on developing a modified optical fibre in the form of micro-braided optical fibre (MBOF) through the textile manufacturing process of braiding for Structural Health Monitoring (SHM). Details of the development and characterisation of MBOF was conducted in this research. Glass fibre composite was used as the host surface for integrating the conventional and micro-braided optical fibre for strain monitoring of the full-lifecycle.

7.1 Experimental methods and MBOF manufacture

MBOF was manufactured using a 24 carrier maypole braiding machine, and four carriers were selected for producing braids with good grip and low diameter. Tow tension was unaltered throughout the braiding process. The topology of the braid formed was diamond, and the braid angle ˜17°. Full braid coverage was achieved with the braid configuration, which is important for an optimum mechanical property. Some challenges were encountered during micro-braiding and these includes selecting bobbins configuration, winding bobbins with braiding yarn, initial machine set up, and determination of optimum parameters such as machine speed and take-up speed.

Other experimental methods in this work include; braiding of tube preforms, vacuum-assisted resin infusion moulding (VARIM), sample preparation for Micro-bond test for interfacial shear strength and burn of test for fibre volume fraction. Sample preparation of conventional OF and MBOF for SEM and cross-section microscopy of the braided tube and composite laminate embedded with OF/MBOF to determine braid angle, tow width, tow thickness and crimp angle.

7.2 Optimisation of optical fibre using micro-braiding for structural health monitoring.

The mechanical characterisation of MBOF was investigated. The sensitivity of the MBOF was compared to that of the conventional OF by measuring the FWHM of the bandwidth change. No significant difference in the FWHM was observed. However, a negative change in strain

was observed due to the braiding yarn's compression on the OF during interlacement. In general, no damage was done to the sensor due to micro-braiding.

The tensile response of both conventional OF and MBOF was investigated. MBOF showed about 85% increase in strain at failure than the conventional OF. This was due to the cushion effect the micro-braiding has on the OF, which increased the elongation of the OF. However, the decrease in Young's modulus observed could be attributed to crimp, causing undulation of the braiding yarn.

The IFSS was determined through the micro-bond test, and results show a 29% percentage difference between the OF and MBOF. This difference was due to the cohesive matrix failure experienced by the MBOF due to the surface morphology. However, the composite laminate manufactured with no OF and OF and MBOF were subjected to a three-point bending test. For the samples with no OF, with OF and with MBOF, comparable results for UFS, strain at failure and flexural modulus were exhibited. It was discovered that the integrity of the composite was not affected negatively by the presence of the MBOF.

7.3 Cure monitoring and SHM of composites using micro-braided distributed optical fibre

A distributed optical fibre sensor was embedded between a composite laminate for real-time cure monitoring in this section. The possibility of strain measurement when part of the DOF is micro-braided, and the remaining part left bare was examined. For clear interpretation of strain reading, the mechanical strain was isolated from the total strain, and both the micro-braided and bare section exhibited a similar strain profile. During cooling, the compressive strain was recorded by both sections of the DOF due to stress relief of the low viscosity resin. However, the variation in the measured residual strain of both section of the DOF was due to the difference in the bare and micro-braided sections' diameter. This caused an increase in resin pocket around the micro-braided section resulting in the higher compressive strain.

The repeated loading cycle of the four-point bending test showed that both the bare and micro-braided sections of the DOF could detect the initiation and growth of crack in a composite panel. A rationale for using micro-braided optical fibre for smart processing of composite is displayed from the results obtained.

7.4 Integration of optical fibre sensor in the braiding process for online strain monitoring of composite tube

Optical fibre sensors (FBG and DOF) with micro-braided and bare sections were embedded axially during the braiding of preforms to monitor the process. By varying the braid angle (80º and 45º), it was discovered that the exerted hoop pressure increased with an increase in braid angle. A similar trend of results was observed for the bare and micro-braided FBG and DOF. Spike in strain value was experienced around the conventional OF's grating part, which was not present for the MBOF. This displays robustness due to the protective layer provided by micro-braiding.

During cure monitoring, loss in signal was experienced by the OF from the reflection spectra due to damage. However, this behaviour was not experienced by the bare DOF. This shows the high susceptibility of the grating part of the FBG sensor to damage due to increase stress concentration around it.

7.5 Recommendation for future work

In this thesis, through a series of experiments, micro-braided optical fibres are proposed as a promising alternative to conventional optical fibres for application in SHM. This thesis's findings can be used for further research in some areas listed below.

- Optimising the triaxial yarn feeding system for optical fibres, as during the triaxial braiding process, the axial fibres have a lot of inter yarn friction which can damage the conventional and micro-braided optical fibre.
- Investigating the micro-braided optical fibre behaviour in ageing condition for application in SHM of severe environment. The durability of utilising micro-braided optical fibre to monitor real-time strain in buried oil and gas pipelines to avoid unnecessary digging for maintenance.
- This study concentrated on using glass fibre as a host surface for embedding the micro-braided optical fibre. The use of other fibres such as carbon and natural fibres are recommended.

- The incorporation of MBOF in the manufacture of cylinders or pipes developed through filament winding. This process will investigate the effect of MBOF on the cylinders/pipes for oil and gas industrial application.

References

1. Ferdinand, P.; Magne, S.; Dewynter-Marty, V.; Rougeault, S.; Maurin, L., "Applications of Fiber Bragg Grating sensors in the composite industry", *MRS Bull.* **2002**, 27, 400–407.

2. Hou, W.; Zhang, W., "Advanced Composite Materials Defects/Damages and Health Monitoring", *2012 Progn. Syst. Heal. Manag. Conf.* **2012**, 1–5. doi:10.1109/PHM.2012.6228804.

3. Greenhalgh, E.S., "Defects and damage and their role in the failure of polymer composites", *Fail. Anal. Fractography Polym. Compos.* **2009**, 356–440.

4. Yang, S.-H.; Kim, K.-B.; Oh, H.G.; Kang, J.-S., "Non-contact detection of impact damage in CFRP composites using millimeter-wave reflection and considering carbon fiber direction", *NDT&E Int.* **2013**, 57, 45–51.

5. Koyama, K.; Hoshikawa, H.; Kojima, G., "Eddy Current Nondestructive Testing for Carbon Fibre-Reinforced Composites", *J. Press. Vessel Technol.* **2013**, 135, 1–5.

6. Katunin, A.; Dragan, K.; Dziendzikowski, M., "Damage identification in aircraft composite structures: A case study using various non-destructive testing techniques", *Compos. Struct.* **2015**, 127, 1–9.

7. Gholizadeh, S., "A review of non-destructive testing methods of composite materials", *Struct. Intergrity Procedia*. **2016**, 1, 050–057.

8. Hung, Y.Y.; Yang, L.X.; Huang, Y.H., "Non-destructive evaluation (NDE) of composites: digital shearography", *Non-Destructive Eval. Polym. Matrix Compos.* **2013**, 84–115. doi:10.1533/9780857093554.1.84.

9. Toh, S.L.; Chau, F.S.; Shim, V.P.W.; Tay, C.J.; Shang, H.M., "Application of Shearography in Nondestructive testing of Composite plates", *J. Mater. Process. Technol.* **1990**, 23, 267–275.

10. Sarasini, F.; Santulli, C., "Non-destructive testing (NDT) of natural fibre composites: acoustic emission technique", *Nat. Fibre Compos.* **2014**, 273–302.

11. Gholizadeh, S.; Leman, Z.; Baharudin, B.T.H.T., "A review of the application of

acoustic emission technique in engineering", *Struct. Eng. Mech.* **2015**, 54, 1075–1095.

12. Gresil, M.; Saleh, M.N.; Soutis, C., "Transverse Crack Detection in 3D Angle Interlock Glass Fibre Composites Using Acoustic Emission", *Materials (Basel).* **2016**, 9, 1–20.

13. Yang, S.; Tian, G.Y.; Abidin, I.Z.; Wilson, J., "Simulation of edge cracks using pulsed Eddy current stimulated thermography", *J. Dyn. Syst. Meas. Control.* **2011**, 133,.

14. Ciampa, F.; Mahmoodi, P.; Pinto, F.; Meo, M., "Recent advances in active infrared thermography for non-destructive testing of aerospace components", *Sensors.* **2018**, 18, 1–37.

15. Ramos, H.G.; Ribeiro, A.L., "Present and future impact of magnetic sensors in NDE", *Procedia Eng.* **2014**, 86, 406–419.

16. Dong, Y.; Ansari, F., Non-destructive testing and evaluation (NDT/NDE) of civil structures rehabilitated using fiber reinforced polymer (FRP) composites, in: Serv. Life Estim. Ext. Civ. Eng. Struct., 2011: pp. 193–222.

17. Giurgiutiu, V., Structural Health Monitoring: with Piezoelectric Wafer Active Sensors, Academic Press, 2007.

18. Li, H.-N.; Li, D.-S.; Song, G.-B., "Recent applications offiber optic sensors to health monitoring in civil engineering", *Eng. Struct.* **2004**, 26, 1647–1657.

19. Majumder, M.; Gangopadhyay, T.K.; Chakraborty, A.K.; Dasgupta, K.; Bhattacharya, D.K., "Fibre Bragg gratings in structural health monitoring—Present status and applications", *Sensors Actuators A.* **2008**, 147, 150–164.

20. Leng, J.; Asundi, A., "Structural health monitoring of smart composite materials by using EFPI and FBG sensors", *Sensors Actuators A.* **2003**, 103, 330–340.

21. Rao, Y.J., "Recent progress in applications of in-"bre Bragg grating sensors", *Opt. Lasers Eng.* **1999**, 31, 297–324.

22. Takeda, S.; Okabe, Y.; Takeda, N., "Delamination detection in CFRP laminates with embedded small-diameter fiber Bragg grating sensors", *Compos. Part A.* **2002**, 33, 971–980.

23. Takeda, N.; Okabe, Y.; Kuwahara, J.; Kojima, S.; Ogisu, T., "Development of smart

composite structures with small-diameter fiber Bragg grating sensors for damage detection: Quantitative evaluation of delamination length in CFRP laminates using Lamb wave sensing", *Compos. Sci. Technol.* **2005**, 65, 2575–2587.

24. Takeda, S.; Minakuchi, S.; Okabec, Y.; Takeda, N., "Delamination monitoring of laminated composites subjected to low-velocity impact using small-diameter FBG sensors", *Compos. Part A*. **2005**, 36, 903–908.

25. Takeda, S.; Okabe, Y.; Yamamoto, T.; Takeda, N., "Detection of edge delamination in CFRP laminates under cyclic loading using small-diameter FBG sensors", *Compos. Sci. Technol.* **2003**, 63, 1885–1894.

26. Tsuda, H.; Toyama, N.; Takatsubo, J., "Damage detection of CFRP using fiber Bragg gratings", *J. Mater. Sci.* **2004**, 39, 2211–2214.

27. Tsuda, H., "Ultrasound and damage detection in CFRP using fiber Bragg grating sensors", *Compos. Sci. Technol.* **2006**, 66, 676–683.

28. Chandarana, N.; Sanchez, D.; Soutis, C.; Gresil, M., "Early Damage Detection in Composites during Fabrication and Mechanical Testing", *Materials (Basel)*. **2017**, 10, 1–16.

29. Sánchez, D.M.; Gresil, M.; Soutis, C., "Distributed internal strain measurement during composite manufacturing using optical fibre sensors", *Compos. Sci. Technol.* **2015**, 120, 49–57.

30. Costa, L.; Gresil, M.; Frazão, O., "Simultaneous measurement of physical parameters using FBGs embedded in unidirectional and bidirectional composite materials", *Smart Mater. Struct.* **2016**, 25, 1–8.

31. Minakuchi, S.; Takeda, N.; Takeda, S.; Nagao, Y.; Franceschetti, A., "Life cycle monitoring of large-scale CFRP VARTM structure by fibre-optic-based distributed sensing", *Compos. Part A*. **2011**, 42, 669–676.

32. Minakuchi, S.; Umehara, T.; Takagaki, K.; Ito, Y.; Takeda, N., "Life cycle monitoring and advanced quality assurance of L-shaped compositecorner part using embedded fiber optic sensor", *Compos. Part A*. **2013**, 48, 153–161.

33. Zangani, D.; Fuggini, C.; Loriga, G., Electronic textiles for geotechnical and civil engineering, in: Electron. Text., 2015: pp. 275–300.

34. Güemes, A.; Messervey, T.B., Smart textile and polymer fibres for structural health monitoring, in: Text. Polym. Compos. Build., 2010: pp. 330–350.

35. Jose, J.P.; Malhotra, S.K.; Thomas, S.; Joseph, K.; Goda, K.; Sreekala, M.S., Advances in Polymer Composites: Macro- and Microcomposites – State of the Art, New Challenges, and Opportunities, in: Polym. Compos., 2012: pp. 3–16.

36. Gay, D.; Hoa, S. V., Composite Materials Design and Applications, 2007. doi:https://doi.org/10.1201/9781420045208.

37. Matthews, F.L.; Rawlings, R.D., Composite Materials: Engineering and Science, Woodhead Publishing Limited, 1999.

38. Haines, G., "The importance of composites in Aerospace and Automotive industries", *Deskt. Eng.* **2017**, 1. https://info.dte.co.uk/the-importance-of-composites-in-aerospace-and-automotive-industries.

39. Staszewski, W.J., "Intelligent signal processing for damage detection in composite materials", *Compos. Sci. Technol.* **2002**, 62, 941–950.

40. Sathishkumar, T.P.; Satheeshkumar, S.; Naveen, J., "Glass fiber-reinforced polymer composites – a review", *J. Reinf. Plast. Compos.* **2014**, 33, 1258–1275.

41. Ramesh, M.; Palanikumar, K.; Reddy, K.H., "Mechanical property evaluation of sisal-jute-glass fibre reinforced polyester composites", *Compos. Part B*. **2013**, 48, 1–9.

42. Mishra, S.; Mohanty, A.K.; Drzal, L.T.; Misra, M.; Parija, S.; Nayak, S.K.; Tripathy, S.S., "Studies on mechanical performance of biofibre/glass reinforced polyester hybrid composites", *Compos. Sci. Technol.* **2003**, 63, 1377–1385.

43. Gojny, F.H.; Wichmann, M.H.G.; Fiedler, B.; Bauhofer, W.; Schulte, K., "Influence of nano-modification on the mechanical and electricalproperties of conventional fibre-reinforced composites", **n.d.,**.

44. Davoodi, M.M.; Sapuan, S.M.; Ahmad, D.; Ali, A.; Khalina, A.; Jonoobi, M., "Mechanical properties of hybrid kenaf/glass reinforced epoxy composite forpassenger car bumper beam", *Mater. Des.* **2010**, 31, 4927–4932.

45. Aramide, F.O.; Atanda, P.O.; Olorunniwo, O.O., "Mechanical Properties of a Polyester Fibre Glass Composite", *Int. J. Compos. Mater.* **2012**, 2, 147–151.

46. Naito, K.; Tanaka, Y.; Yang, Y.M.; Kagawa, Y., Tensile and Flexural Properties of Single Carbon Fibre, in: 17th Int. Conf. Compos. Mater., Edinburgh, United Kingdom, 2009: pp. 1–10.

47. AmesWeb, "Modulus of Elasticity of metals", **n.d.,**. https://www.amesweb.info/Materials/Modulus-of-Elasticity-Metals.aspx.

48. Ku, H.; Wang, H.; Pattarachaiyakoop, N.; Trada, N., "A review on the tensile properties of natural fiber reinforced polymer composites", *Compos. Part B*. **2011**, 42, 856–873.

49. ACI, Specification for Carbon and Glass Fiber-Reinforced Polymer Bar Materials for Concrete Reinforcement, 2008.

50. Wallenberger, F.T.; Watson, J.C.; Li, H., "Glass fibre", *ASM Handb.* **2001**, 21, 1–8.

51. Ehlers, J.-E.; Rondan, N.G.; Huynh, L.K.; Pham, H.; Marks, M.; Truong, T.N., "Theoretical Study on Mechanisms of the Epoxy Amine Curing Reaction", *Macromolecules*. **2007**, 40, 4370–4377.

52. Chawla, K.K., Composite Materials: Science and Engineering, Springer, 2012.

53. Gonçalez, V.; Barcia, F.L.; Soares, B.G., "Composite materials based on modified epoxy resin and carbon fibre", *J. Brazilian Chem. Soc.* **2006**, 17, 1117–1123.

54. Iijima, M.; Tsutsumi, T.; Saito, M.; Tatami, J.; Moriya, T.; Kumada, T.; Izawa, H., "Simultaneous epoxy grafting on SiO2 nanoparticles during bead milling and their effects on the mechanical properties of epoxy-based composites", *Adv. Powder Technol.* **2019**, 30, 1782–1788.

55. Bulut, M.; Alsaadi, M.; Erkliğ, A., "A comparative study on the interlaminar shear strength of S-glass/epoxy composites containing borax, perlite and sewage sludge ash particles", *Mater. Res. Express*. **2019**, 6, 1–9.

56. Jafrey, D.D.; Krishnan, G.S.; Velmurugan, P., "Investigation on the characteristics of bamboo/jute reinforced hybrid epoxy polymer composites", *Mater. Res. Express*. **2019**, 6, 1–9.

57. Zhang, K.; Gu, Y.; Zhang, J.; Li, M.; Wang, S.; Zhang, Z., "Rapid curing vacuum-assisted resin infusion molding using silicone rubber sheet heater and the effect of

cooling process on the properties of carbon fiber/epoxy composites", *J. Compos. Mater.* **2016**, 50, 1837–1850.

58. Cripps, D., "Vacuum Bagging", *NetComposites.* **n.d.**, 1. https://netcomposites.com/guide-tools/guide/manufacturing/vacuum-bagging/.

59. Tzetzis, D.; Hogg, P.J., "Experimental and finite element analysis on the performanceof vacuum-assisted resin infused single scarf repairs", *Mater. Des.* **2008**, 29, 436–449.

60. Zhang, K.; Gu, Y.; Zhang, J.; Li, M.; Wang, S.; Zhang, Z., "Rapid curing vacuum-assisted resin infusion molding using silicone rubber sheet heater and the effect of cooling process on the properties of carbon fibre/epoxy composites", *J. Compos. Mater.* **2016**, 50, 1837–1850.

61. Gu, Y.; Tan, X.; Yang, Z.; Li, M.; Zhang, Z., "Hot compaction and mechanical properties of ramie fabric epoxycomposite fabricated using vacuum assisted resin infusion molding", *Mater. Des.* **2014**, 56, 852–861.

62. Zhang, K.; Gu, Y.; Li, M.; Zhang, Z., "Effect of rapid curing process on the properties of carbon fibre/epoxy composite fabricated using vacuum assisted resin infusion moulding", *Mater. Des.* **2014**, 54, 624–631.

63. Xia, C.; Shi, S.Q.; Cai, L., "Vacuum-assisted resin infusion (VARI) and hot pressing for CaCO3 nanoparticle treated kenaf fibre reinforced composites", *Compos. Part B.* **2015**, 78, 138–143.

64. Rydarowski, H.; Koziol, M., "Repeatability of glass fiber reinforced polymer laminate panels manufactured by hand lay-up and vacuum-assisted resin infusion", *J. Compos. Mater.* **2015**, 49, 573–586.

65. Rufai, O.; Gautam, M.; Potluri, P.; Gresil, M., "Optimisation of optical fibre using micro-braiding for structural health monitoring", *J. Intell. Mater. Syst. Struct.* **2019**, 30, 171–185.

66. Pan, X.; Liang, D.; Li, D., "Optical fiber sensor layer embedded in smart composite material and structure", *Smart Mater. Struct.* **2006**, 15, 1231–1234.

67. Hamouda, T.; Seyam, A.-F.; Peters, K., "Evaluation of the integrity of 3D orthogonal woven composites with embedded polymer optical fibers", *Compos. Part B.* **2015**, 78,

79–85.

68.   Barrias, A.; Casas, J.R.; Villalba, S., "A Review of Distributed Optical Fiber Sensors for Civil Engineering Applications", *Sensors*. **2016**, 16, 1–35.

69.   Kuang, K.S.C.; Cantwell, W.. J.; Scully, P.J., "An evaluation of a novel plastic optical fibre sensor for axial strain and bend measurements", *Meas. Sci. Technol.* **2002**, 13, 1523–1534.

70.   Meng, L.; Wang, L.; Hou, Y.; Yan, G., "A research on low modulus distributed fiber optical sensor for pavement material strain monitoring", *Sensors*. **2017**, 17, 1–13.

71.   Moon, C.K.; Lee, J.; Cho, H.H.; Kim, K.S., "Effect of Diameter and Surface Treatment of Fiber on Interfacial Shear Strength in Glass Fiber/Epoxy and HDPE", *J. Appl. Polym. Sci.* **1992**, 45, 443–450.

72.   Haspel, B.; Hoffmann, C.; Elsner, P.; Weidenmann, K.A., "Characterization of the interfacial shear strength of glass-fiber reinforced polymers made from novel RTM processes", *Int. J. Plast. Technol.* **2915**, 12, 333–346.

73.   Rajwin, A.J.; Giridev, V.R.; Renukadevi, M., "Effect of yarn twist on mechanical properties of glass fibre reinforced composite rods", *Indian J. Fibre Text. Res.* **2012**, 37, 343–346.

74.   Chandra, N.; Ghonem, H., "Interfacial mechanics of push-out tests: theory and experiments", *Compos. Part A*. **2001**, 32, 575–584.

75.   Godara, A.; Gorbatikh, L.; Warrier, A.; Rochez, O.; Mezzo, L.; Luizi, F.; van Vuure, A.W.; Lomov, S.V.; Verpoest, I., "Interfacial shear strength of a glass fiber/epoxy bonding in compositesmodified with carbon nanotubes", *Compos. Sci. Technol.* **2010**, 70, 1346–1352.

76.   Islam, M.R.; Isa, N.; Yahaya, A.N.; Beg, M.D.H.; Yunus, R.M., "Mechanical, interfacial, and fracture characteristics of poly (lactic acid) and Moringa oleifera fiber composites", *Adv. Polym. Technol.* **2017**, 1–9.

77.   Yang, L.; Thomason, J.L., "Interface strength in glass fibre–polypropylene measured using the fibre pull-out and microbond methods", *Compos. Part A*. **2010**, 41, 1077–1083.

78. Hoecker, F.; Karger-Kocsis, J., "Effects of crystallinity and supermolecular formations on the interfacial shear strength and adhesion in GF/PP composites", *Polym. Bull.* **1993**, 31, 707–714.

79. Favre, J.P.; Merienne, M.C., "Characterization of fibre/resin bonding in composites using a pull-out test", *J. Adhes. Adhes.* **1981**, 1, 311–316.

80. Chean, V.; Boumbimba, M.R.; El Abdi, R.; Sangleboeuf, J.C.; Casari, P.; Habti, D.M., "Experimental characterization of interfacial adhesion of an optical fiber embedded in a composite material", *Int. J. Adhes. Adhes.* **2013**, 41, 144–151.

81. Wang, H.; Wang, H.; Li, W.; Ren, D.; Yu, Y., "An improved microbond test method for determination of the interfacial shear strength between carbon fibers and epoxy resin", *Polym. Test.* **2013**, 32, 1460–1465.

82. Emery, I., Primary Structures of Fabrics, 1966.

83. "Lexicon: history of braiding", *Mayer Braidtech GmbH.* **n.d.,**. http://www.mayerbraid.de/lexicon/194_201.htm.

84. Bilisik, K., "Three-dimensional braiding for composites: A review", *Text. Res. J.* **2015**, 83, 1414–1436.

85. Fangueiro, R.; Soutinho, F., Textile structures, in: R. Fangueiro (Ed.), Fibrous Compos. Mater. Civ. Eng. Appl., Woodhead Publishing Limited, 2011: pp. 62–91.

86. McKenna, H.A.; Hearle, J.W.S.; O'Hear, N., Handbook of fibre rope technology, Woodhead Publishing Limited, 2004.

87. Ko, F.K.; Pastore, C.M.; Head, A.A., Atkins & Pearce Handbook of Industrial Braiding, Atkins and Pearce, 1989.

88. Dow, M.B.; Dexter, H.B., Development of Stitched, Braided and Woven Composite Structures in the ACT Program and at Langley Research Center (1985 to 1997) Summary and Bibliography, 1997.

89. Roy, S.S.; Potluri, P., Braiding: From Cordage to Composites, in: Text. Res. Conf., Dhaka, Bangladesh, 2016: pp. 1–4.

90. Branscomb, D.; Beale, D.; Broughton, R., "New Directions in Braiding", *J. Eng. Fibres Fabr.* **2013**, 8, 11–24.

91.   Ma, G.; Branscomb, D.J.; Beale, D.G., "Modeling of the tensioning system on a braiding machine carrier", *Mech. Mach. Theory*. **2012**, 47, 46–61.

92.   Freger, G.E.; Kestelman, V.N.; Freger, D.G., Braiding pultrusion technology : for advanced structural composites, 2005.

93.   Miravete, A., 3-D Textile Reinforcements in Composite Materials, Woodhead Publishing Limited, 1999.

94.   Tong, L.; Mouritz, A.P.; Bannister, M., 3D Fibre Reinforced Polymer Composites, Elsevier Science, 2002.

95.   Ayranci, C.; Carey, J., "2D braided composites: A review for stiffness critical applications", *Compos. Struct.* **2008**, 85, 43–58.

96.   Masters, J.E.; Naik, R.A.; Minguet, P.J., Effects of Preform Architecture on Modulus and Strength of 2-D Triaxially Braided Textile Composites, in: Mech. Compos. Symp., 1994: pp. 349–378.

97.   Lin, H.; Brown, L.P.; Long, A.C., "Modelling and Simulating Textile Structures using TexGen", *Adv. Mater. Res.* **2011**, 331, 44–47.

98.   Melenka, G.W.; Hunt, A.J.; Pastore, C.M.; Ko, F.K.; Carey, J.P., Advanced testing of braided composite materials, in: Handb. Adv. Braided Compos. Mater., 2017: pp. 155–204.

99.   Potluri, P.; Nawaz, S., Development in Braided Fabrics, in: Spec. Yarn Fabr. Struct., 2011: pp. 333–353.

100.   Dabiryan, H.; Johari, M.S.; Bakhtiyari, S.; Eskandari, E., "Analysis of the tensile behavior of tubular braids using energy method, Part II: experimental study", *J. Text. Inst.* **2017**, 1–6.

101.   Zhang, Q.; Beale, D.; Broughton, R.M., "Analysis of Circular Braiding Process, Part 1: Theoretical Investigation of Kinematics of the Circular Braiding Process", *J. Manuf. Sci. Eng.* **1999**, 121, 345–350.

102.   Tate, J.S.; Kelkar, A.D.; Whitcomb, J.D., "Effect of braid angle on fatigue performance of biaxial braided composites", *Int. J. Fatigue*. **2006**, 28, 1239–1247.

103.   Falzon, P.J.; Herszberg, I., "Mechanical Performance of 2-D Braided Carbon/Epoxy

Composites", *Compos. Sci. Technol.* **1998**, 58, 253–265.

104. Rosso, S. Del; Iannucci, L.; Curtis, P.T., "Experimental investigation of the mechanical properties of dry microbraids and microbraid reinforced polymer composites", *Compos. Struct.* **2015**, 125, 509–519.

105. Naik, R.A.; Ifju, P.G.; Masters, J.E., "Effect of Fibre Architecture Parameters on Deformation Fields and Elastic Moduli of 2-D Braided Composites", *J. Compos. Mater.* **1994**, 28, 656–681.

106. Birkefeld, K.; Röder, M.; Reden, T. von; Bulat, M.; Drechsler, K., "Characterization of Biaxial and Triaxial Braids: Fibre Architecture and Mechanical Properties", *Appl. Compos. Mater.* **2012**, 19, 259–273.

107. Omeroglu, S., "The Effect of Braiding Parameters on the Mechanical Properties of Braided Ropes", *Fibres &Textile East. Eur.* **2006**, 14, 53–57.

108. Charlebois, K.M.; Boukhili, R.; Zebdi, O.; Trochu, F., "Evaluation of the Physical and Mechanical Properties of Braided Fabrics and their Composites", *J. Reinf. Plast. Compos.* **2005**, 24, 1539–1554.

109. Chun, H.-J.; Shin, J.-Y.; Daniel, I.M., "Effects of material and geometric nonlinearities on the tensile and compressive behavior of composite materials with fibre waviness", *Compos. Sci. Technol.* **2001**, 61, 125–134.

110. Zhang, Q.; Beale, D.; Adanur, S.; Broughton, R.M.; Walker, R.P., "Structural Analysis of a Two-dimensional Braided Fabric", *J. Text. Inst.* **1997**, 88, 41–52.

111. Potluri, P.; Rawal, A.; Rivaldi, M.; Porat, I., "Geometrical modelling and control of a triaxial braiding machine for producing 3D preforms", *Compos. Part A*. **2003**, 34, 481–492.

112. Heieck, F.; Hermann, F.; Middendorf, P.; Schladitz, K., "Influence of the cover factor of 2D biaxial and triaxial braided carbon composites on their in-plane mechanical properties", *Compos. Struct.* **2017**, 163, 114–122.

113. Rebelo, R.; Vila, N.; Fangueiro, R.; Carvalho, S.; Rana, S., "Influence of design parameters on the mechanical behaviour and porosity of braided fibrous stents", *Mater. Des.* **2015**, 86, 237–247.

114. Lamb, G.E.R.; Costanza, P.; Miller, B., "Influences of Fibre Geometry on the Performance of Nonwoven Air Filters", *Text. Res. J.* **1975**, 452–463.

115. Farrar, C.R.; Worden, K., "An introduction to structural health monitoring", *Philos. Trans. R. Soc.* **2007**, 365, 303–315. doi:doi:10.1098/rsta.2006.1928.

116. Giurgiutiu, V., Structural health monitoring with piezoelectric wafer active sensors, 2014.

117. Pau, L., Failure Diagnosis and Performance Monitoring, Marcel Dekker, Inc., New York, 1981.

118. Worden, K.; Dulieu-Barton, J.M., "An overview of intelligent fault detection in systems and structures", *Struct. Heal. Monit.* **2004**, 3, 85–98.

119. Derriso, M.M.; Chang, F.-K., "Future Roles of Structural Sensing for Aerospace Applications", *Multifunct. Struct. Sensors Antennas*. **2006**, 5-1-5–12.

120. Fu, H.; Seno, A.H.; Khodaei, Z.S.; Aliabadi, M.H.F., Design of a Wireless Passive Sensing System for Impact Detection of Aerospace Composite Structures, in: 5th IEEE Int. Work. Metrol. Aerosp., Rome, Italy, 2018: pp. 585–589.

121. Housner, G.W.; Bergman, L.A.; Caughey, T.K.; Chassiakos, A.G.; Claus, R.O.; Masri, S.F.; Skelton, R.E.; Soong, T.T.; Spencer, B.F.; Yao, J.T.P., "Structural Control: Past, Present, and Future", *J. Eng. Mech.* **1997**, 123, 897–971.

122. Cantero-Chinchilla, S.; Chiachío, J.; Chiachío, M.; Chronopoulos, D., "A robust Bayesian methodology for damage localization in plate-like structures using ultrasonic guided-waves", *Mech. Syst. Signal Process.* **2019**, 122, 192–205.

123. Wang, J.; Shen, Y., "An enhanced Lamb wave virtual time reversal technique for damage detection with transducer transfer function compensation", *Smart Mater. Struct.* **2019**, 28, 1–16.

124. Zhao, G.; Wang, B.; Wang, T.; Hao, W.; Luo, Y., "Detection and monitoring of delamination in composite laminates using ultrasonic guided wave", *Compos. Struct.* **2019**, 225, 1–12.

125. Werneck, M.M.; Allil, R.C.S.B.; Ribeiro, B.A.; Nazaré, F.V.B., A Guide to Fiber Bragg Grating Sensors, in: Curr. Trends Short- Long-Period Fiber Gratings, 2013: pp.

1–24.

126. Lee, D.G.; Mitrovic, M.; Stewart, A.; Garman, G., "Characterization of fibre optic sensors for structural health monitoring", *J. Compos. Mater.* **2002**, 36, 1349–1366.

127. Casas, J.R.; Cruz, P.J.S., "Fiber optic sensors for bridge monitoring", *J. Bridg. Eng.* **2003**, 8, 362–372.

128. Glisic, B., Distributed fiber optic sensing technologies and applications-an overview, 2013.

129. Samiec, D., "Distributed fibre-optic temperature and strain measurement with extremely high spatial resolution", *Opt. Metrol.* **2012**,.

130. Hayes, J., "Fibre is tougher than you think", *Electr. Contract.* **n.d.**,. https://www.ecmag.com/section/systems/fiber-tougher-you-think.

131. Yoshino, T.; Kurosawa, Ki.; Itoh, K.; Ose, T., "Fibre-Optic Fabry-Perot Interferometer and Its Sensor Applications", *IEEE Trans. Microw. Theory Tech.* **1982**, MTT-30, 1612–1621.

132. Lee, B.H.; Kim, Y.H.; Park, K.S.; Eom, J.B.; Kim, M.J.; Rho, B.S.; Choi, H.Y., "Interferometric Fiber Optic Sensors", *Sensors.* **2012**, 12, 2467–2486.

133. Rogers, A., "Review Article-Distributed optical-fibre sensing", *Meas. Sci. Technol.* **1999**, R75–R99.

134. Güemes, A.; Fernandez-Lopez, A.; Fernandez, P., Damage detection in composite structures from fibre optic distributed strain measurements, in: 7th Eur. Work. Struct. Heal. Monit., Nantes, France, 2014: pp. 528–535.

135. Güemes, A.; Fernandez-Lopez, A.; Soller, B., "Optical fiber distributed sensing - physical principles and applications", *Struct. Heal. Monit.* **2010**, 9, 233–245.

136. Bos, J.; Klein, J.; Froggatt, M.; Sanborn, E.; Gifford, D., Fiber optic strain, temperature and shape sensing via OFDR for ground, air and space applications, in: Proc. Vol. 8876, Nanophotonics Macrophotonics Sp. Environ. VII; 887614, San Diego, California, 2013. doi:10.1117/12.2025711.

137. Vaezi-Nejad, S.M., Selected topics in advanced solid state and fibre optic sensors, 2000.

138. Glisic, B.; Inaudi, D., Fibre Optic Methods for Structural Health Monitoring, John Wiley & Sons Inc, Chichester, UK, 2007.

139. Ding, Z.; Wang, C.; Liu, K.; Jiang, J.; Yang, D.; Pan, G.; Pu, Z.; Liu, T., "Distributed optical fiber sensors based on optical frequency domain reflectometry: A review", *Sensors*. **2018**, 18, 1–31.

140. Bergman, A.; Davidi, R.; Shalev, I.A.; Ovadia, L.; Langer, T.; Tur, M., "Increasing the measurement dynamic range of rayleigh-Based OFDR interrogator using an amplifying add-on module", *IEEE Photonics Technol. Lett.* **2016**, 28, 2621–2624.

141. Khondker, A.; Lakhani2, S., "X-Ray Diffraction: A Comprehensive Explanation for Multipurpose Research", *Int. J. Interdiscip. Res. Innov.* **2015**, 3, 60–64.

142. Meltz, G.; Morey, W.W.; Glenn, W.H., "Formation of Bragg gratings in optical fibers by a transverse holographic method", *Opt. Lett.* **1989**, 14, 823–825.

143. Mukhopadhyay, S.C., New Developments in Sensing Technology for Structural Health Monitoring, Springer, 2011.

144. Cai, J.; Qiu, L.; Yuan, S.; Shi, L.; Liu, P.; Liang, D., Structural Health Monitoring for Composite Materials, in: Compos. Their Appl., 2012: pp. 37–60.

145. Goossens, S.; Pauw, B. De; Geernaert, T.; Salmanpour, M.S.; Khodaei, Z.S.; Karachalios, E.; Saenz-Castillo, D.; Thienpont, H.; Berghmans, F., "Aerospace-grade surface mounted optical fibre strain sensor for structural health monitoring on composite structures evaluated against in-flight conditions", *Smart Mater. Struct.* **2019**, 28, 1–13.

146. Méndez, A.; Graver, T., Overview of fiber optic sensors for NDT applications, in: IV NDT Panam. Conf., Buenos Aires, 2007: pp. 1–11.

147. Mulle, M.; Wafai, H.; Yudhanto, A.; Lubineau, G.; Yaldiz, R.; Schijve, W.; Verghese, N., "Process monitoring of glass reinforced polypropylene laminates using fibre Bragg gratings", *Compos. Sci. Technol.* **2016**, 123, 143–150.

148. Guemes, J.A.; M., M.J., "Response of Bragg grating fiber-optic sensors when embedded in composite laminates", *Compos. Sci. Technol.* **2002**, 62, 959–966.

149. Okabe, Y.; Tsuji, R.; Takeda, N., "Application of chirped fiber Bragg grating sensor

for identification of crack location in composites", *Compos. Part A*. **2004**, 35, 59–65.

150. Yashiro, S.; Takeda, N.; Okabe, T.; Sekine, H., "A new approach to predicting multiple damage states in composite laminates with embedded FBG sensors", *Compos. Sci. Technol.* **2005**, 65, 659–667.

151. Lee, D.C.; Lee, J.J.; Yun, S.J., "The mechanical characteristics of smart composite structures with embedded optical fiber sensors", *Compos. Struct.* **1995**, 32, 39–50.

152. Hufenbach, W.; Adam, F.; Fischer, W.J.; Kunadt, A.; Weck, D., "Effect of integrated sensor networks on the mechanical behaviour of textile -reinforced thermoplastics", *Procedia Mater. Sci.* **2013**, 2, 153–159.

153. Javdanitehran, M.; Hoffmann, R.; Groh, J.; Vossiek, M.; Ziegmann, G., "Effect of embedded printed circuit board (PCB) sensors on the mechanical behavior of glass fibre reinforced polymer (GFRP) structures", *Smart Mater. Struct.* **2016**, 25, 1–11.

154. Wei, C.Y.; James, S.W.; Ye, C.C.; Dykes, N.D.; Tatam, R.P.; Irving, P.E., Strain capability of optical fibre bragg grating sensing in composite smart structures, in: Int. Conf. Compos. Mater., Paris, France, 1999: pp. 1–10.

155. Roberts, S.S.J.; Davidson, R., "Mechanical Properties Of Composite Material Containing Fiber Optics Sensors", *Fiber Opt. Smart Struct. Ski. IV*. **1991**, 1588, 326–341.

156. Silva, J.M.A.; Deveza, T.C.; Silva, A.P.; Ferreira, J.A.M., "Mechanical Characterization of Composites with Embedded Optical Fibers", *J. Compos. Mater.* **2005**, 39, 1261–1281.

157. Poggetti, I.; Dyson, J.; Sanchez, D.M.; Albertini, G.; Soutis, C.; Gresil, M.; Corinaldesi, V., "Distributed internal strain measurement of the fluid-solid state coefficients of thermal expansion below the glass transition temperature during a composite manufacturing process", *J. Compos. Mater.* **2018**, 52, 3053–3084.

158. Huang, C.; Zeng, X.; Arcand, A.; Lee-Sullivan, P., "Simultaneous temperature and strain monitoring of composite cure using a Brillouin-Scattering-Based distributed fiber optic sensor", *Smart Struct. Mater.* **2001**, 4328, 70–78.

159. Woerdeman, D.L.; Spoerre, J.K.; Flynn, K.M.; Parnas, R.S., "Cure monitoring of liquid composite molding process using fibre optics sensors", *Polym. Compos.* **1997**,

18, 133–150.

160. He, Y.; Li, Y.; Li, N.; Hao, X., "Online monitoring method of degree of cure during non-isothermal microwave curing process", *Mater. Res. Express*. **2018**, 5, 1–10.

161. Sampath, U.; Kim, D.; Kim, H.; Song, M., "Fiber-optic miniature sensor for in situ temperature monitoring of curing composite material", *J. Mordern Opt.* **2018**, 65, 781–787.

162. Crasto, S.A.; Kim, R.Y., "In Situ Monitoring of Residual Strain Development During Composite Cure", *Polym. Compos.* **2002**, 23, 454–463.

163. Kher, S.; Saxena, M.K., Distributed, advanced fibre optic sensors, in: Appl. Opt. Fibers Sens., 2019: pp. 1–25.

164. Kang, H.-K.; Kang, D.-H.; Bang, H.-J.; Hong, C.-S.; Kim, C.-G., "Cure monitoring of composite laminates using fiber optic sensors", *Smart Mater. Struct.* **2002**, 11, 279–287.

165. Leng, J.S.; Asundi, A., "Real-time cure monitoring of smart composite materials using extrinsic Fabry-Perot interferometer and fiber Bragg grating sensors", *Smart Mater. Struct.* **2002**, 11, 249–255.

166. Kang, H.-K.; Kang, D.-H.; Hong, C.-S.; Kim, C.-G., "Simultaneous monitoring of strain and temperature during and after cure of unsymmetric composite laminate using fibre-optic sensors", *Smart Mater. Struct.* **2003**, 12, 29–35.

167. Hsieh, M.-Y.; Chiang, C.-C.; Lin, C.-L.; Fang, B.-L., Curing residual strain monitoring in different layer of Gr/Epoxy laminated composites using embedded optical fiber Bragg grating sensors, in: Third Int. Conf. Smart Mater. Nanotechnol. Eng., 2012: pp. 840919–8.

168. Ifju, P.G.; Niu, X.; Kilday, B.C.; Liu, S.C.; Ettinger, S.M., "Residual strain measurement in composites using the cure-referencing method", *Exp. Mech.* **2000**, 40, 22–30.

169. Minakuchi, S., "In situ characterization of direction-dependent cure-induced shrinkage in thermoset composite laminates with fiber-optic sensors embedded in through-thickness and in-plane directions", *J. Compos. Mater.* **2015**, 49, 1021–1034.

170. Chehura, E.; Skordos, A.A.; Ye, C.-C.; James, S.W.; Partridge, I.K.; Tatam, R.P., "Strain development in curing epoxy resin and glass fibre/epoxy composites monitored by fibre Bragg grating sensors in birefringent optical fibre", *Smart Mater. Struct.* **2005**, 14, 354–362.

171. Menendez, J.M.; Guemes, J.A., Bragg-grating-based multiaxial strain sensing: its application to residual strain measurement in composite laminates, in: Smart Struct. Mater. 2000, Newport Beach, CA, 2000: pp. 271–281.

172. Lawrence, C.M.; Nelson, D. V.; Spingarn, J.R.; Bennett, T.E., Measurement of process-induced strains in composite materials using embedded fibre optic sensors, in: Proc. SPIE 2718, Smart Struct. Mater. 1996 Smart Sensing, Process. Instrum., 1996: pp. 60–68.

173. Montanini, R.; D'Acquisto, L., "Simultaneous measurement of temperature and strain in glass fiber/epoxy composites by embedded fiber optic sensors: I. Cure monitoring", *Smart Mater. Struct.* **2007**, 16, 1718–1726.

174. Ussorio, M.; Wang, H.; Ogin, S.L.; Thorne, A.M.; Reed, G.T.; Tjin, S.C.; Suresh, R., "Modifications to FBG sensor spectra due to matrix cracking in a GFRP composite", *Constr. Build. Mater.* **2006**, 10, 111–118.

175. Okabe, Y.; Yashiro, S.; Kosaka, T.; Takeda, N., "Detection of transverse cracks in CFRP composites using embedded fibrE Bragg grating sensors", *Smart Mater. Struct.* **2000**, 9, 832–838.

176. Anastasi, R.F.; Lopatin, C., "Application of a Fiber Optic Distributed Strain Sensor system to woven E-Glass Composite", *NASA Langley Tech. Rep. Serv.* **2001**,.

177. Huntsman, Advanced materials Araldite LY 564/Aradur 2954, 2011.

178. AGY, 493 S-2 Glass Yarn, 2013.

179. DSM, "Ultra High Molecular Weight Polyethylene Fiber from DSM Dyneema", *Tech. DataSheet*. **2016**, 49,. https://issuu.com/eurofibers/docs/name8f0d44.

180. Challenges, R., "449 S-2 Glass ® Roving High-Strength Solutions for Your Toughest Reinforcement Challenges", **2013**,. www.agy.com.

181. ASTMD2256/D2256M, Standard test method for tensile properties of yarns by the

single-strand method, 2015.

182. ASTMD7264/D7264M, Standard test method for flexural properties of polymer matrix composite materials., 2015.

183. Wang, H.; Tian, G.; Wang, H.; Li, W.; Yu, Y., "Pull-out method for direct measuring the interfacial shear strength between short plant fibers and thermoplastic polymer composites (TPC)", *Holzforschung*. **2014**, 68, 17–21.

184. Rong, M.Z.; Zhang, M.Q.; Liu, Y.; Yang, G.C.; Zeng, H.M., "The effect of fiber treatment on the mechanical properties of unidirectional sisal-reinforced epoxy composites", *Compos. Sci. Technol.* **2001**, 61, 1437–1447.

185. ASTM Standard D6272, Standard test method for flexural properties of unreinforced and reinforced plastics and electrical insulating materials by four-point bending, 2017. doi:10.1520/D6272-17E01.

186. Hasiotis, T.; Badogiannis, E.; Tsouvalis, N.G., "Application of Ultrasonic C-Scan Techniques for Tracing Defects in Laminated Composite Materials", *J. Mech. Eng.* **2011**, 57, 192–203.

187. ASTMD3171-15, "Standard Test Methods for Constituent Content of Composite Materials", *ASTM Int.* **2015**, 1–11. doi:10.1520/D3529M-10.2.

188. Gibson, R., Principles of Composite Material Mechanics, 4th ed., Boca Raton, 2016.

189. Velmurugan, R.; Manikandan, V., "No Title", *Indian J. Eng. Mater. Sci.* **2005**, 12, 563–570.

190. ASTM, "Standard Test Methods for Linear Density of Textile Fibers", *D1577-07*. **2018**,.

191. Xiao, X.; Kia, H.G.; Gong, X.-J., "Strength prediction of a triaxially braided composite", *Compos. Part A*. **2011**, 42, 1000–1006.

192. Song, S.; Waas, A.M.; Shahwan, K.W.; Faruque, O.; Xiao, X., "Compression response, strength and post-peak response of an axial fibre reinforced tow", *Int. J. Mech. Sci.* **2009**, 51, 491–499.

193. Rawal, A.; Sibal, A.; Saraswat, H., "Tensile behaviour of regular triaxial braided structures", *Mech. Mater.* **2015**, 91, 277–289.

194. Rawal, A.; Kumar, R.; Saraswat, H., "Tensile mechanics of braided sutures", *Text. Res. J.* **2012**, 82, 1703–1710.

195. Du, J.; He, Z., "Sensitivity enhanced strain and temperature measurements based on FBG and frequency chirp magnification", *Opt. Express*. **2013**, 21,.

196. Tosi, D., "Review and Analysis of Peak Tracking Techniques for Fiber Bragg Grating Sensors", *Sensors*. **2017**, 17, 1–35.

197. Hafizi, Z.M.; Epaarachchi, J., Dynamic Response and Signal to Noise Ratio Investigation of NIR-FBG Dynamic Sensing System for Monitoring Thinwalled Composite Plate, in: 3rd Int. Conf. Mech. Eng. Res. (ICMER 2015), IOP Publishing, 2015: pp. 1–11.

198. Antunes, P.; Domingues, F.; Granada, M.; André, P., Mechanical Properties of Optical Fibers, in: Opt. Fiber Technol., 2012: pp. 537–551.

199. Ataş, A.; Gautam, M.; Soutis, C.; Potluri, P., "Bolted Joints in Three Axially Braided Carbon Fibre/Epoxy Textile Composites with Moulded-in and Drilled Fastener Holes", *Appl. Compos. Mater.* **2017**, 24,.

200. Gautam, M.; Katnam, K.B.; Potluri, P.; Jha, C.; Latto, J.; Dodds, N., "Hybrid composite tensile armour wires in flexible risers: A multi-scale model", *Compos. Struct.* **2017**, 162, 13–27.

201. Gautam, M.; Potluri, P.; Katnam, K.B.; Jha, V.; Leyland, J.; Latto, J.; Dodds, N., "Hybrid composite wires for tensile armours in flexible risers:Manufacturing and mechanical characterisation", *Compos. Struct.* **2016**, 150, 73–83.

202. Gautam, M.; Potluri, P.; Ogin, S.; Jain, P., Necking Behaviour of Flattened Tubular Braided Composites, in: 20th Int. Conf. Compos. Mater., Copenhagen, Denmark, 2015: pp. 1–11.

203. PriceEngineering, "Fibre Reinforced Polymers Characteristics and Behaviors", **n.d.**,. http://www.build-on-prince.com/fiber-reinforced-polymers.html#sthash.HDf1AVJd.gt6WJUOJ.dpbs.

204. Desarmot, G.; Favre, J.P., "Advances in Pull-Out Testing and Data Analysis", *Compos. Sci. Technol.* **1991**, 42, 151–187.

205. Miller, B.; Gaur, U.; Hirt, D.E., "Measurement and mechanical aspects of the microbond pull-out technique for obtaining fiber/resin interfacial shear strength", *Compos. Sci. Technol.* **1991**, 42, 207–219.

206. Mader, E.; Freitag, K.H., "Interface properties and their influence on short fibre composites", *Composites.* **1990**, 21, 397–402.

207. Thomason, J.L.; Schoolenberg, G.E., "An investigation of glass fibre/polypropylene interface strength and its effect on composite properties", *Composites.* **1994**, 25, 197–203.

208. Gresil, M.; Poohsai, A.; Chandarana, N., "Guided wave propagation and damage detection in composite pipes using piezoelectric sensors", *Procedia Eng.* **2017**, 188, 148–155.

209. Qing, X.; Kumar, A.; Zhang, C.; Gonzalez, I.F.; Guo, G.; Chang, F.-K., "A hybrid piezoelectric/fibre optic diagnostic system for structural health monitoring", *Smart Mater. Struct.* **2005**, 14, 98–103.

210. Güemes, A.; Fernández-López; Soller, B., "Optical fiber distributed sensing – physical principles and applications", *Struct. Heal. Monit.* **2010**, 9, 233–245. doi:10.1177/1475921710365263.

211. Lau, K.; Chan, C.; Zhou, L.; Jin, W., "Strain monitoring in composite-strengthened concrete structures using optical fibre sensors", *Compos. Part B.* **2001**, 32, 33–45.

212. Muller, A.; Soutis, C.; Gresil, M., "Image reconstruction and characterisation of defects in a carbon fibre/epoxy composite monitored with guided waves", *Smart Mater. Struct.* **2019**, 28, 1–21.

213. Philibert, M.; Soutis, C.; Gresil, M.; Yao, K., "Damage Detection in a Composite T-Joint Using Guided Lamb Waves", *Aerospace.* **2018**, 5, 1–13.

214. LUNA, ODiSI-B Optical Distributed Sensor Interrogator, 2013.

215. LUNA, Distributed Fiber Optic Sensing: Temperature Compensation of Strain Measurement, 2014.

216. LUNA, User's Guide / ODiSI-B, 2007.

217. Barrias, A.; Casas, R.J.; Villalba, S., "Embedded distributed optical fiber sensors in

reinforced concrete structures—A case study", *Sensors*. **2018**, 18, 1–22.

218. Błażejewski, W.; Gąsior, P.; Kaleta, J., Application of optical fibre sensors to measuring the mechanical properties of composite materials and structures, in: Adv. Compos. Mater. Ecodesign Anal., 2011: pp. 221–246.

219. Wang, C.; Hu, Q.; Lu, Q., "Research on a Novel Low Modulus OFBG Strain Sensor for Pavement Monitoring", *Sensors*. **2012**, 12, 10001–10013.

220. Roy, S.S.; Zou, W.; Potluri, P., Influence of Braid Carrier Tension on Carbon Fibre Braided Preforms, in: Recent Dev. Braid. Narrow Weav., 2016: pp. 91–102.

221. Banerjee, A.; Sun, L.; Mantell, S.C.; Cohen, D., "Model and experimental study of fibre motion in wet filament winding", *Compos. Part A*. **1998**, 29A, 251–263.

222. Sante, R. Di; Donati, L., "Strain monitoring with embedded Fiber Bragg Gratings in advanced composite structures for nautical applications", *Measurement*. **2013**, 46, 2118–2126.

223. Endruweit, A.; Long, A.C., "A model for the in-plane permeability of triaxially braided reinforcements", *Compos. Part A*. **2011**, 42, 165–172.

224. Selezneva, M.; Poon, C.; Nakai, A.; Gu, X.; Behdinan, Z.; Behdinan, K.; Kulisek, V., Manufacturing and flexural testing of composite braided hockey sticks with embedded fibre optic sensors, in: Int. Conf. Compos. Mater., Edinburgh, United Kingdom, 2009: pp. 1–11.

225. Zhang, Q.; Chang, X.; Zhang, Y.; Zhang, L.; Zhang, X., "Monitoring of the carbon fibre wound composites curing process based on FBG sensors", *IEICE Electron. Express*. **2018**, 15, 1–9.

226. de Oliveira, R.; Lavanchy, S.; Chatton, R.; Costantini, D.; Michaud, V.; Salathé, R.; Månson, J.-A.E., "Experimental investigation of the effect of the mould thermal expansion on the development of internal stresses during carbon fibre composite processing", *Compos. Part A*. **2008**, 39, 1083–1090.

227. Antonucci, V.; Cusano, A.; Giordano, M.; Nasser, J.; Nicolais, L., "Cure-induced residual strain build-up in a thermoset resin", *Compos. Part A*. **2006**, 37, 592–601.

228. Parlevliet, P.P.; Bersee, H.E.N.; Beukers, A., "Measurement of (post-)curing strain

development with fibre Bragg gratings", *Polym. Test.* **2010**, 29,.

229.   FRCIndustries, Fibre tensile strength test monofilament Polypropylene fibres, 2001.

Appendix

Appendix 1A: Micro-braiding with monofilament yarn

A 46 dTex monofilament Polypropylene (PP) yarn of filament diameter 80 microns and density of 0.91 g/cm^3 was initially used to micro-braid an optical fibre. Figure 1A.1 shows a sample of an MBOF manufactured with PP. During manufacturing with PP yarn, challenges were encountered due to the low strength of PP [229]; continuous breakage was experienced when the braiding yarn was in tension. The take-up speed and machine speed was extremely slow to prevent the braiding yarn from breaking during the micro-braiding process, and this also led to a slower production rate.

From the micrographic image of the MBOF, it can be seen that the braiding yarn does not fully cover the optical fibre. Only 40% coverage was achieved using PP monofilament, which indicates a very low coverage on the optical fibre.
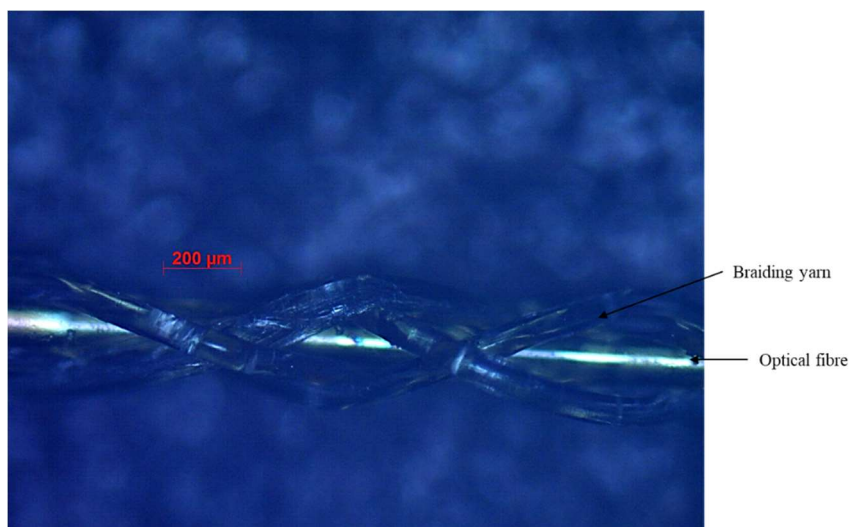
Figure 1A.1. Micrograph of micro-braided optical fibre (MBOF) using monofilament polypropylene

Appendix 2A: Optical image of embedded composite panel

Optical microscopy of the cross-section of composite embedded with OF and MBOF were taken using an Axio-Zeiss optical microscope. A cross-section of the composite sample was

cut using a diamond cutter; the cut out was then mounted in the pot using a mould ring. A mixture of room temperature cure Araldite resin/Araldite hardener was used to cast the specimen shown in Figure 2A.1.

Figure 2A 4A.1. Composite specimen held in resin pot

The specimen was ground by starting with a low grit (aggressive) silicon carbide (SiC) abrasive paper to a high grit paper (finer). Grinding commenced with 120 grit SiC paper. This grade of abrasive paper was used to remove excess resin from the surface of the sample without damaging it as well. During the grinding process, water was used as a lubricant to cool down the sample and remove scraps. The grit size of the abrasive paper increased from P-240, P-400 and P-1200. Water was used as a lubricant during grinding and also to remove debris. The higher the grit size, the more it reduces the scratches on the surface of the sample for easy polishing. To achieve an excellent surface finish, sample polishing was carried out using a micro cloth and 0.05 µ colloidal silica. The polished samples were dried in an oven to remove moisture before observing the optical microscope. Figure 2A.2 and 2A.3 shows the microscopic images of the composite embedded with OF and MBOF. Resin pocket can be seen around the cross-section of the MBOF compared to the OF. Figure 2A. (4-8) shows the sample after grinding and polishing.
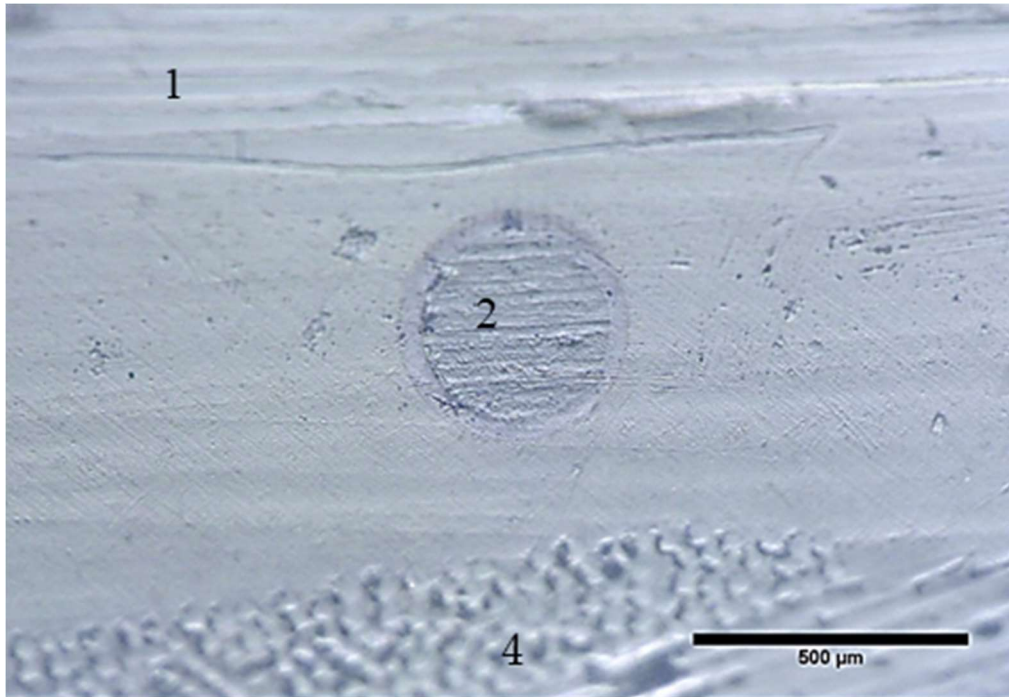
Figure 2A.2. Cross-section of embedded Conventional optical fibre (OF)
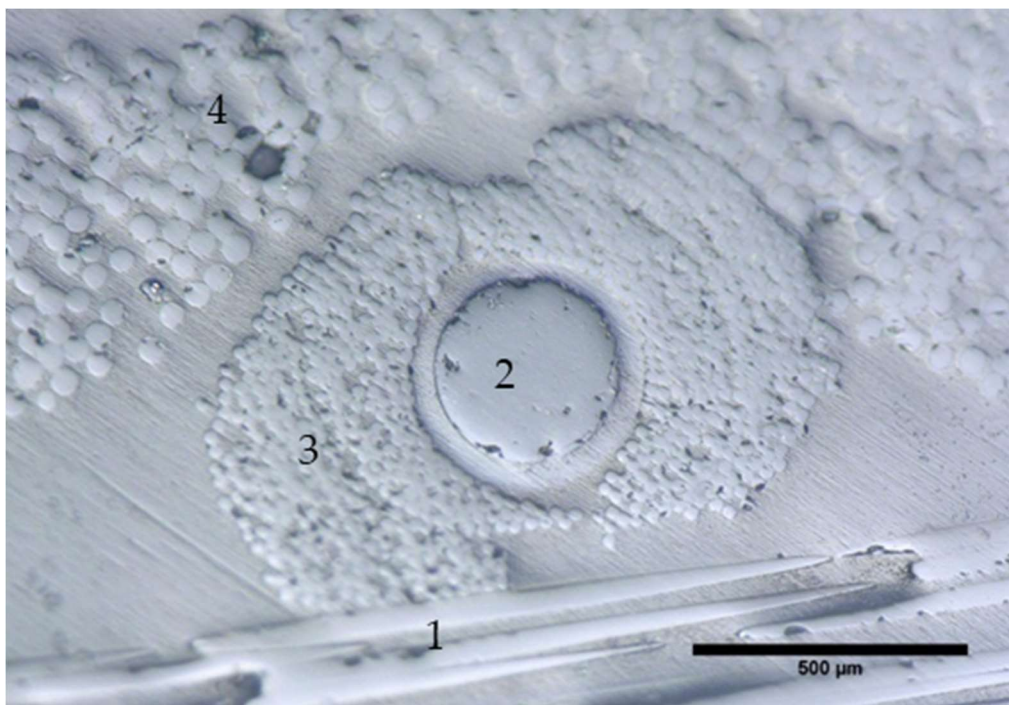

Figure 2A.3. Cross-section of embedded Micro-braided optical fibre (MBOF): (1) longitudinal glass fibre, (2) OF embedded between layers of glass fibre, (3) braiding tows and (4) transverse glass fibre

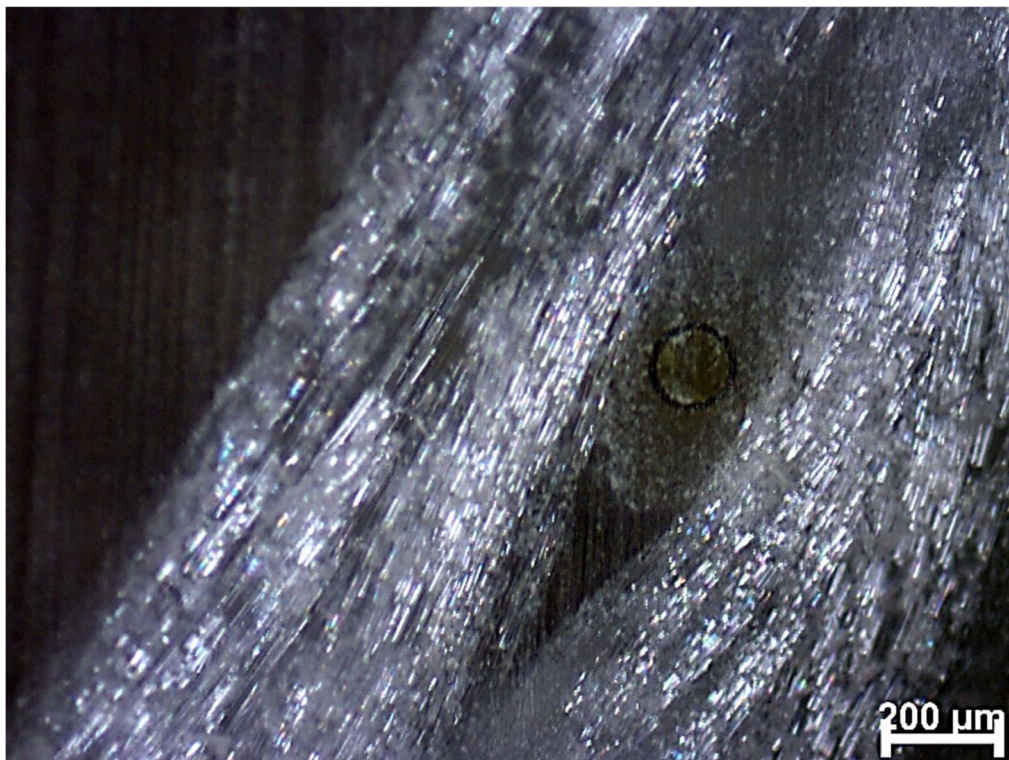Figure 2A.4. Cross-section of sample ground with grit size P-120 abrasive paper

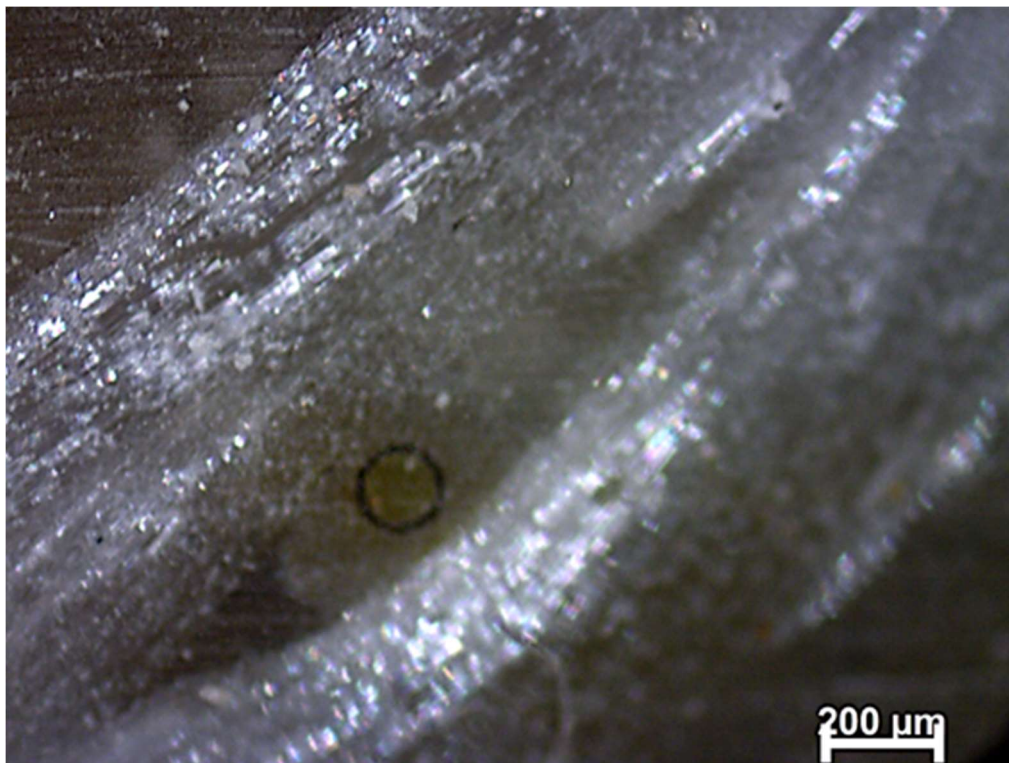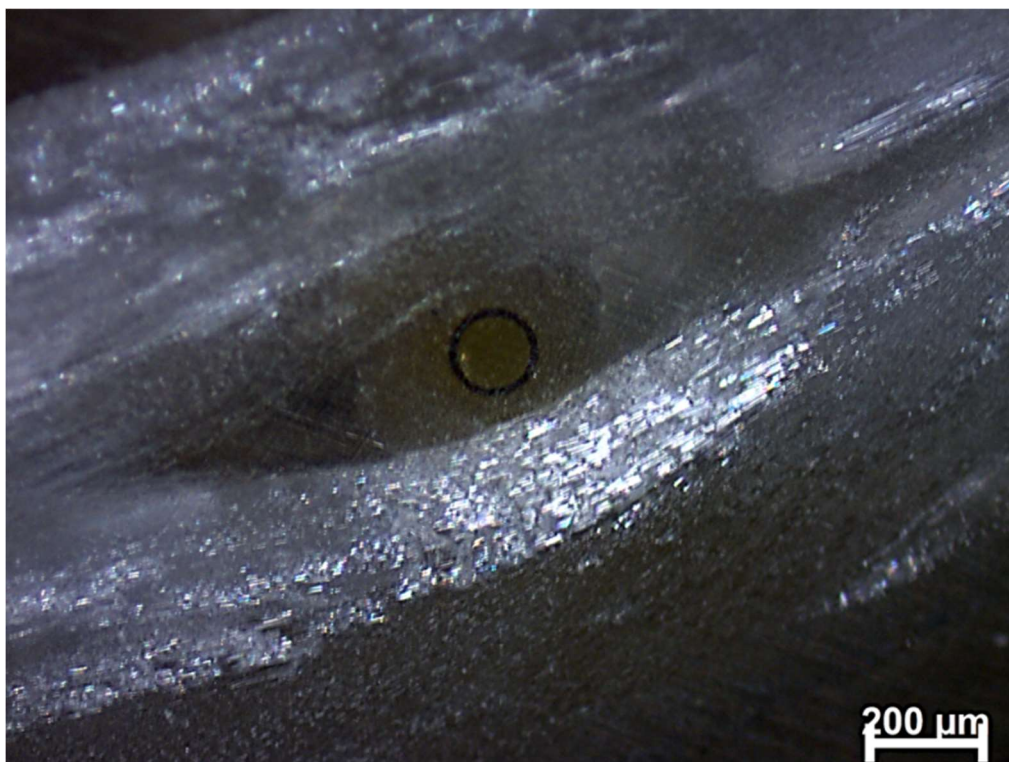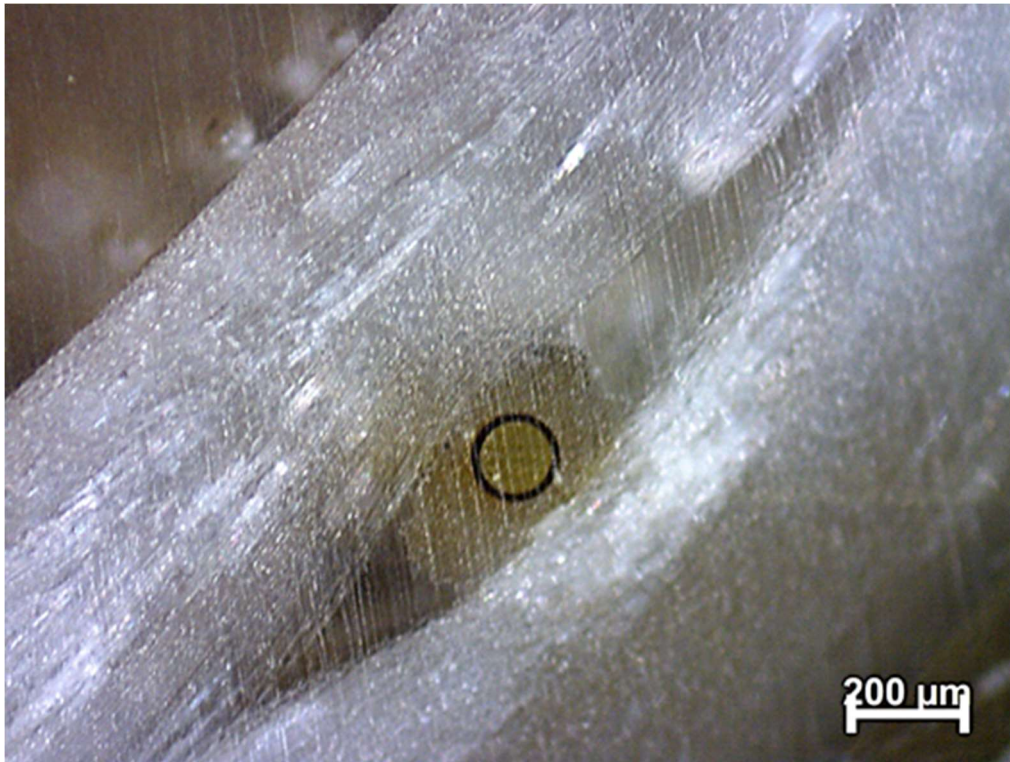Figure 2A.5 Cross-section of sample ground with grit size P-240 abrasive paper

Figure 2A.6. Cross section of sample grinded with grit size P-400 abrasive paper

Figure 2A.7 Cross-section of sample ground with grit size P-1200 abrasive paper

Figure 2A.8 Cross-section of the polished sample

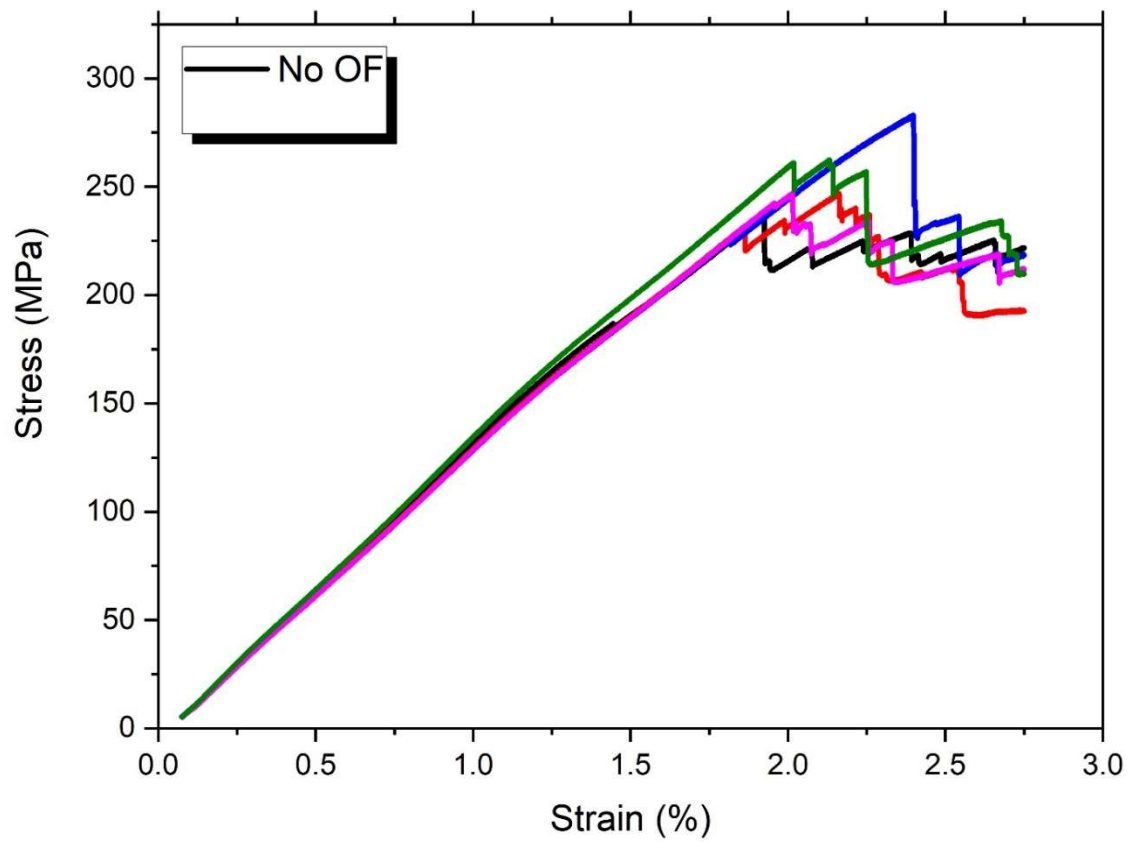**Appendix 3A: Stress vs Strain curve of composite laminate subjected to 3-point bending test**

Figure 3A. 1. Stress-strain curve of the composite panel with no embedded optical fibre (No OF)
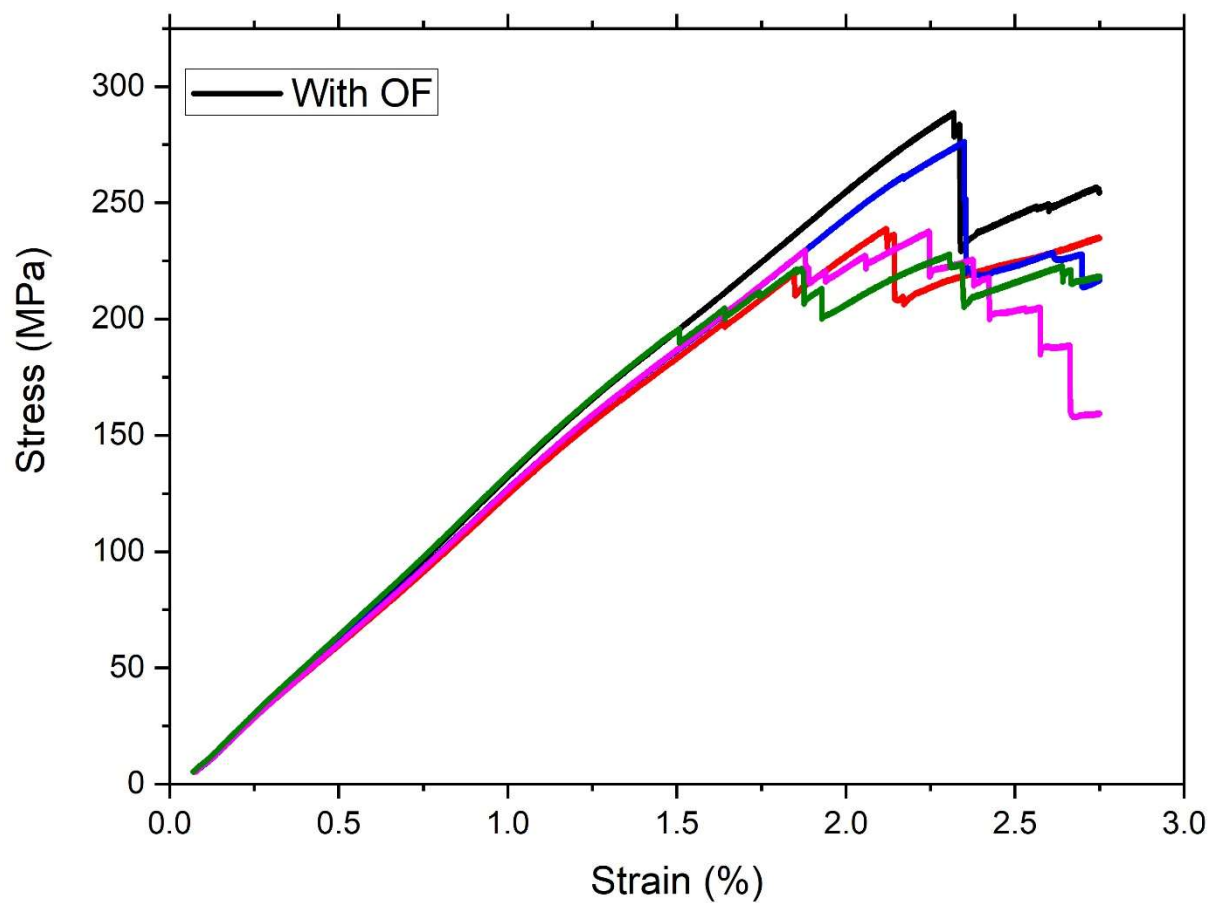
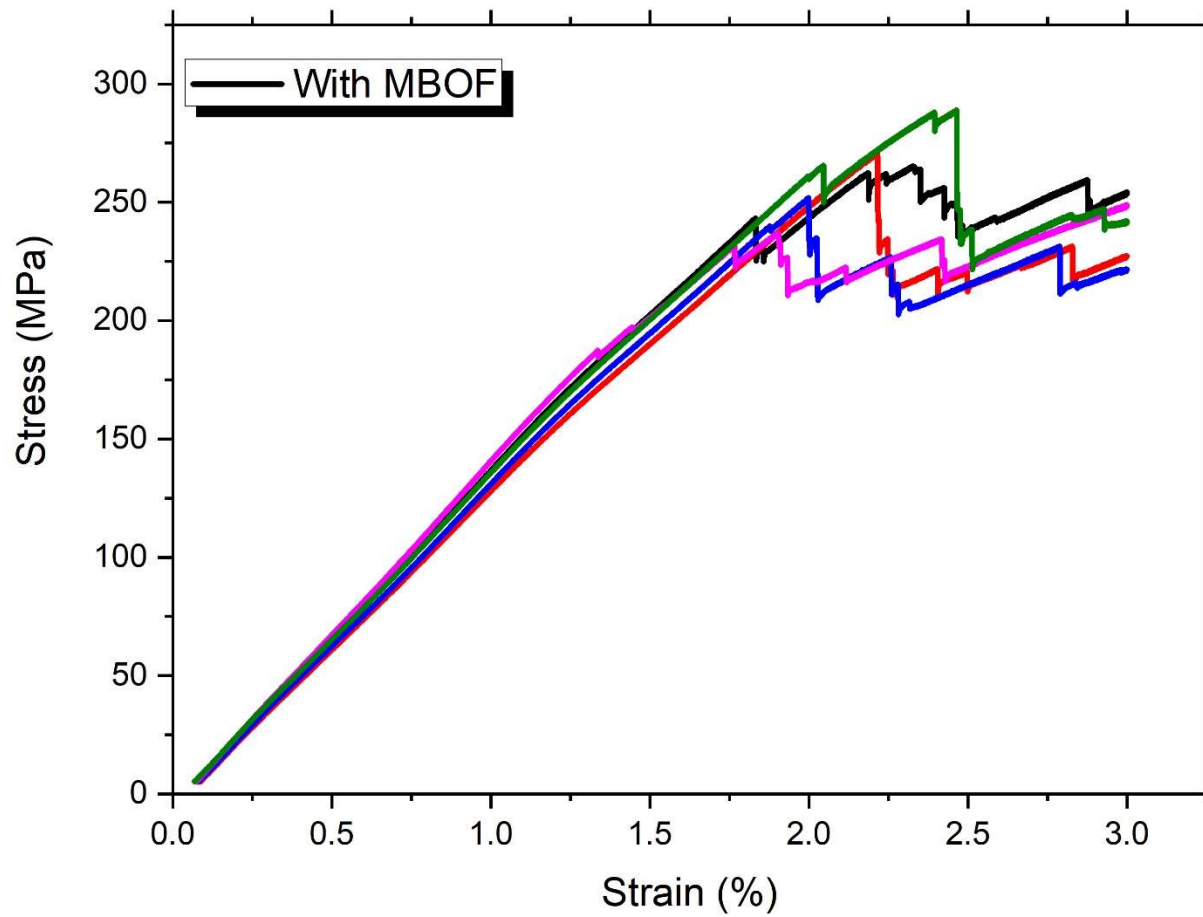Figure 3A. 2. Stress-strain curve of composite panel embedded with conventional optical fibre (OF)

Figure 3A. 3. Stress-strain curve of composite panel embedded with Micro-braided optical fibre (MBOF)

Appendix 4A: Distortion in reflection spectrum

The extent of distortion at the end of braiding was determined by measuring the FWHM for both the OF and MBOF as shown in Figure 4A.1 and 2. It is observed that the FWHM of the OF was 22% higher than the MBOF. The higher FWHM observed in the OF could be due to the non-uniformly strained gratings that led to the distortion of the reflection spectrum because of the exposure of the optical fibre. However, the lower value of FWHM recorded in the MBOF shows that the protective effect the braiding yarn has on the optical fibre. This reduced the magnitude of distortion caused by the interlacement of the braiding yarn. Takeda et al. [22] have also reported the distortion in peak due to non-uniform strain. A right-hand shift in the reflection spectrum was experienced due to external tension from the mandrel.
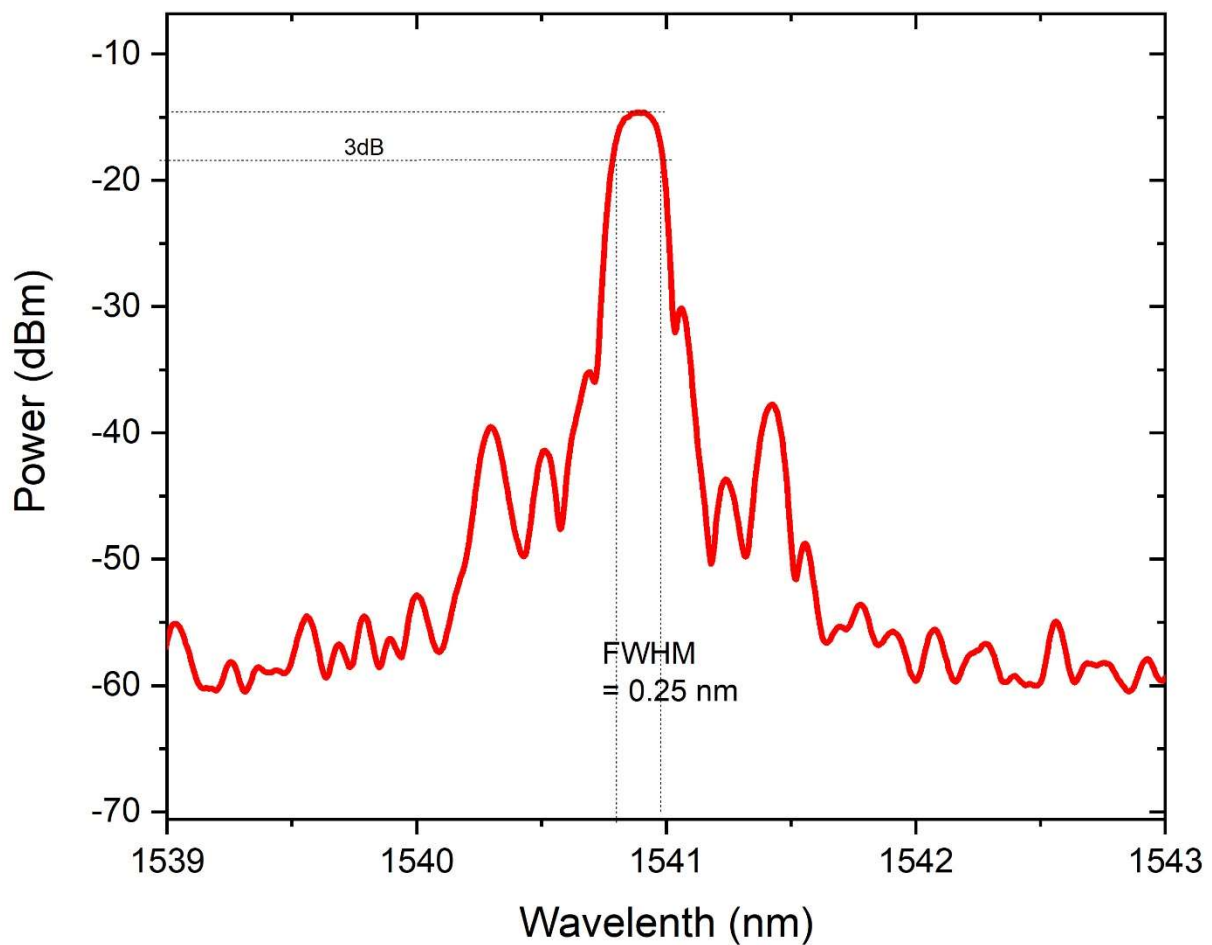

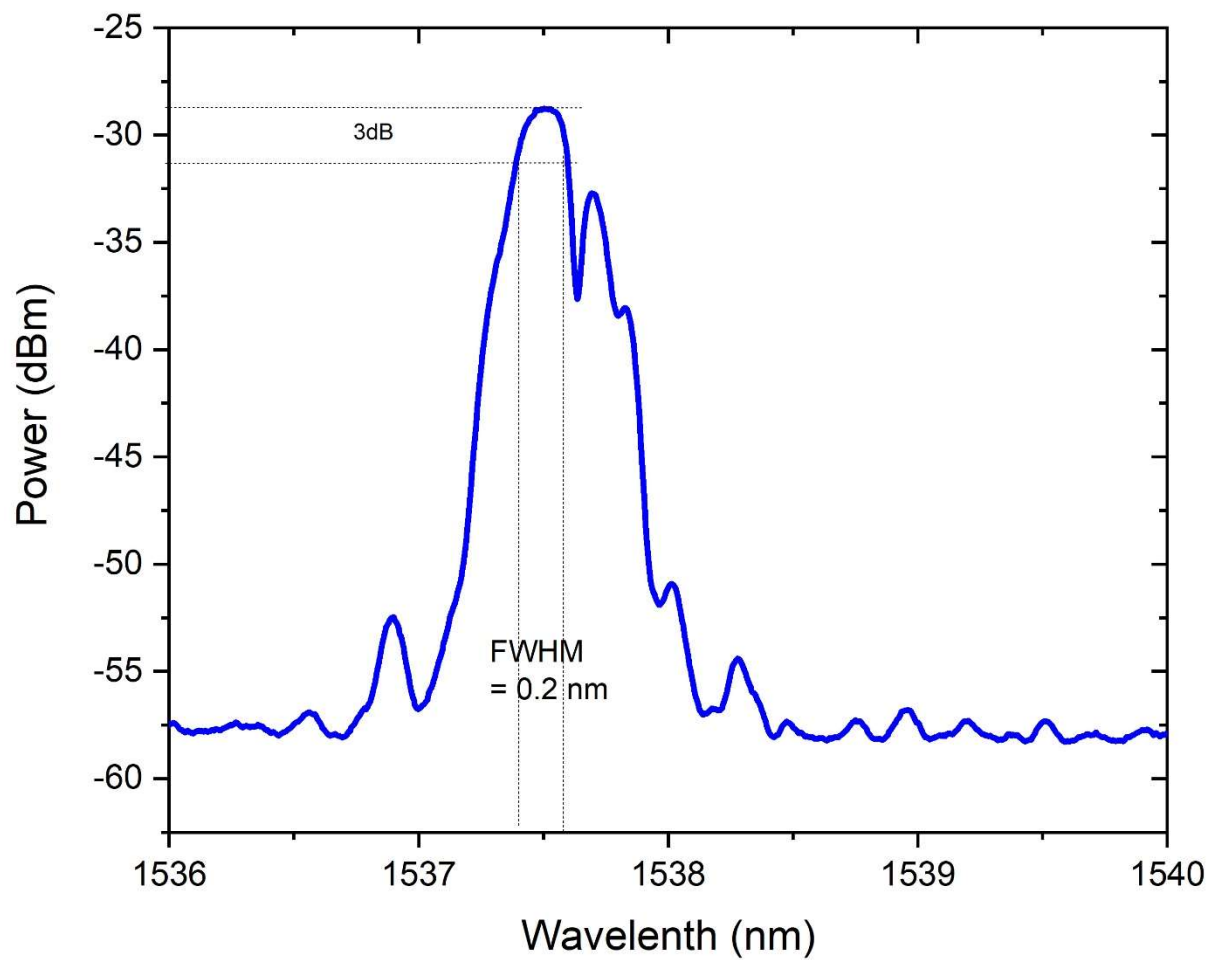Figure 4A.1. Full width half maximum (FWHM) for conventional optical fibre (OF)

Figure 4A.2. Full width half maximum (FWHM) for micro-braided optical fibre (MBOF).